Thesis submitted to the University of Nottingham for the degree of

Doctor of Philosophy

Multiphoton photoelectron circular dichroism and photoelectron angular distributions of aligned polyatomic molecules

Dhirendra Pratap Singh

July 31st, 2020

Supervisors: Professors Katharine Reid and Ivan Powis

Abstract

In this work we have measured photoelectron angular distributions (PADs) from small polyatomic molecules in the weak-field limit. We have conducted experiments in a variety of multiphoton schemes in different polarization geometries with a view to gaining insight into molecular photoionization dynamics. In particular, we have performed novel experiments using the techniques of strong-field alignment and photoelectron circular dichroism.

The use of a strong-field alignment pulse has enabled us to approach a molecular frame measurement in the two-photon ionization of aniline and naphthalene. We have compared our measured PADs with calculations performed using the ePolyScat package. In the case of naphthalene good agreement is observed with molecular frame simulations, but in the case of aniline the experimental results cannot be reproduced by the calculations. This is attributed to perturbation of the ionization process by the alignment pulse in the case of aniline.

Multiphoton photoelectron circular dichroism (MP-PECD) has been used to study the chiral monoterpenes α-pinene, 3-carene and fenchone. MP-PECD experiments performed with table-top femtosecond UV laser sources have previously been shown to enhance the chiral anisotropy observable in one-photon schemes. In this work we use a picosecond laser source which has enabled us in addition to unravel the vibronic dependence of the photoionization dynamics.

Acknowledgements

First and foremost, I would like to express my sincere gratitude to both the supervisors Prof. Katharine Reid and Prof. Ivan Powis for their continuous support in the completion of this work. Both have been very patient and encouraging from the very first day. Their guidance and immense knowledge have helped me in all the time of research and writing of this thesis. Long office discussions and pub chats at various beam times with Ivan have been very insightful and encouraging. Many thanks to other fellow group members: James, Laura, and Adrian. A special thanks to Hassan for making these four years fun and memorable. I would also like to thank other staff members of the chemistry department, Neil Barnes, David (Electrical workshop), Ruth (for sorting out all the travel arrangement), Sue (for supplying gallons of tea over the past four years).

I would like to thank a very significant person in my life, Syama, without whom this journey would have been boring. She has been an incredible pillar of support for these past four years. I would also like to thank all people I came across during this PhD, who I became good friends with and supported me in this journey; Dishil, Graham, Sachin Ji, Payal, Rym and Jenny. I would also like to thank my IISER friends in India and abroad; Debi, Danish, Katu, Kundu Ji, and special thanks to Alok for motivating me to run a marathon, hope we run one together soon.

I would like to thank my parents and my brother Rohit for their incredible support and many sacrifices. I am forever in their debt for giving me this life and good education.

Finally, I would like to thank the Marie Curie funding, EU H2020 MSCA ITN "ASPIRE", without which this project would not have been possible and whole the ASPIRE network, especially the team Nick, Melissa, Joe for organizing all the meetings and running the network smoothly.

"Nobody believes in friendship; people talk about it, that's the thing about friendship - It's a lot rarer than love because there's nothing in it for anybody".

– Are you here (2013, Film, Dir. Matthew Weiner)

Table of Contents

Chapter 1 Introduction

1.1 **Overview**

The process of photoionization involves the interaction of a radiation field with matter and the subsequent ejection of a photoelectrons. In the case of molecular photoionization, the emitted photoelectrons scatter off the molecular ion in such a way that they carry a signature of the neutral and ionic structure. Photoelectron energy spectra provide information on the energy levels of the ion created during the process, whereas photoelectron angular distributions (PADs), which result from the interference of photoelectron partial waves, are sensitive to molecular configuration. PADs have been used as probes of, for example, valence photoionization dynamics of polyatomic molecules [1–3], intramolecular processes such as internal conversion, intersystem crossing and photodissociation [4–7], and the chirality of biologically significant molecules [8–11]. One of the themes in this thesis is an exploration of photoelectron circular dichroism (PECD), in which PADs from chiral molecules are measured with both left- and right-handed circularly polarized light. The PECD technique has been used to differentiate enantiomers and to perform fast real time determination of their absolute handedness [12, 13], exceeding the performance of standard mass spectrometry methods.

In recent years techniques have been developed to maximise the information contained in PADs by relating measurements to the frame of reference of an individual molecule; this gives rise to so-called molecular frame (MF) PADs [14]. The MF-PADs measurements can be achieved by detecting electrons relative to a dissociative bond [15, 16] or through strong field alignment technique [17–19]. Unlike the first method, strong field alignment method can be applied to non-dissociative ionization processes and polyatomic molecules, providing that the molecular polarizability is axis dependent. The pioneering work of Stapelfeldt and co-workers have demonstrated the one- and three-dimensional alignment of both naphthalene [17] and benzonitrile [18]. One dimensional alignment is achieved through interaction of molecular polarizability with linearly polarized light, whereas three-dimensional alignment is achieved through using elliptically polarized light. If the measurements are done in weak field limit, they can provide a means of obtaining a complete description of photoionization dynamics [20–22].

In the work presented in this thesis we use the techniques of PECD and strong-field alignment to study molecular photoionization dynamics of polyatomic molecules. In the experiments described we prepare a molecule in an excited electronic state prior to ionization and then monitor the emitted photoelectrons using velocity-map imaging. Two main topics have been addressed: (i) can the technique of strong-field laser alignment be used to "freeze" molecules prior to ionization and (ii) can state-selection provide enhanced information on molecular chirality compared with other techniques. In this introductory chapter we lay out the ingredients that are needed in order to address these topics.

1.2 **Born-Oppenheimer approximation**

Molecules are inherently quantum mechanical and are therefore described by the Schrödinger equation. Although this cannot be solved exactly for a molecular systems (more than one electron systems) we can make use of the fact that the mass of an electron is much smaller than the mass of a proton to infer that the motion of the nuclei is much slower (picosecond time scales) than the motion of electrons (attosecond time scales). This observation is the root of the Born–Oppenheimer (BO) approximation which allows the two motions to be treated separately. Within the BO approximation the molecular wavefunction can be written in the form,

$$\psi_{total} = \psi_{electronic} * \psi_{vibration} * \psi_{rotation} \tag{1.1}$$

and therefore that the energies due to each type of motion are additive,

$$E_{total} = E_{electronic} + E_{vibration} + E_{rotation} \tag{1.2}$$

where ψ_{total} and E_{total} are the wavefunction and total energy of the system. This approximation gives rise to independent quantum numbers that can be used to describe electronic and vibrational states. The BO approximation is extremely essential to the work presented in this thesis as it provides the framework to discuss the observations in terms of states and various quantum numbers.

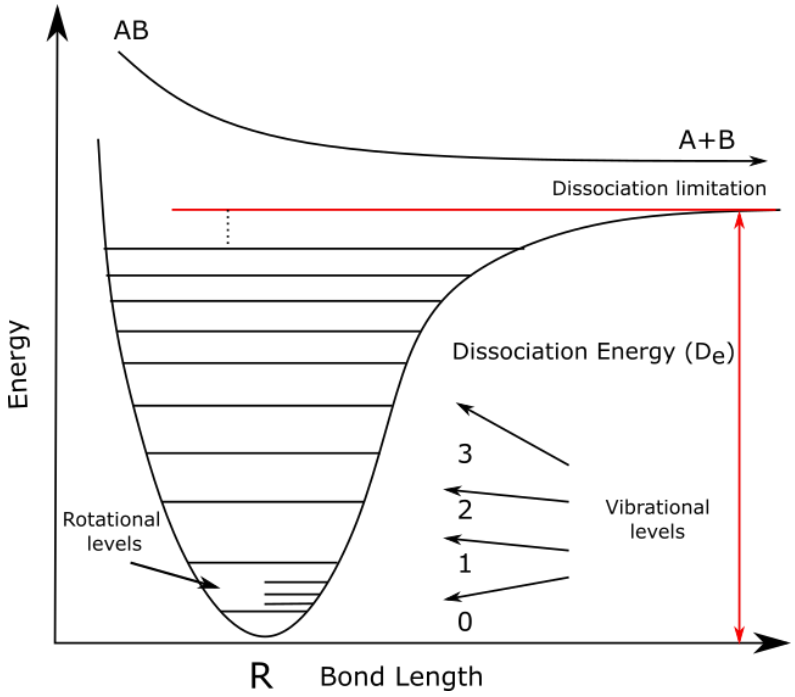

Figure 1.1. Potential energy curve for a diatomic molecule (AB) showing vibrational and rotational levels.

Understanding the molecular system in this framework leads to the concept of potential energy surfaces. A potential energy surface shows the energy of a molecule as a function of the positions of its nuclei. These potential energy surfaces are obtained by solving the electronic Schrödinger equation for different nuclei positions. This potential is then used to solve the nuclear part of the Schrödinger equation. This step of the BO approximation leads to separation of vibrational, and rotational motions of a molecular system. Figure 1.1 shows an example of a potential energy curve for a diatomic molecule, where R is nuclear coordinates and D_e is the dissociation energy. Each electronic state of a molecule has a separate potential energy surface, and the separation between these surfaces yields the electronic spectrum.

1.3 **Photoionization and photoelectron spectroscopy**

In a photoionization process the wavefunction of the ejected electrons can be treated as a sum of partial waves with different angular momenta, each of which carries a phase shift:

$$\phi_e = \sum_{lm} c_{lm} e^{i\delta_l} Y_{lm}(\theta, \phi) \qquad (1.3)$$

where c_{lm} are the coefficients which contains radial and angular information about the state from which the scattering occurred and about the continuum, and δ_l is a scattering induced phase shift. The spherical harmonic functions, $Y_{lm}(\theta, \phi)$, are known as partial

waves and are labeled by an orbital angular momentum quantum number l and a laboratory frame projection quantum number m. The whole process of ionization can be represented in terms of a bound-free matrix element, which contains the details about the dynamics of the photoionization. Within the electric dipole approximation, this ionization matrix element can be written using the photoelectron wavefunction, ϕ_e, the wavefunction of the state from which the electron has been ejected, ψ_i, and the wavefunction of the ion formed, ψ_+,

$$\mu_{i+} = \langle \psi_+, \phi_e | \mu . E | \psi_i \rangle \qquad (1.4)$$

where μ is the electric dipole operator and E the electric field vector of the ionizing radiation. For the bound-free transitions it is necessary to find the square of the transition matrix elements to determine the transition probability. Furthermore, to calculate angular distributions of photoelectrons, I (θ, ϕ), it is necessary to consider the coherent square of the transition matrix elements as the presence of coherence in the angular distribution makes it sensitive to the relative phases of the photoelectron partial-waves, and thus a sensitive probe of the photoionization dynamics.

Photoelectron spectroscopy involves the measurement of the kinetic energies of electrons ejected from a molecule during the process of ionization. In the next sections we will discuss the required topics to follow photoelectron spectroscopy technique used in this work.

1.3.1 Resonance enhanced multiphoton ionization

In order to probe molecular energy levels we use photoionization process. The ionization process regimes are determined by the Keldysh parameter, $\gamma = \omega(2I_P)^{1/2}/E_o$, where ω is the frequency, I_P is the ionization potential and E_o is the maximum electric field of the laser [23]. When $\gamma \ll 1$, it is referred as tunnelling ionization, where the electron can escape from the static barrier formed by the Coulomb potential and laser electric field. In the opposite regime when $\gamma \gg 1$, the electron is ionized from molecules by absorbing multiple photons, known as multiphoton ionization regime. In the work presented in this thesis has been performed in multiphoton ionization regime. We used the technique of Resonance-Enhanced Multiphoton Ionization (REMPI) which provides information on excited electronic states and their vibrational structure. In the REMPI process *n* photons from a tunable light source (the pump) excite molecules to a resonant intermediate state prior to

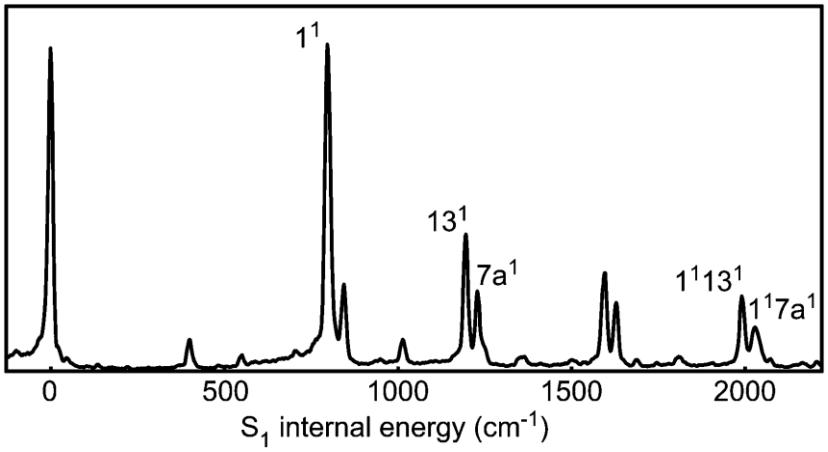

Figure 1.2. An example of a (1+1') REMPI spectrum of p-fluorotoluene [24].

ionization in a probe step with either *m* photons from the same source, or *m′* photons from a different source. The experimental work presented in this thesis, a (1+1) REMPI was used to study the photoionization dynamics of aniline and naphthalene and (2+1) REMPI was used to study α-pinene, 3-carene, and fenchone. In a REMPI spectrum the total ion current is monitored as the wavelength of the pump laser beam is tuned. Figure 1.2 shows an example of (1+1') REMPI spectrum [24]. The resulting spectrum consists of peaks that occur every time the pump laser comes into resonance between a ground state vibrational level and an excited state vibrational level. In order to understand the information this provides we need to introduce the Franck-Condon principle.

1.3.2 Franck-Condon principle

In an electronic transition the propensity of vibrational transitions can be explained on the basis of the Franck-Condon (FC) principle. The FC principle states that when a molecule is undergoing an electronic transition, the nuclear configuration of the molecule experiences no significant change. In analogy to the Born-Oppenheimer approximation, this is due to the fact that nuclei are much more massive than electrons so that the electronic transition takes place faster than the nuclei can respond. Thus, the relative intensity of a vibrational transition from the vibrational level v'' in the ground state of the molecule to v' in the excited or ion state is given by the square of the overlap integral between the ground and excited state vibrational wavefunctions $\chi_{v''}$ and $\chi_{v'}$,

$$FCF = |\langle \chi_{v'} | \chi_{v''} \rangle|^2 \qquad (1.5)$$

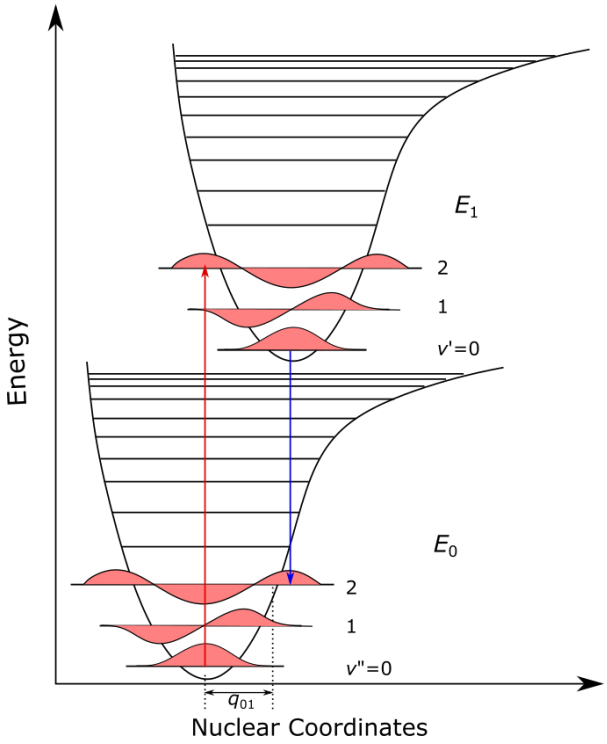

Figure 1.3. Franck–Condon principle energy diagram. Since electronic transitions are very fast compared with nuclear motions, vibrational levels are favoured when they correspond to a minimal change in the nuclear coordinates. The potential wells are shown favouring transitions between v'' = 0 and v' = 2.

which is known as the Franck-Condon factor (FCF). As a result, the probability of populating a specific vibrational level is more likely if there is a significant overlap of the two vibrational wavefunctions. Figure 1.3 shows an example of vibronic transitions for the emission and absorption of a photon. The two potential wells show a favoured transition from $v'' = 0$ to $v' = 2$ upon absorption and emission. In the case where there is little change in the shape of the potential energy surface from the lower to upper electronic state, i.e. little change in bond length, force constants etc., the strong transitions are those in which the vibrational quantum number remains the same in going from the lower to upper electronic state, i.e. $\Delta v = 0$. This generality is known as a propensity rule. An example of this is where an electron in a Rydberg state undergoes a transition to a cation state. As the shape of the Rydberg potential energy surface is almost parallel to the cation state, these transitions tend to follow a $\Delta v = 0$ propensity rule upon ionization from these states. The direct result of this propensity rule can be seen more clearly in Chapter 3, 4, 5.

1.3.3 REMPI-PES

Resonance enhanced multiphoton ionization photoelectron spectroscopy involves the detection of electrons ejected from a molecule during the process of ionization. This technique can be used to identify the molecular properties such as ionization potential, and electron affinity by observing how much energy is imparted to the outgoing electron ejected during ionization. As shown in figure 1.4, vibrational levels below the

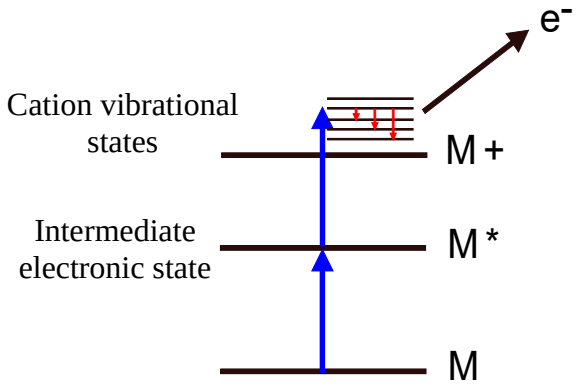

Figure 1.4. Schematic diagram of the (1+1) REMPI-PES process.

energy provided by the probe photon can be populated as excess energy can be carried away by the ejected photoelectron. The vibrational population distribution in the cation follows the Franck-Condon principle, as discussed in Section 1.3.2. The energy distribution of photoelectrons reflects the distribution of vibrational states formed in the cation.

Photoelectron spectra can be measured using a number of techniques, including Time-Of-Flight (TOF) spectroscopy, Zero Electron Kinetic Energy (ZEKE) spectroscopy, and the related Mass Analysed Threshold Ionisation (MATI) spectroscopy. In the time-

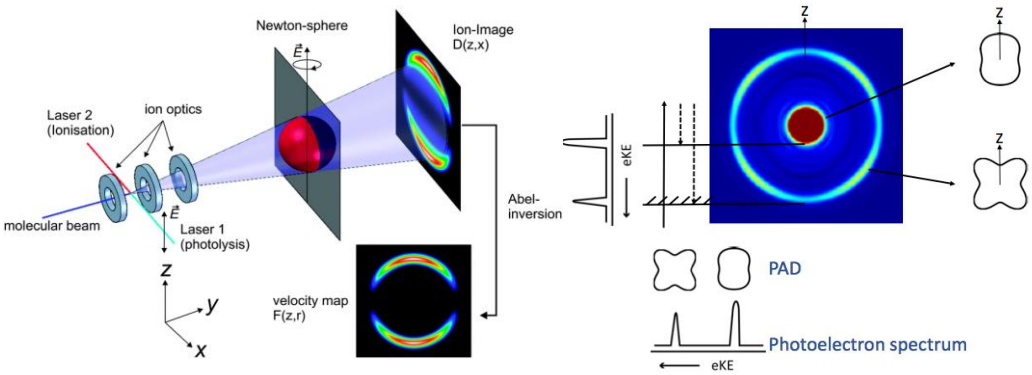

Figure 1.5. (a) Velocity Map Imaging, (b) Photoelectron spectrum and angular distribution.

of-flight method, the kinetic energy of the electrons is determined by the time it takes for them to travel through a field-free region after ionisation.

In this work, however, Velocity Map Imaging (VMI) and PhotoElectron PhotoIon COincidence (PEPICO) methods are used (Chapter 2). VMI spectroscopy is a method to investigate the velocity-distribution of charged particles in a volume. The VMI spectrometer consists of three parts. The electrostatic lens (a combination of three electrodes), the flight tube and the detector system. Figure 1.5 (a) shows the VMI setup, based on the design of Eppink and Parker [25].

1.3.4 Effect of laser pulse duration

Laser pulse width has an important role in multiphoton ionization. A longer pulse is always more efficient when the life-time of an excited state is longer than the pulse widths of the lasers used in the multi-photon ionization process [26]. For an excited state with a short lifetime a strong pumping is required to overcome the fast decay. Thus different laser pulse widths can be chosen according to requirements of the study that needs to be done. For example, a femtosecond laser pulse can be used to study the fast electron dynamics, whereas picosecond and nanosecond pulses can be used to study the vibrational and rotational dynamics respectively, but there are also caveats to using different pulse widths. The femtosecond pulses are broader spectrally, therefore are capable of exciting many energy levels hence the loss of resolution and information on vibrational dynamics. However, picosecond pulses are narrower spectrally and can excite specific energy level, thus, improving resolution and are capable of studying any vibrational dynamics. In the present work we aim to study the effect of vibrational state on PECD; thus a picosecond laser pulse is used to achieve the required vibrational resolution for multiphoton PECD experiments.

1.4 Photoelectron angular distributions

The intensity of photoelectron emission as a function of the angle of ejection with respect to the polarization vector of the ionizing light is known as the photoelectron angular distribution (PAD). The PAD provides complementary information to the photoelectron spectra.

The angle-dependent photoelectron intensity results from the square of the transition dipole matrix given in Eq. (1.4) [27]:

$$I(\theta,\phi) = |\langle \psi_+,\ \phi_e|\mu.E|\psi_i\rangle|^2 \tag{1.6}$$

If we now substitute Eq. (1.3) into Eq. (1.6) we find [27]

$$I(\theta,\phi)\ \propto\ \sum_{L=0}^{L_{max}} \sum_{M=-L}^{L} B_{LM} Y_{LM}(\theta,\phi) \tag{1.7}$$

where $Y_{LM}(\theta,\phi)$ is a spherical harmonic and the B_{LM} coefficients are given by

$$B_{LM} = \sum_{ll'} \sum_{\lambda\lambda'} \sum_{mm'} (-1)^m \sqrt{\frac{(2l+1)(2l'+1)(2L+1)}{4\pi}} \tag{1.8}$$
$$* \begin{pmatrix} l & l' & L \\ m & -m' & M \end{pmatrix} \begin{pmatrix} l & l' & L \\ 0 & 0 & 0 \end{pmatrix} \gamma_{N_+ l\lambda m l'\lambda' m'}$$
$$* r_{l\lambda} r_{l'\lambda'} \cos(\eta_{l\lambda} - \eta_{l'\lambda'})$$

The $\gamma_{N_+ l\lambda m l'\lambda' m'}$ terms are geometrical parameters and incorporate all of the angular momentum coupling in the system, which can be evaluated using algorithms. The dynamics is contained in the magnitudes and phases of the radial dipole matrix elements, $r_{l\lambda}$ and $\eta_{l\lambda}$, whose calculation is beyond the scope of this thesis. However, if we determine the geometrical parameters we can use Eq. (1.8) to determine $r_{l\lambda}$ and $\eta_{l\lambda}$ by fitting photoelectron angular distribution data from experiment [28]. The form of this equation results from the interference of pairs of photoelectron partial waves with orbital angular momenta l and l' where $l + l' = L$. In the laboratory frame, assuming the sample is initially isotropically distributed in space, $L_{max} = 2n$, where n is the number of photons used in the photoionization scheme. The first coefficient in Eq. 1.7, B_{00}, is proportional to the angle-integrated photoelectron intensity and the subsequent B_{LM} coefficients describe the anisotropy of the PADs. The number of terms in Eq. 1.7 can be reduced through the use of symmetry. For example, in the case where there is reflection symmetry L must be even and cylindrical symmetry requires $M = 0$.

In the case of atomic photoionization, there is no body-fixed axis system to refer to, and only the anisotropy of the light gives a point of reference to the emitted photoelectrons. But molecular photoionization is different, in that a reference frame for the photoelectrons is provided by both the molecular axis and the projection of the polarization of the ionizing light onto it. The angular distribution with respect to the molecular axis reflects orbital angular momentum partial waves that contribute to the photoelectron wave function and may show rich structure. In order to maximize the information extracted from angular distributions it is desirable to measure them relative to the molecular frame of the molecules rather than to the laboratory frame.

Molecular frame photoelectron angular distributions have been used to perform the examination of a quantum mechanical phenomenon [7, 8] and provide an extremely useful means to study the continuum resonance both in ionization [29] and dissociation [10, 11]. It has also been shown that MF-PADs provide direct information on molecular orbitals if the ionization is in the tunneling regime [30]. So achieving MF-PADs is extremely useful for fundamental studies. One method of accessing these MF-PADs involves aligning the molecules by interaction with a laser pulse prior to the photoionization. For example, it is possible to align an ensemble of symmetric top molecules using resonant steady-state excitation with polarized light; this causes the molecular symmetry axes to have a well characterized ensemble alignment in space [31].

An alternative is to use non-resonant polarized laser light to create alignment in the molecule. In this technique, the polarizability of a molecular system is exploited to align it along with the polarization of the laser light. In the past few years, this technique has been extended to the alignment of polyatomic molecules in three dimensions as well [17–19]. An advantage of this technique is that it is not inherently limited to small molecular systems. This interaction depends on the polarizability of the molecule; the laser field induces a maximum dipole moment along the most polarizable axis which then aligns with the axis of the laser field [19]. For the work presented in this thesis, we used the strong field alignment technique. In the next section, we will discuss the strong field alignment technique and various lab parameters which can affect the alignment of the molecules.

1.5 **Alignment**

Usually in gas phase photoionization experiments the ensemble of molecules is randomly oriented. The principle axis of the molecules is in all possible directions with respect to the lab frame. The lab frame is defined by the polarization of the ionizing laser pulse in case of linear polarization and propagation direction in case of circularly polarized light. If an anisotropy arises in the randomly oriented molecular ensemble, then the system is said to be aligned with some degree. Thus, alignment refers to order of the molecules with respect to given axes fixed in space. If, in addition, the molecules also have a preferred direction with respect to the space fixed axes, i.e., the inversion symmetry is broken, they are said to be oriented.

In the previous section we briefly mentioned two techniques which can lead to anisotropy in the molecular system. This degree of alignment can be expressed mathematically as [32],

$$P(\theta,\phi) = \sum_{K=0}^{K_{max}} \sum_{Q=-K}^{K} A_{KQ} Y_{KQ}(\theta,\phi) \quad (1.12)$$

where θ and ϕ are defined with respect to a laboratory frame Z-axis defined by the ionizing light beam. The value of coefficients in the Eq. 1.12 can be varied by changing the experimental polarization geometry, and some coefficients can be set to zero by careful choice of geometry. For example, for cylindrical symmetry only $Q = 0$ is allowed, and for reflection symmetry K is even. For one-photon excitation, the

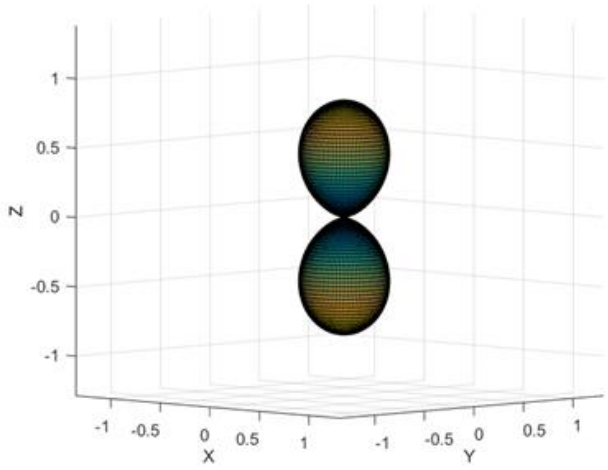

Figure 1.6. Plotted distribution for $P(\theta) = cos^2\theta$.

distribution of molecular axes is described as,

$$P(\theta) = A_{00}Y_{00} + A_{22}Y_{22} \quad (1.13)$$

$Y_{00} = \frac{1}{2}\sqrt{\frac{1}{\pi}}$, and $Y_{22} = \frac{1}{4}\sqrt{\frac{5}{\pi}}(3cos^2\theta - 1)$ are the relevant spherical harmonics. In general, the values of the contributing alignment moments can be determined from a known distribution of molecular axes through the relationship,

$$A_{KQ} = \int_0^{2\pi}\int_0^{\pi} P(\theta,\phi)\frac{Y_{KQ}(\theta,\phi)}{Y_{00}(\theta,\phi)}\sin\theta d\theta d\phi \quad (1.14)$$

However, the full distribution of molecular axes is generally unknown in a given experiment, and one-dimensional alignment is typically characterized by the single parameter $\langle\cos^2\theta\rangle$ [19] where

$$\langle \cos^2\theta \rangle = \int_0^{2\pi}\int_0^{\pi} \cos^2\theta\, P(\theta,\phi)\sin\theta d\theta d\phi \qquad (1.15)$$

A_{KQ} coefficients can be calculated for a specific molecular alignment which is feasible experimentally. For example, setting $P(\theta) = cos^2\theta$, $A_{20} = 2/\sqrt{5}A_{00}$. So, if $A_{00} = 1$ $A_{20} = 0.8944$. Figure 1.6 shows the plotted distribution for $P(\theta) = cos^2\theta$.

1.6 **Strong field alignment**

In strong field alignment (SFA), molecules can be aligned using non-resonant laser fields by exploiting their polarizability anisotropy. This can be understood by solving the Schrödinger equation using the Hamiltonian for a molecule placed in an electric field [33]. If the electric field is given by

$$E = \hat{e_z}E_0\cos(\omega t) \qquad (1.16)$$

then the Hamiltonian of the system is

$$H = BJ^2 - \mu.E \qquad (1.17)$$

where B is the rotational constant of the molecule, J^2 is the squared angular momentum operator, and μ is the dipole moment of the molecule, and

$$-\mu.E = 1/4E_0^2([\alpha_{\parallel} - \alpha_{\perp}]cos^2\theta + \alpha_{\perp}) \qquad (1.18)$$

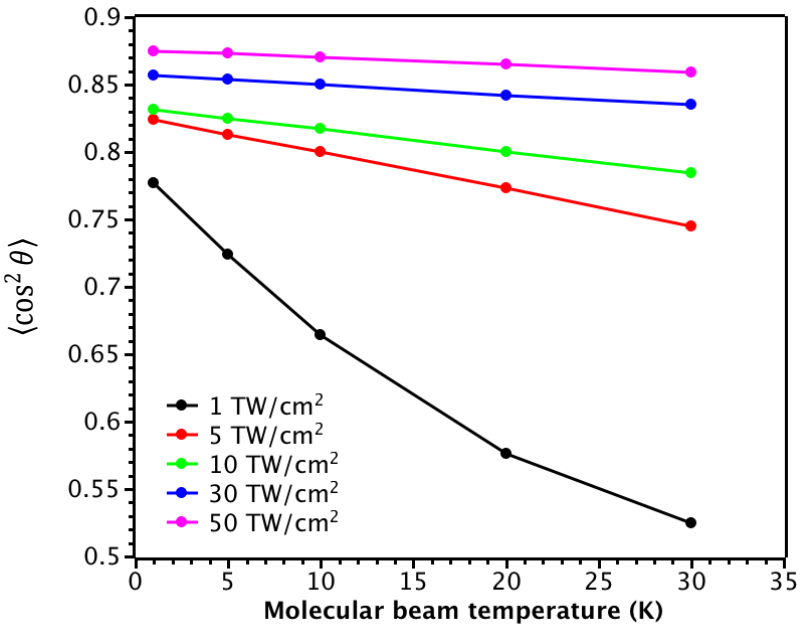

Figure 1.7. Illustrating the effect of laser intensity and molecular beam temperature on the degree of alignment characterized by $\langle cos^2\theta \rangle$ for the symmetric top molecule, methyl iodide.

where, θ is the polar angle between the electric field and the molecular axis, and $\alpha_{\parallel}$ and $\alpha_{\perp}$are the polarizability component parallel and perpendicular to the molecular axis. The $\mu.E$ term will be determined by the interaction between the field and the induced dipole moment averaged over an optical period, as the interaction between field and permanent dipole moment time averages to zero. If $\alpha_{\parallel} > \alpha_{\perp}$, Eq. 1.18 shows potential minima around $\theta = 0^0$ and $\theta = 180^0$. This will force the most polarizable axis of the molecule to align along the direction of the electric field. Experimentally, the degree of alignment for a molecule is usually quantified by the expectation value $\langle \cos^2 \theta \rangle$. An isotropic distribution of molecular axes would result in $\langle \cos^2 \theta \rangle = 1/3$ and a distribution that is perfectly aligned along the laboratory frame Z axis would have $\langle \cos^2 \theta \rangle = 1$. If the duration of the laser pulse is long compared with the rotational period of the molecule the axis which has the largest polarizability will align along the polarization axis as long as the pulse is on; this is called adiabatic alignment. On the other hand, if the duration of the laser pulse is shorter than a rotational period, then a coherent rotational wavepacket is prepared. In this case non-adiabatic alignment, alignment occurs right after the pulse and then decays and fully revives after a rotational period [34]. The rotational period of a linear molecule is 1/2B (B being the rotational constant expressed in Hz). Therefore, a full revival is observed at 1/2B and a half revival at 1/4B for a linear molecule.

The degree of alignment that can be achieved depends on various factors, such as the rotational temperature of the molecular beam, laser intensity, and polarizability of the molecule. Figure 1.7 shows how $\langle \cos^2 \theta \rangle$ depends on molecular beam temperature and laser intensity for methyl iodide. The values shown in this figure were obtained using software provided by the Stapelfeldt group at Aarhus University. It can be seen that high laser intensities and efficient cooling of the molecular beam help to achieve the best degree of alignment. However, it should be noted that high intensities come with the drawback of the strong field causing significant Stark shifts, Coulomb explosion and multiphoton ionization.

It is useful to compare the experimental measure of alignment, $\langle \cos^2 \theta \rangle$ with the alignment coefficients introduced in the previous section. We will briefly discuss the formalism provided by Reid [35] to express this degree of alignment in terms of alignment coefficients. As mentioned in the previous section the degree of alignment can be expressed in terms of spherical harmonics (Eq. 1.12). This equation can be

simplified based on cylindrical symmetry ($Q = 0$). The degree of alignment can also be well represented using a Gaussian form if we assume cylindrical symmetry and no orientation of the molecules [36],

$$P(\theta, \phi) = n_\sigma exp\left(\frac{-sin^2\theta}{2\sigma^2}\right), \tag{1.19}$$

where n_σ is a normalization constant and σ^2 relates to angular width with $0 < \sigma^2 \leq 1$. For small values of σ^2, it is very approximately related to $\langle\cos^2\theta\rangle$ by

$$\lim_{\sigma^2 \to 0} \sigma^2 = 1 - \langle\cos^2\theta\rangle. \tag{1.20}$$

In some strong-field alignment experiments σ^2 is measured directly; alternatively, σ^2 can be determined from an experimentally determined value of $\langle\cos^2\theta\rangle$, using Eqs. 1.15 and 1.19. Once σ^2 is known, the alignment moments needed to characterize the molecular axis distribution can be calculated using Eq. 1.14. Table 1.1 shows the A_{KQ} coefficients corresponding to any experimentally achievable degree of alignment, $\langle\cos^2\theta\rangle$. The next section presents some model calculation showing the effect of degree of alignment (expressed in terms of A_{KQ} coefficients) on lab frame PADs.

Table 1.1. Alignment coefficients for $P(\theta) = cos^n\theta, n = 2, 4, 6, 8$ as well as the corresponding degree of alignment in terms of $\langle cos^2\theta\rangle$

A_{00}	A_{20}	A_{40}	A_{60}	A_{80}	P (θ)	$\langle cos^2\theta\rangle$,
1	0	0	0	0	1	0.5
1	0.8944	0	0	0	$\cos^2\theta$	0.75
1	1.277	0.381	0	0	$\cos^4\theta$	0.83
1	1.491	0.727	0.1344	0	$\cos^6\theta$	0.875
1	1.626	1.007	0.323	0.043	$\cos^8\theta$	0.9

1.6.1 Early work on MFPADs

Early work on MFPADs was done using an axial-recoil approximation method known as COLd Target Recoil-Ion Momentum Spectroscopy (COLTRIMS). If the dissociation of a molecule after photoionization is fast compared to its rotational time scale, one can derive the molecular axis orientation in space by measuring the momentum vectors of the molecular fragments. This technique developed during the late '80s, gives access to "kinematically complete" experiments on atomic and molecular fragmentation processes by coincident and momentum resolved detection of recoiling target ions and emitted electrons. In 2002, Gessner et al. [37] presented the molecular frame angular distribution of NO molecules at a photon energy of 40.8 eV. In 2003 Lebech et al. [20] presented the MFPADs experimental results in comparison with the theoretical results for NO at photon energy of 23.65 eV. Similar work by Lebech [38] explored the valence and inner valence-shell photoionization of

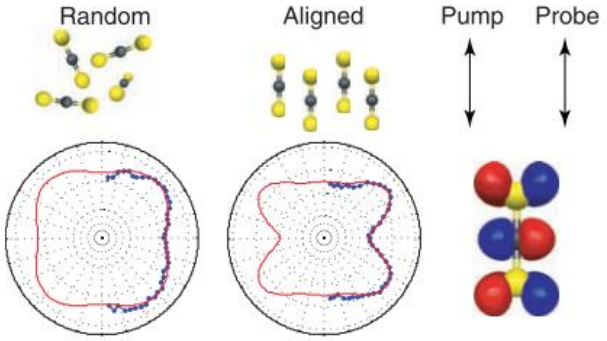

Figure 1.8. Molecular frame PADs of CS_2 molecules [6].

CO in the range of 26-33 eV. In 2014 Stener et al. presented the off-resonance dynamics of MFPADs as a function of photoelectron energy and polarization geometry for CH_3F. This is a very powerful technique, but it is limited to a small molecular system that dissociate in the axial recoil limit.

The strong field alignment technique, as discussed in the previous section, creates an aligned distribution of molecules prior to ionization [19]. In this case the measured PADs will converge on the molecular frame if complete alignment can be achieved in three dimensions, and this technique can, in principle, be applied to large molecular systems. This is a well-established technique which makes use of intense infrared pulses to align molecules in either adiabatic or non-adiabatic regime as mentioned in the previous section. Early work using the SFA technique was presented by

Kumarappan et al. [39]. These authors used two 800 nm pulses, one to align and a second for multiphoton ionization of CS_2. They presented a clear observation of a change in angular distribution between aligned and unaligned system and showed the dependence on the angle between the two pulses (aligning and ionizing). In pioneering work by Stolow and coworkers, a UV pump pulse was used to prepare a dissociative state in laser aligned CS_2 molecules (figure 1.8). The dissociating molecules were ionized with a time delayed UV probe pulse, enabling the dissociation to be tracked through the evolution of the PADs [6]. In 2010, Holmegaard et al. [18] presented work on OCS and benzonitrile molecules using the SFA technique. This time the authors had used an electrostatic field to orient the molecules along with the alignment. The authors presented a clear difference in the angular distribution for oriented molecules when ionized with left and right circularly polarized light. In 2011, Hansen et al. [17] presented work on time-resolved PADs from adiabatically aligned naphthalene molecules. They used a nanosecond pulse to align the system and a 200 fs pulse to kick to the system, which rotates the molecule around the fixed axis. A third probe pulse (30 fs) was used to image the H^+ fragments and electrons while molecule rotates. A clear change in PADs was observed as the molecule rotated around the fixed axis, as a result of the kick pulse. Another method was presented by Maurer et al. to measure the full 3D molecular fame using tomographic reconstruction for naphthalene [40].

In recent years more work has been shown using a single VUV photon from a High Harmonics Generation (HHG) source enabling determination of photoionization dynamics. Kelkensberg et al. presented work using a HHG source and free-electron lasers (FELs) combined with the SFA technique on CO_2 molecules [41]. Similar work was presented by Rouzée et al. using a HHG source and SFA on O_2, N_2, CO, and CO_2 [42, 43]. Recently, Marceau and co-workers have presented the complete photoionization dynamics of CO_2 using time-domain photoionization interferometry [44].

The work presented in this thesis employs intense 800 nm laser pulses to create the aligned distribution of aniline and naphthalene molecules. This work used a sharp spectrally cut pulse at 800 nm (more details in Chapter 2) to reduce the field effect on the photoionization dynamics. The molecules are subsequently ionized in the weak-field regime using a resonant two-photon ionization scheme, with photoelectrons collected using VMI.

1.8 **Chirality**

The word chirality comes from the Greek word cheir, which means 'hand,' because hands are the most widely recognised example of chirality – they are not identical when superimposed on their mirror image. Chirality is a striking property of the biological world. Most, but not all, molecules in the plant and animal world are chiral, and usually only one handedness is found. It can also be found in animals such as snails, where the population can be divided based on shell handedness. These two types of snails are genetically separated, and these two types do not mate, is an excellent example of chirality in selective biology. In nature, various types of chirality can be found, such as central, helical, axial, planar. Figure 1.9 shows such few examples of chirality found in nature. Trefoil knot and Mobius strip are an excellent example of topological chirality. A chiral molecule is non-superimposable on its mirror image, and these mirror images are known as optical isomers or *enantiomers.* In the context of the pharmaceutical world, chirality is extremely important. As most building blocks of nature, for example, our DNA is right-handed, amino acids are left-

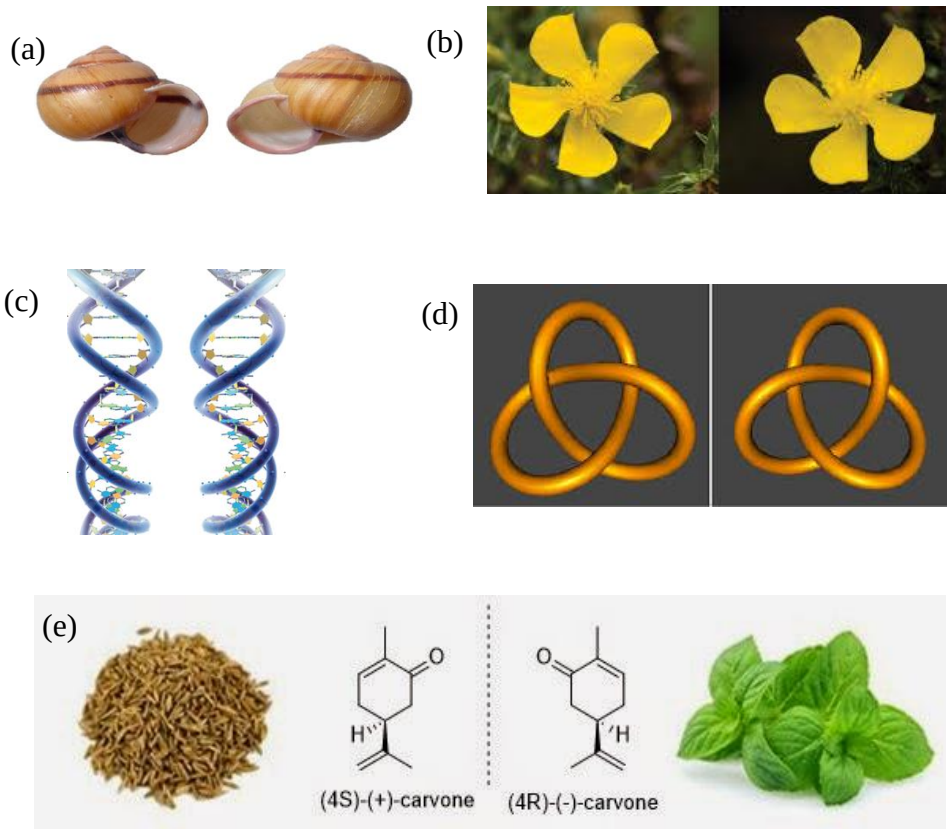

Figure 1.9. Few examples where chirality can be found in nature. (a) chirality in snail shells, (b) chirality in flower pattern, (c) chirality in DNA, (d) topological chirality, trefoil knot, (e) chirality in molecules.

handed, all carbohydrates are right-handed, and even our olfactory receptors are chiral. As a result, chirality plays a huge role in drug delivery and processing. The 'wrong-handed' version of a molecule in a drug can work totally different in the body. There are several techniques available these days to quantify the chiral nature of the molecules. The most common method used today to separate enantiomers is liquid or gas chiral chromatography. Once enantiomers are separated, one can determine their respective enantiomer excess by methods such as circular dichroism, vibrational circular dichroism, optical rotation, nuclear magnetic resonance (NMR) and x-ray crystallography. Most of these methods need the support of a reference compound of known handedness or computer simulation.

All these methods mentioned above have limitations, however. For example, in chromatography, the interaction of each enantiomer with the chiral selector is different, which guides the separation. As a result, this method is very sensitive and relies on very carefully controlled surface chemistry and is also very susceptible to external parameters. Chromatography at the moment cannot be used as a plugin and play machine because every individual chemical requires tweaking with the setting. The technique itself requires skilled operation to get consistent results every single time. Thus, it has not been established as a standard to study chirality. Moreover, the various spectroscopy techniques have their own merits and demerits; some of these techniques are discussed below.

1.8.1 Spectroscopy techniques to determine the chirality of molecules

As mentioned above, many biologically active molecules are chiral; thus, chirality is deeply embedded in our nature. The origin of the homochirality of life on earth remains a subject of research and speculation, and this motivates the understanding and investigation of chirality and chiral phenomena [8]. Since the pioneering work of Pasteur on optical activity (OA), it has been recognized that polarized light provides a tool that is sensitive to chirality [45]. Later, this became the basis for a variety of spectroscopic methods for the study of chiral molecules. One of the techniques used routinely in analytical chemistry is circular dichroism (CD) in photoabsorption. In this technique, the difference in the absorption of left- and right-circularly polarized light by the chiral molecule is measured. The CD signal is measured in the UV-Vis region, where an electronic transition occurs. The resulting dichroism signal is typically small (<<0.01%), as it arises solely from the interference between the electric- and much

weaker magnetic-dipole interaction terms. This technique is often used to quantify the chiral character in complex structures, such as proteins. However, this technique lacks the required precision.

Another extension of CD is vibrational circular dichroism (VCD) [46] which is much more precise. VCD is done in the infrared (IR) region where the vibrational transition occurs. The IR region has more absorption bands than the UV region, which gives this technique an enhanced ability to sense chirality and distinguish enantiomers. VCD is a popular technique used in major pharmaceutical companies these days to distinguish the enantiomers. Another method of chirality detection and analysis emerging for broader use is Raman optical activity (ROA) [47]. This measures the difference in Raman scattering between right and left circularly polarised light in the scattered radiation. ROA is complementary to VCD, and its strength is in its sensitivity to the structure of proteins in the solution.

The work presented in this thesis is based on a variation of angle-resolved photoelectron spectroscopy known as photoelectron circular dichroism (PECD) which can be used to study chiral molecules. In PECD angle-resolved photoelectron intensity is measured following ionization with left- and right- circularly polarized light, with the difference between the two measurements providing the dichroism. The technique provides a sensitive and reliable means of studying chirality in the gas phase can be used to quantify chiral signatures and differentiate enantiomers. One-photon and multiphoton variants of the technique exist which are outlined below.

1.9 One-photon photoelectron circular dichroism

In the late 1970s, a different form of circular dichroism was predicted by Ritchie [48] and later discussed by Cherepkov [49]. It was pointed out that there will be a forward-backwards asymmetry in the photoelectron angular distribution measured upon ionization with left or right circularly polarized light from a randomly oriented chiral molecule, as shown in figure 1.10. This effect arises from the interference between different components of the electric dipole matrix element. As a result, it was suggested that this effect could be of the same order of magnitude as the differential cross-section itself. Initially, this new effect was known as circular dichroism in the photoelectron angular distribution (CDAD), but this was later changed to photoelectron circular dichroism (PECD) to distinguish it from the CDAD effect

which arises from the ionization of aligned or oriented nonchiral molecules. Now we will present the PECD formalism using Legendre polynomials. In PECD experiments there is always a cylindrical symmetry in the system with respect to the lab frame, which is defined by the laser propagation direction. Therefore, *m* is always zero allowing us to use Legendre polynomial for the expression of general form for angular distribution. The general expression for the angular distribution of photofragments ejected from a randomly oriented molecule in the gas phase for the case of one photon is given by:

$$I_{lin}(\theta) = 1 + \beta P_2(cos\ \theta) \tag{1.21}$$

$$I_{cpl}(\theta) = 1 - \left(\frac{\beta}{2}\right) P_2(cos\ \theta), \tag{1.22}$$

Equation 1.21 applies to linearly polarised light, where θ is the ejection angle measured with respect to the electric field vector, while Eq. 1.22 applies to circular polarization, and θ is measured relative to the laser propagation direction. P_2 is the second Legendre polynomial. The parameter β takes a value ranging from −1 to +2; these limits for linear polarization correspond, respectively, to pure $\sin^2$ or $\cos^2$ distributions while β = 0 corresponds to an isotropic distribution. Therefore β

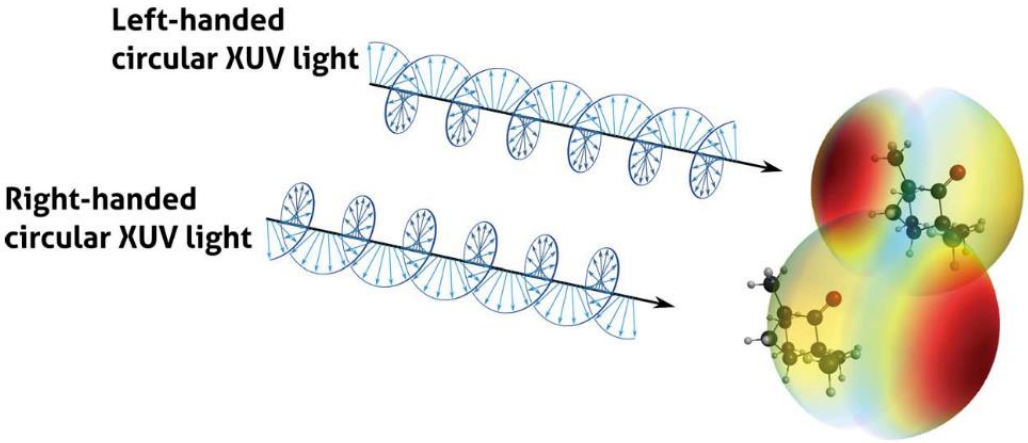

Figure 1.10. Principle of photoelectron circular dichroism [78]. *Photoelectrons will eject forward and backward when right and left CPL is used, respectively.*

characterizes the anisotropy of the distribution and is commonly also referred to as an asymmetry parameter. In a way, Eqs. 1.21 and 1.22 are subcases of a more general form we discussed in the previous section 1.5.

Moreover, Ritchie [48] proposed that even in a pure electric dipole approximation, another term was required for completeness and hence the general form of photoionization angular distribution function, should be written as [50]:

$$I^{\{p\}}(\theta) = 1 + b_1^{\{p\}} P_1(\cos\theta) + b_2^{\{p\}} P_2(\cos\theta), \quad (1.23)$$

where P_1 is the first Legendre polynomial. The coefficients $b_1^{\{p\}}$ and $b_2^{\{p\}}$ depends on the photoionization dynamics. They also depend explicitly on the polarization as expressed by the superscript p (p = 0 linear polarization, p = ±1 left, right circular polarization). These coefficients have the following symmetry relationships [41, 43]:

$$b_1^{\{0\}} = 0 \quad (1.24)$$

$$b_1^{\{+1\}} = -b_1^{\{-1\}} \quad (1.25)$$

$$b_2^{\{0\}} = -(1/2) b_2^{\{\pm 1\}} \quad (1.26)$$

It can be clearly seen from Eq. 1.24 that for linearly polarized light the P_1 term vanishes from Eq. 1.23 and Eq. 1.21 is recovered for linear polarization. Moreover, for linear polarization $b_2^{\{0\}}$ is equivalent to the β anisotropy parameter. For achiral molecules $b_2^{\{p\}} = 0$ for any polarization; only for circular polarization and chiral molecules $b_2^{\{\pm 1\}}$ have non-zero values. Furthermore, the antisymmetry of $b_1^{\{\pm 1\}}$ (Eq. 1.25) leads to a reversal of the forward-backward asymmetry when the helicity of the laser pulse is exchanged, thus giving rise to circular dichroism or difference between the response to left- and right-handed circular polarization in the angle-resolved photoelectron spectrum. A similar reversal is anticipated when the handedness of the enantiomeric molecular target is exchanged keeping the helicity of light the same. Most of the time it is more convenient to measure the dichroism with different helicities of the light while keeping the enantiomers same. From Eq. 1.23 and the antisymmetry property Eq. 1.25 one obtains an expression for the PECD:

$$I_{lcp}(\theta) - I_{rcp}(\theta) = \left(b_1^{\{+1\}} - b_1^{\{-1\}}\right) P_1(\cos\theta) = 2 b_1^{\{+1\}} \cos\theta, \quad (1.27)$$

where $I_{lcp}(\theta)$ and $I_{rcp}(\theta)$ are the angular distribution measured using left and right circularly polarized light respectively. The PECD measurement clearly takes the form of a cosine function with an amplitude given entirely in terms of the single chiral parameter, b_1. In the context of molecular photoionization, measurement of the chiral b_1 parameters by PECD introduces a new observable, in addition to β and the cross-section, σ. The advantage of examining the PECD over the single angular distribution $I_P(\theta)$ is that by looking at the differential angular distribution we are likely to include

some cancellation of purely instrumental asymmetries and consequently improve sensitivity.

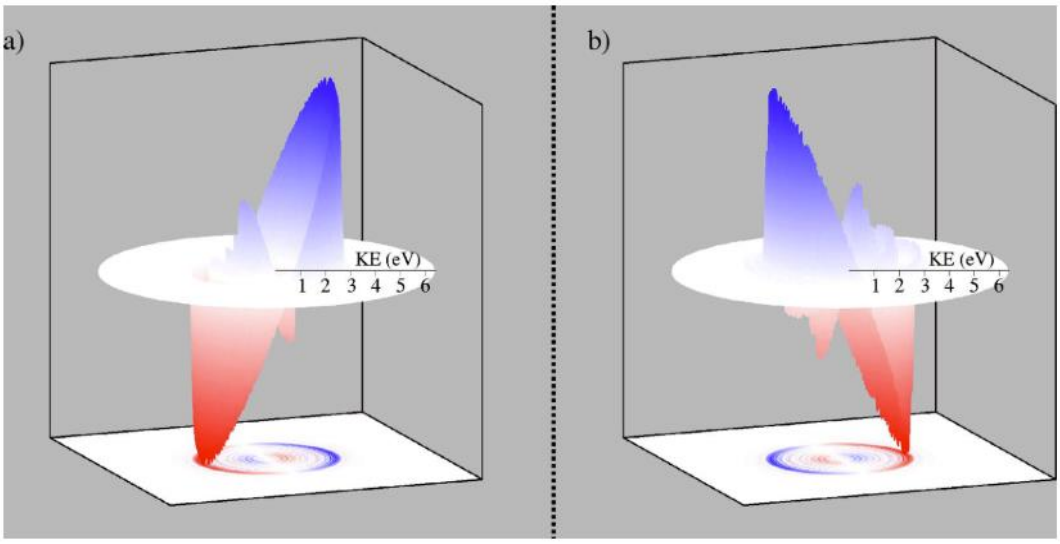

Figure 1.11. Photoelectron circular dichroism angular distribution ($I_{lcp}(\theta) - I_{rcp}(\theta)$) for the hν = 10.3 eV photoionization of (a) R-camphor and (b) S-camphor [51].

Figure 1.11 illustrates an actual experimental observation of the photoelectron circular dichroism obtained from the $h\nu$ = 10.3 eV photoionization of camphor enantiomers [51]. The figure shows the intensity differences $I_{lcp}(\theta) - I_{rcp}(\theta)$ that have been observed by an electron imaging technique. In this example there are clearly two ring structures, an outer ring structure corresponding to ionization of the highest occupied molecular orbital (HOMO), and an inner ring structure corresponding to slower electrons from ionization of the HOMO-1.

The first calculations of the PECD effect were presented by Powis who provided a quantitative estimate of the magnitude of the PECD effect in D-glyceraldehyde, D-lactic acid, and the biomolecule L-alanine using the CMS-$X\alpha$ method [51, 52]. The PECD signal was calculated to range typically from 10% to 40% and sometimes exceeds 60% of the differential cross-section, confirming the prediction by Ritchie that the effect would be orders of magnitude greater than that observed in conventional CD. The first-ever experimental demonstration of PECD was provided by Heinzmann and co-workers [53]. Measurements were carried out on randomly oriented bromocamphor molecules in the gas phase, using vacuum ultraviolet (VUV) radiation from a synchrotron facility. The photoelectrons were detected at a fixed angle with respect to the light beam using two channeltron detectors mounted opposite to each

other. The authors reported the PECD signal of $\pm$ 3%, and it changed sign with the change in helicity of light. Later, Powis and co-workers observed PECD of camphor enantiomers near-threshold using a circularly polarized VUV light source together with a state-of-the-art photoelectron-photoion coincidence (PEPICO) spectrometer [54]. PECD signal of 3% at 9.2 eV photon energy was observed and showed that asymmetry reverses on the exchange of either the helicity of the radiation or of the molecular enantiomer similar to the previous work [53], confirming theoretical predictions of an effect that arises in the pure electric-dipole approximation.

Since these early demonstrations of the effect, PECD has been studied extensively using VUV one-photon ionization scheme and angle-resolved emission detection later applying the velocity map imaging techniques. In the next section, we will briefly discuss various PECD effects. For example, various authors showed in their experiments and calculations that PECD is both an initial state (orbital specific) [11], and the final state (continuum) [55] dependent effect. Due to the pure quantum nature of PECD is also extremely sensitive to molecular structures, such as chemical substitution [56, 57], conformers [58–61], dimerization and clustering [62–64], as well as to dynamical ones such as vibration [65, 66]. Thus, PECD can be used as a probe to investigate such properties.

1.10 Resonance enhanced multiphoton photoelectron circular dichroism

According to Yang's theorem [67], for an n excitation and m ionization process, the expansion terms in Eq. 1.4 are limited to $2(n + m)$. In this work we use a (2+1) REMPI ionization scheme; thus we use $l_{max} = 6$ for analysis of our work and expression for multiphoton (MP) PECD has b_1, b_3 and b_5 terms and PECD value can be defined as shown in Eq. 1.28 (see next section for more detail).

$$MPPECD = 2b_1^{+1} - \frac{1}{2}b_3^{+1} + \frac{1}{4}b_5^{+1} \tag{1.28}$$

Early work on the multiphoton regime started in 2006. It was observed that circular dichroism could occur in the mass resolved multiphoton ionization yield from chiral molecules following REMPI [68–70]. This early work was done using nanosecond laser pulses, and time-of-flight mass spectrometer and it was shown that the technique could be used to distinguish enantiomers and determine enantiomeric excess with 99% confidence limits. Similar work has been done using a femtosecond laser source in the

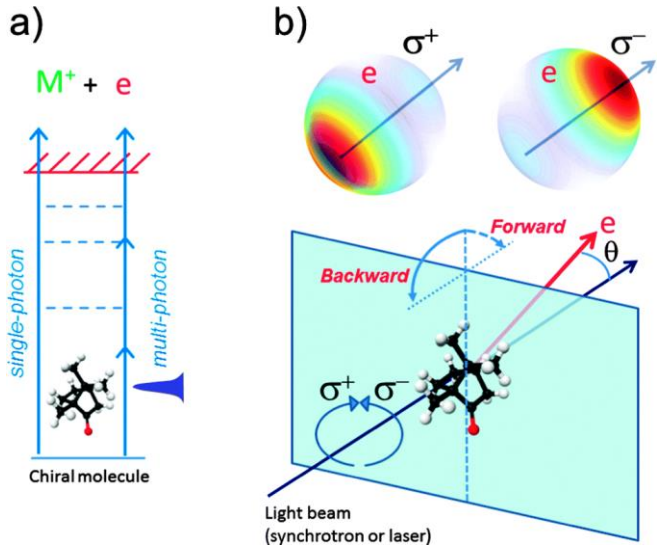

Figure 1.12. (a) Schematic illustration of single-photon and multiphoton ionization of a chiral molecule. (b) Principle of measuring photoelectron circular dichroism [73].

visible and near UV [71, 72]. However, this CD in ion yield is not detectable in all the molecules. Thus, the technique fails to be recognised as a standard tool to explore multiphoton regime.

In recent years PECD following resonant multiphoton ionization with short laser pulses has been investigated, as illustrated schematically in figure 1.12. As we saw in Section 1.9, the single-photon PECD study could be used as a probe for photoionization dynamics. Similarly, using multiphoton ionization, it can be used to shed significant light on intermediate state photoionization dynamics. In 2012, Lux and co-workers presented work on PECD in multiphoton regime using femtosecond laser pulses and a velocity map imaging spectrometer. PECD signals were observed in the range of ± 10% to ± 15% for camphor and fenchone [73]. Shortly afterwards, Lehmann and co-workers presented the REMPI-PECD data for camphor using a state-of-the-art photoelectron-photoion coincidence imaging setup (see Chapter 2), capable of recording mass-selected data [74]. Unlike the previous work by Lux and co-workers [73], in which an effusive source of camphor molecules was used (internal temperature 300 K), here a seeded supersonic molecular beam of camphor was used, with a rotational temperature in the range 1-5 K. These authors presented a method that could be used to quantify the chiral electron asymmetry in a single parameter for a multiphoton ionization scheme, referred to as multiphoton PECD (MP-PECD, Eq. 1.28). The results obtained were interpreted as arising from a sequential mechanism, where resonant two-photon transition brings the molecules into low-lying Rydberg states and the third photon subsequently causes ionization.

Since that time, the REMPI-PECD technique has been used to study various chiral molecules such as methyl oxirane [75], limonene [76], and bicyclic ketones [77] using femtosecond laser pulses, and the universality of PECD as a means of studying chirality has been demonstrated by Beaulieu and co-workers who presented data in the single-photon, multiphoton, above threshold and tunnel ionization regimes [78]. The magnitude of the REMPI-PECD effect has been shown to depend on the wavelength of the photon [79] and the intermediate state accessed in the multiphoton process [80]. It has also been shown that a time-resolved version of this technique could be a very sensitive tool for ultrafast molecular dynamics in chiral systems [81]. To fully understand the molecular dynamics of these chiral system using REMPI-PECD technique, the effects of the initial, intermediate, and final state of the system need to be decoupled. Beaulieu and co-workers have studied the effect of the intermediate state on PECD and demonstrated that the anisotropy created during the photoexcitation process is critical [82]. Further, the authors pointed out that polarization of the photon deriving the excitation process has a negligible effect on PECD, proving the prediction made by Goetz and co-worker in their theoretical work [83].

Most of the studies in the multiphoton regime have employed femtosecond laser pulses. As a result of a large bandwidth associated with femtosecond pulses, the vibrational resolution is lost, thus masking any vibronic dependence on the observed PECD. The goal of the present work is to study the intermediate electronic, vibrational and electron kinetic energy dependence of the PECD observed in chiral molecules such as α-pinene, 3-carene, and fenchone using picosecond laser pulses.

1.11 **Theoretical formulation for REMPI-PECD**

This section presents the formulation for expressing MP-PECD in a single quantity. The photoelectron angular distribution for one-photon ionization with circularly polarized light of a random isotropic sample of chiral molecules in the lab frame, $I_p(\theta)$, can be expressed as, [74]:

$$I_p(\theta) = \frac{I_{tot}}{4\pi}\left(1 + b_1^p P_1(cos\theta) + b_2^p P_2(cos\theta)\right), \quad \text{where} \quad I_{tot} = \int_0^{2\pi}\int_0^{\pi} I_p(\theta)\sin(\theta)d\theta d\phi \tag{1.29}$$

Here, θ is the angle between the velocity vector of the ejected electrons and the propagation direction of the circularly polarized light. P_n is the n^{th} order Legendre

polynomial and b_n^p are the associated coefficients that depend on the polarization p. The polarization is indicated with p = 0 for linear polarized light, p = +1 for Left-Circularly-Polarized (LCP), and p = −1 for Right-Circularly-Polarized (RCP).

The quantitative characterization of the magnitude of the PECD asymmetry in the case of one-photon ionization is achieved by calculating the difference in photoelectron intensity at an angle θ following ionization with LCP and RCP for a given enantiomer. The difference in the angularly resolved intensity can be written as,

$$I_{diff}(\theta) = I_{LCP}(\theta) - I_{RCP}(\theta) = \frac{I_{tot}}{4\pi}.2b_1^{+1}P_1(cos\theta) \tag{1.30}$$

The general convention is to define PECD as the ratio of the intensity at θ = 0 to the average flux, i.e.,

$$PECD = \frac{I_{diff}(\theta = 0)}{I_{avg}} = 2b_1^{+1}, \qquad I_{avg} = \frac{I_{tot}}{4\pi} \tag{1.31}$$

Similarly, the expression for multiphoton PECD can be derived. In the case of multiphoton ionization, assuming that cylindrical symmetry is maintained, the photoelectron angular distribution resulting from n-photon ionization of a chiral molecule can be expressed as,

$$I_p(\theta) = \frac{I_{tot}}{4\pi}\left(1 + \sum_{i=1}^{2n} b_i^p\, P_i(cos\theta)\right) \tag{1.32}$$

For one-photon ionization, the above expression results in $b_i^p = 0, \text{for } i \geq 3$, giving back the one-photon ionization PECD equation. For a (2+1) REMPI ionization scheme, where n = 3, the above equation results in $b_i^p = 0, \text{for } i \geq 7$. The intensity difference can be obtained by measuring the PADs for same enantiomer using LCP and RCP light, or by measuring the PAD with either LCP or RCP for both the S- and R-enantiomers. For this study, we have used the former method to avoid any residual contamination while changing the sample. For a (2+1) ionization scheme, the difference in the angle-resolved intensity following ionization with LCP and RCP for a single enantiomer can be expressed as,

$$\begin{aligned} I_{diff}(\theta) &= I_{LCP}(\theta) - I_{RCP}(\theta) = I_{+1}(\theta) - I_{-1}(\theta) \\ &= \frac{I_{tot}}{4\pi}\left(\sum_{i=1}^{6} b_{2i-1}^{+1}\, P_{2i-1}(cos\theta)\right) \end{aligned} \tag{1.33}$$

The overall magnitude of the multiphoton PECD in terms of Legendre coefficients. For a (2+1) ionization scheme can be expressed as,

$$MPPECD = 2b_1^{+1} - \frac{1}{2}b_3^{+1} + \frac{1}{4}b_5^{+1} \quad (1.34)$$

In all the chapters we use the above equation to express the chiral asymmetry in a single quantity.

1.12 **Thesis layout**

In this chapter we presented the relevant background and theory required for following the subsequent Chapters. Chapter 2 presents the methodology of the work and divided into three sections; firstly, the theory and principles of each technique are discussed; secondly, the experimental set up is described and thirdly the data analysis procedures are outlined. Chapters 3 presents the REMPI, photoelectron spectroscopy and photoelectron circular dichroism measurements recorded via the 3*spd* Rydberg states of fenchone. Further, a comparison is presented with the previous work on fenchone. Chapter 4 presents the REMPI and photoelectron spectroscopy measurements for α-pinene and 3-carene via the 3*spd* Rydberg states. Chapter 5 presents the photoelectron circular dichroism measurements for α-pinene and 3-carene via the 3*sp* Rydberg states. Further discussion is presented on the effects of electronic and vibrational state on PECD. Chapter 6 presents the photoelectron angular distribution from the aligned aniline and naphthalene molecules and a comparison with simulated PADs is also included. In Chapter 7, the conclusions of previous chapters are summarised, and future studies are discussed.

Chapter 2 Experimental methodology

In this chapter, the different experimental techniques used in this work are discussed, followed by the corresponding detection techniques and spectrometers. Data acquisition and analysis is presented for PECD and adiabatic alignment experiments.

2.1 Experimental techniques:

2.1.1 Resonance enhanced multiphoton ionization photoelectron circular dichroism (REMPI PECD)

The REMPI PECD experiments were carried out by a picosecond laser system and a velocity map imaging spectrometer, both are discussed in the coming sections (2.2.1 and 2.2.2 respectively). In these REMPI PECD experiments, molecules (fenchone, α-pinene, and 3-carene) were excited to an intermediate state though the absorption of two photons followed by an ionization step by absorption of another photon. Work presented this thesis (Chapter 3, 4, and 5) used circularly polarized UV photons to drive the excitation step ($S_0 \rightarrow 3spd$ Rydberg states) and ionization step ($3spd \rightarrow D_0^+$). When the whole process is driven by a single wavelength, the technique is labelled as (2+1) REMPI. When two different wavelengths are used, it's called (2+1') REMPI.

2.1.2 Truncated pulse alignment and molecular frame photoelectron angular distributions (MFPADs)

Alignment experiments were carried out at Aarhus University (Denmark), with Prof. Henrik Stapelfeldt's group. In these experiments, the molecules were aligned prior to the (1+1) REMPI. As discussed in Chapter 1, using alignment techniques, we can access the molecular frame photoelectron angular distribution (MFPADs). Molecular alignment can be obtained through laser-induced methods, relying on the interaction between a moderately intense laser field and the anisotropic polarizability of gas-phase molecules (Chapter 1 section 1.6). If the laser field is switched on slowly in comparison to the rotational period(s) of the molecules, it is possible to obtain one-dimensional (1D) alignment, where the most polarizable molecular axis is fixed in space, by a linearly polarized field or three-dimensional (3D) alignment [84], and where all three principal polarizability axes are fixed in space with an elliptically polarized field. The work presented in this thesis uses a slightly different alignment

experimental technique. Spectrally truncated chirped laser pulses were used [85] to align the molecules with an aim to create aligned molecules after the laser pulse is turned off. These pulses were generated by addition of 800nm longpass filter (Thorlabs FELH0800) into the alignment beam path. After transmission through this filter the spectrum is abruptly cut at 800 nm. This technique offers a best of both worlds compromise between adiabatic alignment, which enables a high degree of alignment at the cost of a field present, and impulsive alignment, which enables field-free alignment, but often with a lower degree of alignment. This was followed by ionization using a UV pulse; the molecules (aniline and naphthalene) were excited to an intermediate state (S_1) by absorption of a photon followed by one photon ionization ((1+1) REMPI).

2.2 Experimental setup: REMPI PECD

2.2.1 Picosecond laser system

The REMPI PECD experiments were carried out by using the picosecond laser system, which is described next. The picosecond laser system consists of a Ti:Sapphire oscillator (Coherent, Vitesse), a regenerative amplifier (Coherent, Legend elite), two single-pass amplifiers (Coherent), and two optical parametric amplifiers (Light Conversion, TOPAS). These are described in more detail below, and a schematic of the laser system is shown in figure 2.1. A 50/50 beamsplitter is located between the regenerative and single-pass amplifiers in order to create two separate beams for the pump and time-delayed probe. Each input beam to the TOPAS systems has a fixed wavelength of 800 nm, a pulse width of 1.3 ps, a repetition rate of 1 kHz and a power of 3.4 W. The output beams from the TOPAS systems have independently tuneable wavelengths from 1100 to 2950 nm, which are subsequently converted to ultraviolet wavelengths using sum-frequency and higher-harmonic generation. So the final output

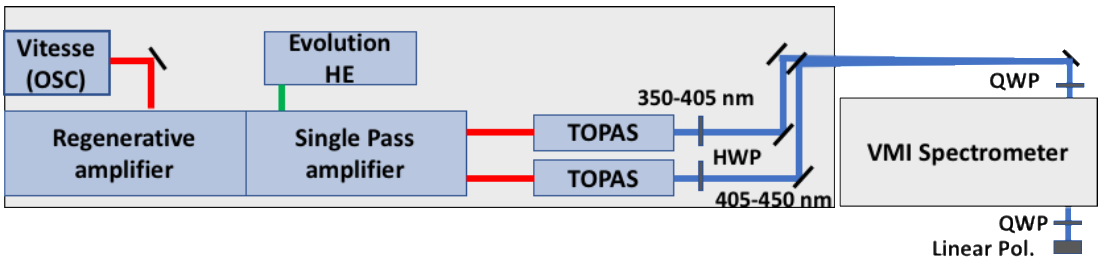

Figure 2.1. A schematic of the picosecond laser setup

of the system is two tuneable beams in the wavelength range 240 – 1140 nm, with a pulse duration of ~ 1.3 ps and a bandwidth of ~ 34 cm^{-1}.

The Vitesse is a mode-locked Ti:Sapphire laser which is pumped by a VERDI diode laser. Vitesse generates 100 fs pulses of light at a wavelength of 800 nm, with a spectral bandwidth of 10 nm and a repetition rate of 80 MHz. These pulses then pass into the Legend Elite regenerative amplifier which contains a pulse stretcher and a Q-switched Evolution-30 Nd:YLF laser pumping the regenerative amplifier. The system uses a chirped pulse amplification technique; the pulses are stretched using a diffraction grating which disperses the different frequencies of the laser pulse, so each wavelength travels a slightly different optical pathlength. This stretches the pulse to ~ 200 ps consequently reducing the peak intensity and preventing damage to the optical components during amplification. The beam also passes through a mask in this stage which blocks some of the wavelengths dispersed by the diffraction grating to reduce the spectral bandwidth ensuring a final pulse duration of ~ 1.3 ps. The regenerative amplifier contains a Ti:Sapphire crystal in a resonant optical cavity which is pumped by Nd:YLF laser. A pair of Pockels cells trap each pulse within the amplifier cavity for approximately 20 round trips. The amplification occurs as the pulse passes through the crystal, resulting in an amplification of greater than 10^6 before the pulse is ejected. The output from the regenerative amplifier is then passed through 50/50 beamsplitter, which is located between the regenerative and single-pass amplifiers in order to create two beams.

The two single-pass amplifiers (SPA) consist of two Ti:Sapphire crystals, both pumped by an Evolution-HE Nd:YLF diode laser, as shown in figure 2.1. The split output of the regenerative amplifier is passed through these two SPAs. The pulses are then compressed to 1.3 ps duration using gratings for both the arms. Upon leaving the two SPAs units, both beams have a wavelength of 800 nm, a repetition rate of 1 kHz and a power of around 3.4 W. Both beams are then sent into an optical parametric amplifier or TOPAS (Light Conversion). These produce infra-red light in the range 1100–2950 nm, which is then converted to ultraviolet light using sum-frequency and higher-harmonic generation. For the present work wavelengths between 350-450 nm were generated. One of these beams was set up to produce range 405-450 nm, and the other beam was setup to generate the 350-405 nm range. Using this 100 nm wavelength

tunability, we were able to explore the 3*spd* Rydberg regions of α-pinene, 3-carene, and fenchone.

The beams are then focussed into the velocity map imaging spectrometer using a 30 cm focusing lens. Both beam paths included a half waveplate and quarter waveplate to control the polarization of laser pulses.

2.2.2 Velocity map imaging spectrometer

The technique used in this work is velocity map imaging (VMI), based on the Eppink and Parker design [25]. A VMI spectrometer focuses all the particle with a given velocity onto the same point on the screen, regardless of their starting position. This gives an image with a series of spherical rings; the outer ring corresponding to the fastest moving photoelectrons and the inner ring corresponding to the slowest photoelectrons.

A schematic of the VMI spectrometer is shown in figure 2.2. The spectrometer is made of two vacuum chambers. The first chamber is the source chamber where a molecular beam is generated using an adiabatic expansion from a kHz rep rate pulse valve (see next section). The second vacuum chamber consists of the VMI spectrometer described above, and this chamber is called the 'ionization' chamber, which is

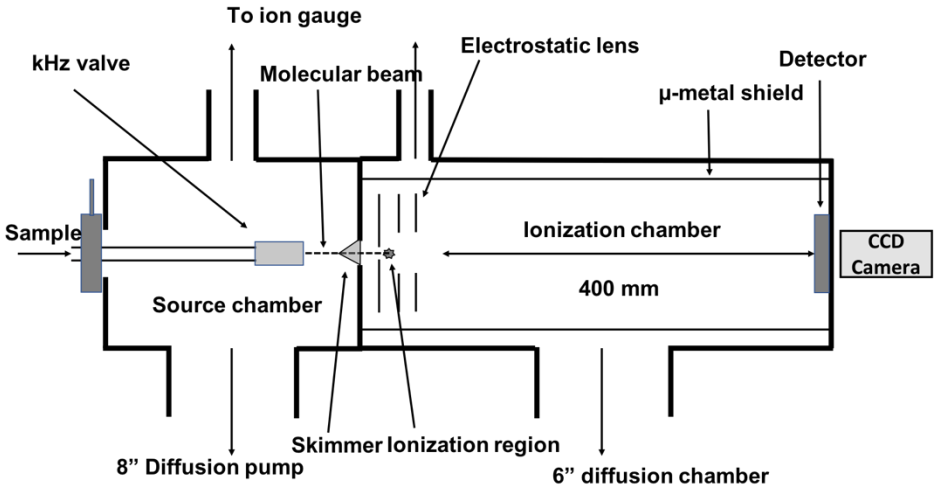

Figure 2.2. Schematic of the velocity map imaging spectrometer.

connected by a skimmer to the first 'source' chamber. The molecular beam then passes through this skimmer and into this detection chamber, where it intersects with the laser beam. At this point, the molecules are vibrationally cold, and the rotation temperatures are expected to be around 10-25 K. These two chambers are differentially pumped by diffusion pumps to maintain a high vacuum of around 2×10^{-5} mbar in the source

chamber (when pulse valve operational) and $1x10^{-7}$ mbar in the detection chamber. To ensure the photoelectrons generated are not subject to any external magnetic fields which would interfere with their trajectories, a double μ-metal shield surrounds the ionization chamber.

The electrostatic extractor lens (figure 2.3) is made up of three circular stainless-steel plates: the repeller plate, the extractor plate and the ground plate (0 V). Each plate has a hole in the centre which allows the molecular beam to pass through. The molecular beam intersects with the laser beams in between the extractor and repeller plates. The extractor voltage is initially held at ~70% of the repeller voltage. This voltages ratio on the repeller and extractor plates is adjusted until a sharp image is obtained. The magnification of the image is determined by the absolute voltage on the plates; the slower electron requires lower extraction voltage as it leads to a longer time of flight and vice-versa. Therefore, the voltages are chosen so that the outermost ring in the image with the largest radius resulting from the fastest electrons is as large as possible without touching the edges of the detector.

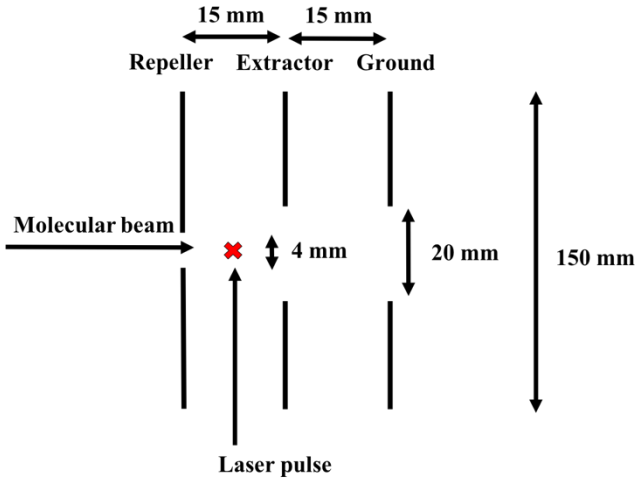

Figure 2.3. Electrostatic lens used for velocity map imaging. The photoelectrons are produced at the cross-section point between molecular beam and laser pulse.

These accelerated photoelectrons travel 400 mm along a field-free region and strike a 40 mm dual microchannel plate/phosphor screen detector (Photek) at the end. The MCPs acts as an amplifier, and it generates a cascade of electrons each time a single photoelectron hits it. This cascade of electrons then hits the phosphor screen, forming a 2D image of the 3D photoelectron velocity distribution. The MCP detector is gated by applying a stepping voltage to improve the signal to noise ratio. A trigger from the pulse valve is used, which itself is triggered by the laser pulse (Q-switch of the regen

pump laser). This only allows photoelectrons from the molecular beam to get amplified and filters out the background electrons. A CCD camera (Basler A302f, 782 (H) x 582 (V) pixels) records the images of the phosphor screen, which are transferred to the computer using a LabView acquisition software. The final images are saved in a FITS format (Flexible Image Transport System).

The VMI spectrometer can also be set up to detect ions, which is necessary for REMPI spectroscopy, by changing the voltages applied to the electrostatic lens and time-gate. Positive voltages are instead applied to the extractor and repeller plates to extract the ions and focus them towards the detector. Unless the ion fragments there will be no rings in the image, so the camera is left running and the integrated signal is recorded as a function of excitation laser wavelength. Moreover, ion detection mode is useful for ensuring there are no clusters in the molecular beam.

2.2.3 Molecular beam: kHz valve

For REMPI PECD work the 40 Hz molecular beam valve in the VMI spectrometer was upgraded to a kHz piezo valve (Amsterdam cantilever piezo valve ACPV2), with an opening diameter of 150 µm. The piezo valve was operated by a EDU1 controller (more details in ref [86]). Figure 2.4 shows the valve, controller, and the mount to hold it inside the source chamber. The valve was mounted directly on a manipulator to controller the direction of the supersonic jet. The TTL trigger input from the laser was

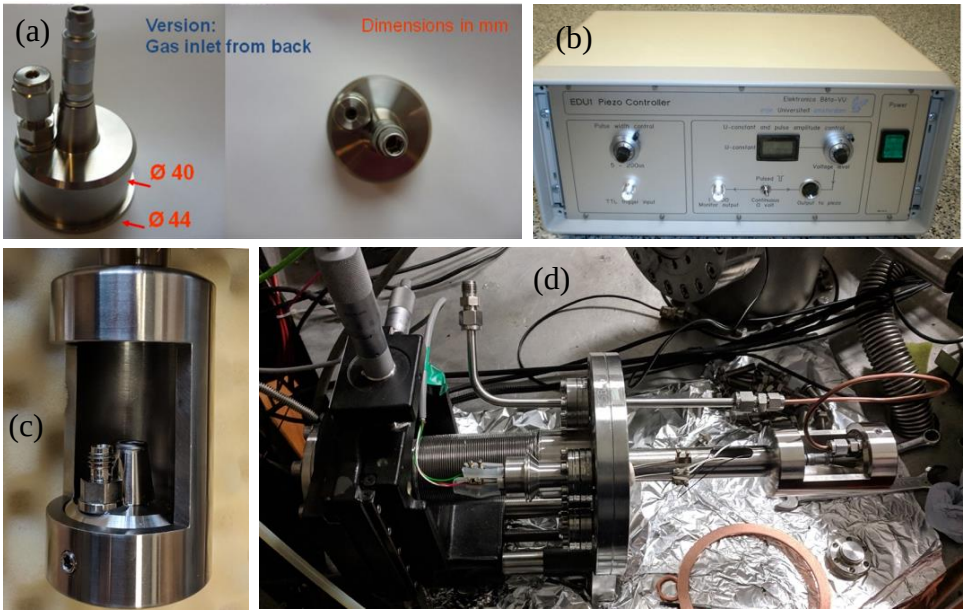

Figure 2.4. Installation of kHz valve (a) kHz valve, (b) controller, (c) mount to hold the valve, and (d) manipulator.

used to control the operating timing of the valve. The opening time of the valve can be adjusted between 5 to 200 microseconds. The valve also requires a constant voltage of about 140-150 V (Max) to operate at a repetition rate between 0-3 kHz. When this centre voltage is at 140-150 V, the valve will be closed, and when this voltage is pulsed to 0 V, it will open the valve.

The sample is introduced into the source chamber through this kHz valve with an inert backing gas of helium (~1 bar,) producing a supersonic jet expansion which cools the molecules. The opening time of the valve is kept between the 25-30 microseconds because this was limited by the pumping capacity of the diffusion pumps. The valve has a very small orifice (diameter ~150 μm), so the high pressure backing gas expands into the source chamber which is at a much lower pressure (10^{-7} mbar maintained by diffusion pumps) forming a supersonic jet expansion of He atoms seeded with sample molecules. At this point, the molecules are vibrationally cold, and the rotational temperature is expected to be around 10-25 K.

2.3 Fourier transform spectroscopy

In this section, we will briefly discuss the VUV Fourier transform (FT) spectroscopy technique, as some later chapters (3, 4, 5) present a comparison of the VUV absorption spectrum with the measured REMPI spectrum of several molecules (α-pinene, 3-carene, and fenchone).

The absorption spectrums of these molecules were recorded using the VUV FT spectrometer on the DESIRS beamline at Soleil synchrotron facility. The FT spectroscopy experimental branch has been previously described in detail [87, 88]; here we shall give only the relevant characteristics. DESIRS is an undulator based beamline that provides the continuum background for the absorption measurement in the shape of a pseudo-Gaussian 7% spectral bandwidth that can be tuned over a large UV-VUV range [89]. Fourteen different spectral windows were required in order to cover the range 5 - 10 eV. A windowless gas cell installed in a vacuum inside the multipurpose environmental sample chamber of the FT spectroscopy branch was used for the measurement. Following three freeze-pump-thaw cycles, room temperature vapour was admitted to the windowless gas cell via a needle valve to control pressure. Typical entrance pressures covered the range 0.10 - 0.27 mbar and were set for each

individual spectral window in order to record approximately a 50% absorbance spectrum.

The FT spectrometer was set to provide a spectral resolution of 17.2 cm^{-1}. In the frame of our experimental conditions, an inspection of the spectrum gave no evidence for any feature requiring a better spectral resolution. During the campaign, and due to technical problems, it was not possible to set the absolute absorption cross-section scale by the procedure usually adopted [88]. Nevertheless, the cross-section was calibrated against a limonene spectrum recorded under comparable flowing conditions, itself cross-calibrated against literature values [90].

2.4 Photoelectron photoion coincidence detection

Femtosecond measurements were also made to get a better understanding of photoionization dynamics at the two timescales (femtosecond and picosecond). A femtosecond laser pulse with a 3 kHz repetition rate and 150 fs pulse duration laser coupled with a dual imaging electron-ion coincidence spectrometer [75, 79, 91] was

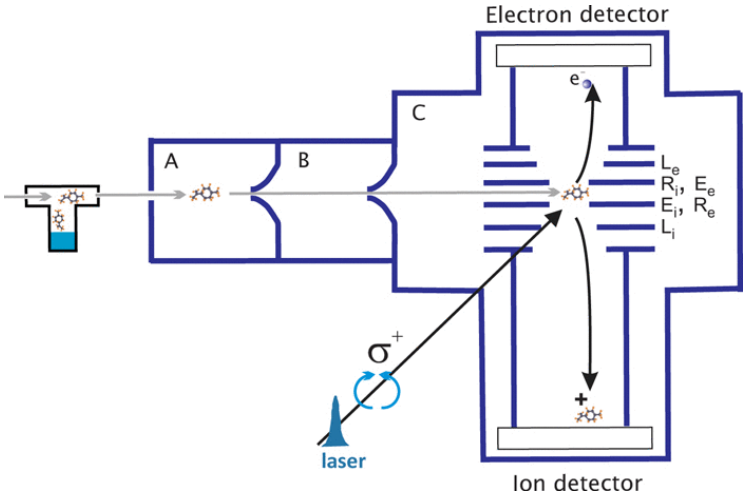

Figure 2.5. Schematic of a PEPICO setup [79]. *After ionization of the molecule the electron and ion pair is detected in delayed coincidence on two opposing time- and position-sensitive delay line detectors mounted perpendicular to the molecular beam and photon beam.*

used for these measurements. These measurements were recorded at Radboud University, Nijmegen (Netherlands). Thus, in this section, we will briefly discuss the detection technique known as photoelectron photoion coincidence (PEPICO).

PEPICO is a combination of photoionization mass spectrometry and photoelectron spectroscopy. Both the electrons and the ions are extracted by applying electric potentials and are detected with time-sensitive detectors. Electron times-of-flight are

typically three orders of magnitude smaller than those of ions, which means that the electron detection can be used as a timestamp for the ionization event, starting the clock for the ion time-of-flight analysis. In contrast with pulsed experiments, such as REMPI, in which the light pulse must act as the time stamp, this allows the use of continuous light sources. In a usual PEPICO experiment, the photoelectrons are detected by a VMI technique while a time of flight mass spectroscopy is used to detect the ion fragments, as shown in figure 2.5 [79]. As these electrons and ions are correlated to each other, the recorded photoelectron images can be filtered with respect to one or more masses appearing in time of flight, providing background free photoelectron images.

2.5 Alignment experiment

2.5.1 Experimental setup

The work presented in this thesis on the alignment of aniline and naphthalene was done at Prof Henrik Stapelfeldt's lab at Aarhus University. Schematics of the key elements in the experimental setup is shown in figures 2.6(a) and 2.6(b), further details can be found in ref [92].

A schematic of the laser setup is shown in figure 2.6(a). Two laser pulses originate from the same pulsed Ti:Sapphire laser system (customized Solstice ACE, model 80L-35F-1K-HP-T Spectra-Physics, 1 kHz, 6W, 40 fs). As shown in the figure one of the laser pulses is an uncompressed 800 nm output of the laser system, which was used as the alignment laser pulse. These laser pulses have a duration of 110 ps (FWHM, truncated) and a pulse energy up to ~700 μJ. The second laser pulse which was used to ionize the molecules was sent to an optical parametric amplifier (TOPAS, model TP8U1, Light Conversion, pumped by 3.0 W (pulse energy: 3 mJ) from the compressed output of the Ti:Sapphire laser system, and followed by subsequent nonlinear optical processes to get the UV pulses. The TOPAS idler output at ~2215 nm was frequency-mixed with an 800 nm beam from the Ti-Sapphire laser in a 0.5-mm thick BBO crystal to generate a visible beam at ~588 nm. This beam is then frequency-doubled in 40-mm thick KDP crystal to yield the final UV probe beam with a duration of 6 ps and a bandwidth of ~0.06 nm. For aniline measurements, the pulses were centered at 293.85 nm to access S_1 origin, and the pulse energy was up to 0.2 μJ. For the naphthalene measurements, the pulses were centered at 293.53 nm to access a

vibrational state in S_1 (S_1 origin cannot be accessed with one colour) with a pulse energy of 2 µJ.

A dichroic mirror (DM) is used to overlap the probe beam and the alignment beam, followed by a plano-convex lens (FL, f=30 cm) which focuses the two collinear beams into the vacuum chamber via the entrance window (EW). The foci of the laser beams

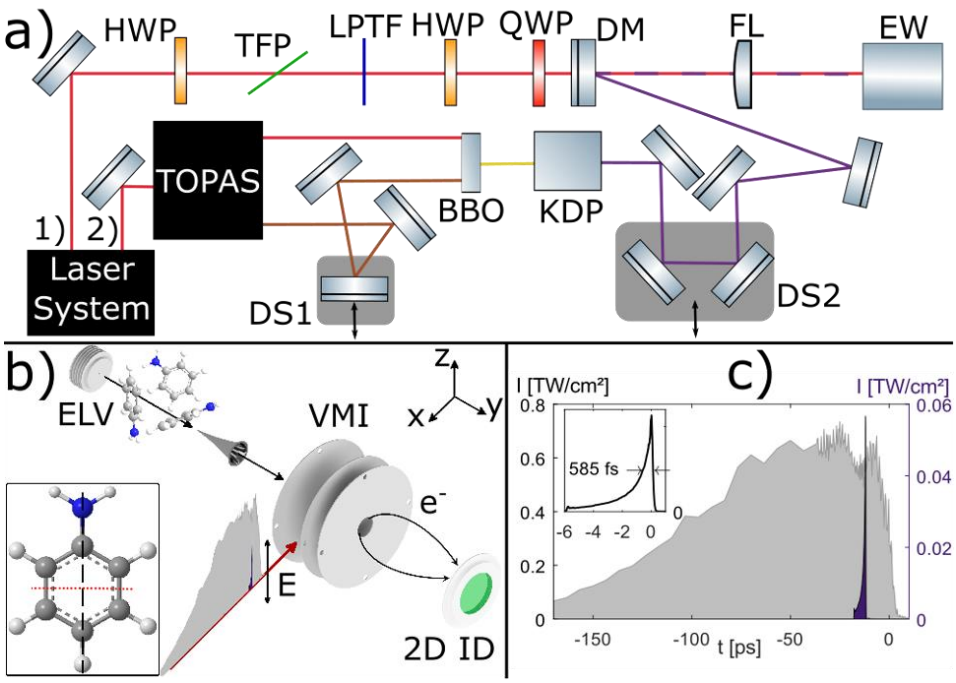

Figure 2.6. (a) Schematic of the laser set-up showing the paths of the alignment beam (1) and the probe beam (2). HWP: Half-wave plate, QWP: Quarter-wave plate, TFP: Thin-film polarizer, LPTF: Long-pass transmission filter, DM: Dichroic mirror, FL: Focusing lens, EW: entrance window, DS: delay stage. The remaining non-labelled components are mirrors. (b) Schematic of the key elements of the experiment. The alignment and the probe pulse are both linearly polarized along the z-axis. ELV: Even-Lavie valve, 2D ID: 2D imaging detector, VMI: velocity map imaging electrodes. The inset shows a sketch of the molecular structure of aniline and the most polarizable axis (MPA, black dashed line) and its transition dipole moment (red dotted line). (c) The grey shaded area shows the intensity profile of the alignment pulse. The probe pulse is indicated by the narrow violet peak and shown in the inset [86].

are positioned at the point where the laser paths cross the molecular beam. The focal spot size, ω_0, of the alignment (probe) beam is 35 µm (20 µm). The intensity of the alignment pulses is controlled by the combination of a half-wave plate (HWP) and a thin-film polarizer (TFP). For the experiments on aniline and naphthalene, a quarter-wave plate (QWP) was included after the half-wave plate, allowing to control the polarization of the alignment pulse, for example, linear polarization for 1D alignment and elliptically polarized pulses for 3-dimensional molecular alignment. Before travelling through the dichroic mirror (DM), the pulses in the alignment beam are

spectrally truncated by a long-pass transmission filter (LPTF). This leads to a temporal truncation where the intensity drops by more than a factor of 100 over ~10 ps [85, 93]. The resulting intensity profile of the alignment pulse, obtained by cross-correlation with the probe pulse, is shown in the inset of figure 2.6c. The timing of the probe pulse with respect to the alignment pulse is controlled by a delay stage (DS2) in the probe beam, placed after the KDP crystal. A molecular beam is formed by expanding a gas mixture of 80 bar of helium and 2 mbar of aniline or 1 mbar of naphthalene into a vacuum chamber through an Even-Lavie valve. The repetition rate of the experiment was 200 Hz. The sample was slightly heated before sending to the source chamber. In the case of aniline (naphthalene), the valve was heated to 36° C (50° C). After passage through a 4 mm diameter skimmer, the molecular beam enters a VMI spectrometer where it is crossed at 90° by two collinearly focused, pulsed laser beams, one to align the molecules and one to ionize them. The electrons produced by the ionization pulse are extracted with a static electric field (140-150 V/cm) in the VMI spectrometer and projected onto a two-dimensional (2D) imaging detector consisting of a microchannel plate detector with an active diameter of 41.5 mm backed by a phosphor screen; see figure 2.6(b). The electron hits on the detector are recorded by a CCD camera (Prosilica GE 680, Allied Vision, 640 (H) × 480 (V) pixels), and the coordinates of each individual electron hit are determined. Thus, the basic experimental observables are two-dimensional velocity images of the photoelectrons. These images analysed using Abel inversion technique to get full three-dimensional angular distribution (see section 2.6).

2.6 Data analysis

To record the REMPI spectra, photoelectron spectra along with anisotropy parameters, and photoelectron circular dichroism from images recorded with a CCD camera, several steps are required. In this section, acquisition and analysis methods are described in detail.

2.6.1 REMPI spectrum

The REMPI spectrum for fenchone, α-pinene and 3-carene were recorded by setting up the VMI spectrometer to ion detections mode by changing the voltages applied to the electrostatic lens and changing the time-gate to detect the parent ions for each molecule. Positive voltages are instead applied to the extractor and repeller plates to

extract the ions and focus them towards the detector. A voltage of 2500/1752 (repeller/ extractor) was applied. The ion image counts were recorded as a function of excitation laser wavelength (giving the REMPI spectrum). REMPI was recorded in the range of 350-450 nm for all these molecules; the first half 405-450 nm was recorded using TOPAS 1 and second half 350-405 nm using TOPAS 2. Laser stepping size of 0.05 nm was used with a delay time of 2 seconds at each step. Laser power was also measured at every 0.5 nm. The final REMPI spectrum was obtained by normalizing the ion counts by the laser power.

2.6.2 Recovering photoelectron spectra: pBASEX

As discussed in Section 2.2, the image recorded by the CCD camera is a 2D projection of the three-dimensional photoelectron velocity distribution. In both cases, when polarizations are linear and circular, the 3D distribution is guaranteed to be cylindrically symmetric about the polarization axis and propagation axis respectively, which are parallel to the plane of the detector. This symmetry in the 2D image allows reconstructing the original three-dimensional distribution, using various inversion methods such as Abel inversion [94], onion peeling [94], BASEX [95], pBasex [96] etc. From that three-dimensional distribution, the photoelectron intensity can be measured as a function of the radius from the centre of the image and the angle with respect to the laser polarization (propagation axis in case of circular polarization).

For the purpose of this work pBasex computer program of Garcia et al. [96], is used, which uses polar (BASEX) rather than Cartesian coordinates for the basis functions. A series of Gaussian functions with width σ, was used to model the kinetic energy distribution of the photoelectrons, expressed as

$$F(R,\theta) = \sum_{k=0}^{k_{max}} \sum_{l=0}^{l_{max}} c_{kl} e^{-(R-R_k)^2/\sigma} P_l(\cos\theta) \qquad (2.1)$$

where θ is measured with respect to the propagation direction (circularly or unpolarized light) or the polarization direction (linearly polarized) of the light, R is the radius from the centre of the image, R_k is the centre of the kth Gaussian, and P_l is the Legendre polynomial of order l. The pBasex program extracts the coefficients c_{kl} such that the 2D projection of $F(R, \theta)$ is similar to the recorded image. Based on the symmetry considerations, further simplification arises, for example, with the use of reflection (in electric field plane) and cylindrical symmetry, the odd-l terms and non-

zero *k* terms disappear from Equation (2.1). Thus, pBasex considers only the terms for l = 0, 2, 4 and 6... For a given electron kinetic energy, the angular distribution of the electrons can then be described in terms of anisotropy parameters, β_{20}, β_{40}, and β_{60}… Whereas for chiral molecules, the reflection symmetry does not apply, hence odd-l terms also contribute to the expression of angular distribution and anisotropy parameters, b_{10}, b_{30}, b_{50}…

The analysis of the photoelectron intensity data was carried out using the pBasex package written in the IGOR pro software by Gustavo Garcia [97]. The output files are produced, giving the photoelectron intensity and anisotropy parameters as a

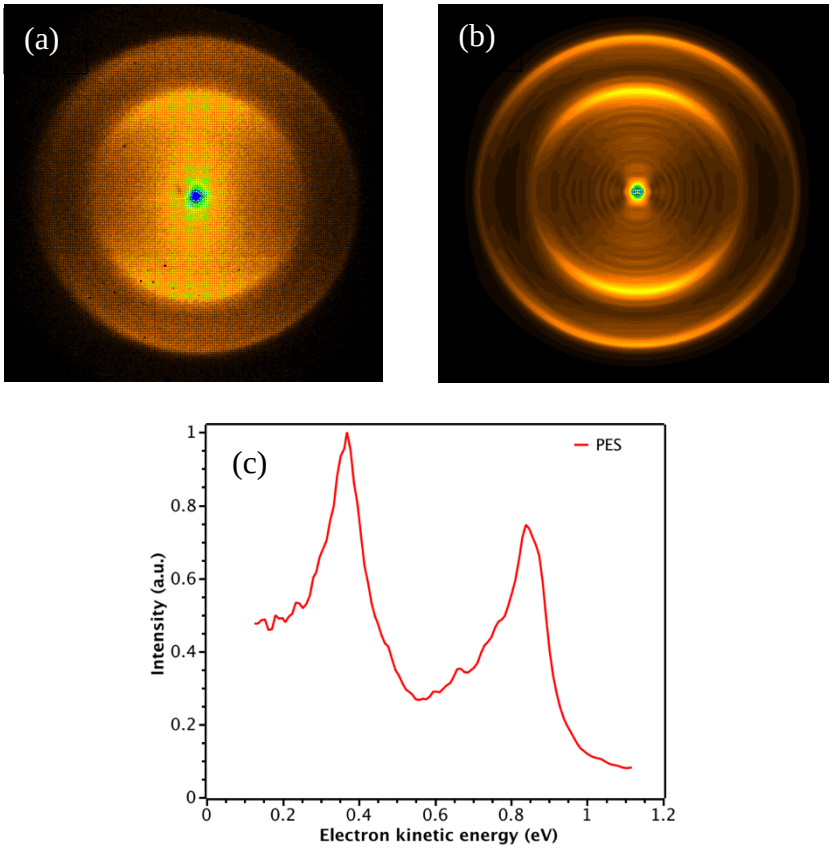

Figure 2.7. Photoelectron image analysis. (a) Raw accumulated image with linear polarized light, (b) Inverted image using pBasex, (c) Extracted photoelectron spectra from the inverted image.

function of the distance in pixels from the centre of the image, which was converted to electron kinetic as well as ionization energy (see next section) using the calibration factor. Figure 2.7 shows a raw image alongside with an inverted image and photoelectron spectrum (PES) as a function of electron kinetic energy. In the following section, we will discuss the calibration used for conversion of radial distance, *r*, from

the centre of the image into electron kinetic energy (eKE) and ionization energy (mainly used axis).

2.6.3 Calibration

The pBasex software, shown in figure 2.8 uses a calibration factor (C) to convert the distance, r, into kinetic energy. This distance is proportional to the speed of the photoelectrons, and so their kinetic energy depends upon r^2. This is expressed as

$$\mathrm{eKE} = V_{rep}\frac{R^2}{C^2} \tag{2.2}$$

where V_{rep} is the VMI repeller voltage, and R is the radius of the image, C is the calibration constant, and eKE is the electron kinetic energy. In this thesis, photoelectron spectra are generally plotted as a function of the ionization energy (IE).

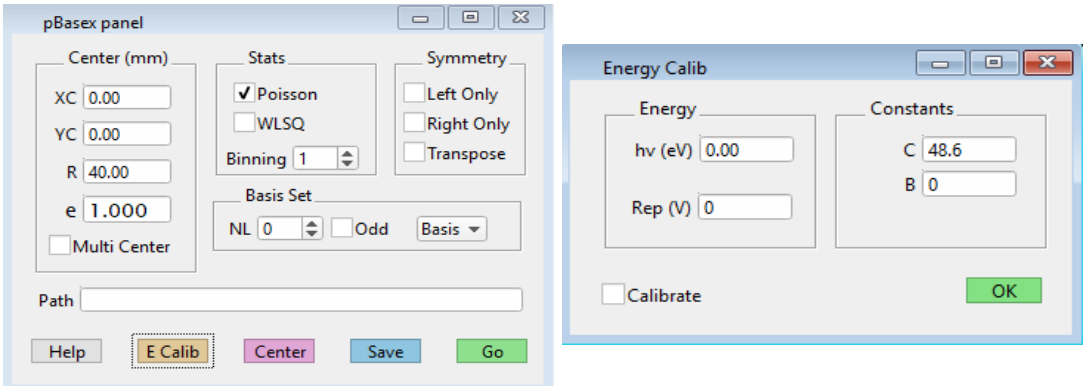

Figure 2.8. pBasex software (Igor Pro). (a) Main panel provide options to select centre, number of photons involved, stats, and symmetry (b) calibration panel, input total photon energy, and calibration constant.

This can be determined through the information of photon energies, the ionization potential (IP) and photoelectron kinetic energy, using the expression

$$\mathrm{h}\nu = \mathrm{IE} + \mathrm{eKE}, \qquad \mathrm{IE} = \mathrm{IP} + E_{int} \tag{2.3}$$

where E_{int}, is the ion internal energy. Equations 2.2 and 2.3 can be used to calculate the calibration constant C by either using a photoelectron peak for which IE is already known, for example, an origin peak for which E_{int} is 0 cm^{-1}, which would correspond to the peak at the largest radius.

For this work energy scale of VMI spectrometer was calibrated using the S_1 origin of aniline [98], the electron peak with the largest radius corresponds to ions with zero internal energy. This provides the calibration constant C, which is used to convert the

entire velocity scale into electron kinetic energy and subsequently into ionization energy for every measured photoelectron spectrum.

2.6.4 PECD data acquisition

REMPI PECD data was accumulated using an acquisition program written in LabView. PECD was measured by recording the LCP and RCP photoelectron images by rotating the quarter waveplate using a rotation mount controlled by a stepper motor (Thorlabs). Each image was recorded for a short time at each polarization to avoid the effects of drifts in laser power or other experimental parameters, and then the quarter-wave plate was rotated to record the image for the other polarization. In each case, 15000 frames were recorded before switching to other polarization, and four pairs of images were recorded. The images were added to produce final LCP and RCP images at each wavelength. Measurements using different polarization were conducted at constant pulse energies. Only one enantiomer (1R,5R) -(+)-α-pinene, 1S- (+)-carene, and 1R-(-)-fenchone were used to record the PECD data. All the samples were purchased from Sigma-Aldrich with >97% enantiomeric excess for α-pinene and >99% for 3-carene.

2.6.5 PECD data fitting

The recoded LCP and RCP images were analysed using the PECD package written in IGOR pro by Gustava Garcia (figure 2.9). This software requires the two images with

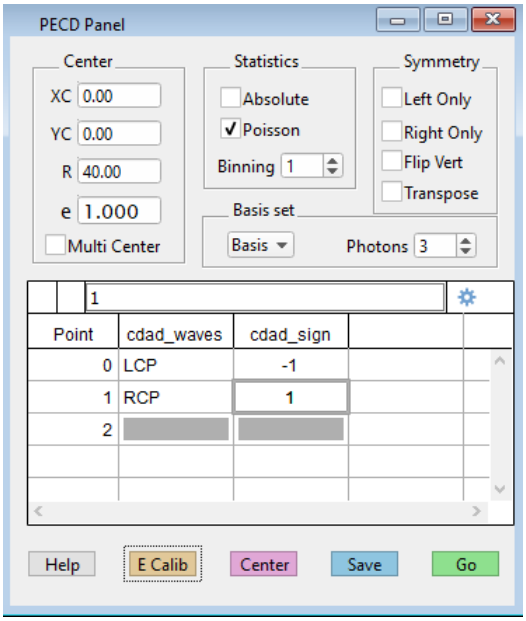

Figure 2.9. PECD analysis software (Igor Pro). Feed in the LCP and RCP image in cdad_waves with corresponding signs. Select centre of the differential image, symmetry, and number of photons involved in the process.

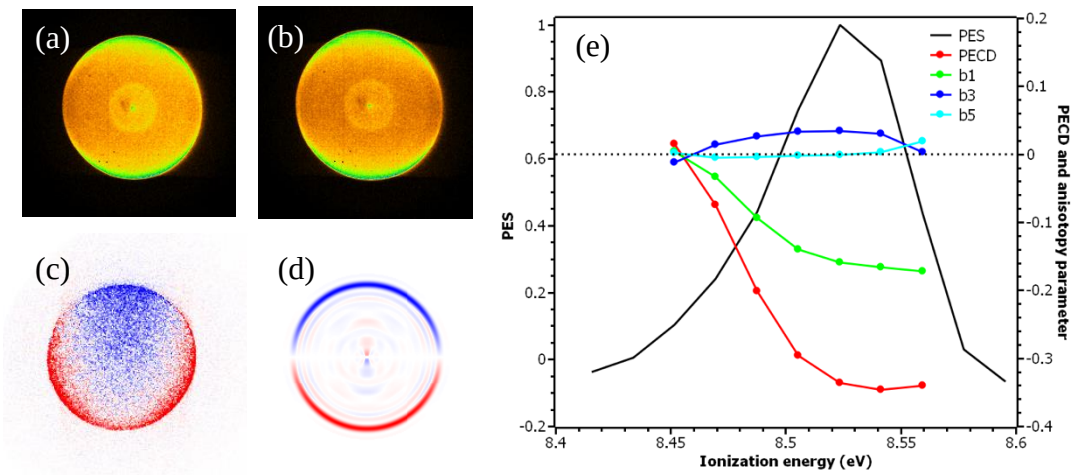

Figure 2.10. PECD analysis. (a) LCP image, (b) RCP image, (d) Differential image, (c) Inverted differential image, and (e) PES, PECD, and anisotropy parameters.

corresponding laser polarization signs. It calculates the differential image of LCP and RCP, followed by a pBasex fitting procedure based on Eq. 2.1 to calculate, photoelectron spectra (b_0), and anisotropy parameters (b_1, b_2, b_3, b_4…..). It also generates the PECD value based on weighted sum of the individual anisotropy parameters (Chapter 1 section 1.8). In this thesis, this PECD value is presented as a function of ionization energy along with the photoelectron spectrum. Figure 2.10 shows an example of PECD analysis for the fenchone molecule. Images were recorded at the origin of the 3*s* Rydberg state using 416.57 nm wavelength. The figure shows the LCP and RCP images, differential image (inverted), and photoelectron spectra alongside the anisotropy parameters.

2.7 Polarimetry

For the REMPI PECD experiment, circularly polarised light was used to ionize the molecules. Excellent control over the polarization of the laser pulse is crucial for these experiments. In has been shown that the degree of circular polarization can affect the PECD results, so an accuracy of better than a few degrees is required in the quarter-wave plates while selecting the angle. In this section, we will discuss how to generate the circularly polarized light and how to quantify the polarization by determining the Stokes parameters. The method presented below is based on the work of Beth and co-workers [99].

2.7.1 Stokes parameter

In 1852 George Gabriel Stokes showed that the polarization of light could be characterized in terms of four intensity parameters [100, 101]. The polarization ellipse of light, which is an amplitude description of light is not accessible directly to measurements. But this polarization ellipse can be shown to be directly related to the Stokes polarization parameters, thus are widely used to describe the polarization of light.

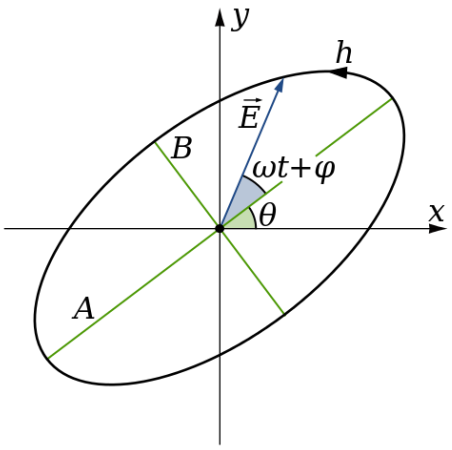

Figure 2.11. Plot of the equation for the polarization ellipse, Eq.(2.6) In general, the ellipse is not in its standard form, where $E_x(z,t)$ and $E_y(z,t)$ are directed along the x-and y-axes.

Polarization of light arises when it consists of two independent orthogonal components, $E_x(z,t)$ and $E_y(z,t)$ having different amplitudes and phases with the direction of propagation in the z-direction. These equations are described as

$$E_x(z,t) = E_a \cos(\omega t - kz + \delta_x) \tag{2.4}$$

$$E_y(z,t) = E_b \cos(\omega t - kz + \delta_y) \tag{2.5}$$

where E_a and E_b are the maximum amplitudes, t represents time, ω is the angular frequency of the field, and δ_x and δ_y are the phase constants. The term $\omega t - kz$ describes the propagation of the wave and is called the propagator. As field components cannot be observed directly, the visual representation of polarization of light can be obtained by eliminating the propagator in Eqs. (2.4 and 2.5) yielding

$$\frac{E_x(z,t)^2}{E_a^2} + \frac{E_y(z,t)^2}{E_b^2} - \frac{2E_x(z,t)E_y(z,t)}{E_aE_b}\cos\delta = sin^2\delta \tag{2.6}$$

where $\delta = \delta_x - \delta_y$. This equation is called polarization ellipse, as shown in figure 2.10. The time average of Eq. 2.6 leads to the observable parameters of this polarization ellipse,

$$S_0^2 = S_1^2 + S_2^2 + S_3^2 \tag{2.7}$$

where

$$S_0 = E_a^2 + E_b^2, \tag{2.8a}$$

$$S_1 = E_a^2 - E_b^2, \tag{2.8b}$$

$$S_2 = 2E_a^2 E_b^2 \cos\delta, \tag{2.8c}$$

$$S_3 = 2E_a^2 E_b^2 \sin\delta. \tag{2.8d}$$

Equation (2.8) defines the four Stokes polarization parameters. They are described in terms of intensities (amplitudes squared) and therefore can be measured. The parameter S_0 describes the total intensity of the optical field, S_1 describes the preponderance of linearly horizontally polarized light (LHP) over linearly vertically polarized light (LVP), S_2 describes the preponderance of linear +45° polarized light (L +45P) over linear −45° polarized light (L−45P), and the fourth parameter S_3 describes the preponderance of right circularly polarized light over left circularly polarized light. The Stokes parameters in Eq. 2.8 can be arranged as the elements of a 4 × 1 matrix as

$$S = \begin{pmatrix} S_0 \\ S_1 \\ S_2 \\ S_3 \end{pmatrix} = \begin{pmatrix} E_a^2 + E_b^2 \\ E_a^2 - E_b^2 \\ 2E_a^2 E_b^2 \cos\delta \\ 2E_a^2 E_b^2 \sin\delta \end{pmatrix} \tag{2.9}$$

this is called the Stokes vector. Different polarization states can be represented as,

$$S_{LHP} = \begin{pmatrix} 1 \\ 1 \\ 0 \\ 0 \end{pmatrix},\ S_{LVP} = \begin{pmatrix} 1 \\ -1 \\ 0 \\ 0 \end{pmatrix},$$
$$S_{RCP} = \begin{pmatrix} 1 \\ 0 \\ 0 \\ 1 \end{pmatrix},\ S_{LCP} = \begin{pmatrix} 1 \\ 0 \\ 0 \\ -1 \end{pmatrix} \tag{2.10}$$

The Stokes vectors have been normalized to unit intensity. In the next section, we discuss how to characterize a quarter-wave plate (QWP) and measure the Stokes parameters.

2.7.2 Quarter wave plate characterization

The laser pulses out of the TOPAS are vertically polarized. To convert the vertically polarized light to circularly polarized light a quarter-wave plate (B.Halle Nachfl. GmbH RAC 5.4.10L) was used. Before the pulse entered the vacuum chamber through the entrance window it passed a polarizer, and a quarter quarter-wave plate. The polarizer ensured a clean linear polarization state of the beam before the pulse passes through the QWP. The QWP was mounted on a motorized rotational stage with an electronic readout with a resolution of better than 0.1 degree. Passing linearly polarized

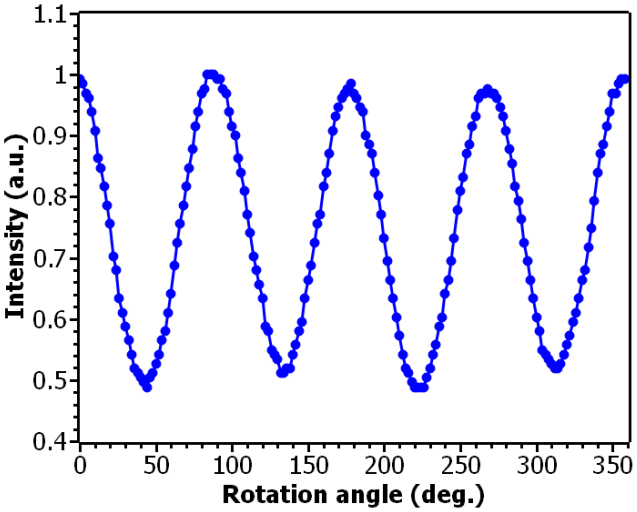

Figure 2.12. Quarter-wave plate characterization. Showing the polarizer transmission as a function of the angle of the QWP.

light through a quarter-waveplate with its axes at 45° (135°) to its polarization axis will convert it to left (right) circular polarization. But these QWP are broadband waveplate, so these angles are always slightly off for a particular wavelength in the broad spectrum range. Therefore, we need to characterize these QWP to get the perfect angles for LCP and RCP. For this characterization, the lasers pulses were transmitted though the QWP and a polarizer and the power was measured in the end using a power meter. The transmission through the polarizer was measured as a function of the quarter-waveplate rotation. The result gives a calibration of the orientation of the major polarization axis with respect to the laboratory frame.

Figure 2.12 shows data from the polarimetry measurements. The data show the peaks have the same height and are separated by 90 degrees from each other. The peaks and valley correspond to the 45-degree angle between fast and the slow axes. To convert linear light to circular light (LCP and RCP), we can place the QWP at the angle of

either peaks or valley in the plot. For this work, we selected angles 45^0 and 135^0 to generate LCP and RCP respectively.

2.7.3 Measuring Stokes parameters

The measurement of the Stokes parameters was carried out by allowing the circularly polarized light to propagate sequentially through a quarter-wave plate and a polarizer. A waveplate can be represented by two orthogonal axes known as the fast and slow axes. The waveplate creates a phase shift ϕ between the orthogonal components of a polarized beam. The quarter waveplate introduces a phase shift of one-quarter of a wave (π/2) between the orthogonal components of the polarized beam. A linear polarizer is also characterized by a pair of orthogonal transmission axes. Ideally, no transmission occurs along one axis, and there is complete transmission along the orthogonal axis.

Figure 2.13. A method for measuring the Stokes polarization parameters for a circularly polarised laser pulse. The figure shows the polarizing elements that generate the Stokes parameters to be measured.

In the measurements, the waveplate was rotated through an angle θ while the polarizer was fixed with its fast axis aligned vertically. Figure 2.13 shows the measurement configuration. The intensity modulation of the optical beam on the detector shown in figure 2.14 is analysed by fitting with equation:

$$I(\theta) = \frac{1}{2}(A + Bsin2\theta + Ccos4\theta + Dsin4\theta), \quad where\ A = S_0 + \frac{S_1}{2}, B = S_3, D = \frac{S_2}{2} \tag{2.11}$$

where $S_0, S_1, S_2,$ and S_3 are the four Stokes parameters needed to characterize the polarization of the light. The S_0 parameter describes the total intensity of the optical field, S_1 describes the preponderance of horizontally over vertically polarized light, S_2, describes the preponderance of linear +45◦ polarized light over linear −45◦ polarized light and, and the fourth stokes parameter, S_3, describes the preponderance of RCP over LCP. Thus, for LCP light $S_3 = -1$ and for RCP light $S_3 = +1$.

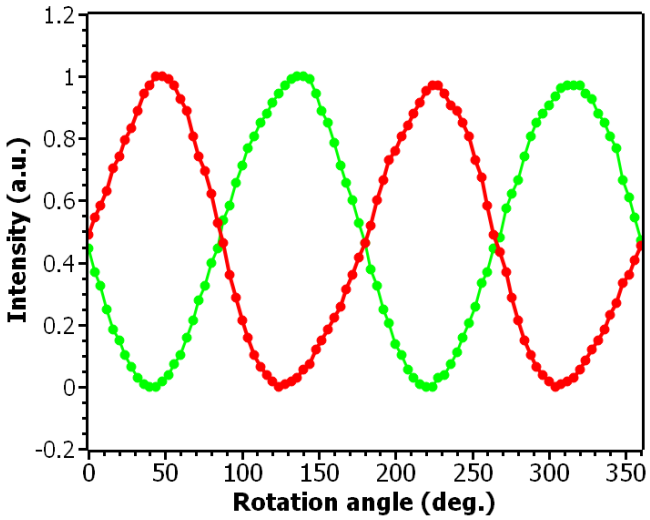

Figure 2.14. Data from polarimetry measurements. The measured transmission for either right-circular polarized light (red curve) or left-circular polarized light (green curve) of picosecond laser pulses centered around 411.2 nm.

A plot of the intensity versus the continuous waveplate rotation angle for Eq. 2.11 is shown in figure 2.14. The Stokes vectors obtained were $S_{RCP,411nm}$ = (1, -0.353, -0.515, 0.963) and $S_{LCP,411nm}$ = (1, -0.027, -0.202, -0.985). For wavelengths at 374 nm the Stokes vectors were $S_{RCP,374nm}$ = (1, -0.745, 0.154, 0.965) and $S_{LCP,374nm}$ = (1, 0.243, 0.731, -0.968). The chiral angular distribution parameters are expected to be affected by the ellipticity of the light source (S_3), which can require a correction in the data [102, 103]. In our case, because of the excellent degree of polarization, $|S_3| > 96\%$, we have not applied a correction.

Chapter 3 Photoelectron spectroscopy and photoelectron circular dichroism of fenchone via 3*spd* Rydberg states

3.1 Introduction

Fenchone is a naturally occurring chiral terpenoid compound ($C_{10}H_{16}O$) that contributes its distinctive odour to plants such as fennel. Alongside its many claimed uses as an essential oil extract (perfumery, aromatherapy, flavouring, and antimicrobial agent) it is also commonly adopted as a benchmark molecule with established chiroptical techniques such as electronic absorption circular dichroism (ECD) [104, 105], vibrational circular dichroism (VCD) [46], Raman optical activity (ROA) [47], and optical rotatory dispersion (ORD) [106]. Importantly in this context, fenchone has a rigid bicyclic structure (figure 3.1) that prevents it from adopting multiple conformations, consequently removing ambiguity about the structural forms present in various media. Fenchone also has relatively high vapour pressure, making it a benchmark molecule also for gas-phase chiroptical techniques. These include cavity ring-down polarimetry [107], and photoelectron circular dichroism (PECD) measured with synchrotron radiation in both soft X-rays C 1s ionization [55] and vacuum ultraviolet (VUV) valence band ionization [11, 51, 54, 108]. Even more recently, fenchone has been a primary molecule of choice in fundamental investigations of laser multiphoton ionization PECD [70, 73, 77, 80, 109, 110] including pump-probe time-resolved measurements [81, 109]. Complementing the fundamental laser based studies, multiphoton ion yield [70] and enantiomeric excess determination [110] experiments have addressed more analytical applications using fenchone as a testcase.

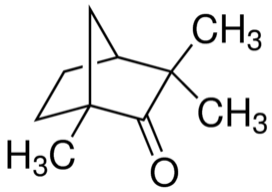

Figure 3.1. Enantiomer (1R)- (-)-fenchone.

In the past two decades, these single-photon and multiphoton ionization studies at a variety of light sources have shown that the PECD measurements are sensitive to electronic [111] and nuclear structure (conformation) [58]. Moreover, Resonance-

enhanced multiphoton ionization has given access to electronic intermediates and, with the help of femtosecond laser excitation and ionization, PECD has been demonstrated in a (2+1) REMPI scheme using fenchone as a testcase [73, 74]. As a result of more angular momentum transfer in higher multiphoton process in comparison to single-photon ionization, even higher order anisotropy parameters were observed.

However, despite this rather intensive uptake of fenchone in resonance enhanced multiphoton studies of chiral molecules, there remains relatively little background detail concerning its excited state spectroscopy and effects of vibronic state and electronic kinetic energy on PECD measurements are still unresolved. Older measurements of the He I photoelectron spectroscopy of fenchone [105, 112] mapped out the valence band ionization profile at low resolution. Very much higher resolution was achieved in REMPI spectra obtained using nanosecond pulse lasers for two-photon excitation via the 3*s* [113, 114] and, more recently, an extended scan to the include the 3*p* region, but with only limited analysis. Recently, the effect of the initial and final state was shown by Kastner and co-workers in a (2+1) REMPI PECD measurements for fenchone via the B- and C-band transitions, which are believed to correspond to 3*s*←n and 3*p*←n excitation, respectively [80, 115].

In this chapter, we report a new, wide range (5.7 eV – 9.0 eV) absorption spectrum, recorded using VUV Fourier transform (FT) spectrometry, that spans from the onset of the Rydberg excitations in fenchone to above its ionization energy. This is complemented and directly contrasted with a picosecond (ps) laser (2+1) REMPI spectrum of the n = 3 Rydberg region recorded at comparable resolution. Laser intensity dependence measurements made with ps and fs pulse duration lasers are recorded to help establish the relative importance of the two-photon absorption, ionization, and relaxation processes in the REMPI spectrum. Polarization dependent measurements of the parent ion yields are then able to be used to estimate the circular-linear dichroism in the two-photon absorption. Finally, vibrationally resolved photoelectron spectra and REMPI PECD, generated with ps excitation, are recorded across the 3*sp* Rydberg region, and these not only provide new insight into the cation vibrational distribution following the ionization step but also suggests very different roles for vibrational dynamics in the intermediate Rydberg states. This work extends the previous studies done by the Baumert group [80] (femtosecond work) on the influence of the electronic character of an intermediate excited state on the observed

PECD in fenchone using a picosecond laser pulse. This enables the resolution of vibrational states in excitation and ionization and consequently the influence of vibrational motion on PECD. This knowledge will help further our goal to disentangle the competing influences on PECD.

The chapter is structured in two main parts; the first part presents one colour photoelectron spectra which were needed in order to locate the excited electronic states and determine the ionization potential. Parent ion yields are presented as a function of laser power and polarization in order to provide further insight into the electronic structure, including the symmetry of the initial and excited states. This part of the work has been submitted for publication, thus this chapter will has some overlap with the manuscript [116]. The second part presents vibrationally resolved picosecond PECD results for ionization via various electronic and vibrational intermediate states. This part of work is in preparation for publication.

3.2 Experimental section

In this experiment long-range (350 - 420 nm, 5.85 - 7.08 eV) vibrationally resolved picosecond (2+1) REMPI PES and PECD measurements were recorded using a picosecond laser and velocity map imaging spectrometer. The experimental setup used in this experiment is described in detail in Chapter 2. In brief, 1.3 ps pulses in the UV range were generated using the Nottingham based Ti:Sapphire ultrafast laser system (described in Chapter 2 Section 2.2.1). In order to record REMPI spectra a wavelength scan was performed over the range 350 - 420 nm with a step size of 0.05 nm and 2 s delay time. REMPI spectra, photoelectron spectra (PES), and PECD measurements were made using S-(+)-fenchone enantiomer. The sample was purchased from Sigma-Aldrich (99.9% enantiomer excess), seeded with helium and introduced through a 150 µm kHz pulsed nozzle (see Chapter 2 Section 2.2.3). The pressure in the interaction chamber was typically 2×10^{-7} mbar, with a background pressure of 5×10^{-8} mbar. Photoelectrons were detected using velocity map imaging, and the 3D distributions were reconstructed using pBasex (Chapter 2 Section 2.6.2). PES measurements were undertaken with linearly polarised light and PECD measurements with circularly polarized light. Details of the methodology used to record the PECD images is presented in Chapters 2. The degree of circular polarization is quantified by the Stokes

parameter S_3 (see Chapter 2 Section 2.7.1), which for all our measurements was well above 96%.

3.3 Results and discussion

In this section (2+1) REMPI spectra in the range 350-420 nm (5.85-7.08 eV) are presented. PES and PECD measurements were recorded for ionization via different vibrational levels of the 3*s* and 3*p* Rydberg intermediate states. In Section 3.4 and 3.5 the REMPI and PES spectra are presented and the relevant intermediate states highlighted. In Section 3.6 the laser power and Section 3.7 laser polarization dependent parent ion yield measurements are presented, followed by the PECD measurements. There is a significant difference in PECD signal for the two electronic states, and a comparison of the resulting anisotropy parameters is presented. In Section 3.8 we present vibrationally resolved PECD measurements in the 3*s* and 3*p* regions. In Section 3.9 we discuss how the results can be used to decouple the effects of photoelectron kinetic energy, vibrational structure and electronic state on PECD.

3.4 (2+1) REMPI spectrum

In figure 3.2 we present a (2+1) REMPI spectrum of fenchone, recorded by monitoring the parent ion mass, m/z 152, while scanning with linearly polarized, picosecond laser pulses. The spectrum was recorded over the range 350 - 420 nm (5.85 - 7.08 eV, two-photon energy) and has been normalized by the pulse energy, which ranged around 12 $\pm$ 2 μJ across the spectrum. The spectral resolution of the 1.3 ps pulses was estimated to be around 50 cm^{-1} (further details in Chapter 2). As a result of the relatively narrow laser bandwidth and the use of a cold molecular beam source, resolved vibrational features were observed, comparable to those seen in a high-resolution VUV absorption spectrum, also shown in figure 3.2. This absorption spectrum was recorded with a VUV Fourier transform (FT) spectrometer at a dedicated branch on the DESIRS beamline at Synchrotron SOLEIL (further detail in Chapter 2 Section 2.3). The state-of-the-art FTS instrument can cover a large UV-VUV spectral range from 4 to 30 eV. The FT scan starts above the region of the first, very weak n-π* valence excitation but then extends beyond the fenchone ionization threshold (8.4 eV). The FT spectrometer was set to provide a spectral resolution of 17.2 cm^{-1} which is around ten times better than the 0.5-2.0 nm resolution spectrum reported by Pulm et al. [105], and while still

in broad agreement the structure here is more pronounced, especially at the lowest energy. A comparison between VUV single-photon absorption measurements and (2+1) REMPI measurements is shown in figure 3.2. There is clearly a very close resemblance between the absorption spectrum and the two-photon REMPI spectrum, both of which show vibrational bands in the energy region corresponding to three different 3*l* Rydberg states. The different regions identified in the REMPI spectrum correspond to the B-, C- and D-band transitions, which are believed to correspond to 3*s*←n, 3*p*←n, and 3*d*←n excitation, respectively [105]. However, the relative intensity of the 3*s* excitation appears much stronger in the REMPI spectra than VUV absorption spectra. This different 3*s*:3*p* ratios in the VUV and REMPI spectra are ascribed to the different photon transition mechanisms for the resonant ground-Rydberg excitations [116].

The 3*s*←n (B-band transitions) are observed in the region 5.9-6.3 eV with the 0-0 transition at 5.95 eV, followed by the peaks corresponding to vibrational levels of the 3*s* Rydberg state. The threshold of the 3*p* transition was assigned with the help of work done by various authors. The theoretical work of Pulm et al. has shown that energy

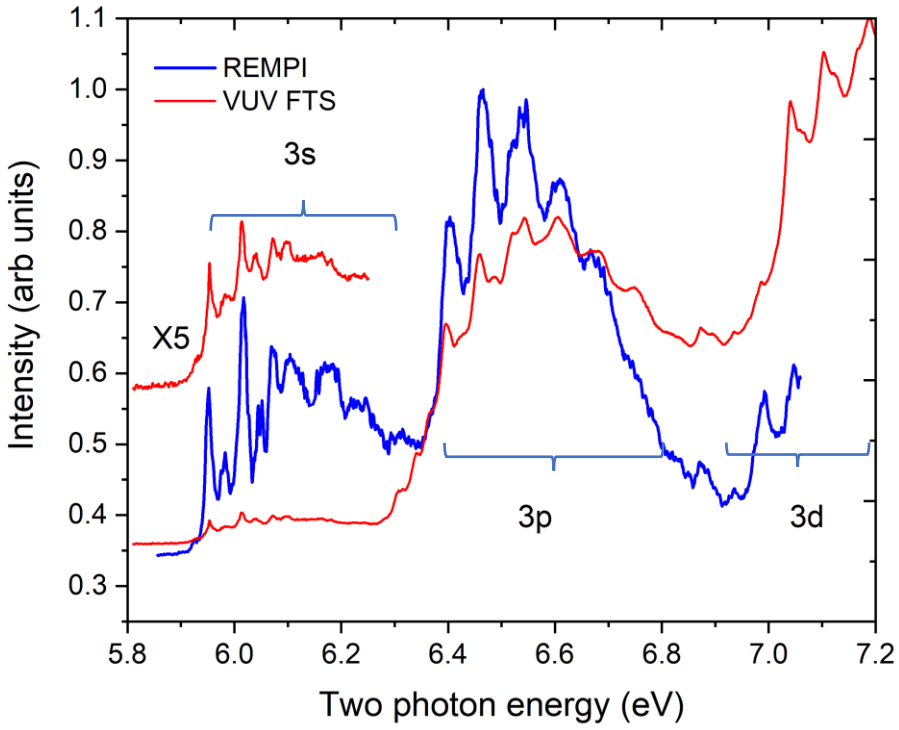

Figure 3.2. REMPI spectrum (blue) in comparisons with VUV Fourier transform spectrometer measurements (red) of fenchone. FTS spectrum is zoomed 5 times in 3s region.

separation between the origins of the B- and C-bands is 0.48 eV [105]. The VUV absorption spectrum shows a separation of 0.44 eV between the bands. The energy separation that we determine from our REMPI spectrum is 0.45 eV, which enables us to assign the peak whose onset is 6.4 eV as the origin of 3*p* state and the region 6.4-6.9 eV to 3*p*←n (C-band) transitions. The three members (*x*, *y*, *z* states) of the 3*p* Rydberg states are perturbed by the bicyclic skeleton so that an interpretation in the local C_2 symmetry frame of the carbonyl group is difficult. Tentatively, the components can be assigned to $3p_x$ (A_2 in local C_2 symmetry), $3p_y$, (A_1) and $3p_z$ (B_2) states with energy ordering of *yzx* (increasing order of energy) for the three components [105]. Theoretically, it has been shown that in the two-photon resonant spectra of fenchone's 3*p* states the $3p_y$ state will be dominant, with weak contribution from $3p_x$, and the $3p_z$ contribution will be negligible [116]. The region above 7.0 eV corresponds to 3*d*←n (D-band) Rydberg transitions.

The peak width in the REMPI spectrum is not the same through different regions which raises the question why the ps REMPI peak widths in the 3*p* region appear broadened compared to those of the 3*s* band? The authors of Refs. [80, 115] have previously noted that the 3*p* lines in their ns REMPI spectrum were broader than the 3*s* lines (the latter most probably reflecting rotational profiles). From the experimental linewidths they were able to estimate $\tau \geq 0.6$ ps as a lower lifetime limit for the 3*s* state. Further, from the extra width of the 3*p* lines they suggested $\tau \geq 80$ fs for the 3*p* state. It is implausible to simply transfer these lifetime broadening arguments to the ps pulse duration REMPI spectrum. Rather, we consider the possibility that the observed ps 3*p* widths reflect the unresolved excitation of both $3p_y$ and $3p_x$ states (we discount $3p_z$ given its much lower predicted two-photon cross-section [116]). Further discussion on the lifetime of these Rydberg states is provided in Section 3.6.

3.5 Photoelectron spectra

Photoelectron images were recorded in the range 365-420 nm (5.9-6.79 eV, two-photon energy) following the preparation of vibrational levels in the 3*s* and 3*p* region. Figure 3.3 shows the photoionization scheme used in this experiment, which allows access to a range of vibrational levels in 3*s* and 3*p*. The photoelectron spectra were extracted from these photoelectron images using pBasex. These photoelectron spectra are plotted as a function of ionization energy (IE) which is calculated by assuming an overall three-photon process and subtracting the measured electron kinetic energies from the three-photon energy. Figure 3.4 provides an overview of the normalized set of REMPI-PES. The series of photoelectron spectra are measured as a function of the

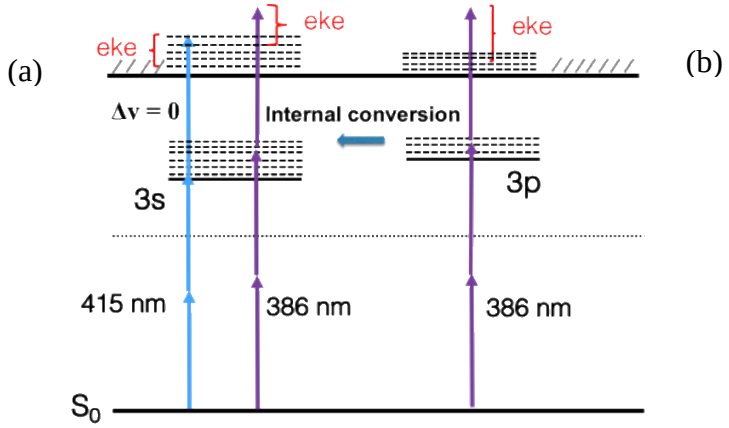

Figure 3.3. Illustration of (2+1) ionization scheme; showing two scenarios (a) ionization via 3s (b) ionization via 3p or vibrationally excited 3s state.

two-photon excitation energy (2ϕ). Each spectrum was normalized by the laser power and acquisition time. A $\Delta v = 0$ propensity rule in the intermediate state ionizations studied here can be expected owing to these Rydberg states possessing a cationic molecular core, so that vertical ionizing transitions with no change in quantum number(s) are favoured (see Chapter 2 Section 2.3). As a consequence of this propensity rule, the photoelectron spectra displays a single intense peak for ionization via 3*s* [386-416 nm (5.96-6.42 eV)] and a double peak for ionization via 3*s* and 3*p* [350-386 nm (6.42-7.08 eV)]. These peaks steadily move to higher IE with increasing excitation energy.

Figure 3.4 shows that as the wavelength (two-photon energy, 2ϕ) is changed different vibrational levels in 3*s* and 3*p* are accessed. The $\Delta v = 0$ propensity rule as mentioned above gives a single intense photoelectron peak at each wavelength for these

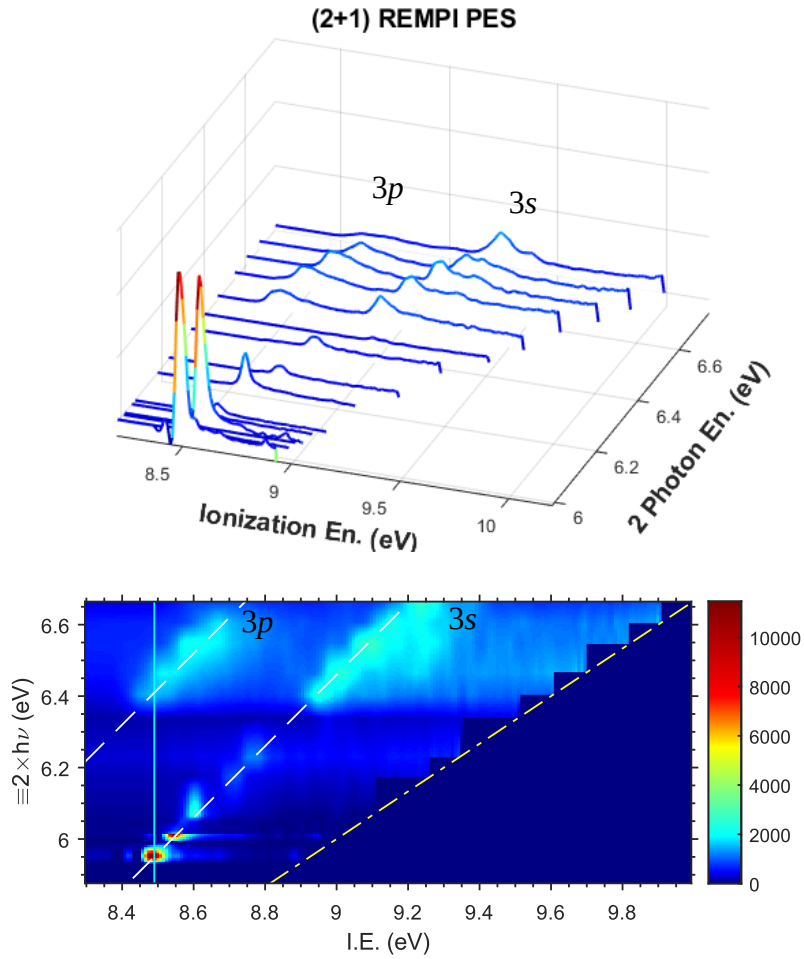

Figure 3.4. REMPI PES of fenchone, recorded with picosecond duration laser pulses, for selected excitation wavelengths, shown against the two-photon equivalent energy. The ionization energy is determined by subtracting the recorded electron kinetic energy from the three-photon equivalent energy. Top panel: waterfall plot to display the spectra recorded for two-photon excitation into the 3sp region. The individual circularly polarized spectra are normalized by measurement time and (laser power)^2, although it is known that in the 3s region the power dependence may exceed 2nd order (see text). Lower panel: pseudo-colour intensity map of the above data. The adiabatic ionization potential (8.495 eV) is marked (solid line) as is the maximum ionization energy accessible in a three-photon process at each excitation (dash-dotted line). Also marked with dashed lines are the ridges seen in the waterfall plot.

Rydberg/states. This results in the formation of two distinct ridges in figure 3.4 corresponding to ionization via 3*s* and 3*p*. The first peak along the 3*s* ridge which rises around 8.49 eV corresponds to the 0-0 transition, matching well with previous literature [80, 105, 115]. Although at this laser wavelength the three-photon equivalent energy (3ϕ = 8.93 eV) is energetically sufficient to ionize several vibrationally excited states. The rest of the photoelectron spectra along this ridge map out a well-resolved vibrational structure in 3*s*, with the peak intensities in reasonable agreement with a Franck-Condon simulation (see figure 3.10), which is used to confirm the assignment.

Once the excitation energy $2\phi \geq 6.4$ eV is reached, a second ridge, slightly broader, appears in the REMPI-PES overview (figure 3.4 (a)) running parallel to the first. This is readily understood as being formed by $\Delta v = 0$ excitations in ionization from the 3*p* state(s). Back-extrapolating, the line of this ridge intersects the line of the adiabatic IE at a point $2\phi = 6.4$ eV (figure 3.4 (b)), which value we have already identified as being indicative of the 3*p* thresholds. At the same time, the initial ridge associated with the ionization of the 3*s* Rydberg state apparently continues throughout the 3*p* excitation band. One might first suppose that this is because above $2\phi = 6.4$ eV both the 3*s* and 3*p* Rydberg states are energetically accessible and so ionization of either can occur in parallel. However, at shorter wavelengths the ionization energies reached along this ridge exceed 9.1 eV and so fall outside the Franck-Condon window for direct vertical ionization from ground state neutral to the cation. More tellingly, these resonance enhanced ionizations also fall beyond the Franck-Condon envelope for the neutral to 3*s* Rydberg excitation, as evidenced in figure 3.10. The probability of there being a direct vertical transition from the ground state neutral to the cation via the 3*s* intermediate accounting for the continuation of this 3*s* ridge is therefore quite negligible.

In fact, following the intensity profile along the peak of this 3*s* ridge one sees it essentially first follows the 3*s* region FC profile seen in figure 3.10. Then, having started to diminish, at the 3*p* threshold the intensity revives and the profile (rather than the absolute intensity) repeats, again following one of the FC envelopes (e.g. the 3*p*). Recognizing that the width of 3*s* ridges has at the same time increased, and the additional contribution made by the broad 3*p* ridge, it becomes clear that the total electron yield increases sharply, as does the REMPI intensity (figure 3.2) above the 6.4 eV 3*p* threshold. The 2nd order laser intensity dependence recorded for excitation above 6.4 eV indicates that the ionization step is saturated (see next section) so that the photoelectron intensity would be expected to follow the vibronic cross-section for the intermediate state excitation. Hence we are led to infer that in the region $2\phi \geq 6.4$ eV the strongly FC favoured 3*p* excitation rapidly dominates over any disfavoured 3*s* excitation, but that some 3*p* population can rapidly interconvert to high vibrational levels of the 3*s* state. It is these highly excited 3*s* states that are then ionized which now will terminate in equally high vibrational levels of the cation lying outside the ground state FC window.

The photoelectron images were recorded via a (2+1) REMPI scheme in a parallel polarization geometry, the photoelectron angular distribution equation (see Chapter 1) is reduced to four terms with L = 0, 2, 4, 6 and M = 0. Figure 3.5 shows the β_{L0} parameters resulting from fitting the spherical harmonics for l_{max} = 6 for ionization via

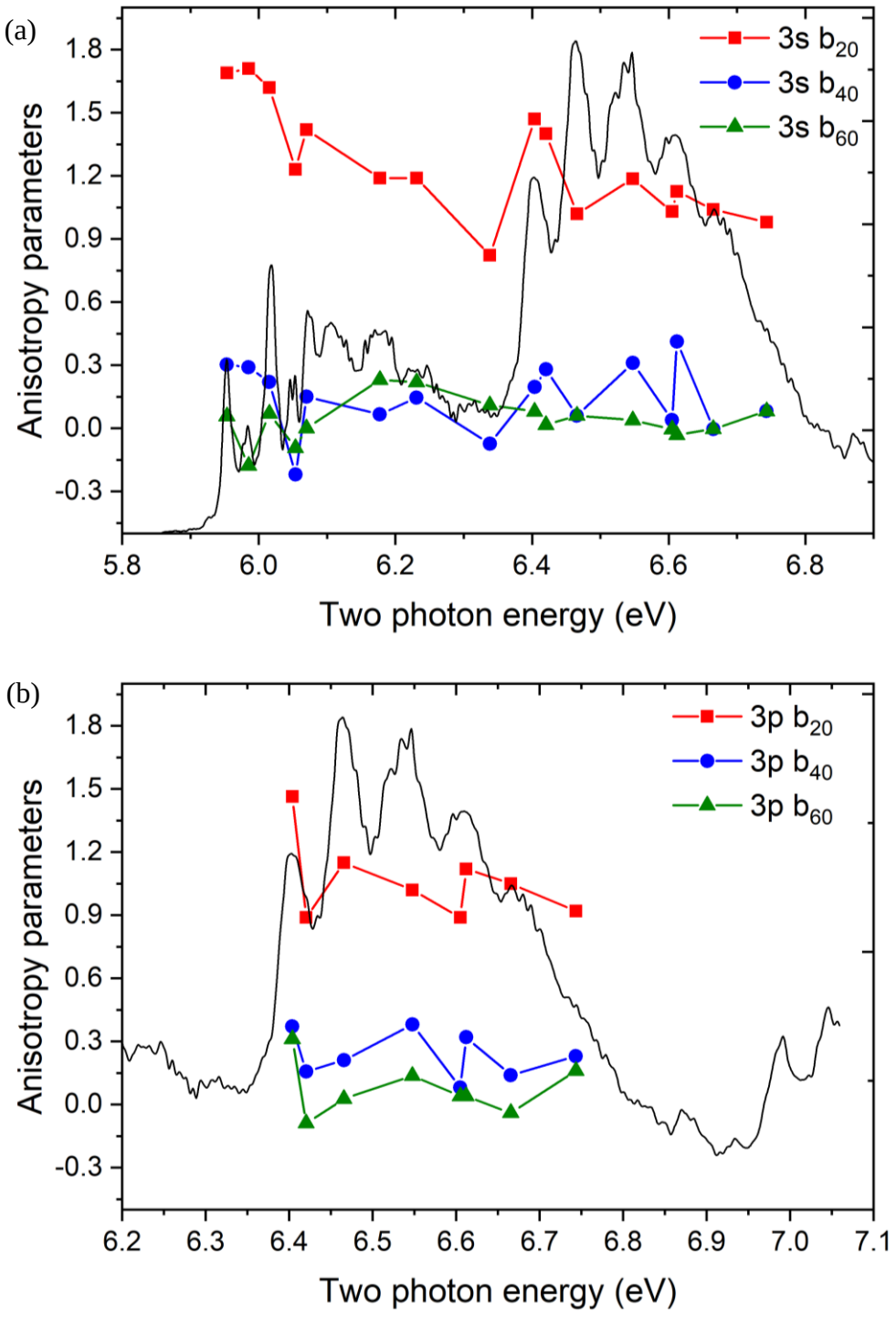

Figure 3.5. Anisotropy parameter b_{20} (red), b_{40} (blue), and b_{60} (green) for ionization via (a) the 3s and (b) the 3p Rydberg state of fenchone.

3*s* (figure 3.5a) and 3*p* (figure 3.5b). Each point corresponds to a different photoelectron peak. Each value was calculated by taking the average over the full width at half maximum (FWHM), which was obtained by fitting the Gaussian over every peak. In the case of ionization of 3*s*, only the β_{20} parameter has a value significantly different from zero, varying between ~0.7 at 390 nm and ~1.7 at around 415 nm. This is consistent with the expectation for ionization of an *s* state. In the case of 3*p*, both β_{20} and β_{40} have values that are significantly different from zero, with β_{20} varying from ~0.9 to ~1.5 and β_{40} varying from ~0.05 to ~0.3.

3.6 Intensity dependence of the REMPI ion yield

In order to explore further the excitation and ionization mechanism, we measured the parent-ion yield as a function of the laser intensity. The probability of multiphoton ionization processes depends on the light intensity raised to the nth power, where n is the number of photons involved. In a (2+1) REMPI process, the ionization proceeds via an intermediate state that is resonant with two photons. Therefore, the ionization cross-section should be proportional to the square of the laser intensity. In order to verify the power law in operation in these measurements, we measured parent ion yield as a function of laser power at several excitation wavelengths along the REMPI spectrum; see figure 3.6. Two different power laws can be observed in the range of 390-416 nm (5.9-6.4 eV) and 350-390 nm (6.4-7.1 eV). The first range corresponds to 3*s* transitions which shows an average of n = 3.2 (~3rd order) and the second corresponds to 3*p* transitions showing an average of n = 2.1 (~2nd order). A similar measurement was done in 3*s* region using femtosecond laser pulse at 407.5 nm (equivalent two- and three-photon energies of 6.09 eV and 9.13 eV respectively) [116]. Femtosecond measurements showed a second-order intensity dependence, usually an indication of saturation of the ionization step, such that the two-photon intermediate state excitation is rate determining step. A simple first-order kinetic model for a (2+1) REMPI process presented by Singh et al. [116], considers competition between the monitored parent (m/z 152) ionization and relaxation by non-ionizing, or unobserved ionization channels gives an approximate result that for a 2nd order power dependence, $1/\tau \ll \sigma^{(1)} I$ and for a 3rd order dependence $1/\tau \gg \sigma^{(1)} I$, where τ is the effective relaxation time, $\sigma^{(1)}$ is the single photon ionization cross-section (excited state to cation), and I the intensity. For a 2nd order process, assuming a typical value of ~10

Mb for the ionization cross-section (one photon, Rydberg state to cation), and considering a mid-range fs laser intensity of 1.2 x 10^{13} W cm^{-2} we obtain that $\tau \gg 4$ fs.

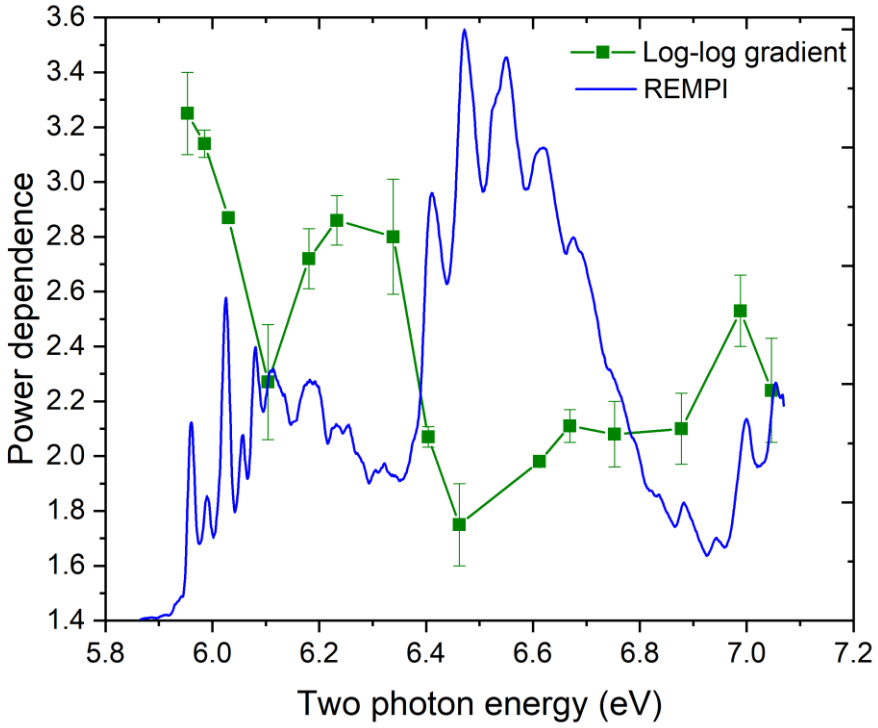

Figure 3.6. Laser power dependence of parent ion yield for S-(+)-fenchone. Linear fit slopes of log_{10}-log_{10} plot of ion yield vs laser power at different wavelengths along the REMPI spectrum plotted for parent ion.

Similarly, a 2nd order intensity dependence is found for the parent ionization channel in the 3*p* resonant excitation using ps duration laser pulses around 376 nm (6.6 eV) (figure 3.6). In contrast ps excitation in the 3*s* resonant region the laser intensity dependence for parent ion production exceeds 2nd order and approaches 3rd order. Conventionally, this now indicates that relaxation into non-ionizing channels is becoming competitive with ionization. Since the laser pulse duration is 1.3 ps we may infer that τ is of similar magnitude. This is, of course quite consistent with the above deduction of a 4 fs lower limit based on the fs laser result, and with the alternative estimate of $\tau_{3s} \geq 0.6$ ps based upon observed ns laser REMPI linewidths [80, 115]. It is also fully consistent with a direct lifetime measurement of $\tau_{3s} = 3.3$ ps made by a delayed pump-probe experiment at 201 nm (single photon resonance) [81].

3.7 Polarization dependence of REMPI ion yield

The two-photon absorption cross-section is polarization dependent, and in particular is sensitive to whether the light is linearly or circularly polarized. This effect is known as circular-linear (C/L) dichroism and is defined by the ratio of the ion yield of circular to linear light used for the ionization process. The magnitude of the effect can provide information on the angle between the permanent dipole moments (ground and excited) [117] and on the symmetry of the excited state [118]. For example, if the molecule belongs to a well-defined symmetry point group, it can be concluded that if the ratio is < 1, the symmetry of the ground and the excited state are the same. In contrast, if the ratio is > 1, the ground and excited states have different symmetries. However, because fenchone has no symmetry properties, the ratio cannot be used in this way here.

Polarization studies of two-photon absorptions, made in the liquid phase, are a well-established technique that can help assign symmetry and hence identify electronically excited states [119-121] but can also have diagnostic value with chiral molecules that lack any symmetry [122, 123]. The circular-linear dichroism effect (difference between the circular- and linear- polarized light excitation strengths) in two-photon resonant gas-phase REMPI studies appears, however, to have been largely neglected after some early interest [124-126]. As was first recognized, the signal (ionization yield) in (2+1) REMPI entails not just the two-photon absorption, but a further ionizing photon interaction that may modify the observed polarization dependence, and hence would generally require more advanced theoretical modelling. However, in the limit of 2^{nd} order laser power dependence, the ionization step may be assumed to be saturated, allowing the REMPI signal to be interpreted as primarily due to the two-photon absorption [125]. Such limiting conditions are nowadays more likely attained with the higher intensities generated by ultrafast lasers, as here, suggesting a renewed interest for two-photon polarization spectroscopy in the gas phase may emerge.

Figure 3.7 presents the measured ratios of the ion yields recorded when the light polarization is switched between left circular and linear (abbreviated as C/L). For each wavelength investigated, repeated C/L measurements were made using several laser powers in the range 9–15 mW. While at the longest wavelengths the C/L ratios may suggest a very slight power dependence elsewhere there is no discernible C/L power

dependence. The values that are plotted in figure 3.7 are laser power averaged, therefore considered to be fully representative of the circular-linear dichroism ratio, C/L, across the REMPI spectrum. From figure 3.7 it is evident that there are very significant C/L changes moving between both within the 3*s* region and when moving from the 3*s* to 3*p* excitation regions.

Much larger, though varying, C/L ratios are observed throughout the 3*s* region below 6.4 eV. In the centre of the 3*s* REMPI band, around 6.1 eV excitation energy, these are very similar to the predicted 3*s* circular-linear dichroism of 1.48–1.49 [116] but decrease somewhat towards the band extremities. In fact one may observe in figure

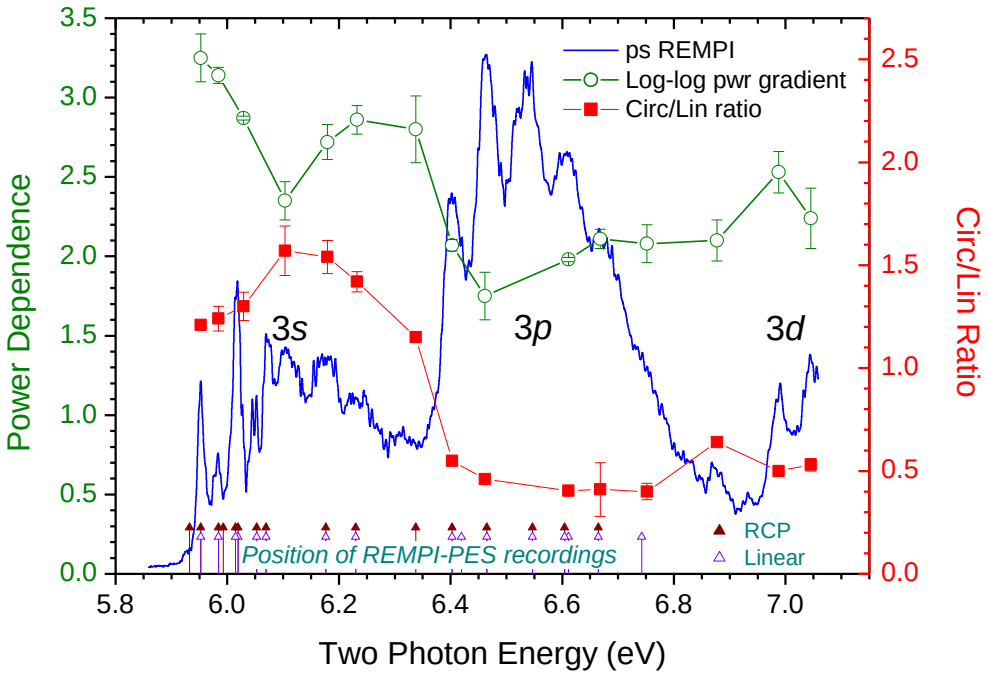

Figure 3.7. Polarization dependence and laser power measurements of parent ion (m/z 152) REMPI signal of fenchone, expressed as the slope of log_{10}-log_{10} plots. Measurements were made with linearly polarized, picosecond duration laser pulses around a mean power 4×10^{11} W cm^{-2}. Also included are C/L ratios of parent ion yield recorded with circular and linear polarized laser light, averaged over the 9–15 mW range. Solid lines joining data points are drawn simply to guide the eye, both for the power dependence data and the C/L ratio data. The ps REMPI spectrum is plotted on the same axis as an overall reference. Along the bottom of the figure are marked the excitation energies where REMPI-PES measurements (see Fig. 3.4) were made, open arrow heads indicating that linear polarization was used, closed arrow heads indicating the use of RCP light.

3.7 a seeming anti-correlation between the laser intensity dependence, which drops from 3.1 to a minimum of ~2.4 in the 3*s* band centre, and the C/L ratios, which rise from ~1.1 to a maximum of ~1.5 in the 3*s* band centre. At the 3*s* band extremities the

near 3rd order laser intensity dependence indicates that the total yields depend on one-photon ionization as much as the two-photon excitation — so a bigger deviation from the pure two-photon excitation dichroism prediction with no explicit incorporation of the ionization step, is to be expected [116]. In contrast, near the ~6.2 eV band centre, the reduction towards 2nd order in the laser intensity dependence may perhaps indicate "partial saturation" of the ionization step. A correspondingly reduced reliance on the one-photon ionization specifics would then explain the observed closer agreement between the experimental C/L and the predicted pure two-photon excitation C/L values 1.48-1.49. A similar inference follows from the femtosecond C/L measurements in the same central region of the 3*s* band (407.5 nm). Here the parent ion REMPI is unambiguously only two-photon limited and the measured C/L value of 1.38 ± 0.09 is close to the predicted two-photon circular-linear dichroism for 3*s* excitation. We already inferred a saturated ionization step in the 3*p* REMPI region from the 2nd order laser intensity dependence (figure 3.7). Hence, the experimental C/L dichroism ratios of ~0.4 shown in the 3*p* region in figure 3.7 are in excellent agreement with theoretical values of 0.4 and 0.38 for the $3p_y$, $3p_x$ states respectively [116].

The variation in laser intensity dependence between the two- and three-photon limiting cases that we observe for excitation wavelengths spanning the 3*s* band (figure 3.7) suggests a delicately balanced interplay between the complex dynamical factors that govern production of the Rydberg state, its evolution and relaxation, and its ionization. An explanation for observed 3*s* band centre dip towards 2nd order might, for example, be that the electron KE dependence of the $\sigma^{(1)}$ photoionization cross-section and the Franck-Condon factors conspire to produce a higher net ionization rate near the band centre. Clearly more theoretical and experimental work would be required to confirm this somewhat speculative interpretation.

The information that has been deduced about the electronic states and peak assignment of fenchone will be helpful in understanding and interpreting the PECD measurements. In the sections that follow we present (2+1) REMPI PECD measurements in the range 365-416 nm (5.9-6.76 eV) by tuning the wavelength, allowing investigation of both the 3*s* and 3*p* intermediate Rydberg states. These measurements will enable us to probe the effects of intermediate electronic and vibrational states on PECD as a function of photoelectron kinetic energy and provide a comparison with the femtosecond and nanosecond measurements done previously [110, 115].

3.8 PECD measured following ionization via 3*s* and 3*p*

Fenchone is an extensively studied molecule and acts as a benchmark molecule for PECD. So far measurements have been done using VUV single-photon ionization [11, 51] and multiphoton ionization using femtosecond laser pulse by various groups [73, 77, 80, 109]. And recently, even nanosecond laser pulses have been used to study REMPI-PECD [115]. These femtosecond and nanosecond measurements were aimed at studying the intermediate state ((2+1) REMPI via 3*s* and 3*p* state) effect on the PECD signal. A summary of all PECD measurements performed so far by all the groups is shown in Table 3.1. The femtosecond work shows an average value for PECD of -13 % for ionization in the 3*s* region. An interesting thing to note is that the femtosecond work of Kastner et al. [80] shows a trend of decrement in PECD value with a higher vibrational character of the intermediate excited state. Also, they report a PECD of -1% for ionization via $3p_1$. Whereas their recent work using a nanosecond laser pulse shows a higher PECD value of -17 % in the 3*s* region with any decrement for higher vibrational states. Also, in the 3*p* region they quote -15% PECD value which is significantly higher than what they observe with a femtosecond laser pulse. The authors also did not observe any pronounced features in the PECD values that correspond with resolved vibrational bands in the REMPI spectrum at the 3*s* origin between 416.57 nm and 412 nm.

Results	*S-Fenchone (PECD %)*	*Wavelength*	*Pulse length*
Kastner et al. [115]	3*s* (-17), 3*p* (-15)	375-420 nm	25 ns
Kastner et al.[80]	3*s* (-15 to 7), 3*p* (-1)	359-431 nm	25 fs
Miles et al.[13]	-13.9±0.4	394 nm	250 fs
Beaulieu et al.[109]	-13	398 nm	25 fs
Lux et al.[73]	-10.1(-13.8 FWHM)	398 nm	25 fs
Present work	3*s* (-35), 3*p* (-10)	350-420 nm	1.3 ps

Table 3.1. Previous PECD values for S- fenchone enantiomers for ionization via the 3s and 3p intermediate states using (2+1) REMPI.

In this section we will present the picosecond (2+1) REMPI PECD measurements in the 3*s* and 3*p* regions, aiming at observing any vibronic and electron kinetic energy effects. A detailed data acquisition procedure is presented in Chapter 2. Briefly, photoelectron images were recorded at various wavelengths in the 3*s* and 3*p* region using left and right circularly polarized light and the differential image of the left and right photoelectron image was analysed with pBasex (for more detail Chapter 2 Section 2.6.2). This generates the photoelectron spectrum and PECD value, alongside individual anisotropy parameters (see Chapter 1 Section 1.8 for multiphoton PECD formulation). These photoelectron spectra are plotted as a function of ionization energy

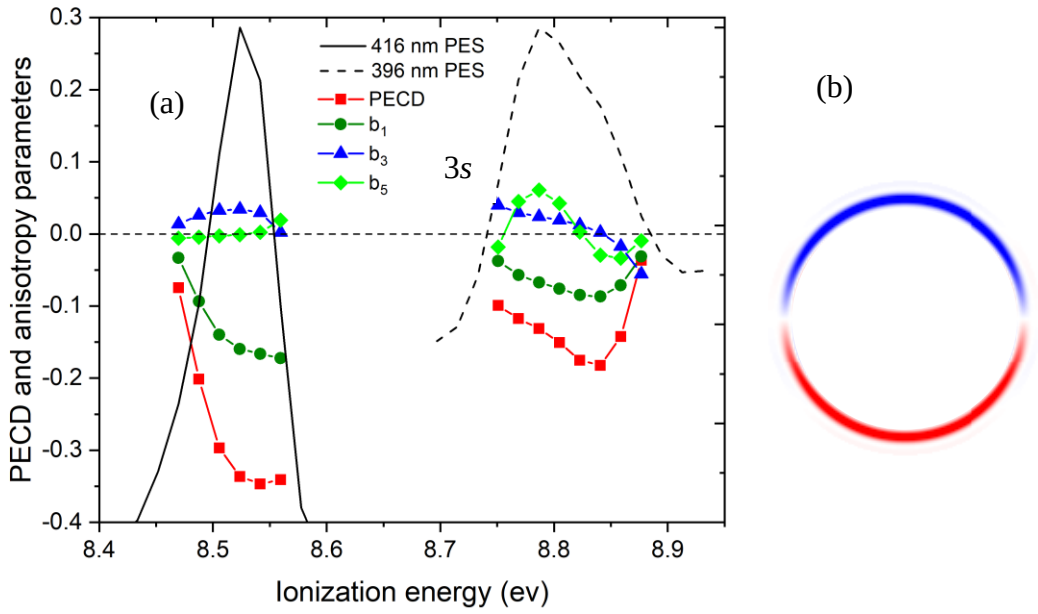

Figure 3.8. (a) VMI PES (black solid/dash line), PECD (red line), and anisotropy parameters b_1 (olive), b_3 (blue), b_5 (green) measurements for S-(+)-fenchone. The VMI-PES has arbitrarily scaled intensity but is plotted on the same ionization energy axis as the PECD measurements. The PECD measurements are for ionization via the 3s Rydberg state, extracted from a pair of images recorded with left- and right- circularly polarised laser pulse at wavelength 416.6 nm (black solid curve), 396 nm (black dash curves). (b) Abel inverted differential image of left and right CPL at 416.6 nm.

which is calculated by assuming an overall three-photon process and subtracting the measured electron kinetic energies from the three-photon energy. Figure 3.8 shows the photoelectron spectra and PECD measurements following (2+1) REMPI at 416.6 nm and at 398.8 nm, both of which allow access only to the 3*s* Rydberg state (see REMPI spectrum in figure 3.2). As discussed in previous sections the wavelength 416.6 nm derives the 0-0 transition from the ground state to 3*s* intermediate state, followed by

$\Delta v = 0$ transition from intermediate to cation state. Thus, the photoelectron peak at 8.5 eV in figure 3.8 corresponds to $\Delta v = 0$ ionization from the 3*s* origin and the peak at 8.75 eV corresponds to $\Delta v = 0$ ionization from a vibrationally excited level in the 3*s*. The PECD signal associated with the 0-0 transition (origin) peak shows a significant value, of about 30-35%, and at highly vibrationally excited 3*s* peak (8.75 eV) a much smaller PECD signal of ~10% was observed. In comparison to Kastner et al.'s [80] femtosecond (2+1) REMPI PECD work in the 3*s* region (Table 3.1), our picosecond PECD results show a higher PECD value (almost double in magnitude). This difference in signal could be a consequence of laser bandwidth. Femtosecond pulses have much broader pulse width when compared to picosecond pulses. As a result they create a broader excited wave packet resulting in a loss of resolution and observables are averaged out over the broader excited envelope. Despite the different PECD value both femtosecond and picosecond result showed same trend in PECD value with higher vibrational character. Something similar albeit for a VUV single-photon study was observed in a study done by Nahon et al. [127]. In this experiment, photon energies of 9.4, 15.5, 18.6 eV were used to measure PECD signal for transition from the neutral ground state to vibrationally excited cation states. They presented a decrease in PECD signal with increased vibrational energy (and concomitant increase in electron kinetic energy).

For a three-photon process, $l_{max} = 6$ was used to analyze the photoelectron images and b_1, b_3, b_5 parameters were obtained. In figure 3.8 shows the contributions from each of the three anisotropy parameters (b_1, b_3 and b_5). For both the 3*s* origin (8.5 eV) and the highly vibrationally excited (8.76 eV) peaks, the maximum contribution to the observed PECD is from b_1 with the higher order anisotropy parameter b_3 and b_5 fluctuating around zero. The differential image is shown in figure 3.8 (b) has twofold symmetry consistent with this observation.

The 0-0 transition for the 3*p* intermediate state is obtained at around 384 nm, 6.4 eV (figure 3.2). Figure 3.9 shows a measurement taken just above the 3*p* origin threshold. A wider range photoelectron spectrum, with associated PECD, measured at 378.8 nm ($2\phi = 6.54$, 0.14 eV above the 3*p* threshold) can be seen. As discussed previously in 3*p* region, at this wavelength ionization can occur through low vibrational levels in 3*p*

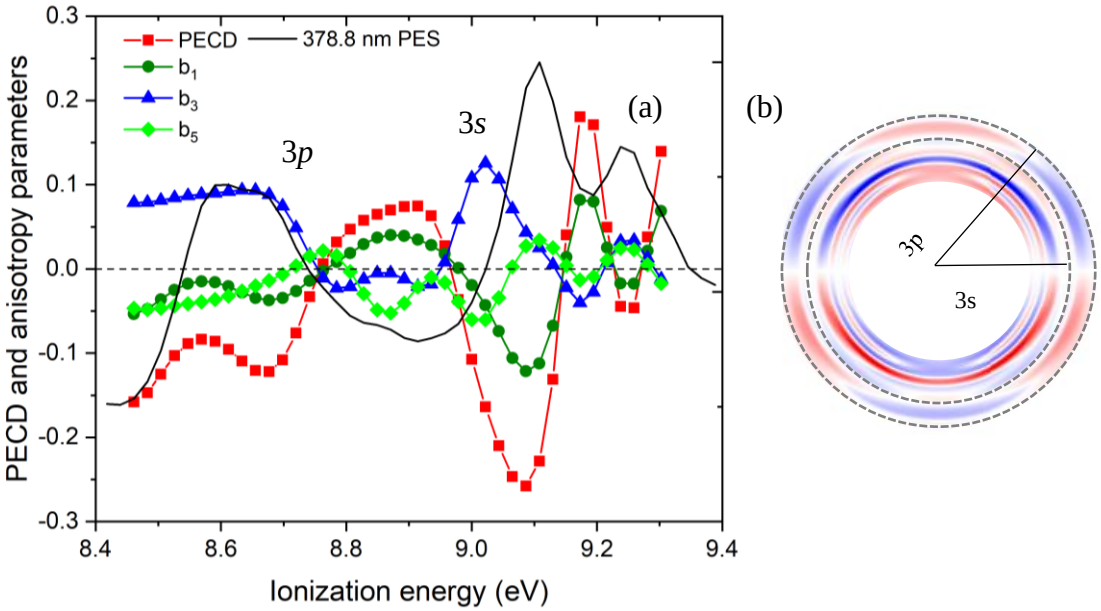

Figure 3.9. (a) VMI PES (black solid line), PECD (red line), and anisotropy parameters b_1 (green), b_3 (blue), b_5 (light blue) measurements for S-(+)-fenchone. The VMI-PES has arbitrarily scaled intensity but is plotted on the same ionization energy axis as the PECD measurements. The PECD measurements are for ionization via the 3s and 3p Rydberg states, extracted from a pair of images recorded with left- and right- circularly polarised laser pulse at wavelength 378.8 nm (black solid curve). (b) Abel inverted differential image of left and right CPL at 378.8 nm.

as well as through high vibrational levels in 3*s*. The 3*s* peaks may result from internal conversion from 3*p* to 3*s* states as FC calculations show that the probability of ionization via 3*s* is reduced after 8.9 eV ionization energy [116]. The first prominent peak in the spectrum, at IE = 8.63 eV sits ~0.14 eV above the adiabatic ionization threshold. Hence all excess internal energy above the 3*p* Rydberg threshold appears as internal energy of the cation. This confirms this peak as a 3*p* $\Delta v = 0$ ionization. However, it is also immediately obvious from the broader width, tailing to higher IE, that the $\Delta v = 0$ propensity is much weakened. The second prominent peak at 9.1 eV (3*s* series) is more intense than the 3*p* peak at 8.63 eV, which is contrary to the relative 3*s*, 3*p* cross-sections at this two-photon excitation energy. It is also much broadened (with a neighbour peak at 9.25 eV), revealing a substantial weakening of the $\Delta v = 0$ propensity which was so rigorously followed in the pure 3*s* excitation region. This weakened propensity supports the contention of very different internal dynamics following excitation above the 3*p* threshold.

The 3*p* peaks show the PECD of ~10 %, which is smaller in magnitude than the 3*s* region. However, the peaks that we believe result from internal conversion from 3*p* to

3*s* show a considerably larger PECD signal (25%) than the one we observe from direct ionization of high vibrational levels in 3*s* (< 10%). For both peaks, 3*p* and 3*s*, the b_3 anisotropy parameter, as well as the b_1 anisotropy parameter, has significant magnitude. For ionization via 3*p* the contribution from b_3 is higher than b_1 parameter (b_1 = -0.01, and b_3 = 0.10), and even b_5 is non-zero. However, for the peak that appears at 9.1 eV following ionization of 3*s*, the b_1 and b_3 parameters have similar magnitude (0.10) and non-zero b_5 ($\pm$ 0.02). In the Abel inverted differential image shown in figure 3.9 (b) the rings associated 3*p* and 3*s* have clear three-fold symmetry, consistent with a significant contribution from b_3. In the next section we present and discuss the full PECD data along the two ridges, 3*s* and 3*p* (Section 3.3.2, figure 3.4).

3.9 Complete PECD data set along the 3*s* and 3*p* ridges: Vibrational and electron kinetic energy effect

In the previous section we discussed the PECD measurements at two particular wavelengths in two different ionization regions (3*s* and 3*p*). In Section 3.3.1, figure 3.4 showed two different ridges corresponding to the ionization via 3*s* and 3*p* intermediate electronic states. In this section we will present complete PECD data along these two ridges and discuss any vibrational effects and electron kinetic energy effect. The photoelectron images were recorded using left-and-right circularly polarized light at every 3-5 nm step along the full REMPI spectrum. These images were analyzed using pBasex to get PES, PECD, and anisotropy parameters at each wavelength point. To fully understand the vibronic and electronic kinetic energy effects on PECD measurements, complete PECD data is presented and discussed along these two ridges covering 3*s* and 3*p* intermediate electronic state. First we need to understand how the photoelectron spectra are behaving along the two ridges and determine if we can resolve any intensity modulation of the peaks related to vibrational features. Secondly, we need to identify if there any changes in PECD along the two ridges which can be attributed to these vibrational features in the PES. Therefore, the intensity variation of $\Delta v = 0$ photoelectron peak along the two ridges (3*s* and 3*p*) is plotted alongside the PECD variation along these ridges on ionization energy scale.

Figure 3.10 shows the intensity variation of photoelectron spectra for ionization via the 3*s* and 3*p* regions. These intensity variation spectra were obtained by separately summing all the PES for 3*s* and 3*p* ridges shown in figure 3.4 (for range 350-420 nm) and plotting this as a function of ionization energy. Finally, a smoothing function (Matlab sgolayfilt) was used to get the final intensity variation of the PESs for both states. The PES intensity variations of these Rydberg states are compared with a FC calculation via the 3*s* state. The peaks match reasonably well; however, the FC calculation dies around 9 eV, whereas the PES continues to show the vibrational modulation. As discussed in the previous sections, this could a consequence of internal conversion from 3*p* to 3*s* state due to the short lifetime of 3*p* state.

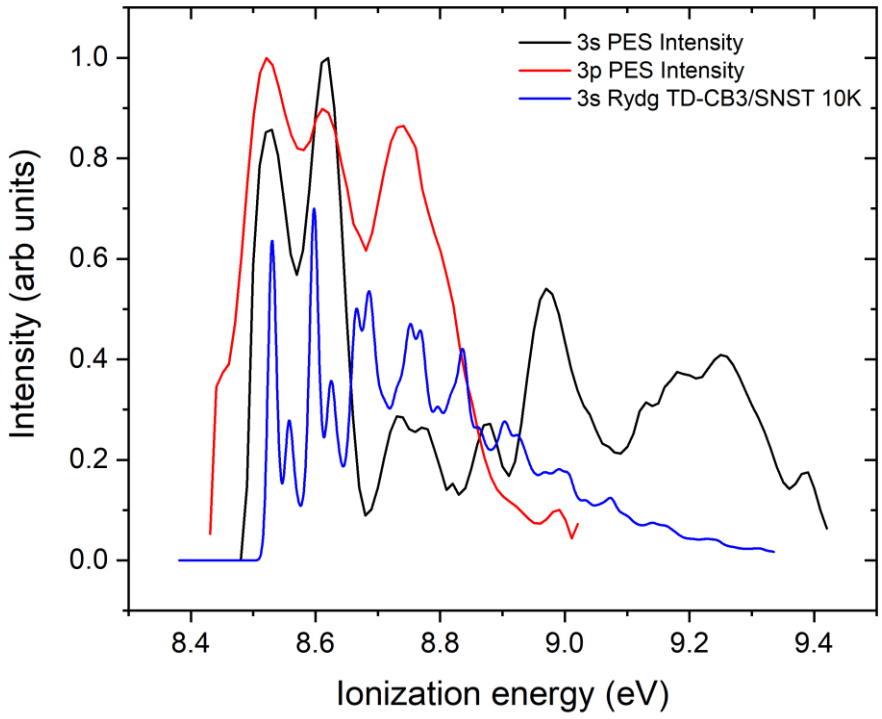

Figure 3.10. Intensity modulation of PESs along the two ridges for ionization via the 3s (black curve) and 3p (red curve) Rydberg state of fenchone. PESs are shown in comparison with the 3s Rydberg state calculation (blue curve).

The photoelectron intensity profile of both the ridges show clear vibrational features matching the FC calculations. Figure 3.11 shows the PECD variation along these two ridges. The PECD values along the two ridges are plotted as a function of ionization energy alongside the photoelectron spectrum. The PECD measurements via both states

show modulation with the principal vibrational features and in both case the preferred emission direction of photoelectrons is the same (i.e. no sign inversion of PECD was observed for ionization via 3*s* and 3*p*). However, the maximum absolute magnitude of the PECD via the 3*p* state is (-10%) considerably smaller than that via the 3*s* state (-35%).

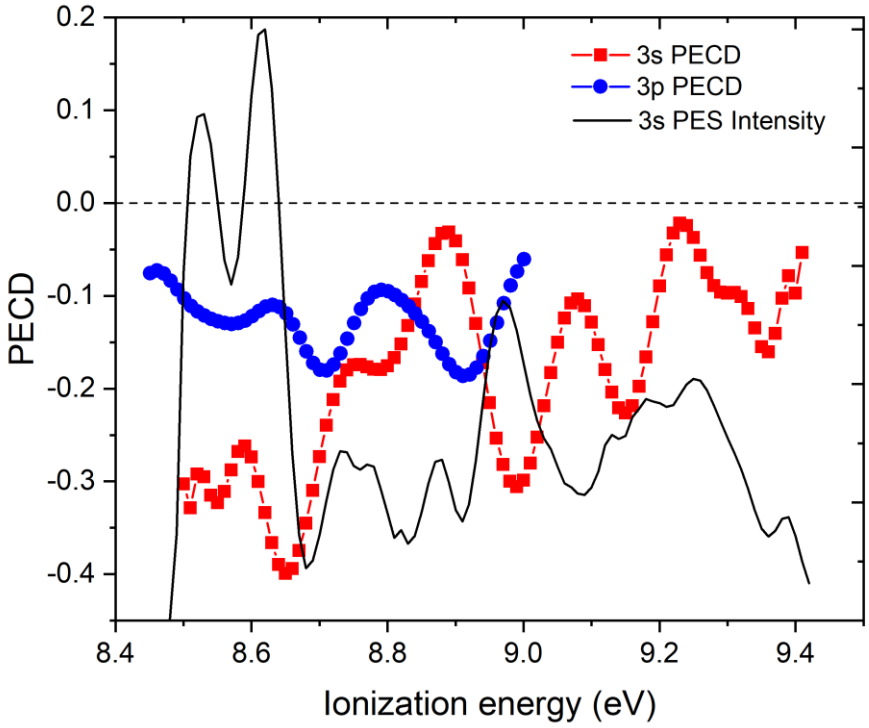

Figure 3.11. Full PECD data along the 3s and 3p ridges: PECD for ionization via 3s (red curve) and 3p (blue curve) is shown along PES intensity along the 3s ridge (black curve) for S-(+) fenchone.

A few striking features were observed for the PECD measured following ionization through 3*s* region; first, as mentioned above, it shows a clear modulation with the principal vibrational peaks. Second, its absolute magnitude changes from 35% to almost zero for the peaks in the 8.5-8.9 eV range which correspond to the ionization via highly excited vibrational levels (higher kinetic energy electrons). Third, a significant change in PECD with different excited vibrational peaks was observed, the 3*s* origin peak shows a PECD value of -35%, whereas the vibrational peak at 8.65 eV shows a higher PECD value of -40% showing a clear vibrational influence. Toward the end in the 3*s* region, for higher vibrational states, the PECD value goes down to almost zero, towards the end of FC window. However, for the peaks beyond the FC

allowed window (9.0-9.4 eV), show a huge PECD value. These peaks are believed to be a result of internal conversion from 3*p* to 3*s* states. The peak at 9.0 eV shows the value -30% (see figure 3.11, 3*s* PECD curve). The following peak at 9.2 eV shows the PECD value of -20%. These observations clearly show a strong indication that the intermediate electronic and vibrational state has an influence on PECD. To get detailed insight, more computational work is required. The PECD value for ionization via the 3*p* state shows a significant smaller value (-10 %) which modulates with the principal vibrational peak. We don't see any decrement in the PECD value for higher vibrational state as observed for ionization via 3*s* state.

To study any trend or effect of electron kinetic energy (eKE), we have to plot the measured PECD value as a function of electron kinetic energy. In figure 3.12 we have plotted the mean PECD value together with the individual anisotropy parameters, as a function of electron kinetic energy for the two ridges (ionization via 3*s* and 3*p* state). The full width half maximum (FWHM) was used to calculate the mean value of the PECD for a given photoelectron peak. The FWHM was calculated by fitting a Gaussian to the PES in both the regions. The width of each Gaussian was used as an averaging window for the anisotropy parameter and PECD. For the 3*s* FC allowed transition PECD is mainly comprised of b_1 parameter and b_3 and b_5 are almost zero except around 0.5 eV electron kinetic energy. However, for the peaks outside the FC window along the 3*s* ridge (internal conversion from 3*p* to 3*s*), the b_3 parameter is also significant. For 3*p* region, PECD has significant contribution form b_1 and b_3, and b_5 is also non-zero. These higher order anisotropy parameters show the effect of anisotropy created in the excited state on PECD.

The change in PECD value in the 3*s* region from 0.5 - 0.6 eV is very significant, and previous eKE studies have shown that PECD does not change significantly over a small change in electron kinetic energy [128]. So it is therefore plausible these effects are vibrational in nature. Similarly, at the sudden change at 0.65 eV eKE, could be an effect of that particular vibrational state. In the 3*p* region, we did not observe any effect which would relate to electron kinetic energy dependency. Though the different

behaviour of the PECD value in the two regions (3*s* and 3*p*), does point to an initial state effect on observed PECD.

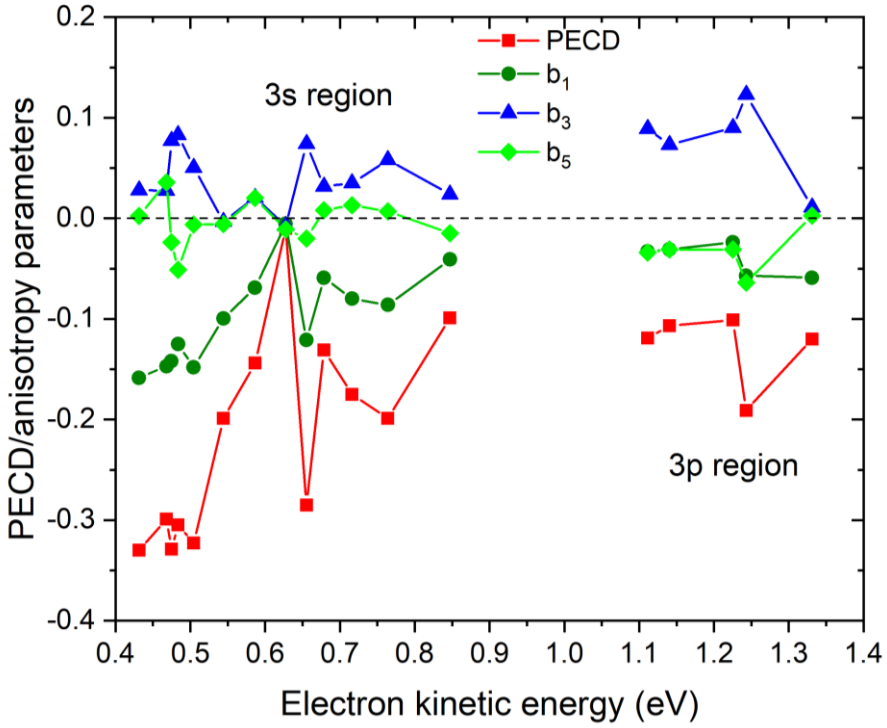

Figure 3.12. Mean PECD value (red) and anisotropy parameters b_1 (green), b_3 (blue), b_5 (light blue) is shown for ionization via the 3s and 3p states of fenchone is plotted against the electron kinetic energy.

3.10 Conclusion

In this chapter we investigated the 3*sp*(*d*) Rydberg state of fenchone. REMPI spectrum was recorded in the range 350-420 nm covering the three Rydberg states. Photoelectron images were recorded via selected electron and vibrational intermediate state. The extracted photoelectron spectra allowed for the assignment of different thresholds for the 3*s* and 3*p* Rydberg state. The parent ion yield was measured as a function of laser power and the polarization of light shedding more light on the lifetime and relaxation dynamics of intermediate states.

Photoelectron images were recorded using left and right circularly polarized light to measure the photoelectron circular dichroism in multiphoton ionization processes. The observed PECD was found to be sensitive to the intermediate vibrational state. Upon comparison between 3*s* and 3*p* PECD, some initial state effect was observed. We did not find any dependency of PECD on electron kinetic energy for ionization via both 3*s* and 3*p* Rydberg states.

Chapter 4 Photoelectron spectroscopy of Monoterpenes via 3*spd* Rydberg state

4.1 Introduction

Monoterpenes are a class of terpenes that consist of isoprene units and have molecular formula $C_{10}H_{16}$. These isoprene units can be attached linearly, leading to the formation of acyclic monoterpenes. Conversely, ocimene and myrcenes can make connections to form rings. The most common monoterpenes contain a six-membered ring, such as limonene. The monoterpene units can undergo reactions to form bicyclic monoterpenes, such as pinene, carene, sabinene, camphene etcetera. Many isomers of monoterpenes are chiral, and in recent decades there has been growing interest in studying them spectroscopically. For this work we will be focusing on molecules α-pinene and 3-carene. α-pinene is a naturally occurring colourless organic oil with a fresh, earthy scent of a pine forest. It is usually found in parsley, dill etc. Like its sibling, β-pinene, α-pinene is most famous for its anti-inflammatory benefits [129]. 3-carene is a colourless liquid with a sweet, turpentine-like odour. It is commonly used in air care products and in the perfume industry products such as air purifiers, air conditioners etc. Monoterpenes such as α-pinene, 3-carene, shown in figure 4.1, are the chiral isomers from the family of terpenes and they have relatively high vapour pressure making they suitable for gas-phase chiroptical techniques. However, spectroscopically, a limited amount of work has been done on these molecules. Kovac and co-workers have tried to analyse the electronic states structure of terpenes by

(a) 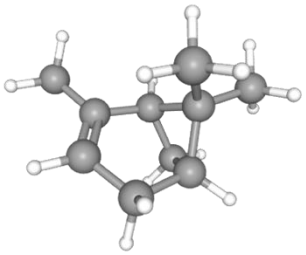 (b) 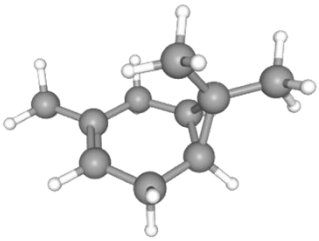

Figure 4.1. (a) α-pinene and (b) 3-carene [157].

comparing the measured photoelectron spectra with related compounds (such as 2-cedrene) [130]. D Kubala and co-workers presented the adiabatic ionization energy and UV absorption study for α-pinene [131].

Chiral molecules have long been studied spectroscopically using chiroptical techniques such as circular dichroism (CD), vibrational circular dichroism (VCD) etc. and in the past two decades, PECD has been used extensively, with the majority of work adopting a one-photon ionization scheme [11, 54, 55, 108]. In recent years, interest has been taken in developing multiphoton ionization schemes via intermediate electronic states. Early work using multiphoton ionization scheme was carried out by the Janssen, Boesl, and Baumert groups [70, 73, 74, 75], using a nanosecond and a broadband femtosecond laser. The Bosel work mainly focused on CD in multiphoton ionization, whereas Janssen and Baumert focused on intermediate state dependency of photoelectron circular dichroism. The groups of Baumert and Janssen have studied the spectroscopy of excited electronic states in bicyclic ketones such as fenchone, [77, 80, 109] and camphor [74, 132], identifying two resonances belonging to B- and C- bands, which involves excitation to states of 3*s* and 3*p* Rydberg character. Extensive theoretical studies of the cation have also been conducted by the same investigators to identify the vibrational character.

However, despite this rather intensive uptake on single-photon and resonance enhanced multiphoton studies of chiral molecules. Only a few chiral molecules have been studied extensively such as fenchone, camphor, limonene (though most of them still lack detailed background on excited state spectroscopy) and molecules such as α-pinene and 3-carene are yet to be explored in the multiphoton regime. There remains relatively little background detail concerning the excited state spectroscopy of these molecules. Older measurements of the He I photoelectron spectroscopy and UV absorption of α-pinene [130, 131] mapped out the valence band ionization profile at low resolution. For 3-carene there is only a low-resolution UV absorption [133] that has been published so far. There is no published REMPI spectra for these two molecules and very little information about different intermediate states. The most recent work on α-pinene and 3-carene is presented by Ganjitabar et al. using synchrotron radiation, exploring the vibrational states in cation and there effect on PECD [128].

In this chapter, we present a detailed study of the electronic structure of α-pinene and 3-carene conducted using a picosecond UV laser source and photoelectron imaging. The ionization energies and approximate lifetimes of three different 3*l* (*spd*) Rydberg states are determined. We report a new, wide range (5.5-7.1 eV) picosecond (ps) laser

(2+1) REMPI spectrum of the $n = 3$ Rydberg region complemented with the absorption spectrum, recorded using VUV Fourier transform (FT) spectrometry. This spans from the onset of the Rydberg excitations in α-pinene and 3-carene to above the ionization energy. Laser intensity dependence measurements using ps laser pulses were recorded to help establish the relative importance of the two-photon absorption, ionization, and relaxation processes in the REMPI spectrum. Polarization dependent measurements of the parent ion yields are then able to be used to estimate the circular-linear dichroism in the two-photon absorption. Finally, vibrationally resolved photoelectron spectra, generated with ps excitation, are recorded across the 3*sp* Rydberg region. These not only provide new insight into the cation vibrational distribution following the ionization step but also suggests very different roles for vibrational dynamics in the intermediate Rydberg states. This knowledge will help further our goal to disentangle the competing influences on PECD (Chapter 5).

The chapter is structured based on experimental techniques (such as REMPI, VMI, ion yield study), where we will discuss the results of a-pinene and 3-carene. First, we present some structural information on these molecules in Section 4.2, followed by the time-of-flight measurements and REMPI measurements. Then we present one colour photoelectron spectra which were needed to locate the excited electronic states and determine the ionization potential. Parent ion yields are presented as a function of laser power and polarization to provide further insight into the electronic structure, including the symmetry of initial and excited states. In these experiments, a (2+1) REMPI scheme was used to ionize the molecules through the 3*s* and 3*p* Rydberg states accessible through excitation in the region 350-450 nm (5.5-7.1 eV).

4.2 **Structural information**

4.2.1 Conformers

Chiral molecules in nature are often found in more than one conformation; structures that differ only by rotation around a single bond. These conformational isomers rapidly interconvert at room temperature, and individual conformers cannot be isolated. Neeman et al. recently has shown using Fourier transform microwave spectroscopy that α-pinene occurs in a single conformer in which the six-membered ring is quasi-planar structure [134]. The bicyclic ring structure of 3-carene also suggests a rigid structural form, but for a long time the precise conformation was uncertain. Another

high-level calculations (CCSD/ aug-cc-pVDZ, B3LYP/aug-cc-pVTZ) reported 3-carene to exist in a single stable conformer with a near planar six-membered ring [135]; see figure 4.1.

4.2.2 Intermediate electronic state

The highest occupied molecular orbitals for α-pinene and 3-carene are π orbitals localized at the C = C position. Most of the low-lying singlet transitions from the ground state upon absorbing a photon involves a π* ← π transition. The next probable electronic transitions to occur are 3*l* ← π Rydberg states, which are usually labelled as B and C bands. Band B results from 3*s* ← π transitions, and band C from 3*p* ← π transitions. Figure 4.2 shows the 3*s* and three 3*p* Rydberg states of α-pinene. Potential energy surfaces for these Rydberg states and cation state are usually parallel. Electrons in these states see the ion core as a point charge, and the states can be well represented

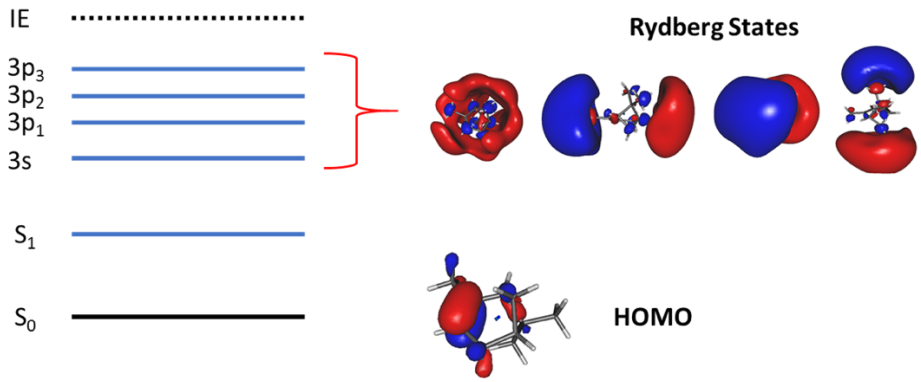

Figure 4.2. HOMO and excited states of α-pinene [137].

by the hydrogen Rydberg equation. The energy of Rydberg states can be refined by including a correction called the quantum defect in the Rydberg formula as,

$$E_B = -\frac{Rh}{(n-\delta)^2} \tag{4.1}$$

where E_B is the binding energy, R is the Rydberg constant, h is the Planck constant, n is the quantum number, and δ is the quantum defect. The typical values of δ for second row atoms and molecules for *ns*, *np*, and *nd* are ~1, ~0.6, ~0, respectively.

4.3 Experimental section

In this experiment long-range (350-450 nm, 5.5-7.1 eV) vibrationally resolved picosecond (2+1) REMPI and PES measurements were recorded using velocity map imaging. These measurements were carried out for both α-pinene and 3-carene using

the experimental setup described in detail in Chapter 2. UV laser pulses in the range 450 - 405 nm and 405- 350 nm were produced using two TOPAS systems, which were pumped with the 800 nm laser output of a dual Ti-Sapphire laser system (described in Chapter 2 Section 2.2.1). The UV laser pulse energy was 15-20 µJ with a pulse duration of 1.3 ps.

Pure enantiomeric samples of (+)-1R,5R-α-pinene and (+)-1S,6R-3-carene were obtained from Sigma-Aldrich and used without further purification. α-pinene was specified to have >97% enantiomeric excess. The enantiomeric excess of 3-carene was not specified, but two-column gas chromatography (GC^2) measurements performed by Ganjitabar et al. for the same sample confirmed an enantiomeric excess of > 99% [128].

Samples were delivered into the spectrometer via a pulsed kHz valve (Amsterdam cantilever piezo valve ACPV2), creating a supersonic jet expansion (see Chapter 2 Section 2.2.3). The UV beam was focused into the spectrometer using a 30 cm focal length lens mounted on a 3-axis stage and crossed with the molecular beam. Rotational temperatures in the range 20 - 30 K (using PGOPHER) were achieved with an absolute 1.5 bar backing pressure of helium gas. In order to record a REMPI spectrum a wavelength scan was performed over the range 350 - 450 nm with a step size of 0.05 nm and 2 s delay time. To extract photoelectron spectra, photoelectron images were recorded using linearly polarized light. Ten thousand frames were recorded at a particular wavelength with a 100 ms exposure per frame.

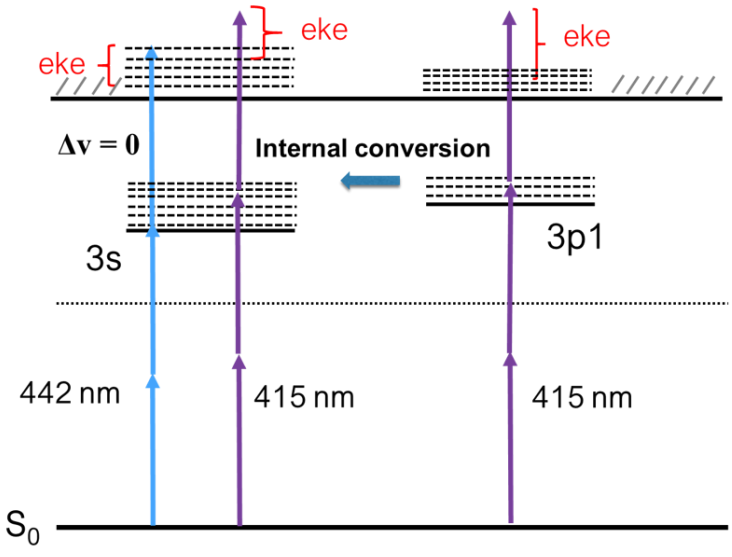

Figure 4.3. Illustration of a (2+1) Ionization scheme; showing two scenarios (a) ionization via 3s (b) ionization via 3p or vibrationally excited 3s state.

4.4 **Results and discussion**

In this section (2+1) REMPI spectra in the range 5.5 - 7.1 eV (350 - 450 nm) are presented. Figure 4.3 shows the photoionization scheme used in these experiments. PES measurements were recorded for ionization via different vibrational levels of the 3*s* and 3*p* Rydberg intermediate states for both α-pinene and 3-carene. In Section 4.5 and 4.6, the time-of-flight and REMPI measurements are presented and the relevant intermediate states highlighted. This is followed by the photoelectron spectra and anisotropy parameters in Section 4.7 and 4.8. In Section 4.9 the laser power and Section 4.10 laser polarization dependent parent ion yield measurements are presented. Each section presents and discusses results for both molecules (α-pinene and 3-carene).

4.5 **Time of flight measurements**

Time-of-flight (ToF) mass spectra, shown in figure 4.4, were recorded for both molecules at the Nijmegen Radboud University using an Electron-Ion coincidence VMI spectrometer (see Chapter 2 for further details). The molecules were excited and ionized using the 400 nm output from a femtosecond laser, with a pulse width of 150 fs and pulse energy of 130 μJ. The dominant peak in the mass spectrum in both cases is the parent (136 amu) with major fragments occurring at masses 121, 93 and 94 amu. α-pinene showed more fragmentation than 3-carene for the same wavelength and laser power; a possible explanation of this observation is discussed in Section 4.9.

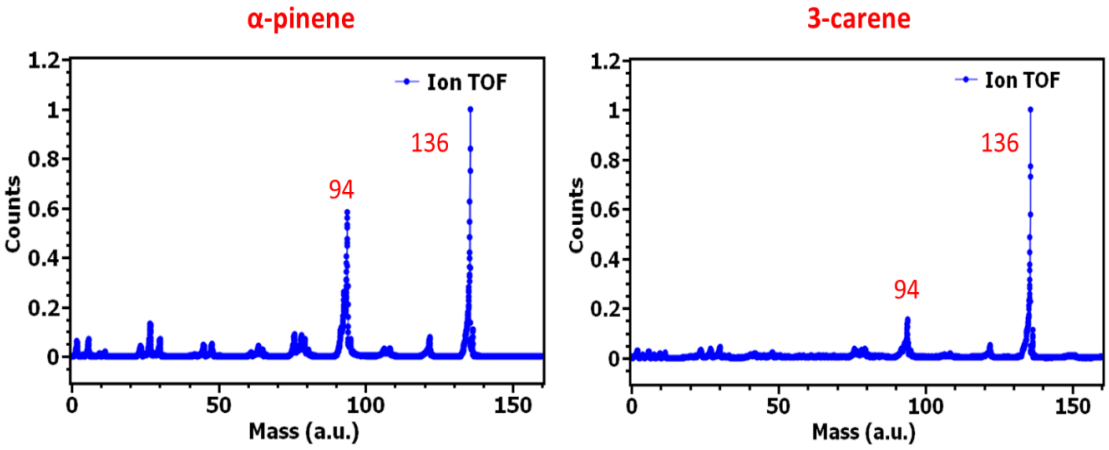

Figure 4.4. Time-of-flight mass spectra for α-pinene and 3-carene.

Using the coincidence detection technique, the time-of-flight photoelectron spectrum (PES) associated with the formation of the 94 amu fragment was compared with the PES associated with formation of the parent ion (mass 136). In the case of both α-

pinene and 3-carene the PES associated with masses 94 and 136 were identical, confirming that fragmentation occurs after photoionization. It is possible that the cation state is unstable and it dissociates after an electron is removed; alternatively, the cation may absorb additional photons prior to dissociation. For ps measurements, fragment 94 was also observed for both molecules and α-pinene showed slightly higher fragmentation than 3-carene. In next section we will discuss the REMPI spectrum measured for these two molecules.

4.6 (2+1) REMPI

UV absorption measurements on α-pinene and 3-carene in the gas phase have been carried out by various groups [106, 130, 131, 133]. These studies allow an estimate of the energies of Rydberg states in the 5.5-7.1 eV range. The absorption spectrum of α-pinene shown in figure 4.5 features a significant band at around 6 eV. The absorption bands (B and C) between 5 and 7 eV arise from the population of 3*l* Rydberg states. Figure 4.3 shows the one-colour (2+1) ionization scheme used. Three-photon ionization at 442 nm provides total energy of 8.4 eV, above the ionization potential of α-pinene at 8.21 eV [130], and this scheme is resonant at the two-photon level with the 3*s* Rydberg state, populating low vibrational states. Use of light at 415 nm allows population of the high vibrational states in the 3*s* Rydberg or alternatively can populate low vibrational levels in the 3*p* Rydberg state. A similar ionization scheme was used for 3-carene, which has a threshold ionization potential of 8.4 eV [136]. REMPI spectra of these monoterpenes have not been recorded before and our own efforts to record REMPI spectra of these molecules using nanosecond laser pulses were not successful. REMPI spectra can however be obtained when picosecond laser pulses are used. A possible explanation for this would arise if the intermediate states that are accessed exhibit short lifetimes; this is discussed further in section 4.9. In this section, a broad wavelength range (2+1) REMPI spectrum is presented for α-pinene in the next section and for 3-carene in Section 4.6.2.

4.6.1 α-pinene

In Figure 4.5 we present a (2+1) REMPI spectrum of α-pinene, recorded by monitoring parent ion mass, m/z 136, while scanning with linearly polarized, picosecond laser pulses. The spectrum was recorded over the range 350 - 450 nm (5.5-7.1 eV, two-photon energy) and has been normalized by the pulse energy, which ranged around 12

$\pm$ 2 μJ across the spectrum. The spectral resolution of the 1.3 ps pulses was estimated to be around 50 cm^{-1} (further details Chapter 2). Figure 4.5 also presents a comparison between the REMPI, VUV absorption [130] and Fourier transform (FT) spectra. Although the three spectra have the same overall intensity profile, in the REMPI spectrum better-resolved features are observed owing to the relatively narrow laser bandwidth and the cold molecular beam source. The FT spectra was recorded with a VUV Fourier transform spectrometer at a dedicated branch on the DESIRS beamline at Synchrotron SOLEIL (further detail Chapter 2 Section 2.3). There is clearly a very close resemblance between the absorption/FT spectra and the two-photon REMPI, and the latter shows vibrational bands in the energy region corresponding to three different 3*l* Rydberg states. In particular, transitions to three Rydberg states, 3*s*, 3*p* and 3*d*, can be discerned, together with a fine structure corresponding to vibrational bands. Three different regions identified in the REMPI spectrum correspond to the B-, C- and D-band transitions, which are believed to correspond to 3*s* ← π, 3*p* ← π, and 3*d* ← π excitation, respectively [130, 131].

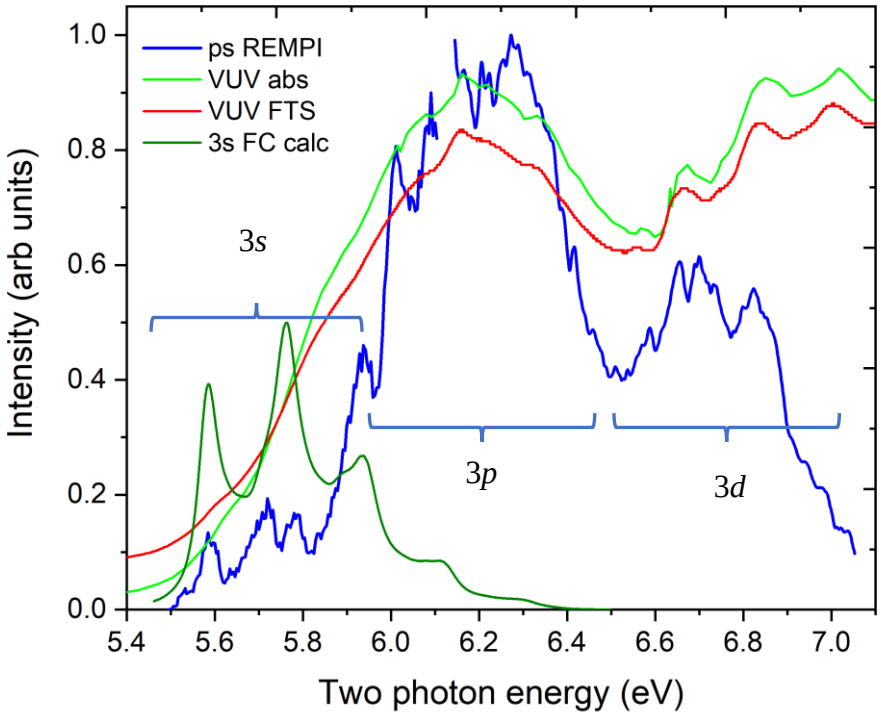

Figure 4.5. Comparison of REMPI spectrum (blue), VUV absorption (green) spectrum, and VUV FT spectrum (red) for α-pinene. The REMPI spectrum shows three different regions corresponding to three different electronic states. The 3s region in the spectra are compared with a 3s Franck-Condon calculation (olive) corresponding to the 3s ← π band [128].

The 3*s* ← π (B-band transitions) are observed in the region 5.5-6.1 eV with the 0-0 transition at 5.6 eV, followed by the peaks corresponding to vibrational levels of the 3s Rydberg state. The overall rise in intensity is consistent with the absorption spectrum. The vibrational structure in this region can be understood through comparison with a Franck-Condon calculation for excitation of the 3*s* Rydberg state (see figure 4.5) [128]. The major vibrational bands *v*" = 0, 1, 2, 3 of FC the calculations, which arise from a progression in the C = C stretching mode show good agreement with the peaks in the REMPI spectra. The first peak (*v*" = 0) is the transitions from the vibrationless neutral ground state to zero/one/two quanta excitation of the lowest energetic normal mode ν_1 (ring breathing). The second, third, fourth peaks (*v*" = 1, 2, 3) are just the same as the first peak but in combination to one, two, three quanta excitation in ν_{56} (C = C stretching mode), respectively [137].

The 3*p* ← π (C-band transitions) are observed in the region 6-6.5 eV with the 0-0 transition at 6.05 eV, followed by the peaks corresponding to vibrational levels of the 3*p* Rydberg state. There is a small gap at 6.1 eV in the REMPI spectrum, which due to the lack of wavelength produced in the region. The 3*d* ← π (D-band transitions) are observed in the region 6.6-7.1 eV with the 0-0 transition at 6.6 eV, followed by the peaks corresponding to vibrational levels of the 3*d* Rydberg state. The intensity of the REMPI spectrum is not the same through the different regions; the 3*p* region is the most intense and 3*s* region the least. The 3*p* region consists of three members (*x*, *y*, *z* states), more theoretical work is required to understand the cross-section for all three states and comment which is more prominent via two-photon absorption. Thus, we will assume that the B-band has unresolved excitation from all three 3*p* states.

4.6.2 3-carene

For 3-carene, a very limited amount of work has been done in regard to excited state spectroscopy. Qiu et al. have recorded the low-resolution VUV absorption spectrum [133], which was used to provide an estimate for the wavelength needed to excite the 3*l* Rydberg state transitions. In Figure 4.6 we present a (2+1) REMPI spectrum of 3-carene, recorded by monitoring parent ion mass, m/z 136, while scanning with linearly polarized, picosecond laser pulses. The spectrum was recorded over the range 350 - 445 nm (5.85 – 7.10 eV, two-photon energy) and has been normalized by the pulse energy, which ranged around 12 ± 2 μJ across the spectrum. The REMPI spectrum

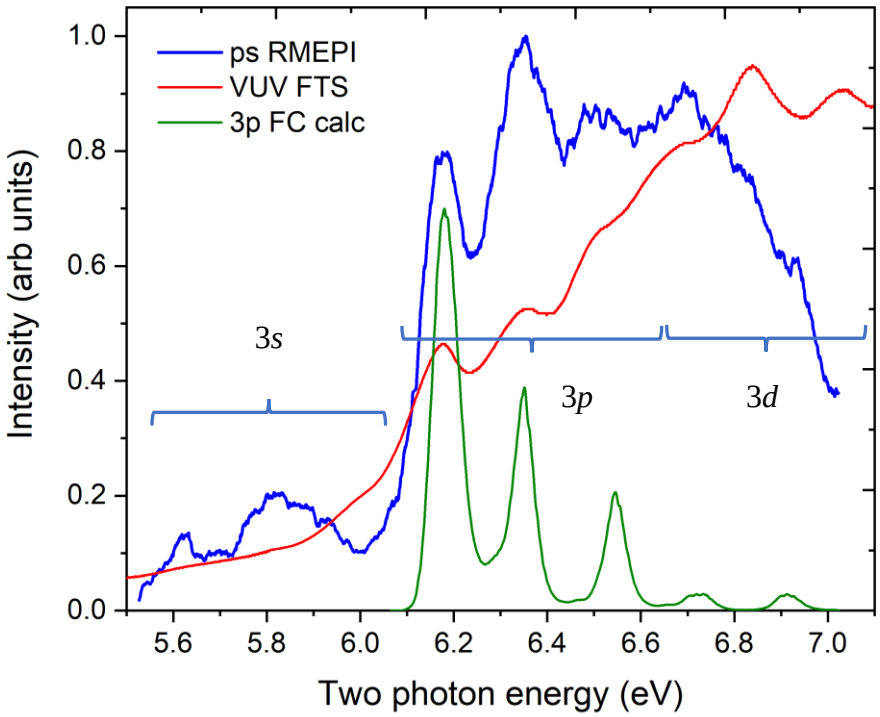

Figure 4.6. Comparison of REMPI spectrum (blue) and VUV FT spectrum (red) for 3-carene. The REMPI spectrum shows three different regions corresponding to three different electronic states. The 3p region in the spectra are compared with a 3p Franck-Condon calculation (olive) corresponding to 3p ← π band [137].

is shown in comparison with a VUV FT spectrum, recorded at Synchrotron SOLEIL as described in previous section. There is clearly a very close resemblance between the absorption spectrum and the two-photon. The REMPI spectrum shows resolved vibrational features, comparable to those seen in the high-resolution FT spectrum. However, the FT spectrum shows very little structure in the 5.5-6.0 eV region in comparison to the REMPI spectrum. The three different regions identified in the REMPI spectrum, in analogy to α-pinene, correspond to the B-, C- and D-band transitions, which are believed to correspond to 3*s* ← π, 3*p* ← π, and 3*d* ← πexcitation, respectively. The D-band region is not very prominent in the REMPI spectrum; thus we will limit our discussion to the first two bands.

The 3*s* ← π (B-band transition) is observed in the region 5.5 - 6.1 eV with the 0-0 transition at 5.6 eV, followed by the weakly resolved peaks corresponding to the vibrational levels of the 3*s* Rydberg state. This weakly resolved band might suggest that the 3*s* Rydberg state has a short lifetime. The 3*p* ← π (C-band transitions) are

observed in the region 6.2 - 6.8 eV with the 0-0 transition at 6.2 eV, followed by the peaks corresponding to vibrational levels of the 3*p* Rydberg state. Figure 4.6 also shows a 3*p* FC calculation in this region, and this will help assign vibrational feature in this region. The first peak is a pack of transitions from the vibrationless neutral ground state to zero or one quanta excitation of the first three lowest energetic vibrational normal modes (ν_1, ν_2, ν_3) in the excited state. The second and third peak is a combination of the first peak and one quanta excitation in mode ν_{56} (C=C bond stretch) and ν_{60} (symmetric stretch in methyl group), respectively. The fourth peak is a combination of the first and one quanta excitation in ν_{56} and ν_{60}. The fifth peak is a combination of the first peak and one quanta excitation in ν_{60} and ν_{65} each [137]. The weak 3*d* ← π (D-band transitions) are observed beyond 6.8 eV.

4.7 **Photoelectron spectra**

One colour photoelectron images of both molecules were recorded over the range 450-350 nm (5.5 – 7.1 eV), with each image corresponding to the excitation of a vibrational in a 3*l (spd)* Rydberg states. An example of images recorded via the 3*s*, 3*p*, and 3*d* Rydberg states using (2+1) ionization are shown in figure 4.7 for α-pinene, along with the photoelectron spectra that have been extracted from these images using pBasex and plotted as a function of electron kinetic energy (see full details of the image

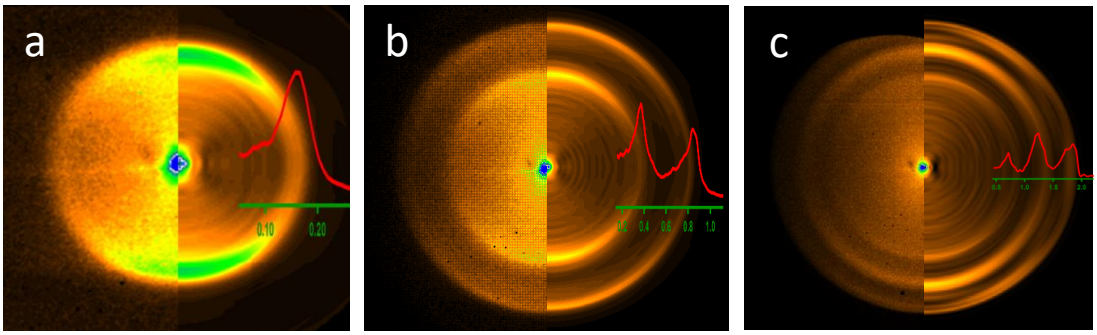

Figure 4.7. Photoelectron image with superimposed photoelectron spectra for α-pinene. (a) Ionization via the 3s Rydberg state; (b) ionization via the 3p Rydberg state and excited vibrational levels in the 3s Rydberg state; (c) ionization via vibrationally excited 3s, 3p and 3d Rydberg states.

analysis in Chapter 2). Figure 4.7(a) shows the photoelectron image resulting from the ionization through the 3*s* Rydberg state, figure 4.7(b), shows the image for the ionization through 3*s* as well as 3*p* state, and figure 4.7(c) shows the image for ionization via all three Rydberg states. In the coming section where we present the full photoelectron spectrum, the spectra are plotted as a function of ionization energy (IE)

which is calculated by assuming an overall three-photon process and subtracting the measured electron kinetic energies from the three-photon energy. The lack of vibrational progression is a consequence of the $\Delta v = 0$ propensity rule. In some cases weak $v = 0$ (3*s* origin), and $v = 1$ (ν_{56} mode) peaks can also be observed. For example, in the photoelectron spectrum resulting from the ionization of the 3*s* state in α-pinene shown in figure 4.8, which features a strong $\Delta v = 0$ peak along with weak $v = 0$ and $v = 1$ peaks.

In the next sections 4.7.1 and 4.7.2, series of photoelectron spectra are measured are presented as a function of the two-photon excitation energy (2ϕ) for α-pinene and 3-carene respectively. Each spectrum was normalized by the laser power and acquisition time.

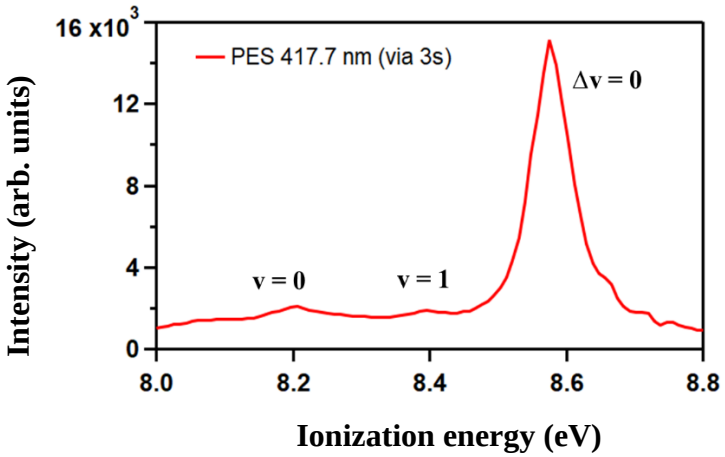

Figure 4.8. Photoelectron spectrum of α-pinene following excitation and ionization through the 3s Rydberg state at 417.7 nm

4.7.1 α-pinene

Figure 4.9 provides an overview of the normalized set of REMPI-PES for α-pinene. As the wavelength (two-photon energy, 2ϕ) is changed different vibrational levels in 3*s*, 3*p* and 3*d* are accessed. The $\Delta v = 0$ propensity rule, as mentioned above gives a single intense photoelectron peak at each wavelength for these Rydberg states. This results in the formation of three main distinct ridges in figure 4.9 corresponding to ionization via 3*s*, 3*p* and 3*d*. The first peak along the 3*s* ridge which rises around 8.2 eV (two photon energy of 5.57 eV), corresponds to the 0-0 transition, matching well with previous literature [128]. Although at this laser wavelength the three-photon equivalent energy (3ϕ = 8.36 eV) is energetically sufficient to ionize several

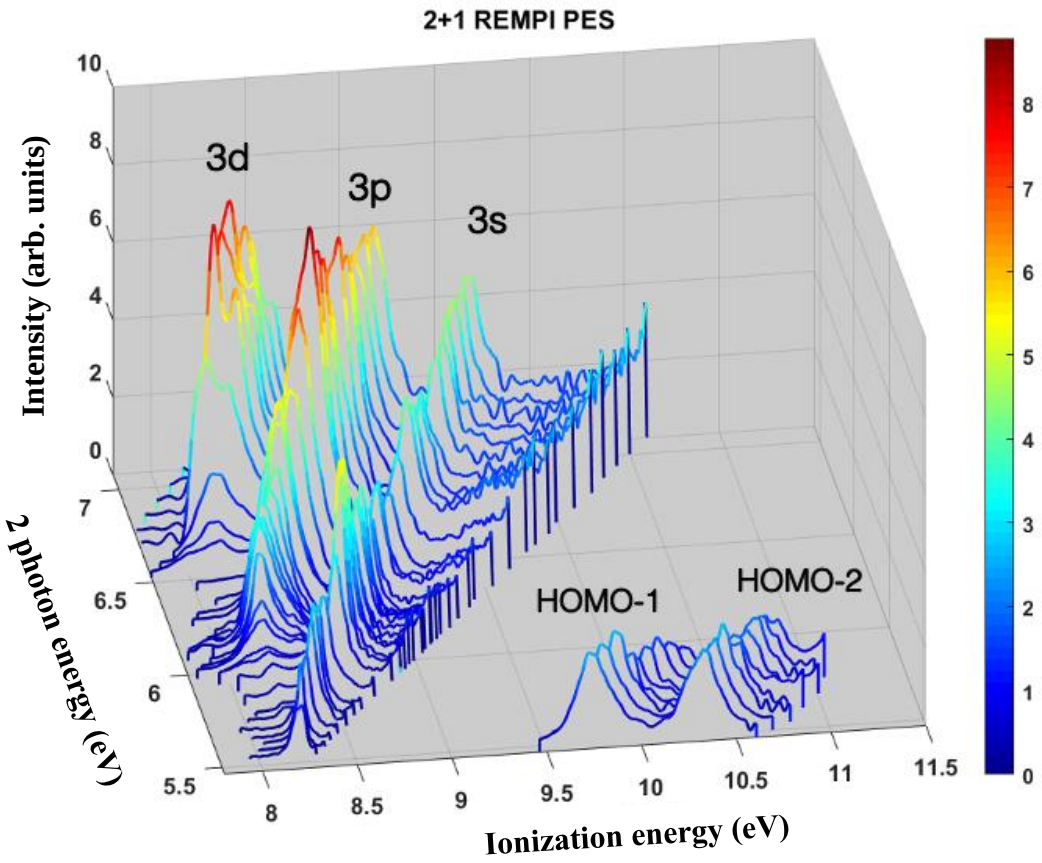

Figure 4.9. Photoelectron spectra recorded over the range of 350-450 nm (5.5-7.1 eV). Plotted along ionization energy and two photon energy for α-pinene, showing three different ridges corresponding to three different electronic states (3spd). Also showing the 4-photon process corresponding to ionization from HOMO-1 and HOMO-2.

vibrationally excited states. The rest of the photoelectron spectra along this ridge map out a well-resolved vibrational structure in 3*s*, with the peak intensities in reasonable agreement with a Franck Condon simulation (see figure 4.5), which is used to confirm the assignment.

Once the excitation energy $2\phi \geq 6.2$ is reached, a second ridge, slightly broader, appears in the REMPI-PES overview (figure 4.9) running parallel to the first. This is readily understood as being formed by $\Delta v = 0$ excitations in ionization from the 3*p* state(s). The threshold for the 0-0 transition is observed to be around 6.2 eV, followed by the vibrational progression of the 3*p* state. This 3*p* ridge has a slight shoulder to the right which might be coming from one of the members of the 3p manifold with a reduced excitation and/or ionization cross-section. At the same time, the initial ridge associated with the ionization of the 3*s* Rydberg state apparently continues throughout the 3*p* excitation band. One might first suppose that this is because above $2\phi = 6.2$ eV both the 3*s* and 3*p* Rydberg states are energetically accessible and so ionization of

either can occur in parallel. However, at shorter wavelengths the ionization energies reached along this ridge exceed 9.0 eV and so fall outside the Franck-Condon window for direct vertical ionization from the ground state neutral to the 3*s* Rydberg excitation. The probability of there being a direct vertical transition from the ground state neutral to the cation via the 3*s* intermediate accounting for the continuation of this 3*s* ridge is therefore quite negligible. One plausible explanation could be that these peaks may result from the ionization of high vibrational states in 3*s* following internal conversion from 3*p* state. Above excitation energy, $2\phi \geq 6.6$, a third ridge, even broader than 3*p*, appears in the REMPI-PES (figure 4.9) running parallel to the first two ridges. This is as being formed by $\Delta v = 0$ excitations in ionization from the 3*p* state(s). Peaks in this ridge appear to be split giving a sense that it might be two closely lying different 3*d* states. The broadening in the photoelectron spectra peaks could be a consequence of the increasing electron kinetic energy as higher energy photons are used for ionization.

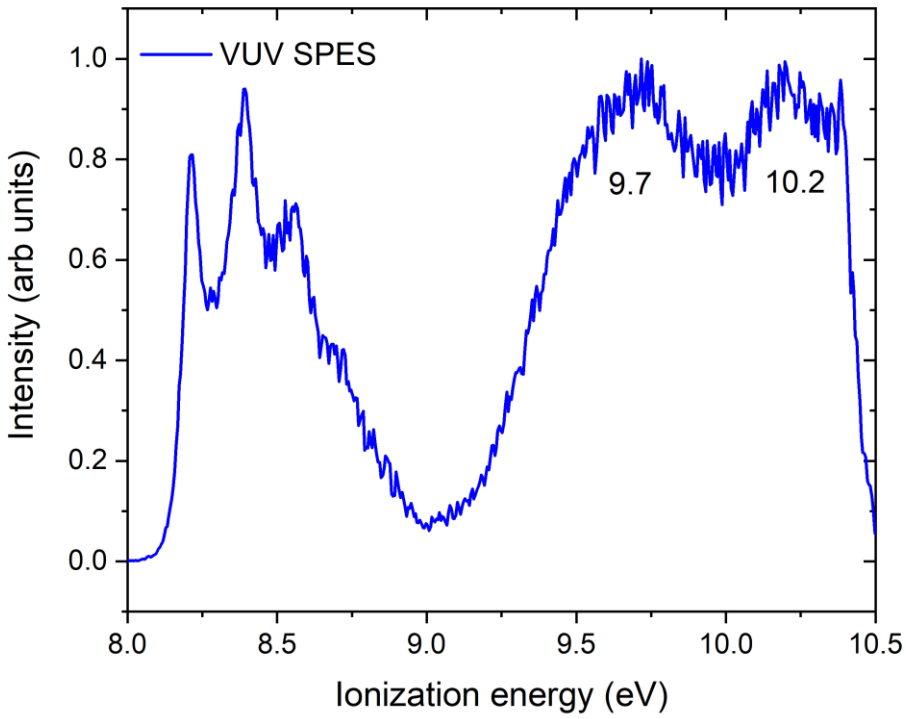

Figure 4.10. One photon VUV slow photoelectron spectrum (SPES) [128].

Below excitation energy, $2\phi \geq 5.4$, two sets of ridges appear at ionization energies of 9.7 and 10.2 eV running parallel to the other three ridges. These two ridges were analyzed by assuming the 3-photon excitation process and one-photon ionization because electron kinetic energy carried by these electrons only made sense for a (3+1)

REMPI process. Upon comparison with a one-photon VUV slow photoelectron spectra (SPES) [128] (figure 4.10), these two ridges were identified to be as ionization form HOMO-1 and HOMO-2.

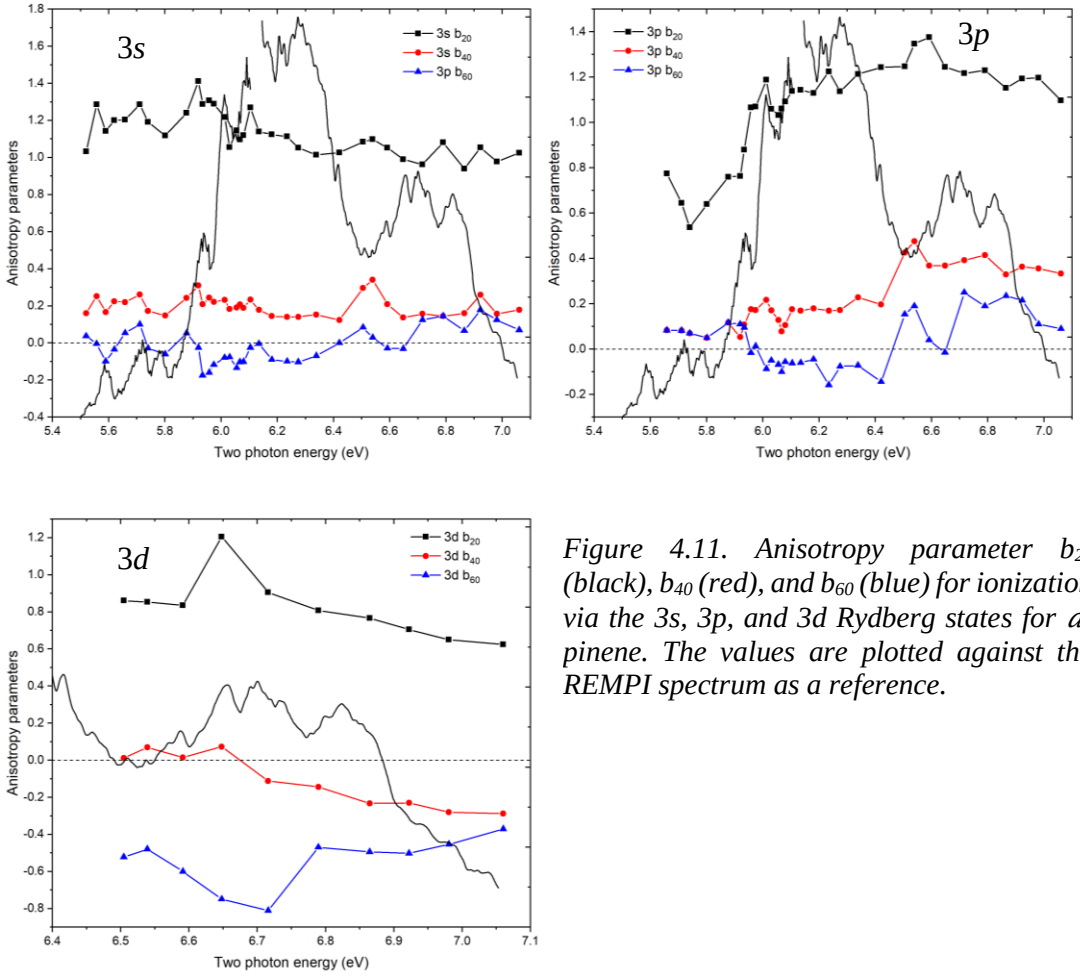

Figure 4.11. Anisotropy parameter b_{20} (black), b_{40} (red), and b_{60} (blue) for ionization via the 3s, 3p, and 3d Rydberg states for α-pinene. The values are plotted against the REMPI spectrum as a reference.

Photoelectron images were recorded using a (2+1) REMPI scheme with parallel polarization of the pump and probe beams, and the photoelectron angular distribution can be described by β_{LM} parameters with L = 0, 2, 4, 6 and M = 0. Figure 4.11 presents the anisotropy parameters along the three ridges (figure 4.9). The values are plotted in reference with the REMPI spectrum as a function of two-photon excitation energy. The 3*s* region shows an average β_{20} value of ~1, β_{40} ~0.2, and β_{60} almost zero. The 3*p* region shows an average β_{20} value of ~1.2, β_{40} ~0.3, and β_{60} almost zero. The β_{L0} in the 3*p* region do show slight jumps in value near the presence of another electronic state. For example, the β_{40} and β_{60} parameters show a small jump in the value near 6.5 eV from 0.2 to 0.4 and -0.1 to 0.1, respectively. The 3*d* region behaves slightly differently, where it shows an average β_{20} value of ~0.8, β_{40} almost zero except at the tail end with

a value of ~0.2, and β_{60} is non-zero this time unlike in the 3*s* and 3*p* regions, with an average value of ~0.5.

4.7.2 3-carene

Figure 4.12 shows the equivalent overview of the normalized set of REMPI-PES for 3-carene, plotted as a function of two-photon excitation energy (2ϕ). Each spectrum was normalized by the laser power and acquisition time. A similar $\Delta v = 0$ propensity rule in the intermediate state ionizations can be expected. This propensity rule gives rise to a single intense photoelectron peak at each wavelength for these Rydberg states. This results in the formation of three ridges similar to α-pinene corresponding to ionization via 3*s*, 3*p*, and 3*d*. The first peak along the 3*s* ridge which rises around 8.46 eV corresponds to the 0-0 transition. The rest of the photoelectron spectra along this ridge map out a well-resolved vibrational structure in 3*s*.

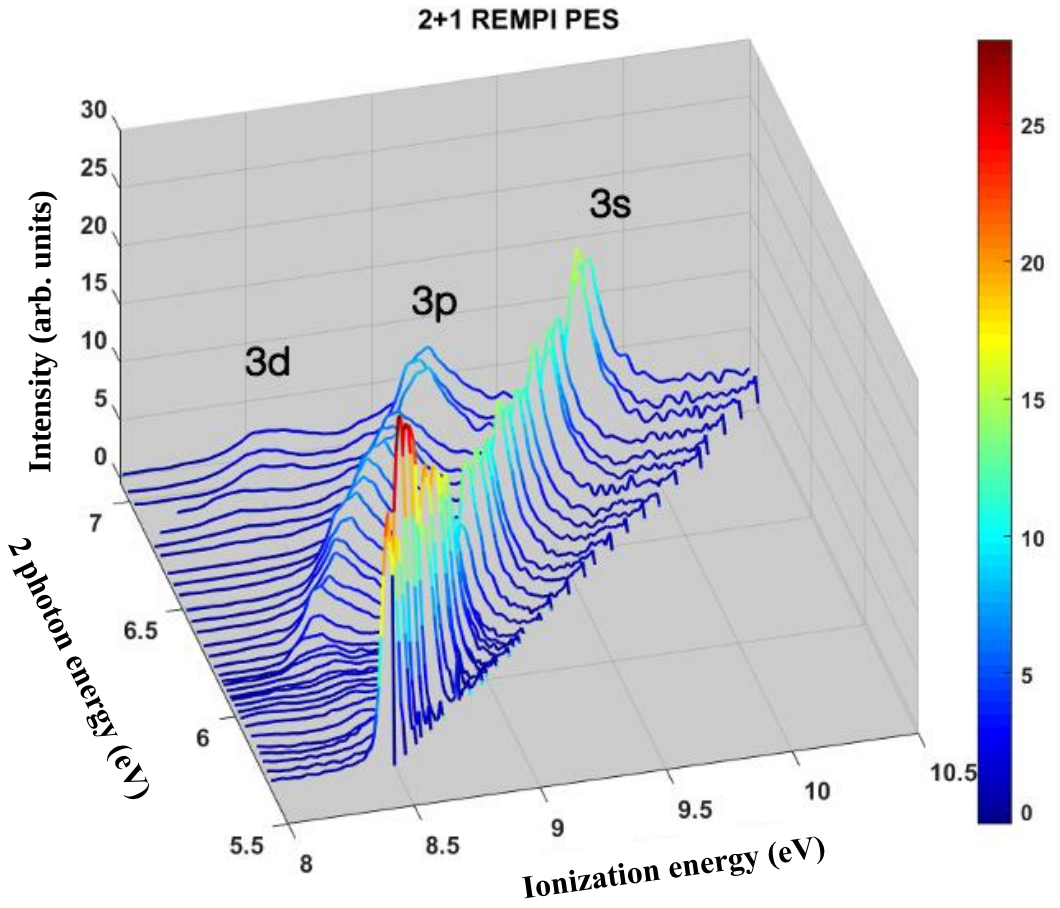

Figure 4.12. Photoelectron spectra recorded over the range of 350-450 nm (5.5-7.1 eV). Plotted along ionization energy and two photon energy for 3-carene, showing three different ridges corresponding to three different electronic states (3spd).

When the excitation energy, $2\phi \geq 6.2$ is reached, a second ridge appears in the REMPI-PES overview running parallel to the first. This is understood as being formed by $\Delta v = 0$ excitations in ionization from the 3*p* state(s). At the same time, the initial ridge associated with the ionization of the 3*s* Rydberg state continues throughout the 3*p* excitation band. For the 3*s* state, peaks at ionization energy greater than 9.0 eV falls outside the Franck-Condon window for the direct vertical ionization from ground sate neutral to 3*s* Rydberg excitation. Thus, most probable explanation for this could be the internal conversion from the 3*p* to 3*s* Rydberg states. The width of the 3*s* ridge in this region has increased at the same time and from the additional contribution made by the broad 3*p* ridge, it becomes clear that the total electron yield increases sharply, as does the REMPI intensity (figure 4.6). Once the excitation energy, $2\phi \geq 6.8$ is reached, a third ridge, slightly weaker intensity appears. This is understood as being formed by $\Delta v = 0$ excitations in ionization from the 3*d* state.

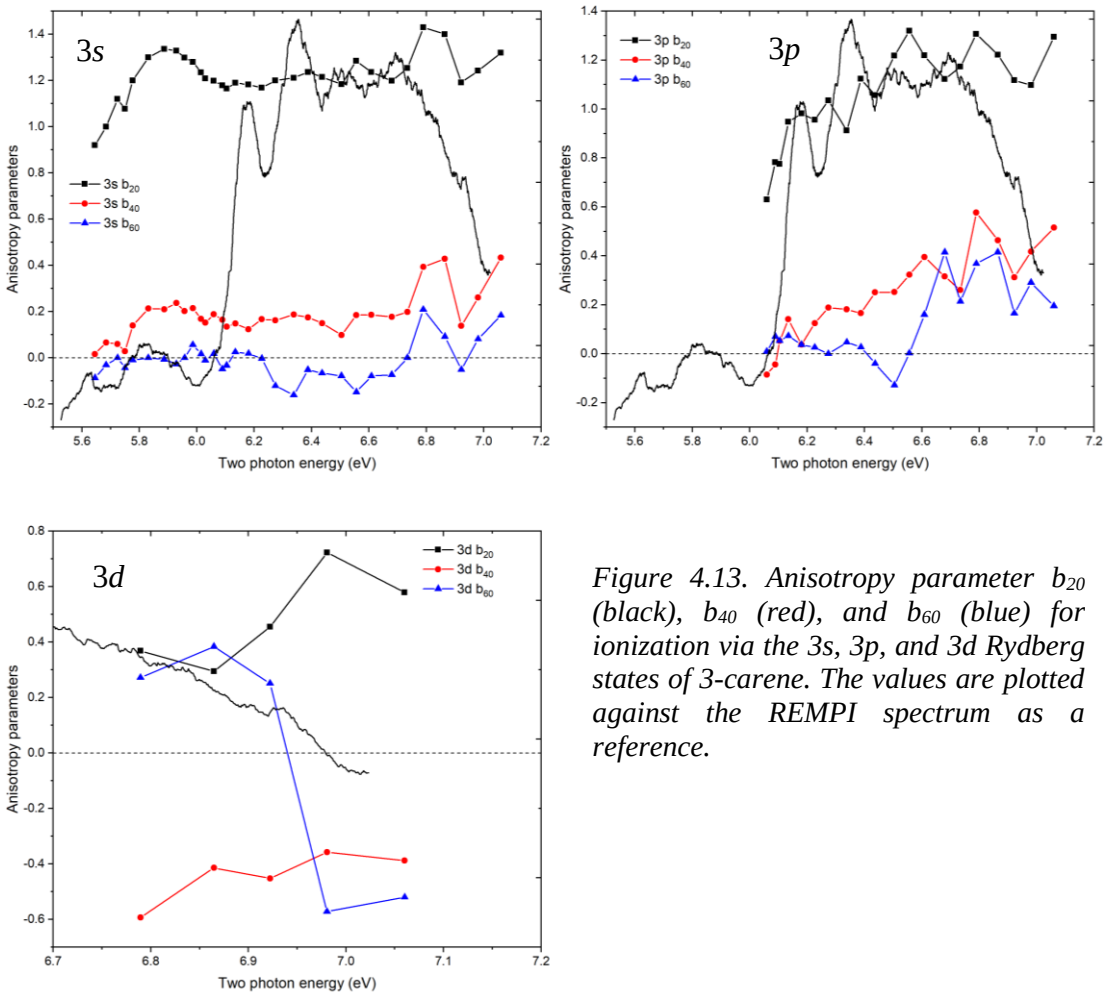

Figure 4.13. Anisotropy parameter b_{20} (black), b_{40} (red), and b_{60} (blue) for ionization via the 3s, 3p, and 3d Rydberg states of 3-carene. The values are plotted against the REMPI spectrum as a reference.

Figure 4.13 presents the anisotropy parameters along the three ridges (figure 4.12) for 3-carene as a function of two-photon excitation energy. The 3*s* region shows an

average β_{20} value of ~1.2, β_{40} ~0.2, and almost zero β_{60}. The 3*p* region shows an average β_{20} value of ~1.2 with an increasing value from the start of the band to end, β_{40} shows similar behaviour with an average value of ~0.3, and β_{60} is almost zero in the first half of the band and the second half shows a value of ~0.3. The 3*d* region shows an average β_{20} value of ~0.5, β_{40} ~ -0.4, and β_{60} shows an absolute value of ~0.3 which changes sign from positive to negative in the middle of the band.

4.8 **Intensity dependence of the REMPI ion yield**

The probability of multiphoton ionization processes depends on the light intensity raised to the n^{th} power, where n is the number of photons involved. In a (2+1) REMPI process, for example, the ionization proceeds via an intermediate state that is resonant with two photons. This 2-photon resonant state, which lives longer than other non-resonant states, enhances the ionization rate relative to non-resonant ionization processes and the ionization cross-section will depend on the square of the laser intensity. This can be verified by plotting the ion yield as a function of laser power.

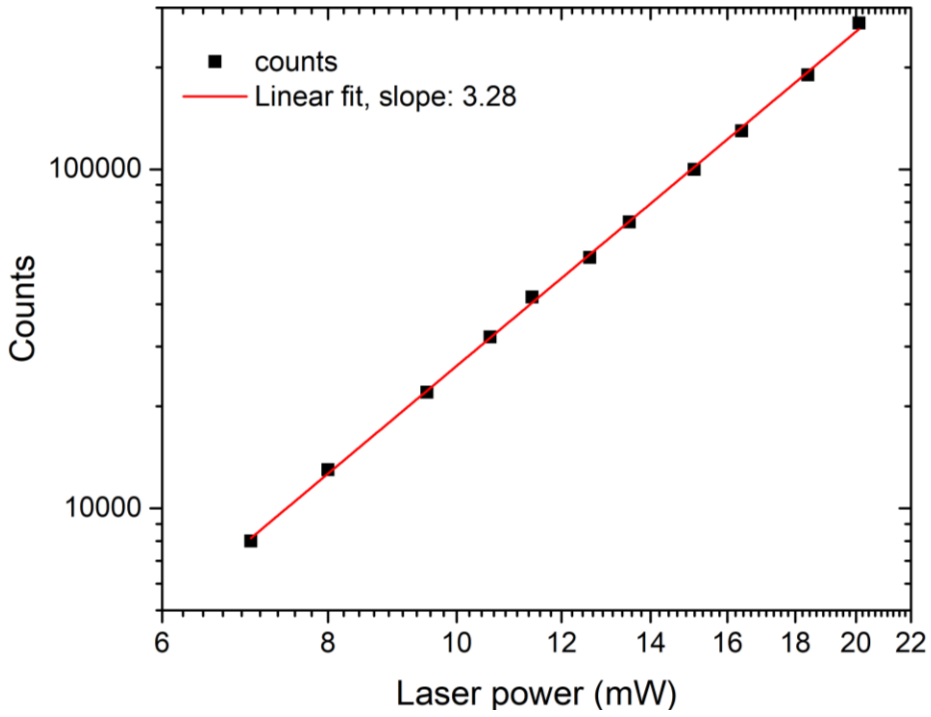

Figure 4.14. Log_{10}-log_{10} plot of ion yield vs laser power following ionization via the 3s Rydberg state in α-pinene.

Figure 4.14 shows a log scale plot for ion yield versus laser power for α-pinene following excitation and ionization at 416 nm and we find that instead of the expected squared dependence the yield depends on the cube of the laser intensity. In order to

fully investigate this power dependence, the yield of the parent ion and the fragment with mass 94 were measured at a series of wavelengths. This is presented in the next sections for α-pinene and 3-carene.

4.8.1 α-pinene

In figure 4.15 we present the parent and fragment ion yield as a function of laser power at several excitation wavelengths along the RMEPI spectrum for α-pinene. Three different power laws can be observed for the parent ion in the range of 5.6 - 6.0 eV, 6.0 - 6.5 eV, and 6.5 - 7.1 eV. The first range corresponds to 3*s* region which an average of n = 3.07 ± 0.05 (~3rd order), the second range corresponds to the 3*p* region with an average of n = 2.63 ± 0.16, and third range corresponds to the 3*d* region with an average of n = 2.71 ± 0.13. The 3rd order laser power dependence is an indication

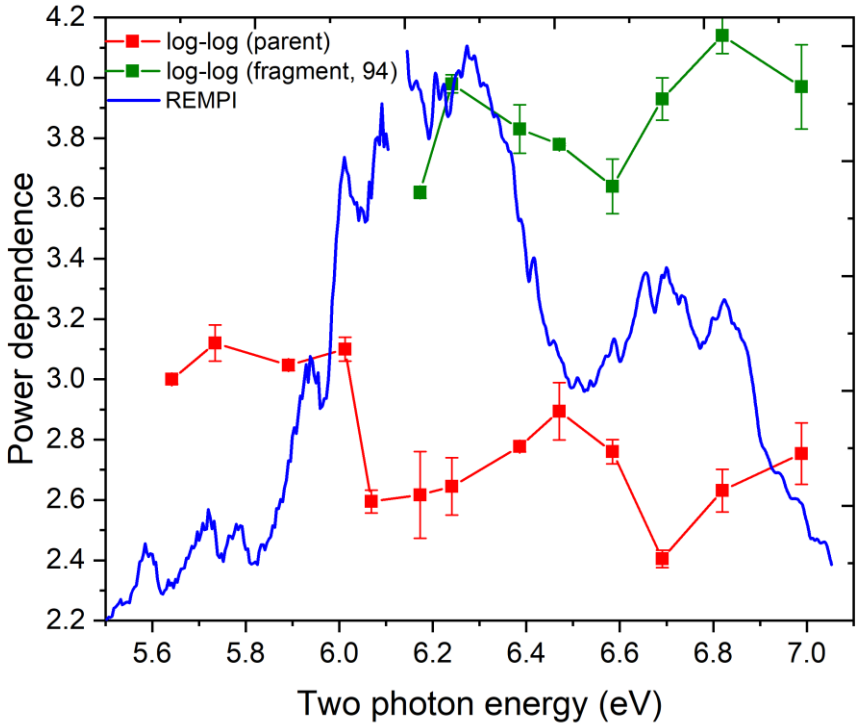

Figure 4.15. Laser power dependence of parent and fragment ion yield for α-pinene. Linear fit slopes of log_{10}-log_{10} plot of ion yield vs laser power at different wavelengths along the REMPI spectrum plotted for parent ion (red) and fragment, 94 amu (olive).

that the ionization step is not saturated and that a third photon will also be a rate determining step and relaxation into the non-ionization channel will be in direct competition with the ionization channels.

In the 3*p* and 3*d* regions the laser intensity dependence for the parent ion production exceeds 2nd order and approaches the 3rd order. Conventionally, this now indicates that relaxation into non-ionizing channels is becoming competitive with ionization. Since the laser pulse duration is 1.3 ps we may infer that excitation lifetime, τ is of similar magnitude. The rough estimate for excited state lifetime can be calculated using the first-order kinetic energy model (Chapter 3), assuming mid-range ps laser power of 10 mW (~3.5×10^{11} Wcm^{-2}) and $\sigma^{(1)} \approx 10$ Mb gives a lower lifetime limit of $\tau \gg 150$ fs. The fragment (94 amu) ion yield shows a 4th order laser intensity dependence indicating at a four-photon process. A plausible explanation could be that the parent ion absorbs another photon to populate a higher-lying state which is dissociative in nature. This could explain why a-pinene show higher fragmentation in comparison to 3-carene (Section 4.5).

4.8.2 3-carene

In figure 4.16 we present the parent and fragment ion yield as a function of laser power at several excitation wavelengths along the RMEPI spectrum for 3-carene. The 3*s* region shows the laser power dependency of an average n = 3.06 ± 0.28 (~3rd order).

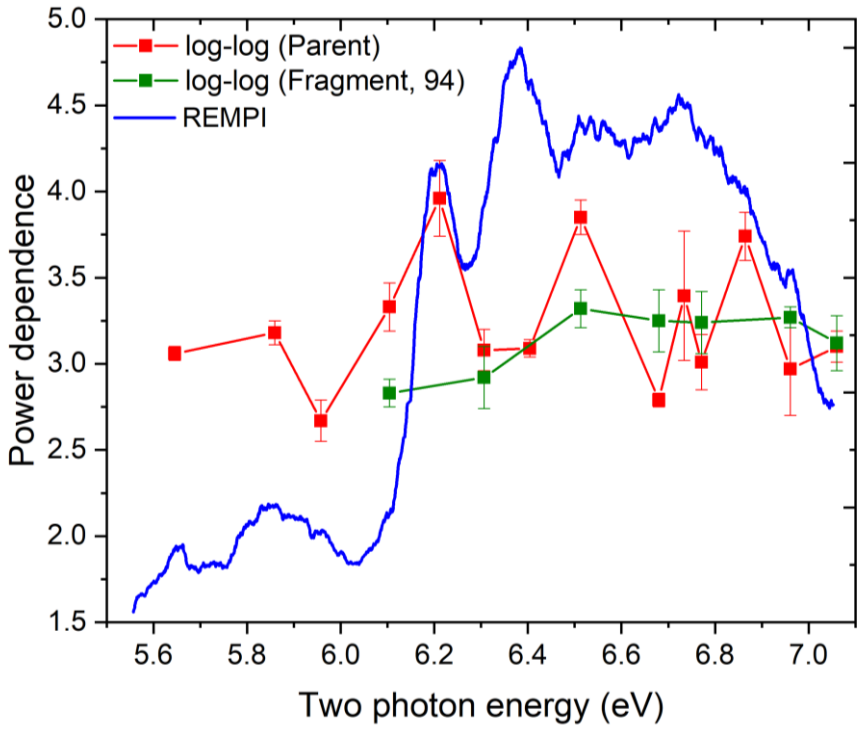

Figure 4.16. Laser power dependence of parent and fragment ion yield for 3-carene. Linear fit slopes of log_{10}-log_{10} plot of ion yield vs laser power at different wavelengths along the REMPI spectrum plotted for parent ion (red) and fragment, 94 amu (olive).

And 3*p* region shows a slightly higher average value of n = 3.3 ± 0.4. In both the regions this indicates that the ionization step is not saturated and relaxation into non-ionization channels such as 3*p* to 3*s* conversion will compete with the ionizing channel. This would be consistent with the photoelectron peaks that are observed beyond the Franck-Condon window in the 3*s* region (Section 4.7.2). This would explain the higher intensity of the 3*p* region in the REMPI spectrum (Section 4.6.2). The fragment (94 amu) ion yield show a laser power dependency of 3rd order. This might indicate that the formed cation is of dissociative nature.

4.9 **Polarization dependence of REMPI ion yield**

The two-photon absorption cross-section depends on the polarization of the photon. The circular-linear dichroism is the ratio of the ion yield when circular/linear polarised light is used for the ionization process. As mentioned in Chapter 3, these measurements can reveal important information about the photophysical properties of organic compounds, such as information about the angle between the permanent dipole moments (ground and excited) [117], and the symmetry of the excited states [118]. In this section we will present and discuss the ratio of the parent ion yield recorded with left circularly and linearly (C/L) polarized light for both the molecules, α-pinene (Section 4.10.1) and 3-carene (Section 4.10.2).

4.9.1 α-pinene

Figure 4.17 presents the measured ratios of the ion yields recorded for different polarization along with the power dependence data to better understand the two-photon absorption. For each wavelength investigated, repeated C/L measurements were made using several laser powers in the range 9–15 mW. No significant power dependence of the C/L ratio was observed. The values that are plotted in figure 4.17 are laser power averaged, and therefore considered to be fully representative of the circular-linear dichroism ratio, C/L, across the REMPI spectrum. From figure 4.17 it is evident that there are very significant C/L changes moving from the 3*s* to 3*p* region and when moving from the 3*p* to 3*d* excitation regions.

Smaller, though varying, C/L ratios are observed throughout the 3*s* region below 6.1 eV. Near the threshold of 3*s*, at 5.6 eV excitation energy, the ratio is 0.7, which increases toward the end of the 3*s* region to 1. In fact, one may observe in figure 4.17 a seeming anti-correlation between the laser intensity dependence, which drops from

3.1 to a minimum of ~2.6 at the end of the 3*s* band, and the C/L ratios, which rise from ~0.7 to a maximum of ~1 toward the end of the 3*s* band. A similar anti-correlation can be seen in the 3*p* region where the laser intensity dependence increases between 2.6 to

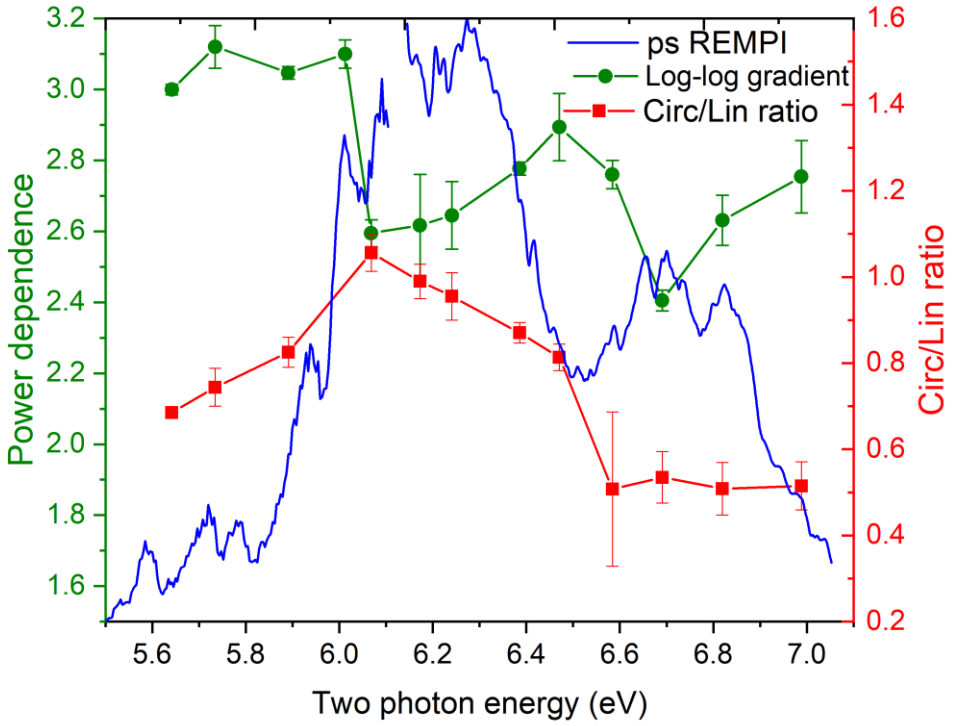

Figure 4.17. Polarization dependence measurements (red) shown in comparison with the power data (green) for parent ion for α-pinene. Measurements were made with left circular and linearly polarized, picosecond duration laser pulses around a mean power 4×10^{11} Wcm^{-2}. The ps REMPI spectrum is plotted on the same axis as an overall reference.

2.9 form 6.1 eV to 6.5 eV excitation energy, and the C/L ratio changes from 1 to a minimum of 0.8. In the 3*d* region, much smaller, though constant, C/L ratios are observed, with a value close to 0.5.

4.9.2 3-carene

Figure 4.18 presents the measured ratios of the ion yields with C/L polarization for 3-carene along with the power dependence data. The C/L measurements were made using several laser powers and no significant power dependence of the C/L ratios was observed. The values that are plotted in figure 4.18 are laser power averaged, therefore fully represent the C/L across the spectrum. The 3-carene C/L data is slightly different to that for α-pinene.

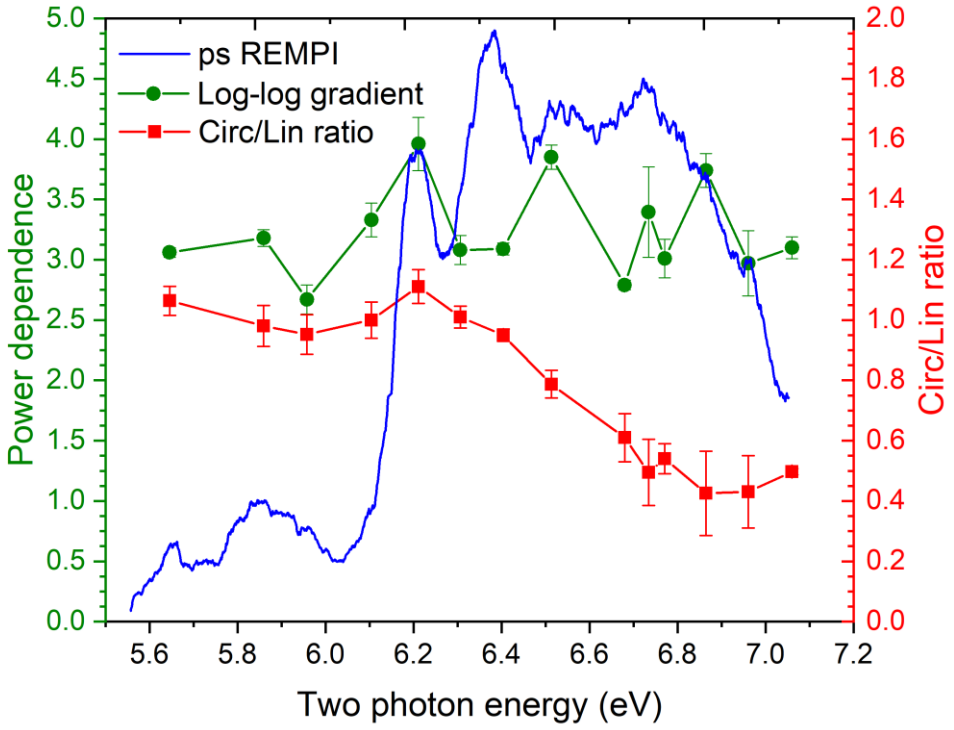

Figure 4.18. Polarization dependence measurements (red) shown in comparison with the power data (green) for parent ion for 3-carene. Measurements were made with left circular and linearly polarized, picosecond duration laser pulses around a mean power 4×10^{11} Wcm^{-2}. The ps REMPI spectrum is plotted on the same axis as an overall reference.

Much larger, though constant, C/L ratios of ~1 are observed throughout the 3*s* region below 6.2 eV excitation energy. The 3*p* region shows a varying C/L value throughout the band. The 3*p* threshold at excitation energy 6.2 eV, shows C/L ratio of ~1 which constantly drops until it recaches minimum of ~0.5 at the end of the 3*p* band. There is no anti-correlation observed with laser intensity measurements like α-pinene. The 3*d* region shows a constant C/L ratio of ~0.5. Clearly more theoretical work would be required to get a better interpretation.

4.10 **Conclusion**

In this chapter we investigated the 3*spd* Rydberg states of α-pinene and 3-carene. (2+1) REMPI spectra were recorded in the range of 350-450 nm covering the three Rydberg manifolds of both the molecules. Photoelectron images were recorded via selected electron and vibrational intermediate states. The extracted photoelectron spectra allowed for the assignment of different thresholds for the 3*s*, 3*p*, and 3*d* Rydberg states. The parent and fragment ion yield were measured as a function of laser power and the

polarization of light, yielding more insight on the lifetime and relaxation dynamics of intermediate states. The information that has been deduced about the electronic states and peak assignments of α-pinene and 3-carene in this chapter will be helpful in understanding and interpreting the PECD measurements (Chapter 5).

Chapter 5 Photoelectron circular dichroism of α-pinene and 3-carene via 3*sp* Rydberg states

5.1 Introduction

Since early demonstrations of the photoelectron circular dichroism (PECD) effect in VUV one-photon ionization experiments, it has been shown that PECD measurements are sensitive to the initial state [11], the molecular structure [108], and the final state [55]. It has also been shown that the PECD is extremely sensitive to the vibrational state of the cation formed [65]. Powis and co-workers have shown vibrationally induced inversion of the PECD in methyl oxirane [66], and more recently the effects of vibronic interactions on the PECD observed in methyl oxirane and limonene [138, 139], and the influence of vibrational excitation in α-pinene, β-pinene, limonene and 3-carene [128]. Ever since first PECD was demonstrated in resonance enhanced multiphoton ionization (REMPI) regime by Lux et al. [73] and followed by Lehmann et al. [74]; interest has been taken in studying the intermediate electronic and vibrational state effects as well as electron kinetic energy effects on PECD in the multiphoton regime.

Since that time, various groups have used the REMPI-PECD technique to study various chiral molecules such as fenchone [77, 80, 109], camphor [74, 132], limonene [76], methyl oxirane [75], and bicyclic ketones [77] using femtosecond laser pulses. The universality of PECD as a means of studying chirality has been demonstrated by Beaulieu and co-workers who presented data in the single-photon, multiphoton, above threshold and tunnel ionization regimes [78]. The magnitude of the REMPI-PECD effect has been shown to depend on the wavelength of the photon [79] and the intermediate state accessed in the multiphoton process [80]. It has also been shown that a time-resolved version of this technique could be a very sensitive tool for ultrafast molecular dynamics in chiral systems [81]. To fully understand the molecular dynamics of these chiral system using the REMPI-PECD technique, the effects of the initial, intermediate and final state of the system need to be decoupled. Beaulieu and co-workers have tried to study the effect of the intermediate state on PECD and demonstrated that the anisotropy created during the photoexcitation process is critical [82].

However, most of the studies in the multiphoton regime have employed femtosecond laser pulses. As a result of a large bandwidth associated with femtosecond pulses, the vibrational resolution is lost, thus masking any vibronic dependence on the observed PECD. The goal of the present work is to study the intermediate electronic, vibrational and electron kinetic energy dependence of the PECD observed in two chiral molecules: α-pinene and 3-carene (figure 5.1), using picosecond laser pulses. In Chapter 4, a

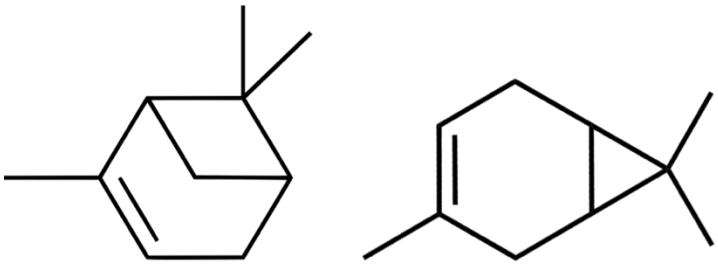

Figure 5.1. Specific enantiomers of terpenes used for photoelectron circular dichroism measurements.

detailed photoelectron spectroscopy study of these two molecules is presented. The (2+1) ionization REMPI and photoelectron spectrum showed three different Rydberg states 3*s*, 3*p* and 3*d* (Section 4.6 and 4.7). The laser power and polarization dependent measurements in Chapter 4 (Section 4.9 and 4.10) also confirmed the existence of three different Rydberg states.

In this chapter the aim is to study and decouple the effect of intermediate excited electronic state, vibrational state and electron kinetic energy on PECD in the (2+1) REMPI scheme. To fully understand the vibronic and electronic kinetic energy effect on PECD measurements, a complete PECD data set is presented and discussed along these two ridges covering the 3*s* and 3*p* intermediate electronic states. First we need to understand how the photoelectron spectra are behaving along the two ridges and can we resolve any intensity modulation of the peaks related to vibrational features. Secondly, we need to identify if there any changes in PECD along the two ridges which can be attributed to these vibrational features in PES. Therefore, in Section 5.5 and 5.9 the intensity variation of $\Delta v = 0$ photoelectron peak along the two rides (3*s* and 3*p*) is plotted alongside with PECD variation along these ridges on the ionization energy scale.

5.2 Experimental section

The experimental setup used in this experiment is described in detail in Chapter 2. Photoelectrons were detected using velocity map imaging and the resulting photoelectron images were reconstructed (using pBasex) to obtain the 3D distribution. For PECD measurements, an assembly of a quarter-waveplate and a polarizer was used to generate circular polarization and to do polarimetry. PECD was measured by recording the LCP and RCP photoelectron images by rotating the quarter waveplate using a rotation mount controlled by a stepper motor (Thorlabs). Each image was recorded for a short time at each polarization to avoid the effects of drifts in laser power or other experimental parameters, and then the quarter-wave plate was rotated to record the image for the other polarization. In each case, 15000 frames were recorded before switching to the other polarization, and four pairs of images were recorded. The images were added to produce final LCP and RCP images at each wavelength. Measurements using different polarization were conducted at constant pulse energies. Only one enantiomer (1R,5R) -(+)-α-pinene and 1S- (+)-carene were used to record the PECD data. Both samples were purchased from Sigma-Aldrich with > 97% enantiomer excess for α-pinene and > 99% for 3-carene.

In Chapter 4, section 4.7, photoelectron spectra measured following three-photon ionization in the range of 350-450 nm (5.51-7.08 eV) were presented and figure 4.9 and 4.12 (Chapter 4). These measurements showed three ridges corresponding to ionization via the 3*s*, 3*p*, and 3*d* intermediate states. Photoelectron images were recorded at various wavelengths in 3*s* and 3*p* region using left and right circularly polarized light for both the molecules. Owing to the limitations of the detector size, PECD data via the 3*d* intermediate could not be measured. A differential image of left and right photoelectron image is produced and analyzed with pBasex (for more detail Chapter 2 Section 2.6.2). This generates the photoelectron spectrum and PECD value, alongside with individual anisotropy parameters (see Chapter 1 Section 1.8 for multiphoton PECD formulation). These photoelectron spectra are plotted as a function of ionization energy (IE) which is calculated by assuming an overall three-photon process and subtracting the measured electron kinetic energies from the three-photon energy.

5.3 Results and discussion: α-pinene

So far α-pinene has only been studied using VUV single-photon ionization [128]. This is the first time it is studied in the multiphoton ionization regime using a picosecond laser pulse. In this section, we present several PECD measurements taken following the excitation of different features in the (2+1) REMPI spectrum of α-pinene. In section 5.4 we report the individual PECD results for (2+1) ionization via the 3*s* and 3*p* Rydberg states. The difference in PECD signal is significant for the two different electronic states, and a comparison of anisotropy parameters is presented. In section 5.5, the complete PECD data in the wavelength range 350-450 nm (5.51-7.08 eV) is presented, showing variation in PECD signal when ionized through these different electronic states (3*sp*). In section 5.6 we address the issue of decoupling the effects of vibrational structure and the intermediate electronic state as well as the effect of electron kinetic energy on PECD.

5.4 Ionization via 3*s* and 3*p* states

In Chapter 4 (Section 4.6.1) we showed that the 3*s* threshold lies at around 5.5 eV excitation energy and the threshold photoelectron peak is at 8.2 eV (Chapter 4 section 4.7.1). Figure 5.2 shows PECD measurements following (2+1) REMPI via the 3*s* Rydberg state at 432 and 419 nm, slightly above the threshold. The photoelectron spectrum (PES) shows a clear $\Delta v = 0$ peak i.e. v' (cation) - v'' (excited) = 0, is consistent with the expected propensity rule (see Chapter 1 Section 1.2.2). Franck-Condon allowed weak $v' = 0$ (at 432 nm) and $v' = 0, 1$ (at 419 nm) peaks are also present (see Chapter 4, Section 4.7.1). In figure 5.2, PES and PECD results for two wavelengths are shown, corresponding to ionization via two different vibrational levels of the intermediate 3*s* Rydberg state. The observed PECD values are very striking for ionization via these vibrational levels. A huge PECD of ~ 25-35% was observed for FC allowed weak $v' = 0$ and 1 peaks (non $\Delta v = 0$ peaks). Similarly, large PECD effects have been reported in one-photon ionization of the same molecule by Ganjitabar and co-workers [128]. However, surprisingly a relatively small PECD value is observed for $v' = 1$ and 2 peaks when they are excited as the main $\Delta v = 0$ peaks (8.4 at 432 nm

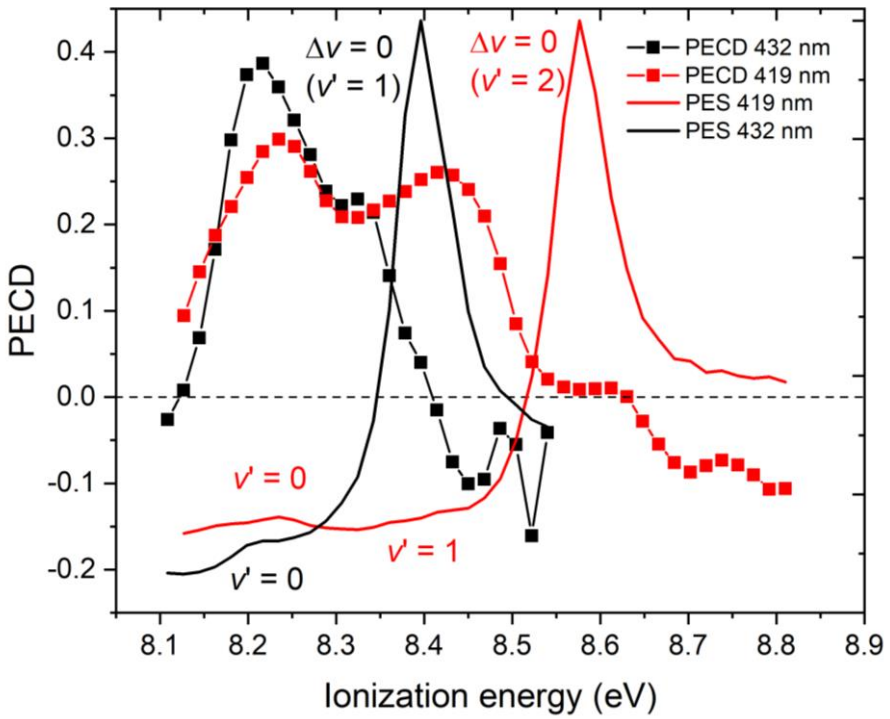

Figure 5.2. VMI PES and PECD measurements for R-(+)- α-pinene. The PECD measurements are for ionization via the 3s Rydberg state for the given enantiomer at wavelength 432 nm (black curves), 419 nm (red curves).

and 8.6 eV at 419 nm, figure 5.2), with magnitude varying between 0 and 10% across the peak. For the 432 nm measurements the PECD even changes sign across the peak (8.4 eV), going from positive to negative. The PECD value measured at 419 nm is almost zero for the main $\Delta v = 0$ peak (8.6 eV, $v' = 2$). This dramatic vibrational dependence of PECD has not been observed before. This shows the dependence of PECD on the initial excited state ($v'' = 0, 1, 2$) and final states ($v' = 0, 1, 2$) of the cation. When the initial and final state are same (i.e. main $\Delta v = 0$ peaks) the PECD value is small but when initial and final states are different (i.e. for weak FC allowed $v' = 0$ peak at 432 nm and $v' = 0, 1$ at 419 nm, where initial states were $v'' = 1$ and $v'' = 2$ respectively), we observed huge PECD values. As discussed in Chapter 1 section 1.11, in the multiphoton regime b_i^p anisotropy parameters with $i > 1$ contribute to the PECD. For a three-photon ionization process, b_i^p parameters with $i = 1, 3$ and 5 can contribute. For a three-photon process, up to $l_{max} = 6$ was used to analyze the photoelectron images and b_1, b_3, b_5 parameters were obtained. Furthermore, it has been shown by various

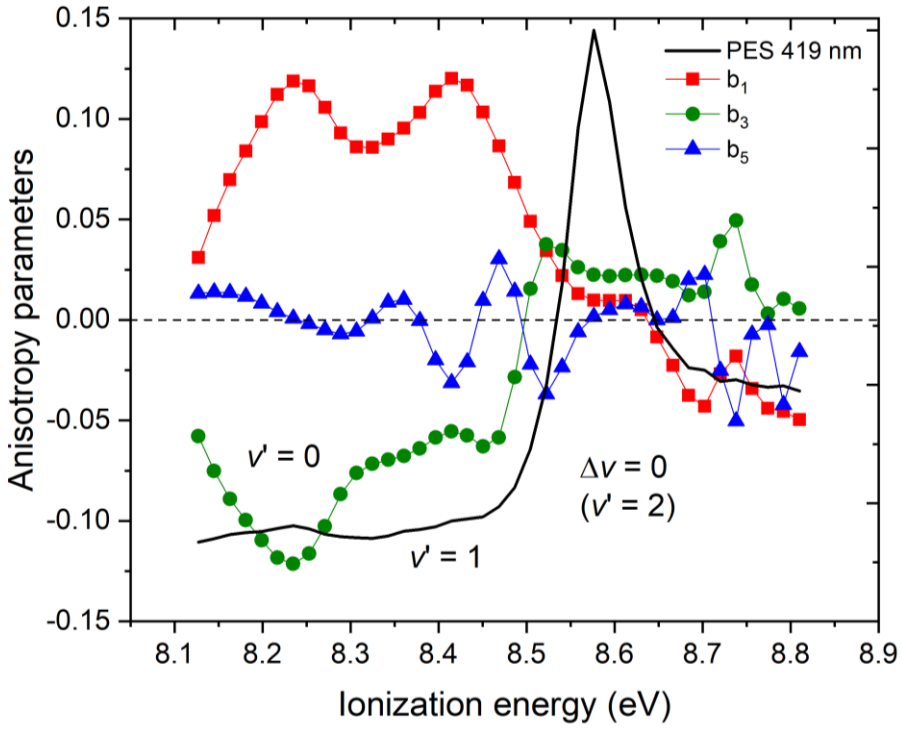

Figure 5.3. Anisotropy parameters for the PECD measurement for ionization via the 3s Rydberg state. The VMI-PES (black curve) has arbitrarily scaled intensity but is plotted on the same ionization energy axis as the b_1 (red curve), b_3 (green curve), and b_5 (blue curve) anisotropy parameters.

authors that the b_3 parameter arises due to the alignment of the excited intermediate state [81, 109]. Figure 5.3 shows the individual anisotropy parameters, b_1, b_3, and b_5 for one measurement in the 3*s* region. The b_5 anisotropy parameter is close to zero, but b_1 and b_3 show interesting behaviour for different peaks. For the $v' = 0$ and 1 peaks, b_1 shows an average value of ~0.10 and tracks the predicted positions of the vibrational peaks, even though they are not observed clearly in the photoelectron spectrum. For the $\Delta v = 0$ peak, b_1 is less than ~.02. The b_3 parameter is negative with values ~ –0.12 for the $v' = 0$ peak and ~ –0.05 for the $v' = 1$ peak, but close to zero for the $\Delta v = 0$ peak. Such significant values of b_3 have not been observed before and demonstrate how PECD depends on intermediate state alignment. Previously authors have quoted maximum b_3 value of ~0.05 for various molecules [73, 74, 79, 140].

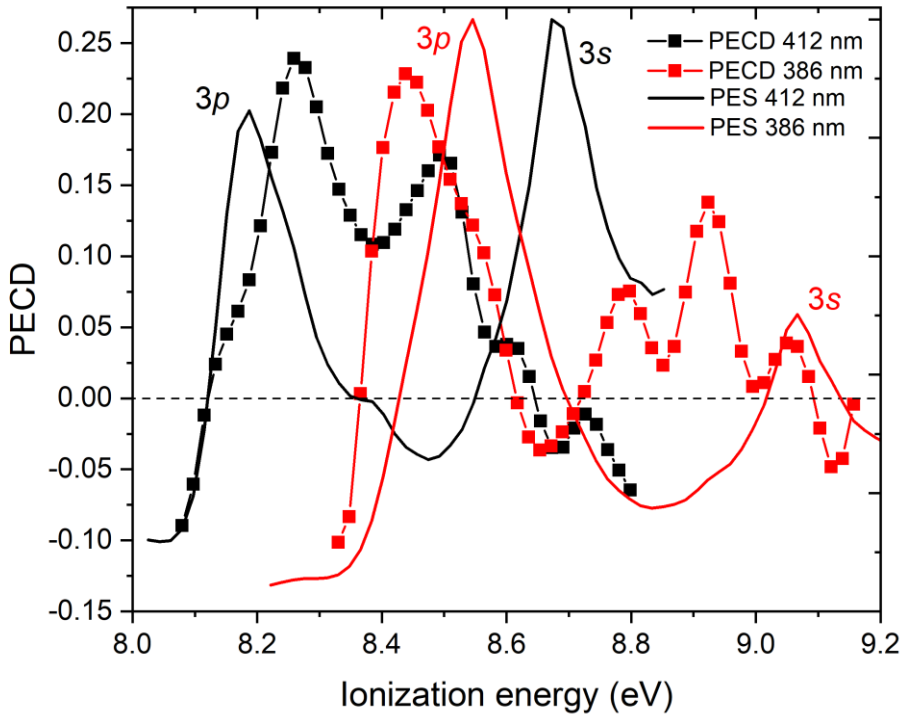

Figure 5.4. VMI PES and PECD measurements for R-(+)- α-pinene. The PECD measurements are for ionization via the 3p Rydberg state for the given enantiomer, extracted from a pair of images recorded with left- and right- circularly polarized laser pulse at wavelength 412 (red curves), and 386 nm (green curves).

The 3*p* origin threshold is found to be around 6.0 eV (2ϕ) excitation energy (Chapter 4 Section 4.6.1). Figure 5.4 shows the (2+1) REMPI-PECD measurement taken at the 3*p* origin threshold and just above it. A wider range photoelectron spectrum, with associated PECD, measured at 412 and 386 nm (2ϕ = 6.0 and 6.4 eV (0.4 eV above the 3*p* threshold)) can be seen. The total three-photon energies at wavelengths of 412 and 386 nm are 9.01 and 9.66 eV, which are sufficient to access high-lying vibrational states of 3*s* as well as low vibrational states of 3*p*. Consequently, in the photoelectron spectra at these two wavelengths, we can observe a $\Delta v = 0$ peak from 3*s* as well as from 3*p*. Interestingly, the PECD measurements for the ionization processes via the 3*p* Rydberg state are significantly different from those observed following ionization via 3*s*. The $\Delta v = 0$ peaks resulting from ionization via 3*p* shows PECD values in the range of 20-25%, whereas $\Delta v = 0$ peaks resulting from ionization via 3*s* shows a very small PECD. We note that whereas the vibrational peak that appears at 8.6 eV following ionization via 3*p* shows a PECD of 20%, the same vibrational peak in figure 5.5, which

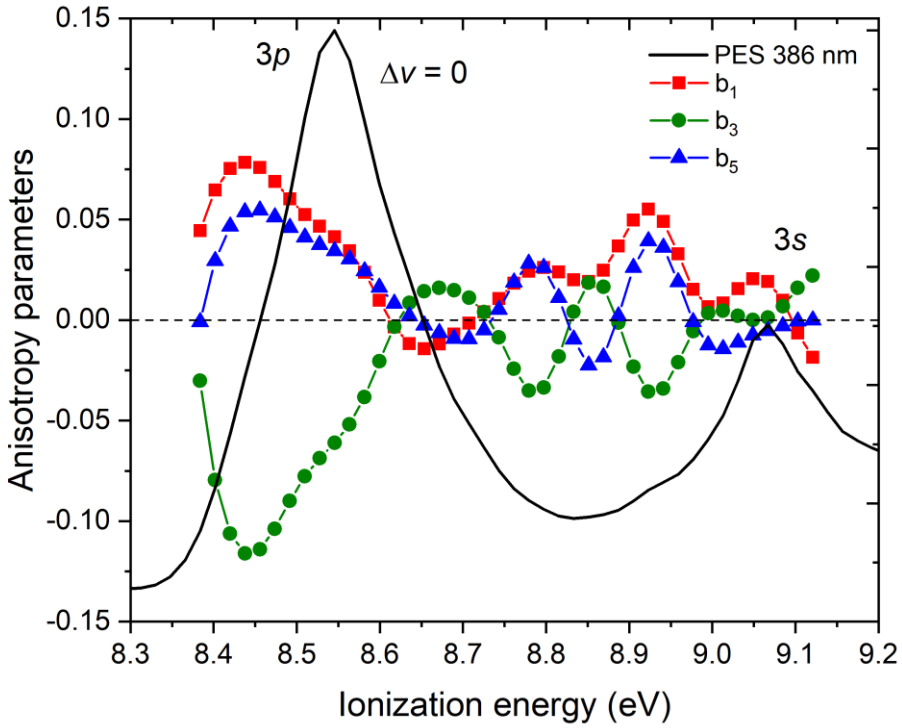

Figure 5.5. Anisotropy parameters contributing to the PECD measurement following ionization via the 3p Rydberg state for α-pinene. The VMI-PES has arbitrarily scaled intensity but is plotted on the same ionization energy axis as the b_1 (red curve), b_3 (green curve), and b_5 (blue curve) anisotropy parameters.

results from ionization via 3*s* shows almost zero PECD. The difference in PECD value could be attributed to either an electron kinetic energy effect or the influence of a different excited electronic state on the ionization dynamics. These effects are decoupled in the next sections (5.5 and 5.6) where complete PECD data along the full REMPI spectrum are presented for these two intermediate excited states (3*s* and 3*p*).

Further insight can be obtained by looking at individual anisotropy parameter for observed PECD following ionization of the 3*p* Rydberg state. Figure 5.5 shows the anisotropy parameters for one of the measurements in the 3*p* region. The $\Delta v = 0$ peak following ionization via 3*s* has very small contributions from all three parameters which have values ~ ±0.02. However, PECD following ionization via 3*p* has significant contributions for all three parameters. In fact b_3 parameter (0.13) is larger than the b_1 parameter (0.08), and even the b_5 parameter is ~ 0.06. This again a very striking observation which has not been seen before in the literature.

So far, we have presented measurements at specific wavelengths in the 3*s* and 3*p* excitation region. In the next section, we present measurements of complete PECD data in the range 350-450 nm (5.51-7.08 eV) following ionization through these two Rydberg states to facilitate the decoupling of the effects of electron kinetic energy and electronic and vibrational structure on the observed PECD.

5.5 Complete PECD data set along the 3*s* and 3*p* ridges: Vibrational effects

In this section we will present complete PECD data set along two of these ridges (3*s* and 3*p*) and discuss any vibrational effects and electron kinetic energy effects. The photoelectron images were recorded using left-and-right circularly polarized light at every 3-5 nm step along the full REMPI spectrum. These images were analyzed using pBasex to get PES, PECD, and anisotropy parameters at each wavelength point. Figure 5.6 shows the intensity variation of photoelectron spectra for ionization via the 3*s* and 3*p* regions. These intensity variation spectra were obtained by separately summing all the PES for the 3*s* and 3*p* ridges shown in Chapter 4 figure 4.9 (for range 350-450 nm)

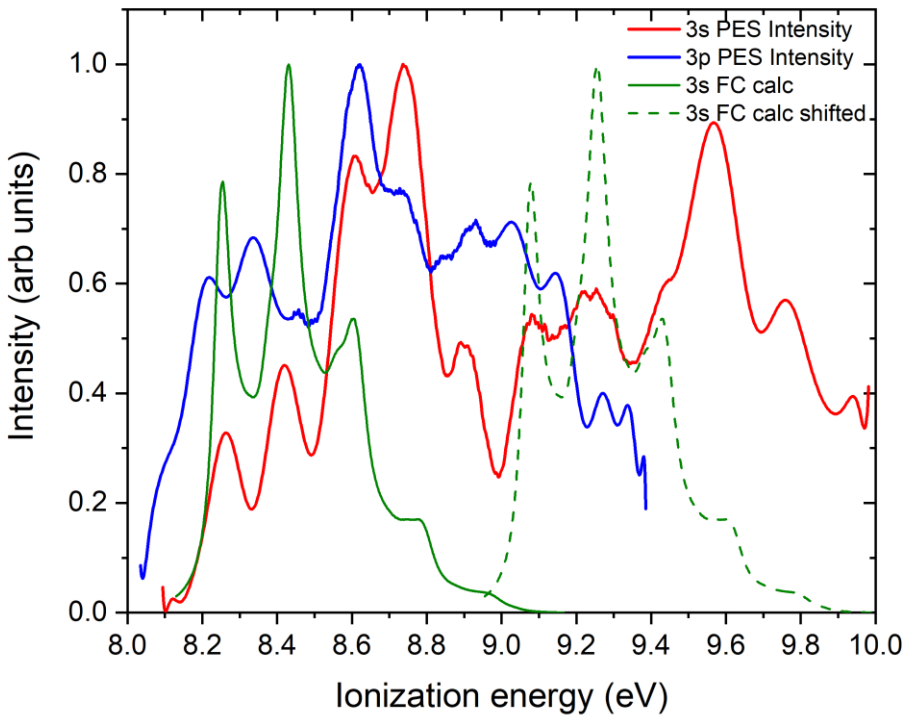

Figure 5.6. Intensity modulation of PES for ionization via the 3s (red curve) and 3p (blue curve) Rydberg states for α-pinene. PESs are shown in comparison with a 3s FC calculation (green dash/line curves). A 0.81 eV shifted FC calculation is shown in comparison with VMI peaks beyond the FC window.

and plotting as a function of ionization energy axis. Finally, a smoothing function (Matlab sgolayfilt) was used to get the final intensity variation of PESs for both states. The PES intensity variations of these Rydberg states are compared with a FC calculation via the 3*s* state. The peaks match reasonably well; however, the intensity of FC peaks decays around 9 eV, whereas PES continues to show the vibrational modulation. As discussed in the previous sections, this could a consequence of internal conversion form the 3*p* manifolds to the 3*s* states. Comparison with the FC simulation shows that the PES shows the same vibrational structure with similar FC factors in the ranges 8.2-9.0 eV and 9.0-10.0 eV. Ionization via 3*p* shows similar vibrational feature as 3*s* in the photoelectron spectrum.

Figure 5.7 shows the PECD variation along these the two ridges. The PECD data along the 3*s* and 3*p* ridges is convoluted using the same method as that used for the PES. The PECD values along two ridges are plotted as a function of ionization energy alongside the photoelectron spectrum. The PECD measurements via both states show

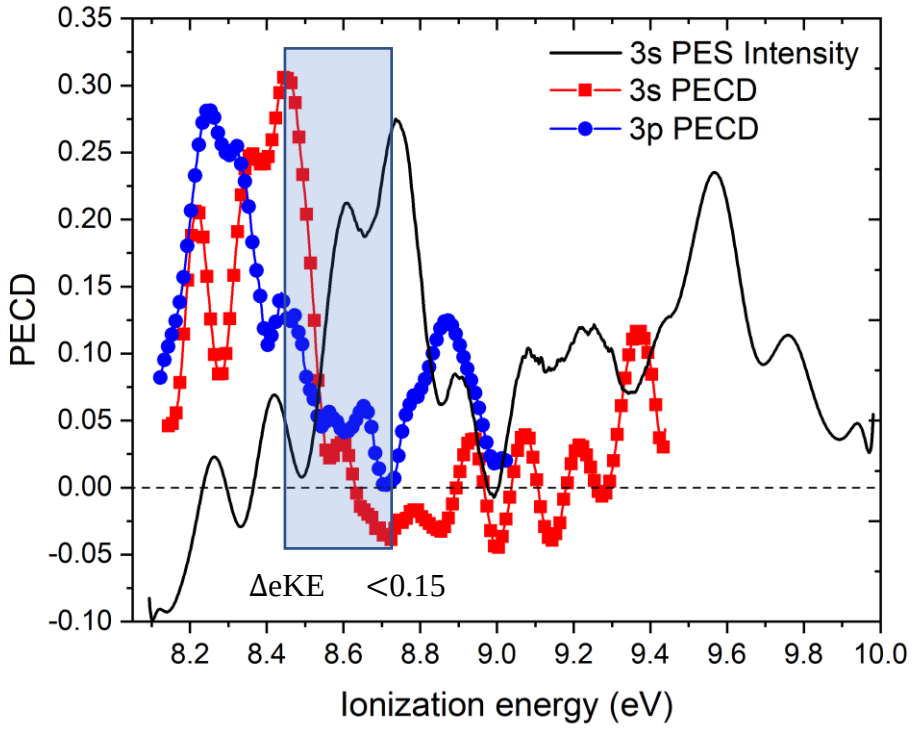

Figure 5.7. Complete PECD data set for ionization via the 3s (red curve) and 3p (blue curve) are shown along with the PES intensity along the 3s ridge (black curve) for α-pinene (see text). The PES and the PECD are plotted on the same ionization energy axis. The blue overlay box represents the change in eKE between the three peaks

modulation with the principal vibrational features and in both cases the preferred emission direction of photoelectrons is same except 3*s* PECD changes sign toward the end of 3*s* region (at 8.6 eV).

A few striking features were observed for the PECD measured following ionization through the 3*s* region; first, as mentioned above, it shows a clear modulation with the principal vibrational peaks. Second, a significant change in PECD with different excited vibrational peaks was observed. For example, the size of the PECD signal changes from ~30% for the second peak to less than 5% for the third peak and changes sign for the fourth peak. In order to understand this change in PECD, assignment of the vibrational structure is required. The FC calculations can be used to assign the vibrational bands in the 3*s* region which arise from a progression in the C=C stretching mode [128]. The peaks at 8.4, 8.6, and 8.8 eV arise from the excitation of the same mode ν_{56}, which is the double bond stretching, with one, two, and three quanta excitation respectively [137]. So the only change in these peaks is the quanta of excitation but the PECD value changes dramatically. Because the change in electron kinetic energy change from the second to the fourth peak is less than 0.15 eV, therefore, we infer that the change in PECD is caused by a vibronic effect rather than by a change in electron kinetic energy. For the peaks beyond the FC allowed window (9.0-9.8 eV), which are believed to result from internal conversion from 3*p* to 3*s*, the PECD value seems to increase from zero to a positive value. Unfortunately, data beyond 9.5 eV could not be recorded because of limitations imposed by the detectors size.

Figure 5.7 also shows the PECD results for ionization via the 3*p* intermediate (blue curve) which show similar behaviour. Near the onset of the 3*p* ionization, the PECD value is ~25%, slightly higher than observed in 3*s* region. Again, the PECD reduces to almost zero by the fourth peak (at ~8.7eV), suggesting the influence of vibrational structure on the observed PECD. To study any trend or effect of electron kinetic energy, we have to plot the measured PECD value as a function of electron kinetic energy. The next section discusses the effect of electron kinetic energy on PECD.

5.6 Electron kinetic energy effect on observed PECD

As mentioned previously in section 5.5, for ionization via the 3*s* Rydberg state, we observe peaks corresponding to $v' = 0$ and 1 alongside with the main $\Delta v = 0$ peak. The $v' = 0$ peak at 8.2 eV ionization energy, results from the ring breathing mode and the $v' = 1$ peak appearing at 8.4 eV ionization energy and results from one quantum of excitation in the C=C stretching mode. Figure 5.8 shows the PECD for these two peaks as a function of electron kinetic energy. The $v' = 0$ peak shows striking PECD value of ~35% which reduces to ~ 5% with the increase in electron kinetic energy (over the range of 0.5 eV). The $v' = 1$ peak shows PECD around 25% and decreases to ~7% with an increase in electron kinetic energy (over the range of 0.4 eV). This observation is purely an electron kinetic energy influences the observed PECD for first two peaks in 3*s* vibrational progression (figure 5.8 inset).

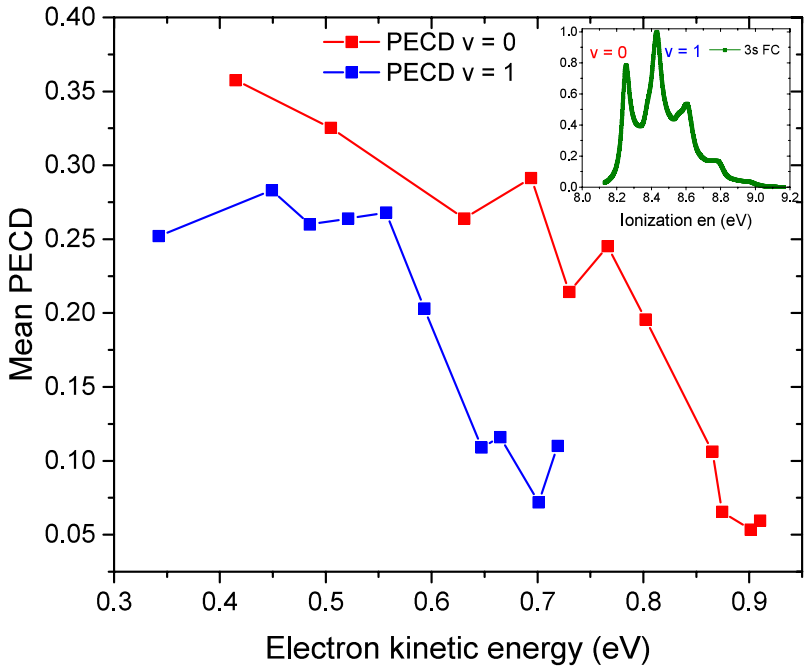

Figure 5.8. eKE effect: Mean PECD value for v' = 0 (red data set) and v' = 1 (blue data set) peaks when ionized via the 3s state is shown on eKE axis for α-pinene. Inset: 3s FC calculation [128].

In figure 5.9 we have plotted the mean PECD value together with the individual anisotropy parameters, as a function of electron kinetic energy for the two ridges (ionization via the 3*s* and 3*p* states). The full width half maximum (FWHM) was used to calculate the mean value of the PECD for a given photoelectron peak. The FWHM was calculated by fitting a Gaussian to the PES spectrum in both the regions. The width

of each Gaussian was used as an averaging window for the anisotropy parameter and PECD. For the 3*s* FC allowed transition PECD is mainly comprised of b_1 and b_3 parameter with value changing across the 3*s* band. The b_5 is approximately zero throughout the 3*s* band region. The b_1 behaves slightly different than b_3; b_1 shows a decreasing value up to 0.4 eV and then increasing value, whereas b_3 shows a constant decreasing behaviour. For 3*p* region, PECD has significant contribution from b_1 and b_3, and b_5 is also non-zero. These higher order anisotropy parameters show the effect of anisotropy created in the excited state on PECD. Another interesting observation comes out when we look at the mean PECD value from the 3*s* and 3*p* regions. The tail of 3*s* region (PECD value from 0.4 to 0.7 eV) seems to follow the start of the 3*p* region. This similar behaviour can be observed in the individual anisotropy parameters between the two regions. The reason behind this behaviour of the PECD value is not very clear but shows a clear eKE effect on PECD.

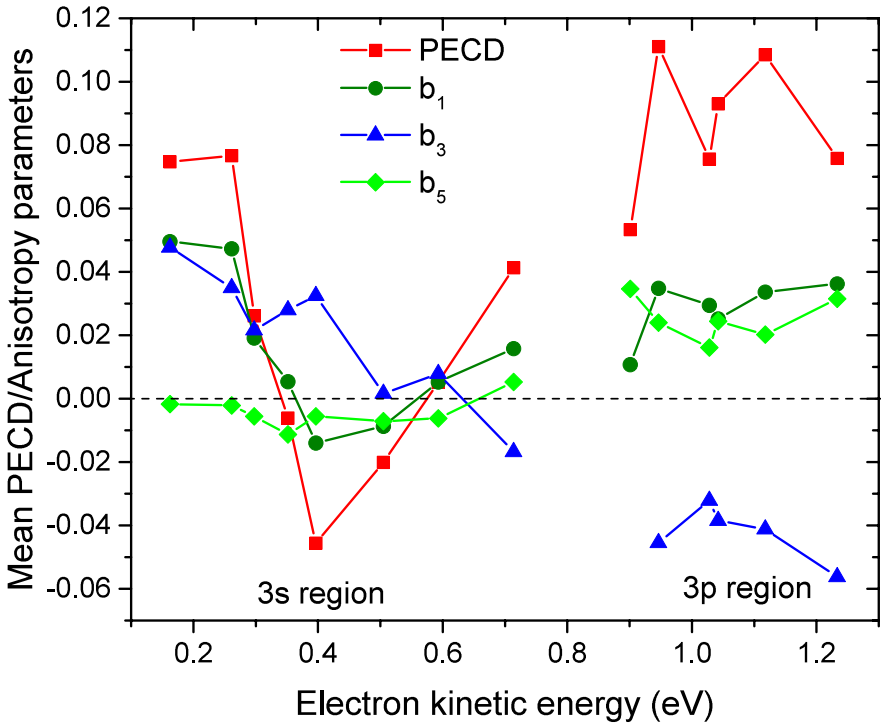

Figure 5.9. Mean PECD value (red) and anisotropy parameters b_1 (green), b_3 (blue), b_5 (light blue) is shown for ionization via 3s and 3p is plotted against the electron kinetic energy for α-pinene.

5.7 Results and discussion: 3-carene

In this section, we present PECD measurements taken at several wavelengths following (2+1) REMPI of 3-carene. In section 5.8 we show PECD results for (2+1) ionization via 3*s* and 3*p* Rydberg states at a particular wavelength. The difference in PECD signal is significant for the two different electronic states, and a comparison of anisotropy parameters are presented. In section 5.9, a complete PECD data set for a wavelength range 350-450 nm (5.51-7.08 eV) is presented, showing the complete variation of PECD signal when ionized via these different electronic states. Further, a discussion about decoupling the effect of electron kinetic energy, vibrational structure and accessed intermediate electronic state on PECD is presented.

5.8 Ionization via 3*s* and 3*p* states

As discussed in Chapter 4 (Section 4.6.2) the 3*s* threshold lies at around 5.6 eV excitation energy and the threshold photoelectron peak is at 8.4 eV (Chapter 4 section 4.7.2). Figure 5.10 shows the photoelectron spectra and PECD measurements

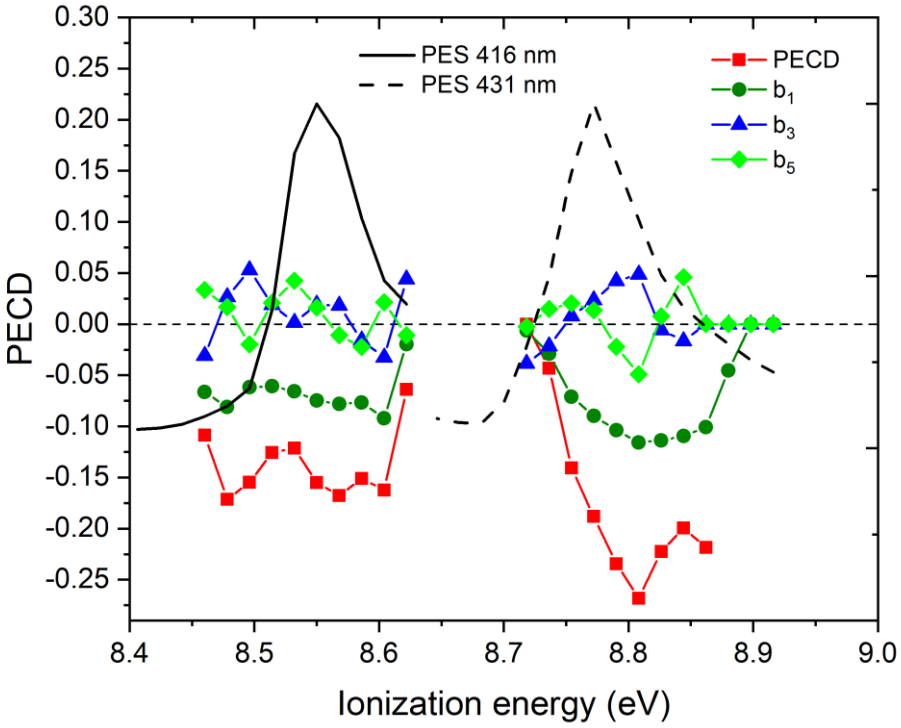

Figure 5.10. VMI PES, PECD and anisotropy parameters measurements for 1S-(+)- 3-carene for ionization via the 3s region at wavelengths of 431 and 416 nm. The VMI-PES has arbitrarily scaled intensity but is plotted on the same ionization energy axis as the PECD measurements.

following (2+1) REMPI via the 3*s* Rydberg state at two wavelengths, slightly above the threshold. A total three-photon energy at 431 and 416 nm only allows access to the 3*s* vibrational states. The photoelectron spectrum at these two wavelengths shows a clear $\Delta v = 0$ peak, governed by propensity rule. Unlike α-pinene, 3-carene does not show weak FC allowed $v' = 0$ and 1 peaks in photoelectron spectrum along with main $\Delta v = 0$. The PECD value shows a significant difference for the two measurements. The PECD corresponding to $\Delta v = 0$ peak at 431 nm is 10% which increases to 25% for $\Delta v = 0$ at 416 nm, and both show a negative value. This increase in the absolute magnitude of PECD for the ionization via higher vibrational states in 3*s* (415 nm), could either be an electron kinetic energy effect or a vibronic effect (more details next section). The PECD measurements in the 3*s* region for α-pinene and 3-carene show different trends. The former showed smaller PECD values than the latter. Both molecules are isomers; hence this difference in PECD value could shed some light on its dependency on molecular structure. Figure 5.10 also shows the breakdown of PECD into anisotropy parameters, b_1, b_3, b_5 for the two measurements in 3*s* region. Contribution from b_3 and b_5 is almost negligible for the near-threshold measurement (432 nm) and at 416 nm they have a small contribution of ~0.05. The major contribution is only from parameter b_1 which show an average value of ~0.10 at both wavelengths, which is different from α-pinene where all three parameters were very small (< 0.05) for ionization via the 3*s* Rydberg state.

Figure 5.11 shows the (2+1) REMPI-PECD measurement for ionization via 3*s* and 3*p* Rydberg state. The 0-0 transition of the 3*p* intermediate state is obtained, 6.4 eV (2ϕ) (Chapter 4 figure 4.12). Figure 5.11 shows a measurement taken just above the 3*p* origin threshold. A wider range photoelectron spectrum, with associated PECD, measured at 378 nm (2ϕ = 6.58, 0.28 eV above the 3*p* threshold) can be seen. At this wavelength ionization can occur through low vibrational levels in 3*p* as well as through high vibrational levels in 3*s*. The 3*s* peaks may result from internal conversion from 3*p* to 3*s* states as FC calculation shows that the probability of ionization via 3*s* is reduced after 9.0 eV ionization energy. Consequently, in the photoelectron spectrum

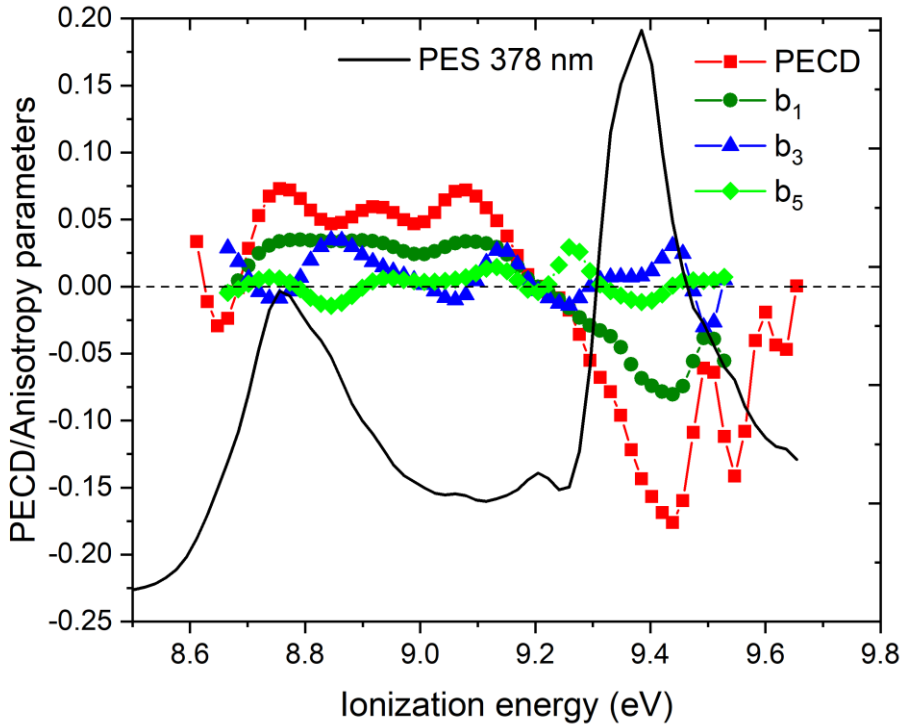

Figure 5.11. VMI PES (black), PECD, and anisotropy parameters measurements for 1S-(+)-3-carene for ionization via the 3p region at 378 nm. The VMI-PES has arbitrarily scaled intensity but is plotted on the same ionization energy axis as the PECD measurements.

at this wavelength, we can observe two $\Delta v = 0$ peaks, from 3*s* as well as 3*p*. Interestingly the PECD measurements for ionization process via the 3*p* Rydberg state shows a significant difference in comparison to ionization via 3*s*. The PECD value changes sign for ionization via these two Rydberg states, going positive 5% for 3*p* to negative 15% for 3*s* states (figure 5.11). This could be an electron kinetic energy effect. Figure 5.11 also shows the breakdown of PECD into anisotropy parameters, b_1, b_3, and b_5. The major contribution is from b_1 parameter, and b_3 and b_5 show almost zero value for both the peaks corresponding to ionization via 3*s* and 3*p*. Whereas for α-pinene we observed significant b_3 and b_5, this shows that photoionization dynamics for the molecules are significantly different.

So far, we have presented measurements at specific wavelengths in the 3*s* and 3*p* regions. In the next section, we present measurements complete PECD data in the range 350-450 nm (5.51-7.08 eV) following the ionization through these two Rydberg

states to facilitate the decoupling of the effects of electron kinetic energy and electronic and vibrational structure on the observed PECD.

5.9 Complete PECD data along the 3*s* and 3*p* ridges: vibrational and eKE effect

In this section complete data set of PECD values for ionization via the 3*s* and 3*p* states is presented. Figure 5.12 shows the intensity variation of photoelectron spectra for ionization via 3*s* and 3*p* region in comparison with FC calculations. The PES peaks match reasonably well the FC calculation; however, FC spectrum decays around 9.2 eV, whereas PES continues to show the vibrational modulation beyond 9.2 eV. As discussed in the previous sections, this could be a consequence of internal conversion from 3*p* to 3*s* state due to the short lifetime of 3*p* state.

The photoelectron intensity profile of both the ridges show clear vibrational features matching the FC calculations. These vibrationally resolved peaks have been assigned by Ganjitabar and co-workers [137]. The first peak is a combination of various transition from the neutral ground state to vibrationally excited 3*s* state. The second

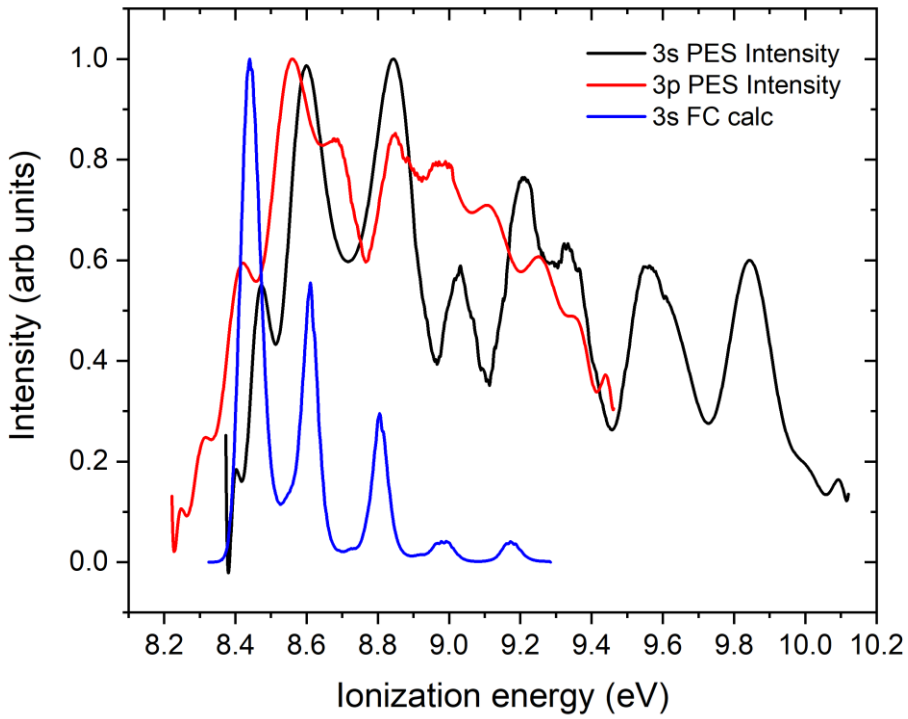

Figure 5.12. Intensity modulation of PES for ionization via 3s (black curve) and 3p (red curve) Rydberg states for 3-carene. The intensity modulations are shown in comparison with 3s FC calculation in the 3s region.

peak is a combination of one quanta excitation in mode v_{56} (C=C symmetric stretch) and the transitions in peak one. Third peak is a combination of one quanta excitation in mode v_{60} (symmetric stretch in the methyl group) and peak one transitions. The fourth and fifth peaks are a combination of one quanta excitation in mode v_{56} and v_{60} plus peak one transitions.

Figure 5.13 shows the PECD variation along these two ridges. The PECD values along two ridges are plotted as a function of ionization energy alongside the photoelectron spectrum. The PECD measurements via both states show modulation with the principal vibrational features and the preferred emission direction of photoelectrons is opposite for the 3*s* and 3*p* states (i.e. sign inversion of PECD was observed for ionization via 3*s* and 3*p*). However, the maximum absolute magnitude of the PECD via the 3*p* state is (10%) considerably smaller than that via the 3*s* state (-30%).

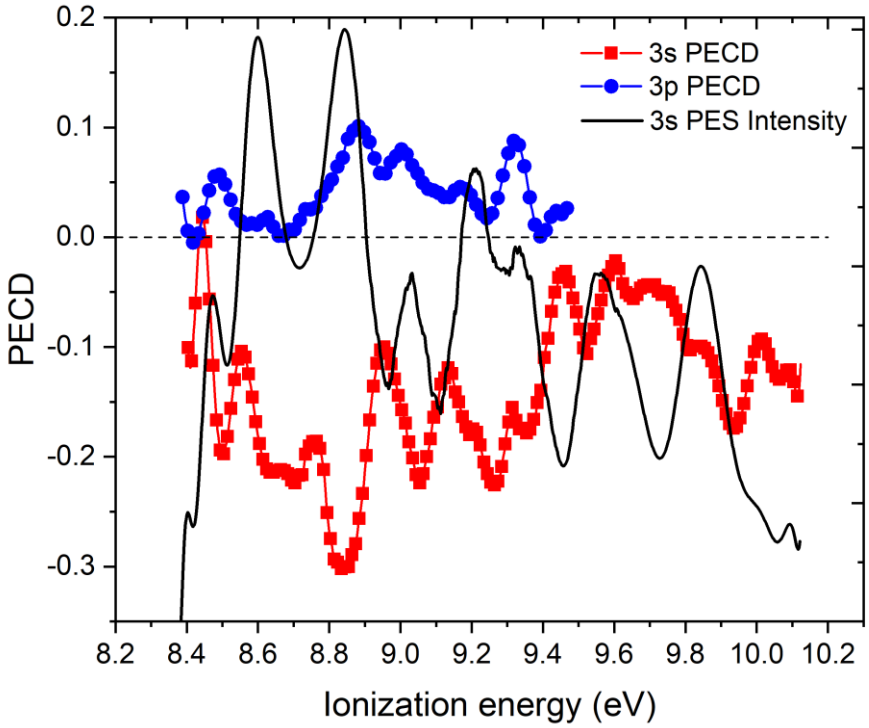

Figure 5.13. Complete PECD data for ionization via the 3s (red curve) and 3p (blue curve) states are shown along with the PES intensity along 3s ridge (black curve) for 3-carene. The PES and the PECD are plotted on the same ionization energy axis.

A few striking features were observed for the PECD measured following ionization through the 3*s* region; first, as mentioned above, it shows a clear modulation with the principal vibrational peaks. Second is the change in the sign of PECD value for

ionization via the 3*s* and 3*p* Rydberg states. Third, the absolute maximum PECD value for ionization through these two states is observed for the third peak, which is the one quanta excitation in the v_{60} mode (symmetric stretch in the methyl group). This shows clear vibrational influence on the PECD value, whereas the change in sign of the PECD value can be an electron kinetic energy effect (as discussed next). Toward the end in the 3*s* region, for higher vibrational states, significant PECD values are observed. However, the peaks beyond the Franck-Condon allowed window (9.2-10.0 eV), which are believed to result from internal conversion from 3*p* to 3*s*, also show significant PECD values. The peak at 9.3 eV shows the value of -22% (see figure 5.13, 3*s* PECD curve) and the peak at 9.9 eV shows the PECD value of -10%. These observations clearly show a strong indication that the intermediate electronic and vibrational state has an influence on PECD. To get a detailed insight, more computational work is required. The PECD value for ionization via the 3*p* state show significantly smaller value (10%) than the 3*s* state. The same vibrational peak for the 3*s* and 3*p* states shows drastically different value, for example, the peak at an ionization energy 8.6 eV, shows a -20% PECD for ionization via the 3*s* state and zero for ionization via the 3*p* state. These observations show indication of eKE or intermediate electronic state influence on the PECD value.

To study any trend or effect of electron kinetic energy, we have to plot the measured PECD value as a function of electron kinetic energy. In figure 5.14 we have plotted the mean PECD value (figure 5.14a) together with the individual anisotropy parameters (figure 5.14b), as a function of electron kinetic energy for the two ridges (ionization via the 3*s* and 3*p* states). The full width at half maximum (FWHM) was used to calculate the mean value of the PECD for a given photoelectron peak. The FWHM was calculated by fitting a Gaussian to PES spectrum in both the regions. The width of each Gaussian was used as an averaging window for the anisotropy parameter and the PECD. In figure 5.14a, the change of PECD value in the 3*s* region is significant over the 0 - 0.8 eV range, going to an absolute maximum of ~ -25% at 0.3 eV (which was mode v_{60} peak) and then falling to almost zero at 0.8 eV. For the 3*p* region the PECD value changes sign and reaches an absolute magnitude of 10%. Interestingly the data point beyond 0.4 eV are from peaks which are assigned to internal conversion from 3*p* to 3*s*. Surprisingly this tail end of the 3*s* region seems to follow the PECD value from the 3*p* region. This is a unique behaviour which we also observed for α-

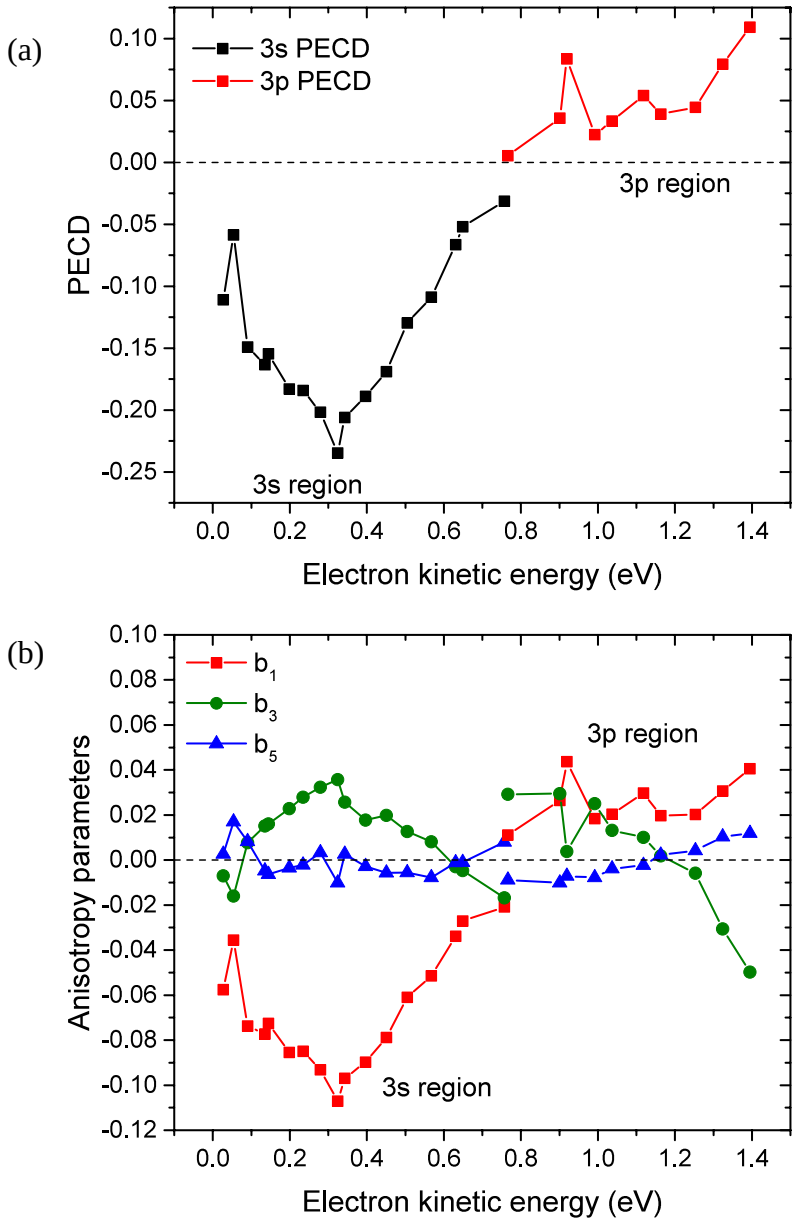

Figure 5.14. (a) Mean PECD value for ionization via 3s and 3p region for 3-carene is plotted against the electron kinetic energy. (b) Mean anisotropy parameters are shown a function of electron kinetic energy for both the regions.

pinene. This reason behind not very clear yet but it does hint towards an electron kinetic energy effect. Figure 5.14b shows the anisotropy parameters for the two regions. In both regions, PECD is mainly comprised of b_1 parameter. For 3*s* region b_3 shows an average value of 0.02 and for 3*p* region b_3 changes sign, going from 0.03 to -0.05 towards the end. For both the regions b_5 is almost zero.

5.10 Intermediate state effect: comparison with VUV measurements

In this section we will compare VUV one-photon ionization and multiphoton ionization PECD result for similar total photon energy and for a similar vibrational feature. This will narrow down any change in observed PECD between the two regimes to an influence of an intermediate state effect. Ganjitabar and co-workers have shown the PECD for one-photon ionization [128]. For the 3-carene measurements, they showed that PECD was strongly modulated with the principal vibrational peaks in the PES and does not change greatly over a limited range of photon energy (9-9.5 eV). They observed an absolute magnitude of the recorded PECD of -17% for origin peak (8.4 eV) and almost zero PECD for highly vibrationally excited states (at 9 eV). For multiphoton ionization, we observed a different trend for PECD value. Figure 5.15 shows the comparison of one-photon and (2+1) ionization processes (9.2 eV total photon energy) and their recorded PECD. The PECD results for multiphoton ionization process show a complete opposite trend than one-photon ionization. An almost zero

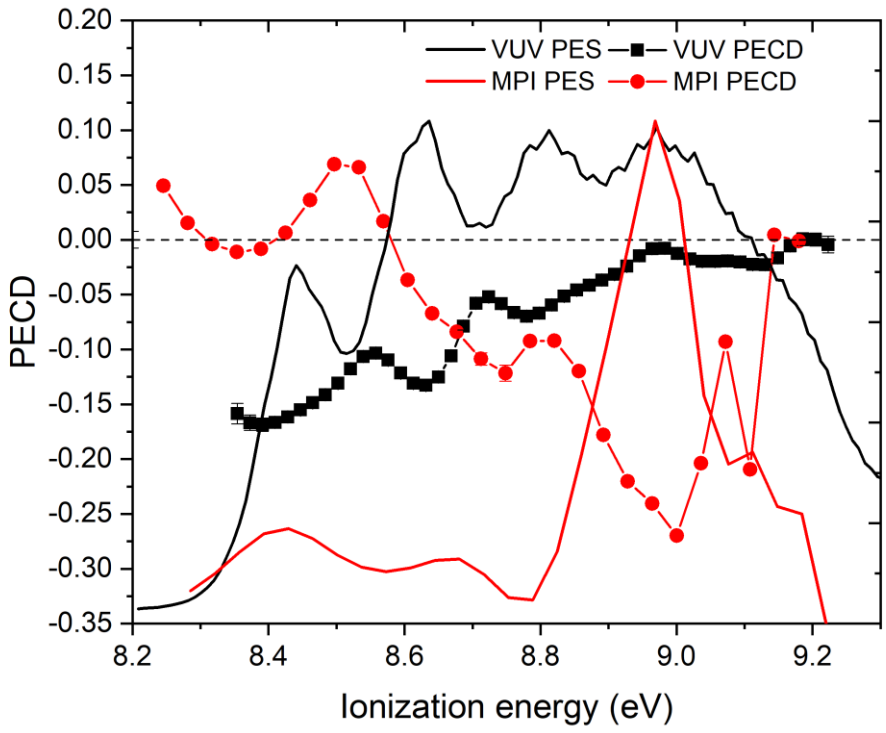

Figure 5.15. Intermediate state effect: VUV VMI PES and PECD is shown in comparison with (2+1) REMPI PES and PECD for 3-carene. For total photon energy for both cases is 9.2 and 9.3 eV respectively. VMI-PES has arbitrary intensity but plotted on the same ionization energy as PECD.

PECD value was observed for the origin peak for multiphoton ionization and a higher value (-25%) for highly excited vibrational peaks at 9 eV. Both the measurements have similar electron kinetic energy and show similar vibrational peaks, leaving the only difference being photon number and intermediate state. Thus, the change in the PECD signal for multiphoton ionization process could be a consequence of intermediate state effects.

5.11 Conclusion

In this chapter we investigated the (2+1) REMPI-PECD for α-pinene and 3-carene via 3*sp* Rydberg states. PECD was measured by recording photoelectron images in the range of 370-450 nm by changing CPL from left to right on one enantiomer. Both molecules showed striking results, PECD was found to be sensitive to the vibrational features as well as electron kinetic energy.

The α-pinene results shed some light on the effect of initial and final states on PECD. The complete PECD data along the two ridges corresponding to 3*s* and 3*p* ionization showed the vibrational dependency of PECD, where PECD values reduced from 30% to almost zero. Electron kinetic energy effects were observed for $v' = 0$ and 1 peaks (for 3*s* state) over the range of 1 eV. The 3-carene results were also found to be sensitive to intermediate electronic and vibrational states. The absolute maximum PECD was observed for the same vibrational state for ionization via the 3*s* and 3*p* states, hinting towards a vibrational dependency. PECD value also changed sign for ionization via the two states showing an electron kinetic energy effect. Furthermore, the unique behaviour of PECD in the 3*s* region for non-FC allowed peaks shows some interesting dynamics. The 3-carene results also shed some light on intermediate state effect upon comparison with VUV one-photon ionization PECD result. The two ionization regimes showed completely opposite behaviour (figure 5.15). To fully understand these results more theoretical work is required.

Chapter 6 Photoelectron angular distribution of aligned aniline and naphthalene

6.1 Introduction

Photoelectron angular distributions (PADs) are uniquely sensitive to electronic structure and dynamics, to nuclear configuration and dynamics, and to the chirality and conformation of isolated complex systems such as biomolecules and supramolecular assemblies [14]. PADs can be measured in a variety of experimental scenarios, and these scenarios dictate the information that can be gleaned. Of particular interest have been techniques that enable PADs to be measured "from the point of view of a molecule"; so-called *molecular frame* (MF) PADs [20, 37, 38, 141]. Although complete descriptions of photoionization dynamics have been achieved for light molecular systems without the need to access MFPADs [2], only MFPADs can provide rich information on the photoionization dynamics of heavier and more complex molecular systems.

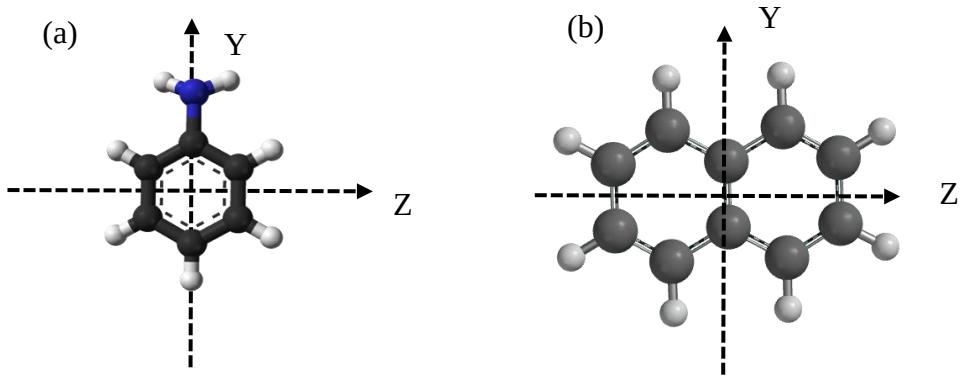

Figure 6.1. Structure of (a) aniline and (b) naphthalene. Most polarizable axis in aniline is Y and in naphthalene is Z axis.

There are two main techniques that have been used to access MFPADs. The first of these relies on a dissociative ionization process in which the emitted photoelectron is detected in coincidence with one or more ionic fragment [20, 37, 38, 141]. This technique, although powerful, is limited to small molecular systems that dissociate in the axial recoil limit. The second technique uses a strong laser field to create an aligned distribution of molecules prior to ionization [142]. In this case the measured PADs will converge on the molecular frame if complete alignment can be achieved in three

dimensions, and the technique can, in principle, be applied to large molecular systems. Laser-induced alignment falls into two main regimes, nonadiabatic and adiabatic (See Chapter 1). In a nonadiabatic regime, alignment is induced by fs and ps pulses, which are short in comparison to the rotational period of the molecule. The rotational wave packets created hereby lead to molecular alignment in regularly spaced, narrow time windows termed revivals. A major advantage of the revivals is that they occur after the laser pulse is turned off, such that the influence of the aligning field on aligned molecules is eliminated. For this study a rapid truncated ps pulse is used to create the alignment in the molecular system.

For this work aniline and naphthalene were used to measure aligned PADs. Aniline is the simplest aromatic amine with an amino group attached to a phenyl group. The symmetric representations for aniline are assumed under an approximate C_{2v} symmetric point group [143], see figure 6.1. Aniline has been extensively studied spectroscopically [24, 98, 143–145] and a number of vibrational frequencies in the first excited state (S_1) have been determined. The transitional dipole moment for $S_1 \leftarrow S_0$ is perpendicular to the most polarizable axis (figure 6.1). Naphthalene is also an aromatic molecule with D_{2h} symmetry. Naphthalene has also been studied spectroscopically by many groups [146–150]. The transition dipole moment for $S_1 \leftarrow S_0$ is parallel to the most polarizable axis (figure 6.1). Naphthalene has slightly higher polarizability than aniline, therefore, would show slightly better molecular alignment.

In this work we employ intense 800 nm laser pulses to create aligned distributions of aniline and naphthalene molecules. The molecules are subsequently ionized using a resonant two-photon ionization scheme, with photoelectrons collected using VMI. The resulting PADs have been compared with the results of calculations that have been conducted using the ePolyScat code developed by Lucchese and co-workers [151, 152] in order to provide insight into the S_1 excited state photoionization dynamics of both molecules, and into the degree of alignment created. This work has been submitted for publication and much of the text is taken from the manuscript [92].

6.2 Experimental section

This experiment was performed in Prof Henrik Stapelfeldt's lab at Aarhus University. The setup used has been described in detail previously in Chapter 2. Briefly, the details used in this work are described in what follows. A molecular beam of aniline

(naphthalene) was produced from a seeded mixture in 80 bars of He and expanded into the vacuum system using a pulsed Even-Lavie valve, which was heated to 36°C. The molecular beam passed through a 4 mm skimmer prior to entering the interaction region of the velocity map imaging spectrometer [25]. Aniline was ionized using a (1+1) scheme via the vibrational origin of the S_1 state (34032.1 cm^{-1}) [153]. The resulting photoelectrons, which had a maximum possible kinetic energy of ~0.72 eV, were then accelerated in a static field towards a 40 mm dual MCP detector and the photoelectron image was recorded with a camera (Prosilica GE 680, Allied Vision) controlled using LabView 2017.

A scheme of the laser setup is shown in Chapter 2 figure 2.6a. Both the pump/probe and alignment beams were generated by the output of a 1 kHz, Ti:Sapphire laser system (Solstice, Spectra Physics). The system has two 800 nm output beams, with typical powers of 3 mJ/pulse with a 45 fs pulse duration. The output used to generate the alignment pulse was not compressed prior to exiting the laser system and had an initial pulse duration of 300 ps (instead of the typical 45 fs). The probe pulse of 293.85 nm was generated by frequency doubling a 587.7 nm beam in a 40 mm long KDP crystal. The 587.7 nm beam was generated by collinear mixing of the 2214.6 nm output of an optical parametric amplifier (TOPAS) with an 800 nm beam in a 0.5 mm BBO crystal, cut at 22.4°. By using the long KDP crystal, the UV light is generated with a reduced bandwidth (0.6 nm @ 293.85 nm), supporting a 6 ps pulse duration with a peak intensity of 0.042 TW/cm^2 in the interaction region of the chamber. The probe pulse was linearly polarised, parallel to the detector plane as shown in Chapter 2 figure 2.6b.

The intensity of the alignment laser is controlled by varying its polarization with a half wave plate (HWP) followed by a thin film polarizer (TFP) (Chapter 2 figure 2.6a). This was followed by a telescope to ensure that the spot size of the alignment beam is larger than the spot size of the probe beam, so that preferentially only aligned molecules are probed. The alignment beam is truncated with a bandpass filter, reducing the pulse duration to 150 ps at FWHM. The relative timing of the probe and the alignment pulse was 20 ps. Finally, the beam passes through a second HWP and quarter-wave plate (QWP) to obtain the desired polarization for the measurement. In this study, we only consider only results obtained using linearly polarised light, parallel to the plane of the detector, which is collinearly overlapped with the probe beam prior

to entering the spectrometer through a 30 cm focusing lens. The intension behind using the truncated pulse alignment was to get field free alignment, which did not prove to be fully successful as discussed in Section 6.6.

6.3 Theory

The various axes and angles that are referred to throughout this section and in the rest of this chapter are defined in figure 6.2. Molecular frame photoelectron angular distributions were generated using radial dipole matrix elements calculated by performing quantum scattering calculations using the ePolyScat package [151, 152]. These ePolyScat calculations were performed by Paul Hockett and a detailed discussion is presented in the manuscript [92]. The MFPAD depends on the photoelectron kinetic energy, E, and on $(\theta_{\hat{n}}, \phi_{\hat{n}})$, i.e. the angle between the polarization of the probe pulse and the MPA. Furthermore, because of the 3D structure of the molecules the MFPAD will not be cylindrically symmetric. Therefore, the MFPAD can be expressed as [27]:

$$I^{MF}(\theta_{\hat{k}}, \phi_{\hat{k}}; E, \theta_{\hat{n}}, \phi_{\hat{n}}) \propto \sum_{L=0}^{2n} \sum_{M=-L}^{L} \beta_{LM} Y_{LM}(\theta_{\hat{k}}, \phi_{\hat{k}}) \quad (6.1)$$

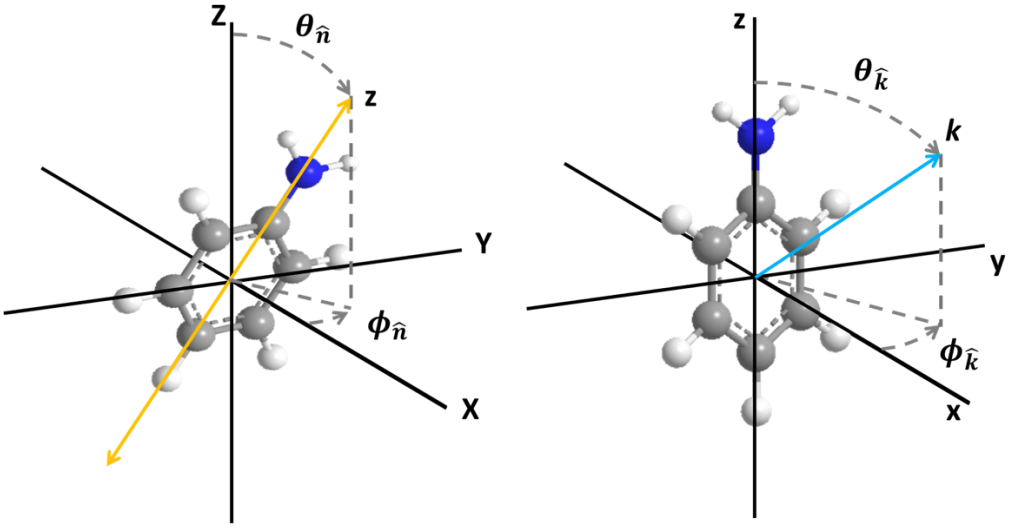

Figure 6.2. Relationship between the laboratory frame (X, Y, Z) and molecular frame (x, y, z) axis systems and the emission direction of the photoelectron for aniline. The most polarizable molecular axis (MPA) is shown in yellow in the left-hand panel and defined as z. The direction of photoelectron ejection is shown in blue and defined as k. $(\theta_{\hat{n}}, \phi_{\hat{n}})$ defines the orientation of the MPA with respect to the laboratory frame. The photoelectron emission direction is given by $(\theta_{\hat{k}}, \phi_{\hat{k}})$ in the molecular frame and by (θ_{LF}, ϕ_{LF}) in the laboratory frame.

where n is the summation index represented in term of the highest orbital angular momentum component of the incoming wave. In the molecular frame $n = l_{max}$, the highest photoelectron orbital angular momentum component.

The ePolyScat calculations also provide values of β, the coefficient of $P_2(\cos\theta)$ in the photoelectron angular distribution that arises following ionization of an isotropic distribution of MPAs. In the case of aniline, the trend in these values, as a function of photoelectron kinetic energy, can be compared with the trend in the values of the equivalent coefficient that have been determined in (1+1) two-photon ionization experiments by Qu et al. [98]. Although the experimental values will be influenced by the small anisotropy introduced in the two-photon ionization process, this comparison enables us to verify that the calculated energies are in good agreement with the experimental energies.

Two separate processes were used to generate the simulated photoelectron images, one for ionization of a "completely aligned" sample ($\langle\cos^2\theta_{\hat{n}}\rangle = 1$ or $\langle\cos^2\theta_{\hat{n}}\rangle = 0$ corresponding to parallel and perpendicular alignment respectively) and one for ionization of an isotropic sample ($\langle\cos^2\theta_{\hat{n}}\rangle = 1/3$). For the completely aligned sample, a full 3D velocity distribution for a single component of the ionisation continuum (a_u/b_{1u} for naphthalene; a_2/b_1 for aniline) was created in the molecular frame using the radial dipole matrix elements at the chosen photoelectron kinetic energy. The molecular frame PAD was then rotated so that the most polarisable axis was aligned vertically (a_u/a_2) or horizontally (b_{1u}/b_1) and then azimuthally averaged. The resulting 3D distribution was then projected onto a 2D plane to create simulated photoelectron images. For the isotropic sample a 3D laboratory frame PAD was created using the β parameter calculated by ePolyScat at the chosen photoelectron kinetic energy and then projected onto a 2D plane to create simulated photoelectron images.

6.4 Results and discussion: Aniline

Qu et al. [98], presented the work on two photon REMPI spectrum for aniline (figure 6.2) and established the number of vibrational states in the first excited state of neutral (S_1). In the present work we measured the aligned PADs through (1+1) REMPI via origin of the S_1 state. Photoelectron images were collected following the excitation of aniline to its S_1 origin at ~293.8 nm and ionization following the absorption of a second photon from the same laser beam. The raw electron image obtained with the 293.85 nm probe pulse only, corresponding to a target of randomly oriented molecules, is shown in figure 6.4a, and the Abel inverted image in figure 6.4b. At least three rings are observed corresponding to three different channels of ionization. The angular

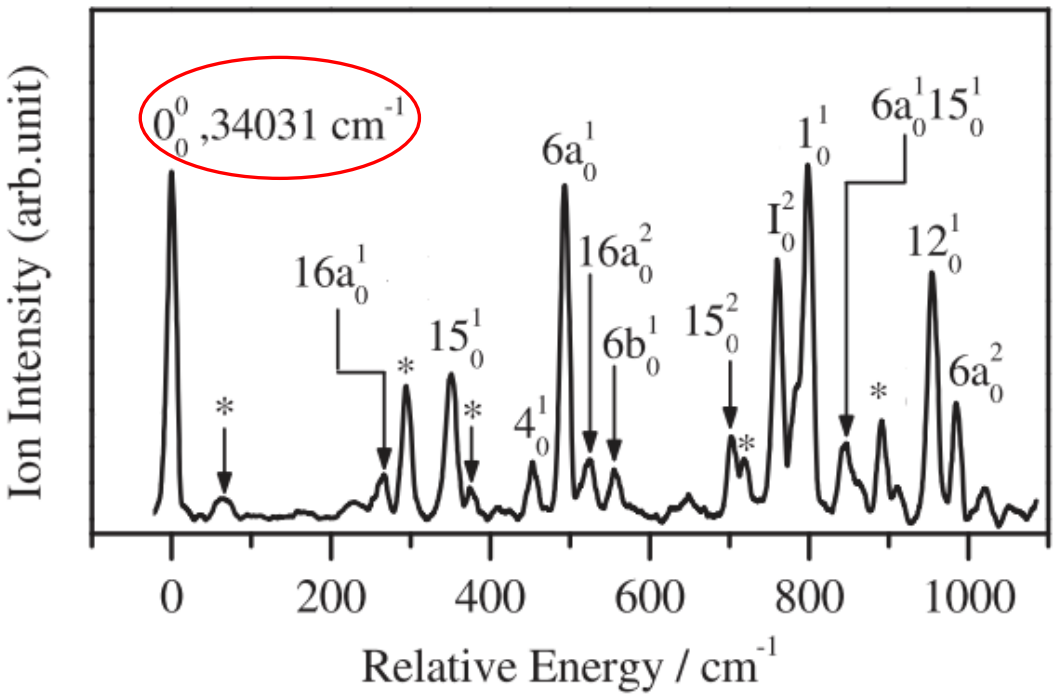

Figure 6.3. Two-photon REMPI spectrum of aniline. The highlighted (red circle) is the vibrational mode studied in this study [98].

distributions of the three rings are essentially isotropic. The maximum available photoelectron kinetic energy following the absorption of two photons is ~0.72 eV and therefore the strongest peak corresponds to the formation of the cation in its ground vibrational state. Qu et al. measured a relatively high-resolution photoelectron spectrum following the ionization of S_1 aniline [98] with which this spectrum can be compared. This work mainly focusses on these electrons. The middle and outer peaks correspond to the aniline cation being vibrationally excited.

Figure 6.4c shows the photoelectron spectrum for ionization via aniline origin along with the anisotropy parameter b_{20} and b_{40}. The b_{40} parameter show almost zero value for the whole spectrum and b_{20} parameter is almost zero except at origin peak where is show a small value. This shows that the rings are almost isotropic for probe only

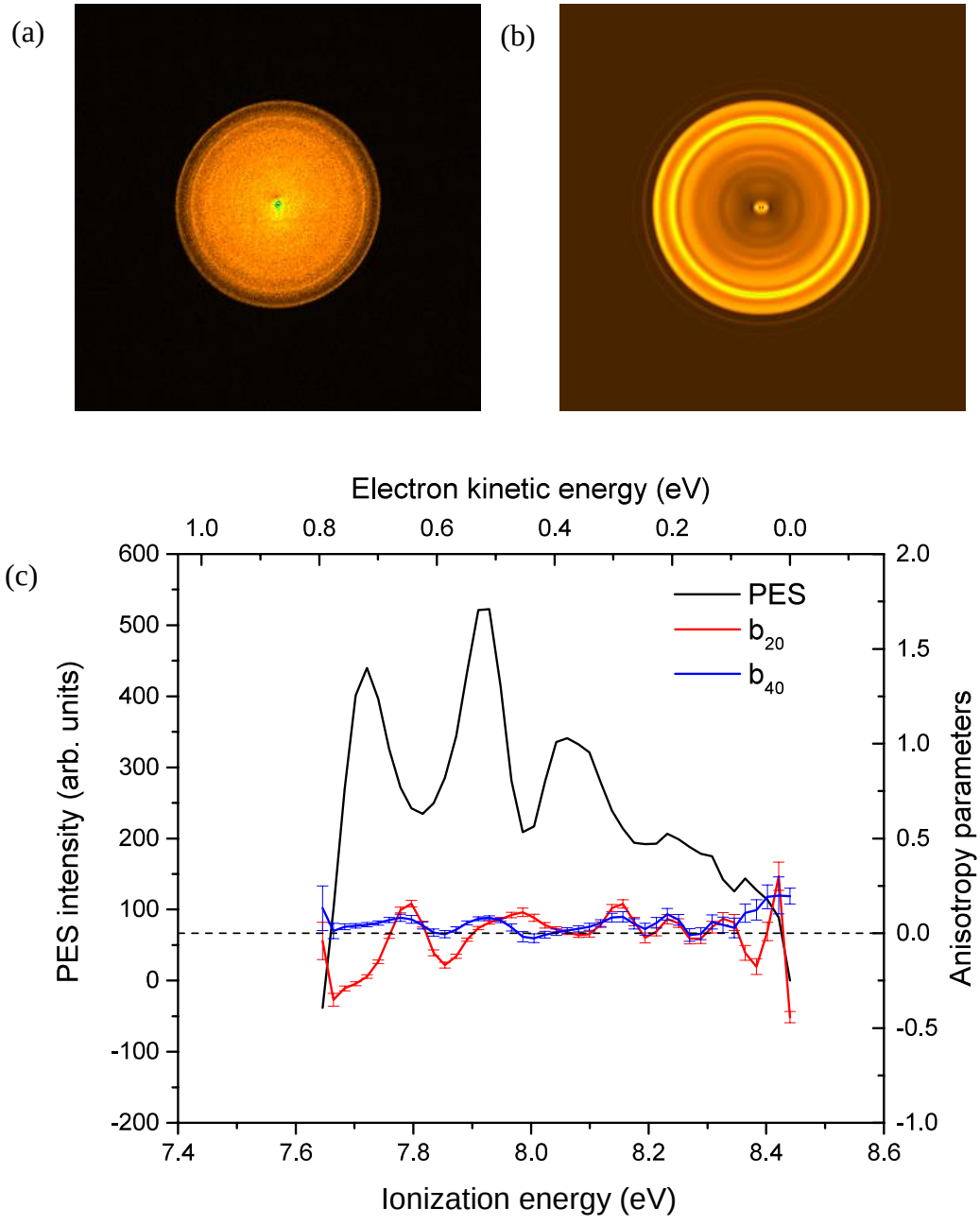

Figure 6.4. Photoelectron electron image and analysis. (a) Raw image of aniline measured at origin of S_1. (a) Corresponding Abel inverted image. Second panel (c) shows the analysis; photoelectron spectrum is shown along with the anisotropy parameters.

measurement (in the absence of an alignment beam). In the next section we will present the results with an alignment pulse present prior to the ionization for various configuration of probe and alignment beams.

6.5 Alignment measurements

Photoelectron images were measured with alignment pulse present prior to the (1+1) REMPI. Figure 6.5 shows the raw images for the measurements for probe only and with alignment pulse present. A distribution of randomly oriented aniline molecules [figure 6.5a(i)] was excited to the S_1 origin using light at ~293.85 nm that is linearly polarized along the Z and ionized following the absorption of a second photon from the same laser beam. The resulting raw photoelectron image is shown in figure 6.5a(ii). The image shows three prominent rings, labelled 1-3 in figure 5a(ii), with the photoelectron intensity approximately isotropic in all rings.

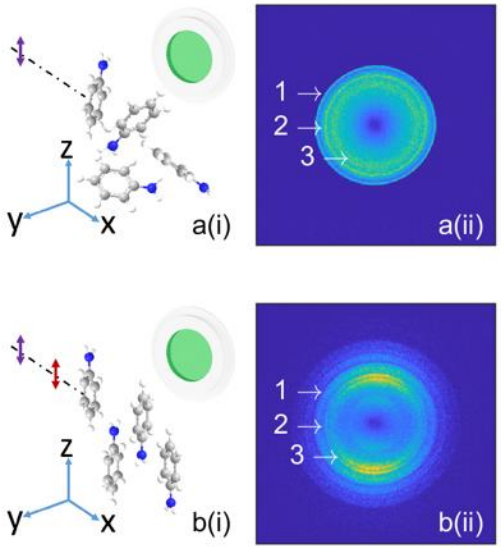

Figure 6.5. (a) No alignment pulse present, (i) spatial orientations of the aniline molecules that are ionized relative to the detector; (ii) raw photoelectron images produced when the 293.85 nm probe pulse ionizes the aniline molecules. (b) as for (a) but with the alignment pulse introduced. The peak intensity of the alignment pulse is 8.1 $\times 10^{11}$ W/cm².

Figure 6.5b shows the effect that introducing an alignment pulse, linearly polarized along Z, has on the observed photoelectron image. This pulse causes the molecules to align such that the distribution of MPAs is confined with respect to the polarization direction of the probe pulse, as indicated in figure 6.5b(i). The raw and Abel inverted images are shown in figure 6.5b(ii) and can be compared with the images in figure

6.5a(ii) which were obtained without the alignment pulse. Two prominent changes can be seen: first, the rings are now clearly anisotropic with an enhanced intensity along the z-axis, and secondly evidence of additional rings can be seen. This indicate that an 800 nm photo is getting absorbed in presence of the

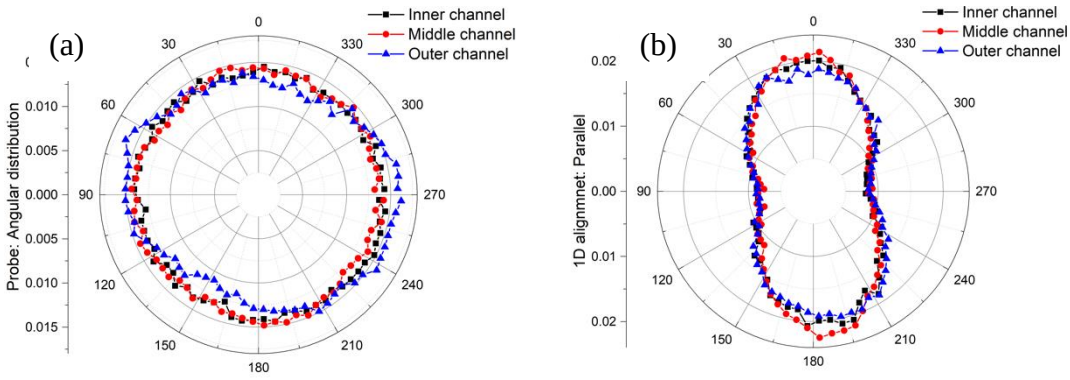

Figure 6.6. Angular distribution of Probe only (a) and 1D parallel aligned molecules (b) for all three channels for aniline.

probe photon ionizing through a channel of (1+1'+1) REMPI (more discussion next section). Figure 6.6 shows the angular distribution for two cases: probe pulse only and 1D parallel alignment case. All three channels clearly shown the change in PADs upon alignment.

Figure 6.7 we present the photoelectron spectrum from 1D alignment in comparison with the photoelectron spectrum of probe only measurements. Figure 6.7 also presents the anisotropy parameters for 1D alignment case. The 1D alignment PES shows the three main peaks (7.2, 7.7, and 8.0 eV) along with a fourth peak which was weakly present in the probe only measurement. Along with these main peaks we can also see three other peaks below the ionization energy (7.2 eV). This can be explained if some of the electronically excited aniline molecules absorb an 800 nm photon from the alignment pulse before absorbing the second UV photon in a (1+1'+1) ionization scenario. If this occurs, then aniline molecules that are ionized to create cations in the ground vibrational state would release photoelectrons with a kinetic energy of ~2.27 eV. As we will see, this process significantly affects the anisotropy observed in the

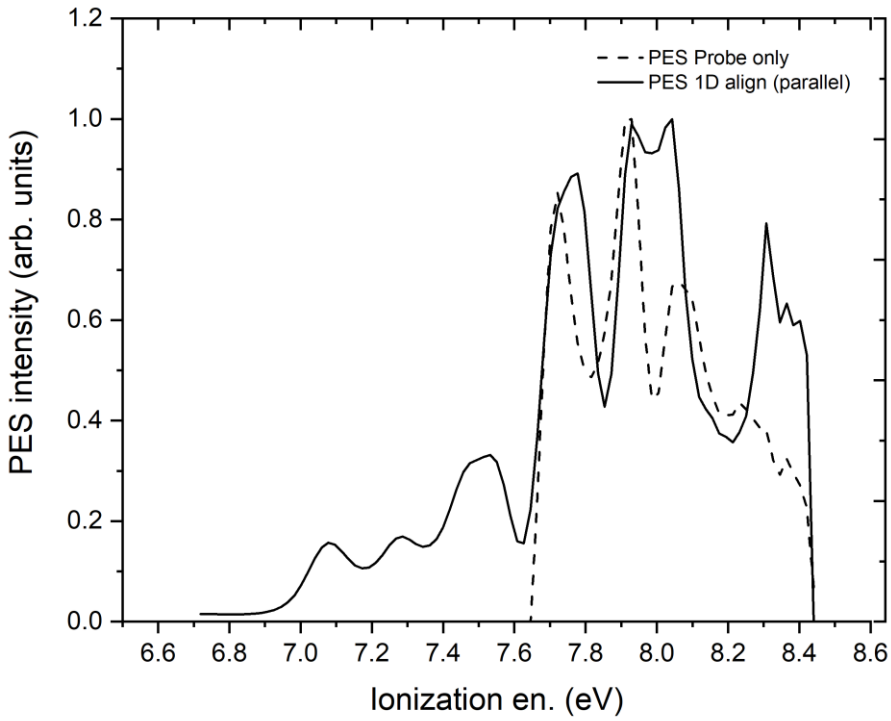

Figure 6.7. Photoelectron spectra of aniline for probe only and 1D aligned parallel case. The photoelectron spectrum for 1D alignment is shown in comparison with PES of probe only measurement.

photoelectron images. Figure 6.10 shows the anisotropy parameters (b_{20}, b_{40}, b_{60}, and b_{80} in the presence of alignment pulse) for the 1D alignment case. The b_{20} parameters shows an average value of ~0.5 across the photoelectron spectrum and b_{40}, b_{60}, and b_{80} remain close to zero. This shows the effect of alignments pulse on PADs, because of the presence of certain degree of alignment in the molecular system the PADs show some anisotropy.

In the next we section we will try to compare the measured PAD with simulated MFPADs for the origin peak.

6.6 Analysis for aniline

In order to gain insight into the measured photoelectron anisotropy for the aniline measurements, we have performed ePolyScat calculations of the photoionization dynamics from which we can calculate MFPADs. The MFPAD depends on the photoelectron kinetic energy, E, and on $(\theta_{\hat{n}}, \phi_{\hat{n}})$, i.e. the angle between the

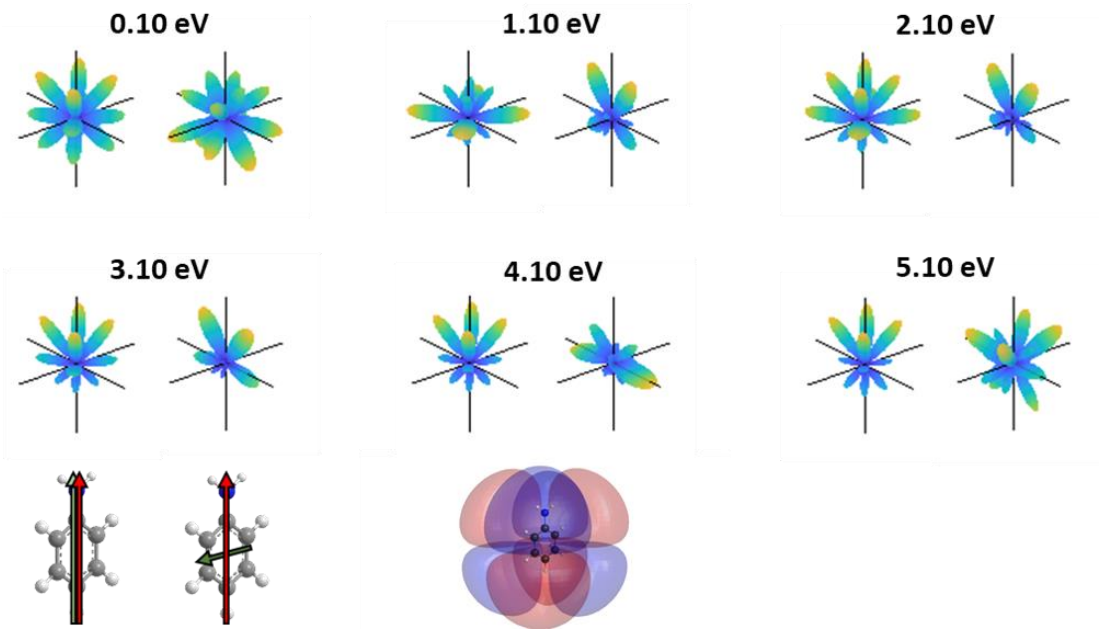

Figure 6.8. Iso-surfaces showing molecular frame PADs following the ionization of aniline at different photoelectron kinetic energies. The panel on the bottom left shows the orientation of the aniline molecule relative to the alignment field (red arrow) and the probe field (green). The green arrow defines the laboratory frame Z axis. The molecular orbital used to describe the initial electronic state of aniline is shown on the bottom right.

polarization of the probe pulse and the most polarizable axis. Furthermore, because of the 3D structure of the aniline molecule the MFPAD will not be cylindrically symmetric or have inversion symmetry.

In figure 6.8 we show examples of the resulting MFPADs at different kinetic energies of the photoelectron. For these calculations the polarization of the probe laser beam was parallel to the MPA, i.e. $\theta_{\hat{n}} = \phi_{\hat{n}} = 0$. The MFPADs change dramatically over the 0 – 3 eV range of kinetic energy because of a strong shape resonance in this region [98]. In order to establish whether our measured photoelectron images are consistent with the calculated MFPADs, we have projected them into the laboratory frame for a series of assumed degrees of alignment, characterized by $\langle \cos^2 \theta \rangle$.

The LFPAD results from an average over all the possible directions of the MPA in the laboratory frame, weighted by the anisotropy introduced by the experiment. In the absence of the alignment pulse a small degree of anisotropy is generated by the two-photon ionization process, but this is swamped by the effect of the alignment pulse which confines the distribution of MPAs along the laboratory frame Z-axis, according to the value of $\langle \cos^2 \theta_{\hat{n}} \rangle$. In order to establish whether our measured photoelectron images are consistent with the calculated MFPADs, we have projected them into the

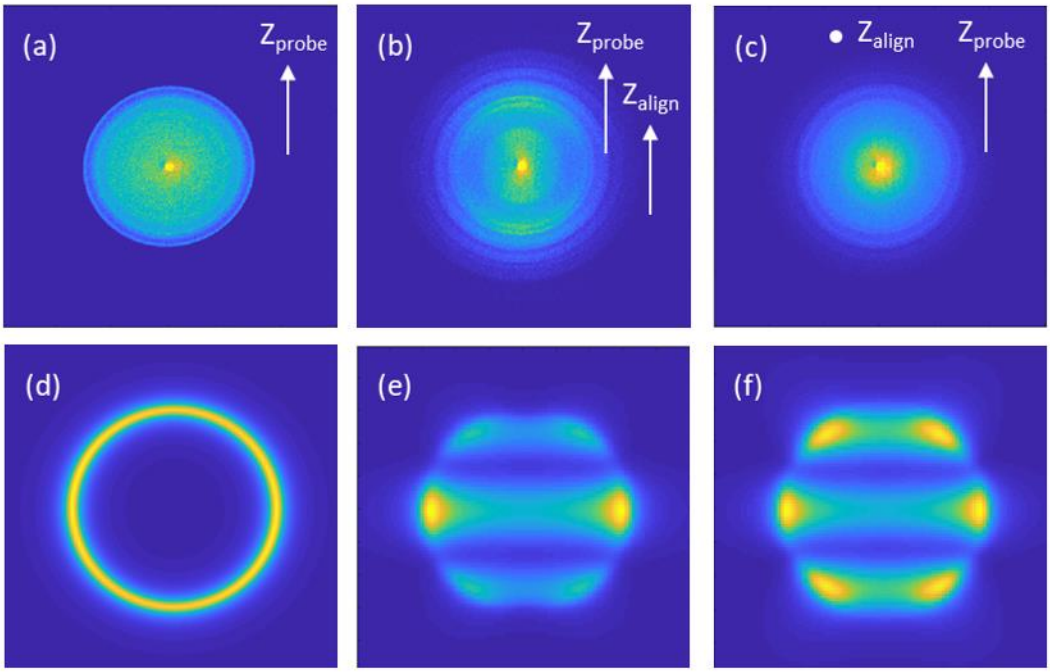

Figure 6.9. Comparison of experimental and simulated photoelectron images of aniline; in all cases the polarization vector of the ionizing beam, Z_{probe}, points vertically. Panels (a)-(c) show the raw experimental images for (a) probe only, (b) alignment and probe polarizations parallel (taken from Fig. 6.8b) and (c) alignment and probe polarizations perpendicular. Panels (d)-(f) show shows the simulated photoelectron images for 0.72 eV photoelectron kinetic energy for (d) an unaligned sample, (e) a sample with $\langle cos^2\,\theta_{\hat{n}}\rangle = 1$ (a_2 continuum) and (f) $\langle cos^2\,\theta_{\hat{n}}\rangle = 0$ (b_1 continuum). The radius of the ring in the simulated images is chosen arbitrarily.

laboratory frame for a series of assumed degrees of alignment, characterized by $\langle \cos^2\,\theta_{\hat{n}}\rangle$. This process introduces a "blurring" of the MFPAD, the details of whose lobes and nodes may be lost if the alignment is insufficiently good [35]. Although in principle it should be possible to perform this projection analytically, we have for the time being adopted the numerical procedure described Arlt et al. [92]. This gives rise to simulated laboratory frame PADs which can be compared with the experimental PADs.

The results of these simulations are shown in figure 6.9 and compared with the equivalent experimental image taken from figure 6.5b. We have also included in figure 6.9, the experimental and simulated photoelectron images that result when the polarization of the alignment beam is perpendicular to the polarization of the probe beam. In this figure we can see that the simulated images do not reproduce what is seen in the experiment. In order to investigate whether this is caused by the fact that

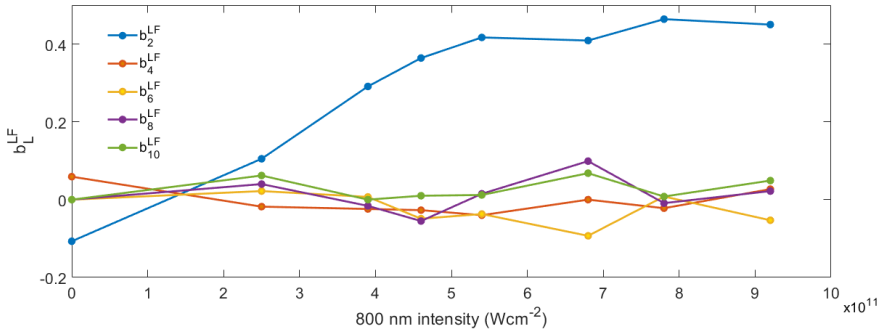

Figure 6.10. Normalized photoelectron anisotropy parameters, b_L^{LF}, in the presence of different alignment field intensities, determined from the inversion of the measured aniline photoelectron images. All b_L^{LF} values are assumed to contain an error of ±0.15.

aniline does not align well, a series of photoelectron images were recorded for a series of different intensities of the alignment pulse and in each case the angular distributions were fitted. The anisotropy parameters obtained from the fits are presented in figure 6.10. For the probe pulse only, the b_L^{LF} parameters are small with b_2^{LF} = –0.1 and b_4^{LF} = 0.06, consistent with the near circularly symmetric electron image. As the intensity of the alignment pulse is increased, the values of b_L^{LF} with $L > 2$ remain close to zero. Conversely, the value of b_2^{LF} increases steadily to a value of ~0.5, consistent with photoelectron intensity being concentrated along the direction of the polarization direction of the probe pulse. At higher alignment intensities, the value of b_2^{LF} continues to increase but at a much lower rate.

The change in the values of b_2^{LF} seen in figure 6.10 can be attributed to an increased degree of alignment, i.e. an increased value of $\langle \cos^2 \theta_{\hat{n}} \rangle$, as the intensity increases. The fact that the b_2^{LF} values are increasingly positive tells us that as the alignment improves the photoelectrons emission peaks increasingly along the polarization vector of the probe beam. In figure 6.9 we have seen that the simulation for completely aligned aniline molecules shows photoelectron emission peaking perpendicular to the polarization vector of the probe beam [92]. Therefore, we can see that even at a high degree of alignment we do not expect the experimental images to converge on the molecular frame. We attribute this discrepancy to the absorption of a 800 nm photon by aniline in its S_1 electronic state. The absorption of the 800 nm photon will lead to excitation of a higher-lying electronic (Rydberg) state and allow access to higher-lying vibrational states in the cation. The evidence for this process can be seen in figure 6.7 where the photoelectron spectrum is qualitatively different when the alignment pulse is introduced.

6.7 Naphthalene

Naphthalene was ionized in a (1+1) scheme through S_1 state using ~293.5 nm light linearly polarized along the Z direction (figure 6.11). The raw photoelectron image that is measured in the absence of the alignment pulse is shown in figure 6.11a(ii). Two prominent rings are observed in the image and the photoelectron emission direction is localized along the polarization of the probe pulse in both rings. The effect of introducing an alignment pulse that is linearly polarized along the Z-axis can be seen in figure 6.11b; this pulse is expected to induce 1D alignment, confining the long axis of the molecules along the z-axis as illustrated in figure 6.11b(i). In figure 6.11b(ii) it can be seen that, in the case of the outer ring, the intensity of the electron emission along the Z-axis decreases, and a four-lobed structure appears.

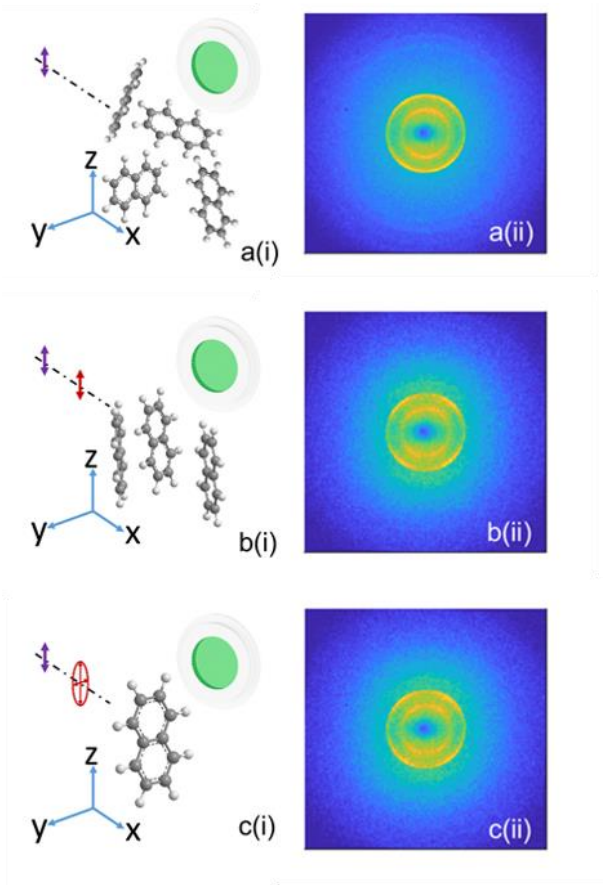

Figure 6.11. Photoelectron images from naphthalene. (a) No alignment pulse present, (i) spatial orientations of the naphthalene molecules that are ionized relative to the detector; (ii) raw photoelectron images produced when the 293.85 nm probe pulse ionizes the naphthalene molecules. (b) as for (a) but with the linearly polarized alignment pulse introduced. (c) as for (a) but with the elliptically polarized alignment pulse introduced, with an intensity ratio between the major and minor axis of 3:1. The peak intensity of the alignment pulse 5.8 × 10^{11} W/cm².

Measurements were also made with an elliptically polarized alignment beam to induce 3D alignment; in this case the major polarization axis was directed along the Z-axis and the minor polarization axis along the Y-axis with an ellipticity ratio of 3:1. The resulting alignment is illustrated schematically in figure 6.11c(i). The outermost ring in the image shows the same characteristic four-lobed structure, see figure 6.11c(ii), with the suppression of the electron emission along the Z-axis a little more pronounced than when the molecules are 1D aligned.

Because cylindrical symmetry has been preserved to measure the images shown in figures 6.11a and 6.11b the pBASEX software can be used to invert the images. However, when the naphthalene molecules are aligned in three dimensions (figure 6.11c) cylindrical symmetry is broken. Although alternative routines, such as FINA [154, 155], do exist to deal with this situation, in this work we have not determined a kinetic energy distribution or angular distribution for the image shown in figure 6.11c so this image will not be discussed in what follows.

The rings observed in the image appear as distinct peaks in the kinetic energy distribution, shown for randomly oriented molecules by the blue curve in figure 6.12. The peak corresponding to the outermost ring is labelled peak 1 in figure 6.12 and centered at 0.33 eV. This peak corresponds to the formation of the naphthalene cation in its vibrational ground state. Peak 2 corresponds to the next ring and is centered at

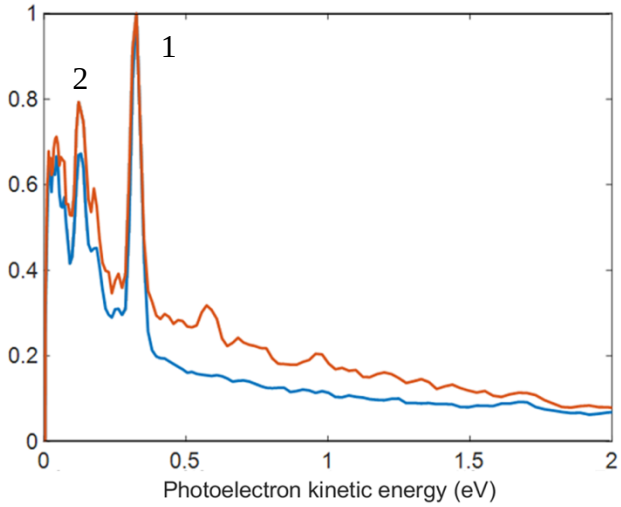

Figure 6.12. Kinetic energy distribution of the photoelectrons produced when the 293.5 nm probe pulse ionizes naphthalene molecules. The blue curve corresponds to randomly oriented molecules and is obtained from the image in Fig. 6.13a(ii). The red curve corresponds to 1D aligned molecules and is obtained from the image in Fig. 6.13b(ii).

0.12 eV; this peak corresponds to the formation of the vibrationally excited naphthalene cation. The kinetic energy distribution extends almost to 2 eV, even with no alignment pulse present. Such high energies indicate that the naphthalene molecule can absorb three photons from the probe pulse (I.P = 8.1 eV and two photon energy = 8.44). The kinetic energy distribution that results when the molecules are aligned in one dimension by the 800 nm pulse is shown by the red curve in figure 6.12. It can be seen that the alignment pulse only causes minor changes in the photoelectron spectrum.

In order to gain insight into the measured photoelectron anisotropy we have performed ePolyScat calculations of the photoionization dynamics in order to determine MFPADs, as described in Section 6.3. In figure 6.13 we show examples of the resulting MFPADs at different photoelectron kinetic energies and in two different geometries: $(\theta_{\hat{n}}, \phi_{\hat{n}}) = (0, 0)$ and $(\theta_{\hat{n}}, \phi_{\hat{n}}) = (\frac{\pi}{2}, \frac{\pi}{2})$. The dramatic change in the MFPADs over the 0 – 5 eV range of kinetic energy can be attributed to the presence of a shape resonance by analogy with experimental observations on other similar molecules [92].

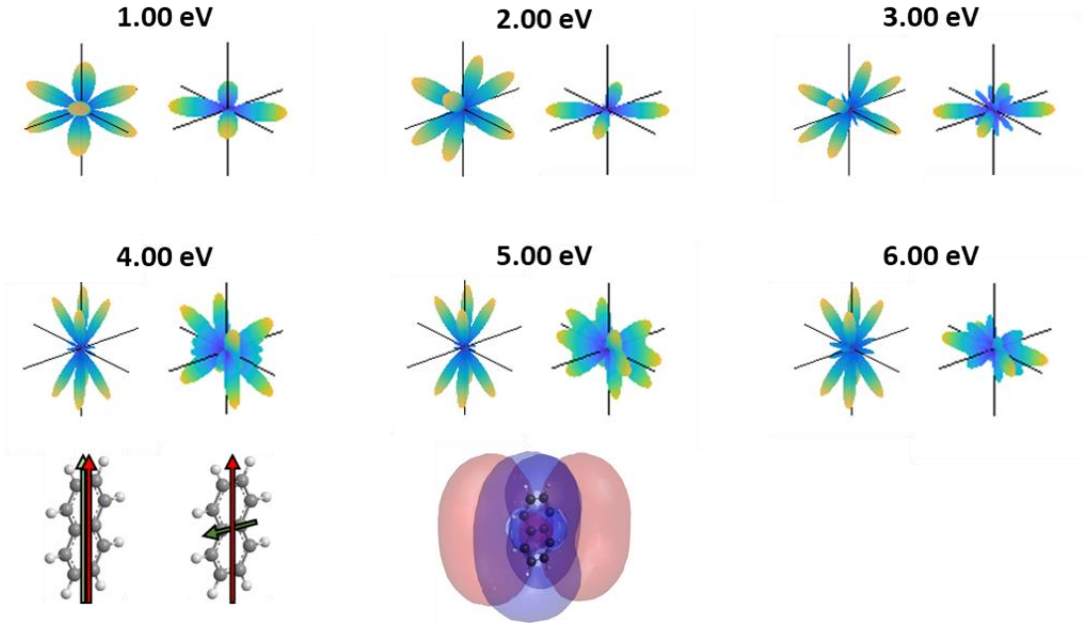

Figure 6.13. Iso-surfaces showing molecular frame PADs following the ionization of naphthalene at different photoelectron kinetic energies. The panel on the bottom left shows the orientation of the aniline molecule relative to the alignment field (red arrow) and the probe field (green). The green arrow defines the laboratory frame Z axis. The molecular orbital used to describe the initial electronic state of naphthalene is shown on the bottom right.

The relatively high symmetry of the molecular structure restricts the contributing photoelectron partial waves, resulting in relatively simple MFPADs. In particular, they have up-down symmetry at all kinetic energies. As the kinetic energy increases more lobes appear in the MFPADs for both polarization geometries. The LFPAD results from an average over all the possible directions of the MPA in the laboratory frame, weighted by any anisotropy in the distribution of MPAs that is introduced by the experiment. When the alignment pulse is introduced the distribution of MPAs is confined along the laboratory frame Z-axis, according to the value of $\langle \cos^2 \theta_{\hat{n}} \rangle$. In the limit of $\langle \cos^2 \theta_{\hat{n}} \rangle = 1$ the LFPAD would converge on the MFPAD.

In order to establish how close to a molecular frame measurement we have achieved in the photoelectron images shown in figure 6.11b we have used the output of the ePolyScat calculations at 1 eV photoelectron kinetic energy to create simulated photoelectron images (section 6.3) in two limiting cases (a) ionization of a distribution of naphthalene molecules that is completely aligned in one-dimension ($\langle \cos^2 \theta_{\hat{n}} \rangle = 1$) and (b) ionization of an isotropic distribution of naphthalene molecules ($\langle \cos^2 \theta_{\hat{n}} \rangle =$

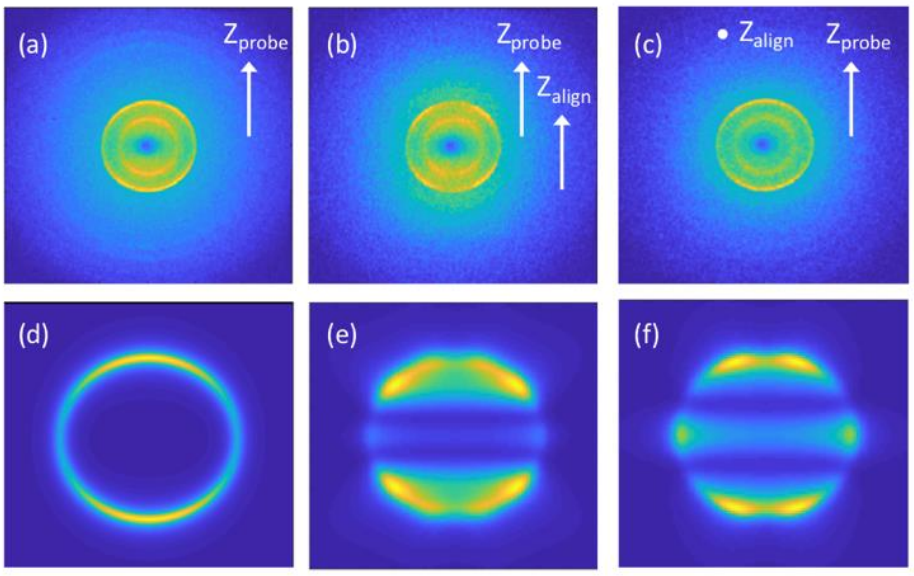

Figure 6.14. Comparison of experimental and simulated photoelectron images of naphthalene; in all cases the polarization vector of the ionizing beam, Z_{probe}, points vertically. Panels (a)-(c) show the raw experimental images for (a) probe only, (b) alignment and probe polarizations parallel (taken from Fig. 6.14b) and (c) alignment and probe polarizations perpendicular. Panels (d)-(f) show shows the simulated photoelectron images for 1 eV photoelectron kinetic energy for (d) an unaligned sample, (e) a sample with $\langle cos^2 \theta_{\hat{n}} \rangle = 1$ (a_u continuum) and (f) $\langle cos^2 \theta_{\hat{n}} \rangle = 0$ (b_{1u} continuum). The radius of the ring in the simulated images is chosen arbitrarily.

1/3). The results of these simulations are shown in figure 6.14 and compared with the equivalent experimental image taken from figure 6.11b. We have also included in figure 6.14 the experimental and simulated photoelectron images that result when the polarization of the alignment beam is perpendicular to the polarization of the probe beam. In this figure we can see that the four-fold structure that appears in the outer ring of the experimental images when the alignment beam is introduced in the parallel geometry is reproduced in the simulations, and that these simulations also reproduce the experimental images in the isotropic (probe only) and crossed polarization cases. This agreement is remarkable considering that (i) the 1 eV calculations are compared with 0.33 eV photoelectrons in the experiment (more precise 0.3 eV calculation are in progress) and (ii) the complicated nature of the excited electronic state in naphthalene has not been fully accounted for in the calculations.

6.8 Conclusion

In this chapter we presented the photoelectron angular distribution from an aligned molecule of aniline and naphthalene through (1+1) REMPI. Photoelectron images were recorded using linearly polarized UV pulses. Molecules were aligned using 800 nm pulses prior to ionization. Depending on the polarization of the alignment pulse molecules can be aligned in one dimension or three dimensions. For both molecules, the one-dimensional alignment case has been presented and discussed.

In case of aniline, for the one-dimensional alignment (polarization of probe and alignment being parallel), a clear change in the photoelectron angular distribution was observed. Upon alignment, photoelectron spectra showed a few extra peaks in the spectrum which showed possible absorption of 800 nm photon. A clear change in anisotropy parameter was also observed, where b_{20} changed from zero for probe only to 0.5 for the aligned case. Further, a comparison of calculated LFPADs with experimental PADs is presented, although the experimental results cannot be reproduced by the calculations. This is attributed to perturbation of the ionization process by the alignment pulse in the case of aniline. For example, absorption of 800 nm photon leading to a (1+1'+1) REMPI process.

For naphthalene photoelectron images were also recorded after aligning the molecules using 800 nm pulses. Measurements were done via S_1 vibrational states, for unaligned case origin channel showed a two-fold symmetry in the angular distribution with

preferred ejection of electron in the direction of probe polarization. When molecules were aligned the four-fold symmetry appeared in the photoelectron angular distribution. Similar to aniline a comparison of simulated PADs and experimental PADs were presented. The simulation reproduced the four-fold structure in the PADs for parallel and perpendicular cases and two-fold structure in the probe only case.

Chapter 7 Conclusions and future directions

In this work, photoelectron angular distributions in the weak-field limit have been measured for polyatomic molecules. We have performed novel experiments using the techniques of strong-field alignment in which the use of a strong-field alignment pulse has enabled us to approach a molecular frame measurement in the two-photon ionization of aniline and naphthalene. We have compared our measured PADs with calculations performed using the ePolyScat package. Comparison with calculated photoelectron images that result from the ionization of unaligned and fully aligned distributions of molecules demonstrates that an excellent degree of alignment is required to measure photoelectron angular distribution in the molecular frame. We have also performed PECD experiments using a (2+1) REMPI scheme with a picosecond laser system. The use of picosecond laser pulses has enabled the resolution of vibrational structure in the photoelectron spectrum, allowing decoupling of electronic and vibrational effects. The tunability of the picosecond laser system has enabled the study of the intermediate electronic state (3*spd* Rydberg state) in three molecules (fenchone, α-pinene, 3-carene). Measurements of the REMPI spectrum has shed light on the ionization threshold of different Rydberg states and provided a rough estimate of the excited state lifetime. Ion yield measurements as a function of laser power and polarization have shed light on the two-photon absorption cross-sections for the observed Rydberg states.

In this chapter the most significant findings will be summarised, and the prospects for future work discussed.

7.1 REMPI- PECD

7.1.1 REMPI spectrum and parent ion yield measurements

In the present work, by recording a (2+1) REMPI spectrum with a picosecond laser for the low-lying Rydberg states of fenchone, α-pinene, and 3-carene, we have revealed new vibrational structure in the lower energy 3*spd* region. Complementing this with the FT VUV absorption spectrum. Three different regions identified in the REMPI spectra correspond to the B-, C- and D-band transitions, which are believed to correspond to 3*s*, 3*p*, and 3*d* excitation, respectively, for all three molecules [130, 131].

Extensive use has been made of laser intensity dependence measurements that shed light on the extent of competition between the two-photon excitation, ionization, and relaxation processes in the REMPI spectrum. For fenchone (figure 7.1), the 3*p* excitations display a second-order power dependence from which we deduce that the

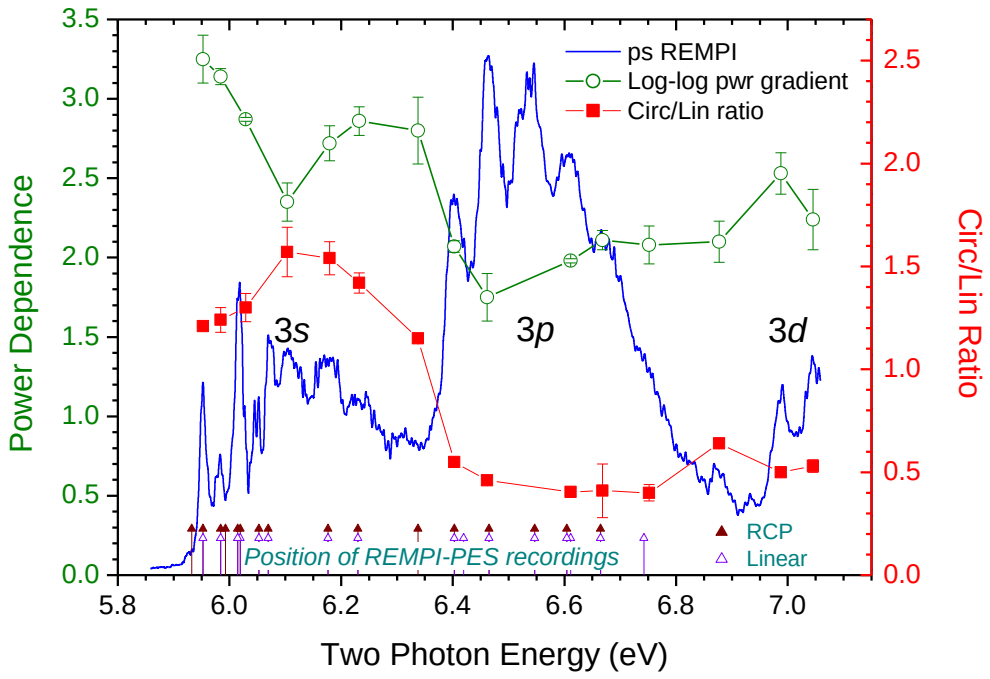

Figure 7.1. Polarization dependence and laser power measurements of parent ion (m/z 152) REMPI signal, expressed as the slope of log_{10}-log_{10} plots. Also included are C/L ratios of parent ion yield recorded with circular and linear polarized laser light, averaged over the 9–15 mW range. Solid lines joining data points are drawn simply to guide the eye, both for the power dependence data and the C/L ratio data. The ps REMPI spectrum is plotted on the same axis as an overall reference. (Ref. Chapter 3, Fig. 3.7)

two-photon absorption is rate-limiting. The 3*s* excitation is similarly second order at higher intensities reached with a femtosecond laser pulse, but as the laser intensity is decreased there are indications that a more subtle interplay of the excitation and relaxation/ionization dynamical processes becomes more controlling, and the observed power dependence becomes intermediate between 2nd and 3rd order.

For α-pinene (Chapter 4), the 3*s* region showed an average photon order of n = 3.1 (~3rd order), the 3*p* showed a value of n = 2.6, and third range corresponds to the 3*d* region with an average of n = 2.5. The 3*p* and 3*d* regions show a dynamic value which changes across the band. The 3rd order laser power dependence is an indication that the ionization step is not saturated, and it will be a rate determining step and relaxation

into non-ionization channel will be in direct competition with the ionization channels. For 3-carene (Chapter 4), throughout the REMPI spectrum, a ~3rd order power dependency was observed, hinting that the ionization step is not saturated.

In investigation of REMPI circular-linear dichroism, the ratio of signal (ion yield) recorded with circular and linear light polarization has also shown to have the capability to aid diagnosis of the spectroscopy. Circular-linear dichroism is well established in two-photon liquid phase spectroscopy but seems to have been largely overlooked in gas phase REMPI, due to the possibility of ill-defined contributions from any photon dynamics, including ionization, occurring after the two-photon absorption, but nevertheless contributing to the observed effects. We showed that the laser power dependence measurements serve as a guide, and when a 2nd order dependence applies the experimental circular-linear (C/L) dichroism measurements may be in very good accord with theoretical predictions utilizing calculated two-photon absorption cross-sections [116]. Conversely, it has been possible to infer for fenchone, from the apparent lack of such agreement that the 3p_z sub-state is a vanishingly small contributor to the overall REMPI 3*p* excitation, corroborating the same inference based upon the relative weakness of the linear 3p_z cross-section. For fenchone, two different C/L values were observed (see figure 7.1). The 3*s* region showed a value of ~1.5 and 3*p*/3*d* regions a value of ~0.5. The REMPI circular-linear dichroism measurements are particularly revealing in the 3*s* excitation since they appear to be inversely correlated to the photon intensity dependence for fenchone and α-pinene. For α-pinene, the C/L values were in range ~0.8-1 for the 3*s* region and ~0.5 for the 3*d* region. Whereas 3-carene showed a value of 1 in 3*s* region and decreasing value in the 3*p* region (changing from 1 to 0.5). These investigation of REMPI circular-linear dichroism, the ratio of signal (ion yield) recorded with circular and linear light polarization has shown to have the capability to aid diagnosis of the spectroscopy of intermediate electronic state. The laser power dependence measurements serve as a guide, and when a 2nd order dependence applies the experimental circular-linear dichroism measurements may be in very good accord with theoretical predictions utilising calculated two-photon absorption cross-sections [116]. The REMPI circular-linear measurements can also help assign symmetry for nonchiral molecules and hence identify electronically excited sates [123].

7.1.2 Photoelectron spectra

A series of REMPI photoelectron spectra, recorded at excitation energies throughout the 3*s*, 3*p*, and 3*d* excitation region for fenchone (Chapter 3), α-pinene (Chapter 4), and 3-carene (Chapter 4), provide much more insight into the vibrational dynamics of these Rydberg states and the cation. For all three molecules, three ridges were observed corresponding to $\Delta v = 0$ peak for ionization via 3*s*, 3*p*, and 3*d* Rydberg state. For fenchone and 3-carene, below the 3*p* excitation threshold, the 3*s* REMPI-PES show that the anticipated $\Delta v = 0$ propensity is rigorously followed, with a single photoelectron peak. Above the 3*p* threshold a second series of $\Delta v = 0$ peaks appear in the REMPI-PES that are clearly attributable to excitation via the 3*p* Rydberg intermediate, while the 3*s* $\Delta v = 0$ trend appears to be continued. However, this leads to excitations that clearly fall outside the Franck-Condon envelope reachable from the ground state geometry, and instead have an intensity distribution that tracks the Franck-Condon envelope of the 3*p* resonant intermediate. From this it is inferred that rather than the 3*s* and 3*p* intermediate states being excited in parallel, the dominant mechanism above the 3*p* threshold is for its excitation to be followed by a rapid internal conversion to highly excited vibrational levels of the 3*s* state before it is now ionized. A further indication of much more complex vibronic dynamics above the 3*p* threshold is that the propensity for $\Delta v = 0$ ionizations is much weaker, with both principal REMPI-PES peaks showing vibrational progressions ranging to higher vibrational quantum number. For α-pinene we observed the similar behaviour except in the 3*s*

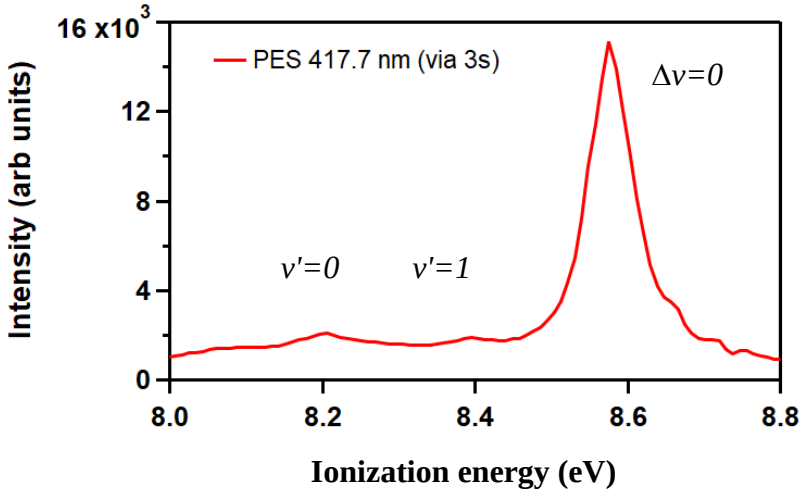

Figure 7.2. Photoelectron spectrum of α-pinene following ionization via the 3s Rydberg state at 417.7 nm showing v' = 0,1 (ν_1 and ν_{56} modes respectively) and Δv=0 peaks.

region, where $\Delta v = 0$ propensity rule was not rigorously followed. The $v' = 0$ and 1 (v_1 and v_{56} modes respectively) peaks were observed along with the main $\Delta v = 0$ peak (figure 7.2*)*.

7.1.3 Vibrational and electron kinetic effects on PECD

PECD measurements were recorded along the two regions (3*s* and 3*p*) for all three molecules. The data in 3*d* region could not be recorded due to the size limit of the detector. For fenchone, the PECD signal associated with the 0-0 transition (origin) peak showed a significant value, of about 30-35%, and for a highly vibrationally excited 3*s* peak (8.75 eV) a much smaller PECD signal of ~10% was observed. In comparison to Kastner et al.'s [80] femtosecond (2+1) REMPI PECD work in 3*s* the region (Table 7.1), our picosecond PECD results show a higher PECD value (almost double in magnitude). This difference in signal could be a vibrational effect which are not usually resolved with femtosecond laser pulses. Despite the different PECD value, both femtosecond and picosecond result showed a decrement in PECD value with higher vibrational character of the excited state.

Results	*S-Fenchone (PECD %)*	*Wavelength*	*Pulse length*
Kastner et al. [115]	3*s* (-17), 3*p* (-15)	375-420 nm	25 ns
Kastner et al.[80]	3*s* (-15 to 7), 3*p* (-1)	359-431 nm	25 fs
Miles et al.[13]	-13.9±0.4	394 nm	250 fs
Beaulieu et al.[109]	-13	398 nm	25 fs
Lux et al.[73]	-10.1(-13.8 FWHM)	398 nm	25 fs
Present work	3*s* (-35), 3*p* (-10)	350-420 nm	1.3 ps

Table 7. 1. Previous PECD values for S- fenchone enantiomers for ionization via 3s and 3p intermediate state using (2+1) REMPI.

A few striking features were observed for the PECD measured following ionization through 3*s* region; first, it showed a clear modulation with the principal vibrational peaks. Second, its absolute magnitude changes from 35% to almost zero for the peaks in the 8.5-8.9 eV range which correspond to the ionization via highly excited vibrational levels (higher kinetic energy electrons). Third, a significant change in PECD with different excited vibrational peaks was observed, the 3*s* origin peak shown

a PECD value of -35%, whereas the vibrational peak at 8.65 eV shows a higher PECD value of -40% illustrating a clear vibrational influence on the PECD value. Toward the end of the 3*s* region, for higher vibrational states, the PECD value goes down to almost zero, towards the end of FC window. However, the peaks beyond the FC allowed window (9.0-9.4 eV), which are believed to result from internal conversion from 3*p* to 3*s* states, show huge PECD values. The peak at 9.0 eV shows the value of -30% (See figure 3.11 3*s* PECD curve). The following peak at 9.2 eV shows the PECD value of -20%. These observations clearly show a strong indication that the intermediate electronic and vibrational state has an influence on PECD. To get detailed insight, more computational work is required.

The α-pinene REMPI-PECD results shed some light on the initial and final state effect on PECD and showed some unique results. The complete PECD data along the two

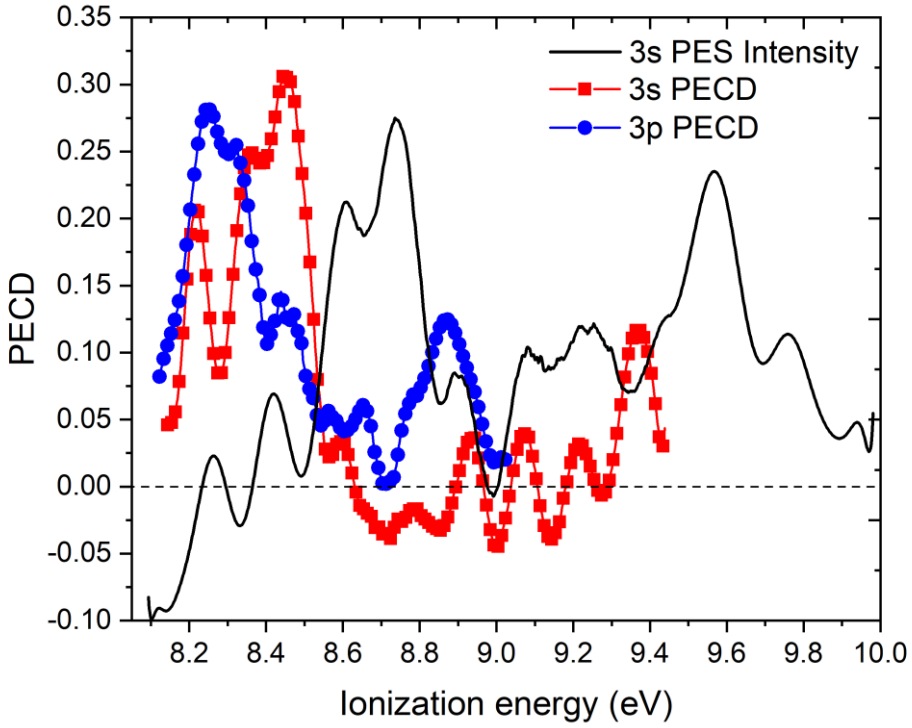

Figure 7.3. Complete PECD data for ionization via 3s (red curve) and 3p (blue curve) are shown along with the PES intensity along 3s ridge (black curve) for α-pinene (see text). The PES and the PECD are plotted on the same ionization energy axis.

ridges showed that vibrational dependency of PECD (figure 7.3), where PECD value reduced from 30% to almost zero. Electron kinetic energy effects were observed for *v*' = 0 and 1 peaks over the range of an eV (figure 7.4). The *v*' = 0 peak shows striking

PECD value of ~35% which reduces up to ~ 5% with the increase in electron kinetic energy (over the range of 0.5 eV). The *v*' =1 peak shows PECD around 25% and decreases to ~7% with an increase in electron kinetic energy (over the range of 0.4 eV). This observation is purely an electron kinetic energy influences on PECD for the first two peaks in 3*s* vibrational progression (figure 7.4 inset).

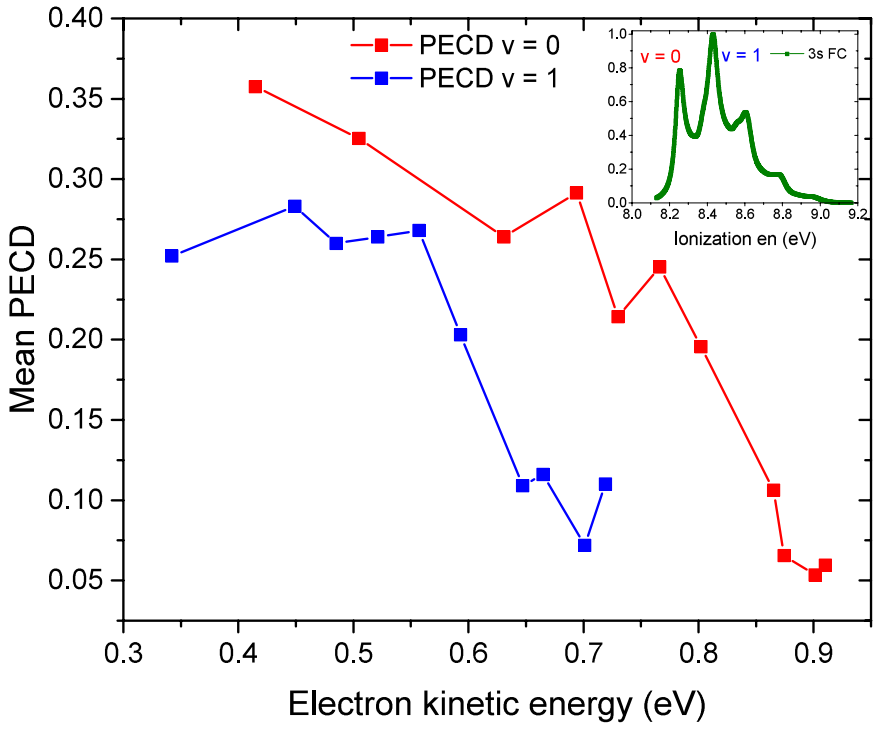

Figure 7.4. eKE effect: Mean PECD value for v' = 0 (red data set) and v' = 1(blue data set) peaks (v_1 and v_{56} modes respectively) when ionized via 3s state is shown on eKE axis for α-pinene. Inset: 3s FC calculation.

The PECD measurements in 3*s* region for α-pinene and 3-carene showed a different trend. The former showed a smaller PECD value than the later. Both molecules are isomers, hence this difference in PECD value could be due to its dependency on molecular structure. For 3-carene, interesting electron kinetic energy behaviour was observed. In Chapter 5, figure 5.14a showed that the change in sign of the PECD for ionization via the 3*s* and 3*p* could be a consequence of electron kinetic energy, this trend is not fully understood yet, more theoretical work is required to unravel this mystery. The PECD along the 3*s* and 3*p* ridges for 3-carene also showed some vibrational dependency.

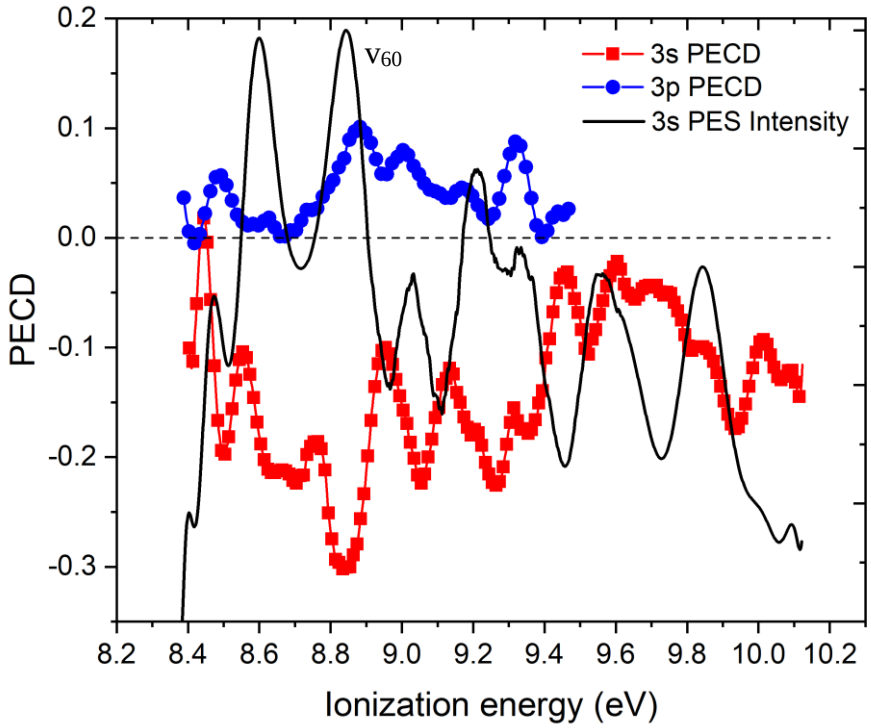

Figure 7.5. Complete PECD data for ionization via 3s (red curve) and 3p (blue curve) are shown along with the PES intensity along 3s ridge (black curve) for 3-carene. The PES and the PECD are plotted on the same ionization energy axis.

A few striking features were observed for the PECD measured following ionization through 3*s* region (figure 7.5); first, it showed a clear modulation with the principal vibrational peaks. Second is the change in the sign of PECD value for ionization via the 3*s* and 3*p* Rydberg states. Third, the absolute maximum PECD value for ionization through these two states is observed for the third peak, which is the one quanta excitation in ν_{60} mode (symmetric stretch in methyl group), this shows the clear vibrational influence on the PECD value.

7.1.4 Intermediate state effects

For 3-carene we observed a unique result hinting toward an effect of intermediate on PECD. For multi-photon ionization we observed a different trend for PECD value when compared to single-photon ionization for similar photon energies. Figure 7.6 shows the comparison of one-photon and (2+1) ionization processes (9.2 eV total photon energy) and their recorded PECD. The PECD results for multi-photon ionization process show a complete opposite trend than one-photon ionization. An almost zero PECD value was observed for the origin peak for multi-photon ionization

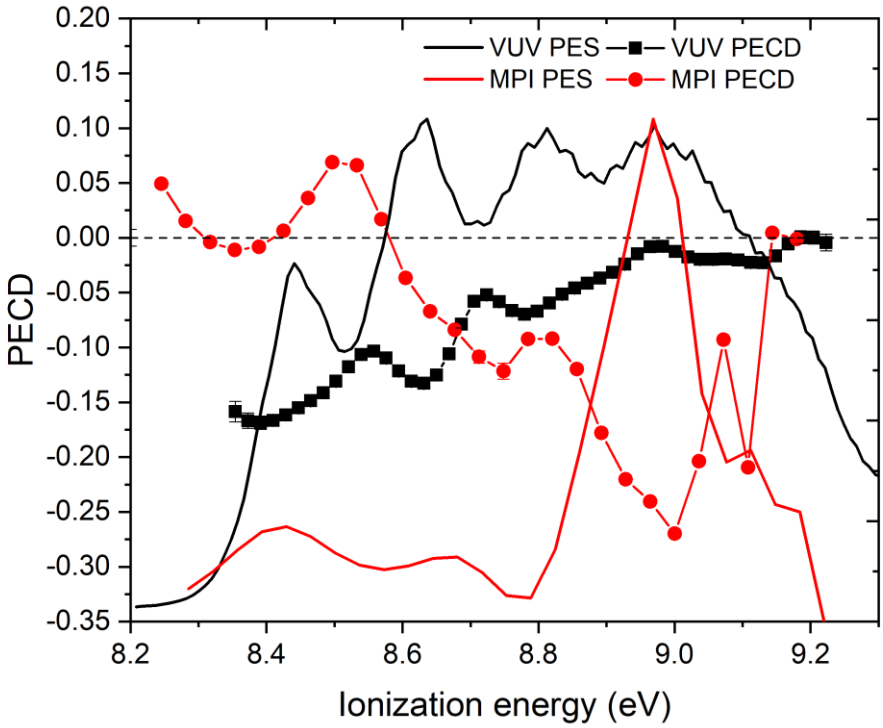

Figure 7.6. Intermediate state effect: VUV VMI-PES and PECD is shown in comparison with (2+1) REMPI-PES and PECD. For total photon energy for both cases is 9.2 and 9.3 eV respectively. VMI-PES has arbitrary intensity but is plotted on the same ionization energy as PECD

and a higher absolute magnitude for highly excited vibrational peaks at 9.0 eV, whereas for one photon ionization an opposite trend was observed (figure 7.6). Both the measurements have similar electron kinetic energy and show similar vibrational peaks, leaving the only difference being number photon and intermediate state. Thus, the change in the PECD signal for multi-photon ionization process could be a consequence of intermediate effect.

7.2 Approaching MFPADs in Aniline and Naphthalene

In Chapter 6 we presented the photoelectron angular distributions from aligned aniline and naphthene molecules. The alignment was achieved by interaction with a 100 ps infrared laser pulse with ionization achieved in a two-photon resonant scheme using a low intensity UV pulse of ~6 ps duration. We have presented photoelectron images measured following the ionization of aligned distributions of gas phase naphthalene and aniline molecules. The resulting images are found to exhibit anisotropy that increases when the alignment pulse is present with the aniline PADs peaking along the polarization vector of the ionizing light and the naphthalene PADs developing a

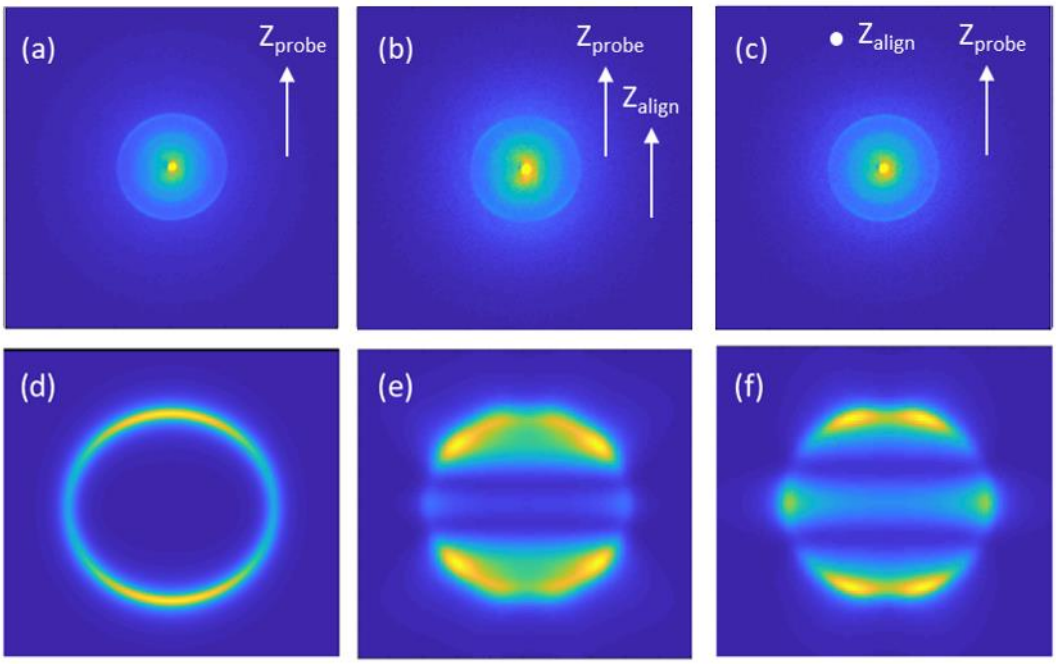

Figure 7.7. Comparison of experimental and simulated photoelectron images of naphthalene; in all cases the polarization vector of the ionizing beam, Z_{probe}, points vertically. Panels (a)-(c) show the raw experimental images for (a) probe only, (b) alignment and probe polarizations parallel (taken from Fig. 3b) and (c) alignment and probe polarizations perpendicular. Panels (d)-(f) show shows the simulated photoelectron images for 1 eV photoelectron kinetic energy for (d) an unaligned sample, (e) a sample with $\langle cos^2\,\theta_{\hat{n}}\rangle = 1$ (a_u continuum) and (f) $\langle cos^2\,\theta_{\hat{n}}\rangle = 0$ (b_{1u} continuum). The radius of the ring in the simulated images is chosen arbitrarily.

characteristic four-lobed structure. The PADs that result from the ionization of unaligned and fully aligned distributions of molecules are calculated using the ePolyScat method and converted into two-dimensional photoelectron images.

Comparison with calculated photoelectron images that result from the ionization of unaligned and fully aligned distributions of molecules demonstrates that an excellent degree of alignment has been achieved in the case of naphthalene and that the photoelectron images are largely determined by the photoelectron angular distribution in the molecular frame (figure 7.7). However, the aniline work represents a cautionary tale as it is clear that additional processes occur following the one-photon resonant step and that this affects the measured photoelectron angular distribution.

7.3 Future direction

7.3.1 MP-PECD

Photoelectron circular dichroism following single-photon ionization has been extensively studied over the years with considerable interest in recent years in the extension to multiphoton ionization. Thus far, multiphoton PECD studies have been limited to a few classic chiral molecules, such as fenchone and camphor. Very few REMPI studies have been performed on these molecules and so there is a lack of information available on the relevant excited state spectroscopy. The work presented in this thesis makes a contribution in that direction. Other chiral molecular systems which have been studied by one-photon PECD would be worth exploring and characterizing in the multi-photon regime; examples include limonene, and methyl oxirane.

In this work, we explored the influence of the character of an intermediate Rydberg state on PECD in a (2+1) REMPI scheme. A next step would be to explore (1+1) REMPI, this would further shed some light on the difference between one-photon and two-photon absorption and its effect on PECD and the degree of weak-field alignment that can be created. We made some attempts to conduct (1+1) REMPI PECD measurements on α-pinene using 200 nm femtosecond light pulses at the ARTEMIS beamline (CLF), but these were not fully successful for due to lack of time and will be repeated in the near future.

One of the aims of the present work was to decouple the effects of photoelectron kinetic energy and vibration on PECD. To fully decouple these effects, one would require two-colour experiments in, for example, a (2+1') or (1+1') REMPI scheme. By populating the same intermediate vibrational state and using different photon energies to ionize the vibrational dependence can be decoupled. Although we attempted (2+1') REMPI experiments using the Nottingham picosecond laser system, these were not fully successful. The two-colour ionization cross-section was not sufficient to do a PECD experiment. We attribute this to the short (picosecond) intermediate lifetimes of the systems studied. Therefore, we anticipate that shorter laser pulses are needed for these two-colour experiments. We have future plans to perform such an experiment on α-pinene at the ARTEMIS beamline.

In order to understand the dynamics associated with the intermediate state accessed, a time-resolved PECD experiment is required. We attempted time-resolved PECD experiments at Nottingham, but again due to the short lifetimes of intermediate states, these were not successful.

The ultimate goal of the REMPI-PECD experiment would be to record REMPI-PECD in the molecular frame. The importance of molecular alignment in PECD experiments has been discussed by Beaulieu et al. [82]. This could be approached either via an electron-ion coincidence measurement (COLTRIMS) or the technique discussed in this work (laser-induced molecular alignment). However, for COLTRIMS experiments a challenge is the necessity of finding a small chiral system with limited fragmentation, and for the strong field alignment technique to work the molecule would need to have suitably anisotropic polarizability.

7.3.2 MF-PADs

In the present work we implemented strong-field alignment with a truncated pulse, in order to minimize the influence of the alignment pulse on the photoionization dynamics. However, we have seen that in the case of aniline significant perturbations still occur which affect the measured PAD. New techniques are therefore needed that maximize alignment and minimize perturbations.

Recently Chatterley et al. [93] have demonstrated alignment of diiodobiphenyl in helium nanodroplets using the truncated pulse alignment technique. The authors compared the alignment achieved in the isolated molecule with the alignment achieved when the molecule was embedded in helium nanodroplets and showed that the alignment can last up to 10 ps after the alignment pulse. This type of experiment could be used to measure the molecular frame PADs in the field-free environment.

In the present work we have used a (1+1) REMPI scheme to measures the PADs, but this brings about complications because of the interaction of the alignment pulse with the excited state. Use of an XUV source would enable one-photon ionization to be accomplished which would circumvent this problem. Although various groups have used the XUV light from free-electron lasers (FELs) [41] and from high harmonic generation method (HHG) [43] to perform alignment experiments, this has yet to be extended to polyatomic molecules of the size studied in this thesis.

Bibliography

[1] P. Hockett and K. L. Reid, “Complete determination of the photoionization dynamics of a polyatomic molecule. II. Determination of radial dipole matrix elements and phases from experimental photoelectron angular distributions from $\tilde{A}^1A_u$ acetylene,” *J. Chem. Phys.*, vol. 127, no. 15, p. 154308, Oct. 2007, doi: 10.1063/1.2790443.

[2] P. Hockett, M. Staniforth, K. L. Reid, and D. Townsend, “Rotationally resolved photoelectron angular distributions from a nonlinear polyatomic molecule,” *Phys. Rev. Lett.*, vol. 102, no. 25, p. 253002, Jun. 2009, doi: 10.1103/PhysRevLett.102.253002.

[3] P. Hockett, M. Staniforth, and K. L. Reid, “Photoelectron angular distributions from rotationally state-selected NH_3 (B^1 E″): dependence on ion rotational state and polarization geometry,” *Mol. Phys.*, vol. 108, no. 7–9, pp. 1045–1054, Apr. 2010, doi: 10.1080/00268971003639266.

[4] T. Suzuki, “Femtosecond time-resolved photoelectron imaging,” in *Ann. Rev. Phys. Chem.*, 2006, vol. 57, pp. 555–592, doi: 10.1146/annurev.physchem.57.032905.104601.

[5] A. M. Rijs, M. H. M. Janssen, E. t. H. Chrysostom, and C. C. Hayden, “Femtosecond coincidence imaging of multichannel multiphoton dynamics,” *Phys. Rev. Lett.*, vol. 92, no. 12, p. 123002, Mar. 2004, doi: 10.1103/PhysRevLett.92.123002.

[6] C. Z. Bisgaard, O. J. Clarkin, G. Wu, A. M. D. Lee, O. Gessner, C. C. Hayden, and A. Stolow, “Time-resolved molecular frame dynamics of fixed-in-space CS_2 molecules,” *Science*, vol. 323, no. 5920, pp. 1464–1468, Mar. 2009, doi: 10.1126/science.1169183.

[7] O. Gessner, A. M. D. Lee, J. P. Shaffer, H. Reisler, S. V. Levchenko, A. I. Krylov, J. G. Underwood, H. Shi, A. L. L. East, D. M. Wardlaw, E. t. H. Chrysostom, C. C. Hayden, and A. Stolow “Femtosecond multidimensional imaging of a molecular dissociation,” *Science*, vol. 311, no. 5758, pp. 219–222, Jan. 2006, doi: 10.1126/science.1120779.

[8] R. Hadidi, D. K. Bozanic, G. A. Garcia, and L. Nahon, “Electron asymmetries in the photoionization of chiral molecules: possible astrophysical implications,” *Adv. Phys. X*, vol. 3, no. 1, p. 1477530, Jan. 2018, doi: 10.1080/23746149.2018.1477530.

[9] M. Tia, B. C. d. Miranda, S. Daly, F. G. Levrel, G. A. Garcia, L. Nahon, and I. Powis, “VUV photodynamics and chiral asymmetry in the photoionization of gas phase alanine enantiomers,” *J. Phys. Chem. A*, vol. 118, no. 15, pp. 2765–2779, Apr. 2014, doi: 10.1021/jp5016142.

[10] G. A. Garcia, L. Nahon, C. J. Harding, and I. Powis, “Chiral signatures in angle-resolved valence photoelectron spectroscopy of pure glycidol enantiomers,” *Phys. Chem. Chem. Phys.*, vol. 10, no. 12, p. 1628, Mar. 2008, doi: 10.1039/b714095a.

[11] I. Powis, C. J. Harding, G. A. Garcia, and L. Nahon, “A valence photoelectron imaging investigation of chiral asymmetry in the photoionization of fenchone

and camphor," *ChemPhysChem*, vol. 9, no. 3, pp. 475–483, Feb. 2008, doi: 10.1002/cphc.200700748.

[12] A. Comby, E. Bloch, C. M. M. Bond, D. Descamps, J. Miles, S. Petit, S. Rozen, J.B. Greenwood, V. Blanchet, and Y. Mairesse, "Real-time determination of enantiomeric and isomeric content using photoelectron elliptical dichroism," *Nat. Commun.*, vol. 9, no. 1, p. 5212, Dec. 2018, doi: 10.1038/s41467-018-07609-9.

[13] J. Miles, D. Fernandes , A. Young , C. M. M. Bond, S.W. Crane, O. Ghafur, D. Townsend, J. Sa, and J.B. Greenwood, "A new technique for probing chirality via photoelectron circular dichroism," *Anal. Chim. Acta*, vol. 984, pp. 134–139, Sep. 2017, doi: 10.1016/j.aca.2017.06.051.

[14] K. L. Reid, "Photoelectron angular distributions: developments in applications to isolated molecular systems," *Mol. Phys.*, vol. 110, no. 3, pp. 131–147, Feb. 2012, doi: 10.1080/00268976.2011.640292.

[15] D. Akoury, K. Kreidi, T. Jahnke, T. Weber, A. Staudte, M. Schöffler, N. Neumann, J. Titze, L. Ph. H. Schmidt, A. Czasch, O. Jagutzki, R. A. Costa Fraga, R. E. Grisenti, R. Díez Muiño, N. A. Cherepkov, S. K. Semenov, P. Ranitovic, C. L. Cocke, T. Osipov, H. Adaniya, J. C. Thompson, M. H. Prior, A. Belkacem, A. L. Landers, H. Schmidt-Böcking, and R. Dörner, "The simplest double slit: Interference and entanglement in double photoionization of H_2," *Science*, vol. 318, no. 5852, pp. 949–952, Nov. 2007, doi: 10.1126/science.1144959.

[16] M. S. Schöffler, J. Titze, N. Petridis, T. Jahnke, K. Cole, L. P. H. Schmidt, A. Czasch, D. Akoury, O. Jagutzki, J. B. Williams, N. A. Cherepkov, S. K. Semenov, C. W. McCurdy, T. N. Rescigno, C. L. Cocke, T. Osipov, S. Lee, M. H. Prior, A. Belkacem, A. L. Landers, H. Schmidt-Böcking, Th. Weber, and R. Dörner "Ultrafast probing of core hole localization in N_2," *Science*, vol. 320, no. 5878, pp. 920–923, May 2008, doi: 10.1126/science.1154989.

[17] J. L. Hansen, H. Stapelfeldt, D. Dimitrovski, M. Abu-samha, C. P. J. Martiny, and L. B. Madsen, "Time-resolved photoelectron angular distributions from strong-field ionization of rotating naphthalene molecules," *Phys. Rev. Lett.*, vol. 106, no. 7, p. 073001, Feb. 2011, doi: 10.1103/PhysRevLett.106.073001.

[18] L. Holmegaard, J. L. Hansen, L. Kalhøj, S. Louise Kragh, H. Stapelfeldt1, F. Filsinger, J. Küpper, G. Meijer, D. Dimitrovski, M. Abu-samha, C. P. J. Martiny and L. B. Madsen, "Photoelectron angular distributions from strong-field ionization of oriented molecules," *Nat. Phys.*, vol. 6, no. 6, pp. 428–432, Jun. 2010, doi: 10.1038/nphys1666.

[19] H. Stapelfeldt and T. Seideman, "Colloquium : Aligning molecules with strong laser pulses," *Rev. Mod. Phys.*, vol. 75, no. 2, pp. 543–557, Apr. 2003, doi: 10.1103/RevModPhys.75.543.

[20] M. Lebech, J. C. Houver, A. Lafosse, D. Dowek, C. Alcaraz, L. Nahon, and R. R. Lucchese, "Complete description of linear molecule photoionization achieved by vector correlations using the light of a single circular polarization," *J. Chem. Phys.*, vol. 118, no. 21, pp. 9653–9663, Jun. 2003, doi: 10.1063/1.1570402.

[21] D. Dowek, M. Lebech, J. C. Houver, and R. R. Lucchese, “Circular dichroism in molecular frame photoemission,” *Mol. Phys.*, vol. 105, no. 11–12, pp. 1757–1768, Jun. 2007, doi: 10.1080/00268970701501802.

[22] T. Teramoto, J Adachi, M Yamazaki, K Yamanouchi, M Stener, P Decleva, and A Yagishita, “Extensive study on the C 1s photoionization of CS_2 molecules by multi-coincidence velocity-map imaging spectrometry,” *J. Phys. B At. Mol. Opt. Phys.*, vol. 40, no. 20, pp. 4033–4046, Oct. 2007, doi: 10.1088/0953-4075/40/20/006.

[23] R. Wang, Q. Zhang, D. Li, S. Xu, P. Cao, Y. Zhou, W. Cao, and P. Lu, “Identification of tunneling and multiphoton ionization in intermediate Keldysh parameter regime,” *Opt. Express*, vol. 27, no. 5, p. 6471, Mar. 2019, doi: 10.1364/OE.27.006471.

[24] J. A. Davies, L. E. Whalley, and K. L. Reid, “Probing the origins of vibrational mode specificity in intramolecular dynamics through picosecond time-resolved photoelectron imaging studies,” *Phys. Chem. Chem. Phys.*, vol. 19, no. 7, pp. 5051–5062, Feb. 2017, doi: 10.1039/C6CP08132K.

[25] A. T. J. B. Eppink and D. H. Parker, “Velocity map imaging of ions and electrons using electrostatic lenses: Application in photoelectron and photofragment ion imaging of molecular oxygen,” *Rev. Sci. Instrum.*, vol. 68, no. 9, pp. 3477–3484, Sep. 1997, doi: 10.1063/1.1148310.

[26] C. H. R. Ooi, W. L. Ho, and A. D. Bandrauk, “Effects of ultrashort laser pulses on angular distributions of photoionization spectra,” *Sci. Rep.*, vol. 7, no. 1, pp. 1–22, 2017, doi: 10.1038/s41598-017-05915-8.

[27] K. L. Reid, “Photoelectron angular distributions,” *Annu. Rev. Phys. Chem.*, vol. 54, no. 1, pp. 397–424, Oct. 2003, doi: 10.1146/annurev.physchem.54.011002.103814.

[28] P. Hockett, “Photoionization Dynamics of Polyatomic Molecules,” University of Nottingham, Nottingham, 2009.

[29] M. Yamazaki, J. Adachi, Y. Kimura, M. Stener, P. Decleva, and A. Yagishita, “N 1s photoelectron angular distributions from fixed-in-space NO_2 molecules: Stereodynamics and symmetry considerations,” *J. Chem. Phys.*, vol. 133, no. 16, p. 164301, Oct. 2010, doi: 10.1063/1.3505549.

[30] M. Meckel, D. Comtois, D. Zeidler, A. Staudte, D. Pavičić, H. C. Bandulet, H. Pépin, J. C. Kieffer, R. Dörner, D. M. Villeneuve, and P. B. Corkum, “Laser-induced electron tunneling and diffraction,” *Science*, vol. 320, no. 5882, pp. 1478–1482, Jun. 2008, doi: 10.1126/science.1157980.

[31] K. L. Reid, T. A. Field, M. Towrie, and P. Matousek, “Photoelectron angular distributions as a probe of alignment evolution in a polyatomic molecule: Picosecond time- and angle-resolved photoelectron spectroscopy of S_1 para-difluorobenzene,” *J. Chem. Phys.*, vol. 111, no. 4, pp. 1438–1445, Jul. 1999, doi: 10.1063/1.479403.

[32] K. L. Reid and J. G. Underwood, “Extracting molecular axis alignment from photoelectron angular distributions,” *J. Chem. Phys.*, vol. 112, no. 8, pp. 3643–3649, Feb. 2000, doi: 10.1063/1.480517.

[33] J. J. Larsen, H. Sakai, C. P. Safvan, I. Wendt-Larsen, and H. Stapelfeldt, "Aligning molecules with intense nonresonant laser fields," *J. Chem. Phys.*, vol. 111, no. 17, pp. 7774–7781, 1999, doi: 10.1063/1.480112.

[34] V. Kumarappan, S. S. Viftrup, L. Holmegaard, C. Z. Bisgaard, and H. Stapelfeldt, "Aligning molecules with long or short laser pulses," *Phys. Scr.*, vol. 76, no. 3, pp. C63–C68, Sep. 2007, doi: 10.1088/0031-8949/76/3/n09.

[35] K. L. Reid, "Accessing the molecular frame through strong-field alignment of distributions of gas phase molecules," *Philos. Trans. R. Soc. A Math. Phys. Eng. Sci.*, vol. 376, no. 2115, p. 20170158, Mar. 2018, doi: 10.1098/rsta.2017.0158.

[36] B. Friedrich and D. Herschbach, "Alignment and trapping of molecules in intense laser fields," *Phys. Rev. Lett.*, vol. 74, no. 23, pp. 4623–4626, Jun. 1995, doi: 10.1103/PhysRevLett.74.4623.

[37] O. Geßner, Y. Hikosaka, B. Zimmermann, A. Hempelmann, R. R. Lucchese, J. H. D. Eland, P. M. Guyon, and U. Becker, "$4\sigma^{-1}$ Inner valence photoionization dynamics of NO derived from photoelectron-photoion angular correlations," *Phys. Rev. Lett.*, vol. 88, no. 19, p. 193002, Apr. 2002, doi: 10.1103/PhysRevLett.88.193002.

[38] M. Lebech, J. C. Houver, G. Raseev, A. S. dos Santos, D. Dowek, and R. R. Lucchese, "Valence and inner-valence shell dissociative photoionization of CO in the 26–33 eV range. II. Molecular-frame and recoil-frame photoelectron angular distributions," *J. Chem. Phys.*, vol. 136, no. 9, p. 094303, Mar. 2012, doi: 10.1063/1.3681920.

[39] V. Kumarappan, L. Holmegaard, C. Martiny, C. B. Madsen, T. K. Kjeldsen, S. S. Viftrup, L. B. Madsen, and H. Stapelfeldt, "Multiphoton electron angular distributions from laser-aligned CS_2 molecules," *Phys. Rev. Lett.*, vol. 100, no. 9, p. 093006, Mar. 2008, doi: 10.1103/PhysRevLett.100.093006.

[40] J. Maurer, D. Dimitrovski, L. Christensen, L. B. Madsen, and H. Stapelfeldt, "Molecular-frame 3D photoelectron momentum distributions by tomographic reconstruction," *Phys Rev Lett*, vol. 109, no. 12, p. 123001, Sep. 2012, doi: 10.1103/PhysRevLett.109.123001.

[41] F. Kelkensberg, A. Rouzee, W. Siu, G. Gademann, P. Johnsson, M. Lucchini, R. R. Lucchese, and M. J. J. Vrakking, "XUV ionization of aligned molecules," *Phys. Rev. A*, vol. 84, no. 5, p. 051404, Nov. 2011, doi: 10.1103/PhysRevA.84.051404.

[42] A. Rouzée, F. Kelkensberg, W. K. Siu, G. Gademann, R. R. Lucchese, and M. J. J. Vrakking, "Photoelectron kinetic and angular distributions for the ionization of aligned molecules using a HHG source," *J. Phys. B At. Mol. Opt. Phys.*, vol. 45, no. 7, p. 74016, Apr. 2012, doi: 10.1088/0953-4075/45/7/074016.

[43] A. Rouzée, A. G. Harvey, F. Kelkensberg, D. Brambila, W. K. Siu, G. Gademann, O. Smirnova and M. J. J. Vrakking, "Imaging the electronic structure of valence orbitals in the XUV ionization of aligned molecules," *J. Phys. B At. Mol. Opt. Phys.*, vol. 47, no. 12, p. 124017, Jun. 2014, doi: 10.1088/0953-4075/47/12/124017.

[44] C. Marceau, V. Makhija, D. Platzer, A. Y. Naumov, P. B. Corkum, A. Stolow, D. M. Villeneuve, and P. Hockett, "Molecular frame reconstruction using time-domain photoionization interferometry," *Phys. Rev. Lett.*, vol. 119, no. 8, p. 083401, Aug. 2017, doi: 10.1103/PhysRevLett.119.083401.

[45] L. Pasteur, "Sur les relations qui peuvent exister entre la forme cristalline, la composition chimique et le sens de la polarisation rotatoire," *Ann. Chim. la Phys.*, vol. 24, no. 1848, pp. 442–459, 1848, doi:10009487760/en.

[46] G. Longhi, S. Abbate, R. Gangemi, E. Giorgio, and C. Rosini, "Fenchone, Camphor, 2-Methylenefenchone and 2-Methylenecamphor: A vibrational circular dichroism Study," *J. Phys. Chem. A*, vol. 110, no. 15, pp. 4958–4968, Apr. 2006, doi: 10.1021/jp057178y.

[47] G.-S. Yu, T. B. Freedman, and L. A. Nafie, "Dual circular polarization Raman optical activity of related terpene molecules: Comparison of backscattering DCPI and right-angle ICP spectra," *J. Raman Spectrosc.*, vol. 26, no. 8–9, pp. 733–743, Aug. 1995, doi: 10.1002/jrs.1250260821.

[48] B. Ritchie, "Theory of the angular distribution of photoelectrons ejected from optically active molecules and molecular negative ions," *Phys. Rev. A*, vol. 13, no. 4, pp. 1411–1415, Apr. 1976, doi: 10.1103/PhysRevA.13.1411.

[49] N. A. Cherepkov, "Circular dichroism of molecules in the continuous absorption region," *Chem. Phys. Lett.*, vol. 87, no. 4, pp. 344–348, Apr. 1982, doi: 10.1016/0009-2614(82)83600-2.

[50] I. Powis, "Photoelectron circular dichroism of the randomly oriented chiral molecules glyceraldehyde and lactic acid," *J. Chem. Phys.*, vol. 112, no. 1, pp. 301–310, Jan. 2000, doi: 10.1063/1.480581.

[51] L. Nahon, G. A. Garcia, C. J. Harding, E. Mikajlo, and I. Powis, "Determination of chiral asymmetries in the valence photoionization of camphor enantiomers by photoelectron imaging using tunable circularly polarized light," *J. Chem. Phys.*, vol. 125, no. 11, p. 114309, Sep. 2006, doi: 10.1063/1.2336432.

[52] I. Powis, "Photoelectron Spectroscopy and Circular Dichroism in Chiral Biomolecules: L-Alanine," *J. Phys. Chem. A*, vol. 104, no. 5, pp. 878–882, Feb. 2000, doi: 10.1021/jp9933119.

[53] N. Böwering, T. Lischke, B. Schmidtke, N. Müller, T. Khalil, and U. Heinzmann, "Asymmetry in photoelectron emission from chiral molecules induced by circularly polarized light," *Phys. Rev. Lett.*, vol. 86, no. 7, pp. 1187–1190, Feb. 2001, doi: 10.1103/PhysRevLett.86.1187.

[54] G. A. Garcia, L. Nahon, M. Lebech, J.-C. Houver, D. Dowek, and I. Powis, "Circular dichroism in the photoelectron angular distribution from randomly oriented enantiomers of camphor," *J. Chem. Phys.*, vol. 119, no. 17, pp. 8781–8784, Nov. 2003, doi: 10.1063/1.1621379.

[55] U. Hergenhahn, E. E. Rennie, O. Kugeler, S. Marburger, T. Lischke, I. Powis, and G. Garcia, "Photoelectron circular dichroism in core level ionization of randomly oriented pure enantiomers of the chiral molecule camphor," *J. Chem. Phys.*, vol. 120, no. 10, pp. 4553–4556, Mar. 2004, doi: 10.1063/1.1651474.

[56] M. Stener, G. Fronzoni, D. Di Tommaso, and P. Decleva, “Density functional study on the circular dichroism of photoelectron angular distribution from chiral derivatives of oxirane,” *J. Chem. Phys.*, vol. 120, no. 7, pp. 3284–3296, Feb. 2004, doi: 10.1063/1.1640617.

[57] G. A. Garcia, H. Dossmann, L. Nahon, S. Daly, and I. Powis, “Photoelectron circular dichroism and spectroscopy of trifluoromethyl- and methyl-oxirane: a comparative study,” *Phys. Chem. Chem. Phys.*, vol. 16, no. 30, p. 16214, Jun. 2014, doi: 10.1039/C4CP01941E.

[58] D. Di Tommaso, M. Stener, G. Fronzoni, and P. Decleva, “Conformational Effects on Circular Dichroism in the Photoelectron Angular Distribution,” *ChemPhysChem*, vol. 7, no. 4, pp. 924–934, Apr. 2006, doi: 10.1002/cphc.200500602.

[59] S. Turchini, D. Catone, G. Contini, N. Zema, S. Irrera, M. Stener, D. Di Tommaso, P. Decleva, and T. Prosperi, “Conformational effects in photoelectron circular dichroism of alaninol,” *ChemPhysChem*, vol. 10, no. 11, pp. 1839–1846, Aug. 2009, doi: 10.1002/cphc.200800862.

[60] G. A. Garcia, H. H. Soldi-Lose, L. Nahon, and I. Powis, “Photoelectron circular dichroism spectroscopy in an orbitally congested system: The Terpene Endoborneol,” *J. Phys. Chem. A*, vol. 114, no. 2, pp. 847–853, Jan. 2010, doi: 10.1021/jp909344r.

[61] S. Turchini, D. Catone, N. Zema, G. Contini, T. Prosperi, P. Decleva, M. Stener, F. Rondino, S. Piccirillo, K. C. Prince, and M. Speranza, “Conformational sensitivity in photoelectron circular dichroism of 3-Methylcyclopentanone,” *ChemPhysChem*, vol. 14, no. 8, pp. 1723–1732, Jun. 2013, doi: 10.1002/cphc.201200975.

[62] L. Nahon, G. A. Garcia, H. Soldi-Lose, S. Daly, and I. Powis, “Effects of dimerization on the photoelectron angular distribution parameters from chiral camphor enantiomers obtained with circularly polarized vacuum-ultraviolet radiation,” *Phys. Rev. A*, vol. 82, no. 3, p. 032514, Sep. 2010, doi: 10.1103/PhysRevA.82.032514.

[63] S. Daly, I. Powis, G. A. Garcia, H. Soldi-Lose, and L. Nahon, “Photoionization of epichlorohydrin enantiomers and clusters studied with circularly polarized vacuum ultraviolet radiation,” *J. Chem. Phys.*, vol. 134, no. 6, p. 064306, Feb. 2011, doi: 10.1063/1.3536500.

[64] I. Powis, S. Daly, M. Tia, B. C. de Miranda, G. A. Garcia, and L. Nahon, “A photoionization investigation of small, homochiral clusters of glycidol using circularly polarized radiation and velocity map electron–ion coincidence imaging,” *Phys. Chem. Chem. Phys.*, vol. 16, no. 2, pp. 467–476, 2014, doi: 10.1039/C3CP53248H.

[65] G. Contini, N. Zema, S. Turchini, D. Catone, T. Prosperi, V. Carravetta, P. Bolognesi, L. Avaldi, and V. Feyer, “Vibrational state dependence of β and D asymmetry parameters: The case of the highest occupied molecular orbital photoelectron spectrum of methyl-oxirane,” *J. Chem. Phys.*, vol. 127, no. 12, p. 124310, Sep. 2007, doi: 10.1063/1.2779324.

[66] G. A. Garcia, L. Nahon, S. Daly, and I. Powis, "Vibrationally induced inversion of photoelectron forward-backward asymmetry in chiral molecule photoionization by circularly polarized light," *Nat. Commun.*, vol. 4, no. 1, p. 2132, Oct. 2013, doi: 10.1038/ncomms3132.

[67] C. N. Yang, "On the Angular Distribution in Nuclear Reactions and Coincidence Measurements," *Phys. Rev.*, vol. 74, no. 7, pp. 764–772, Oct. 1948, doi: 10.1103/PhysRev.74.764.

[68] U. B. von Grafenstein and A. Bornschlegl, "Circular dichroism laser mass spectrometry: Differentiation of 3-methylcyclopentanone enantiomers," *ChemPhysChem*, vol. 7, no. 10, pp. 2085–2087, Oct. 2006, doi: 10.1002/cphc.200600376.

[69] A. Bornschlegl, C. Logé, and U. Boesl, "Investigation of CD effects in the multi photon ionisation of R-(+)-3-methylcyclopentanone," *Chem. Phys. Lett.*, vol. 447, no. 4–6, pp. 187–191, Oct. 2007, doi: 10.1016/j.cplett.2007.09.012.

[70] C. Logé and U. Boesl, "Multiphoton ionization and circular dichroism: New experimental approach and application to natural products," *ChemPhysChem*, vol. 12, no. 10, pp. 1940–1947, Jul. 2011, doi: 10.1002/cphc.201100035.

[71] L. Yang, X. Wang, Y. Cui, Y. Tian, H. Chen, and Z. Wang, "Modification of renewable resources-lignin-by three chemical methods and its applications to polyurethane foams," *Polym. Adv. Technol.*, vol. 25, no. 10, pp. 1089–1098, Oct. 2014, doi: 10.1002/pat.3356.

[72] P. Horsch, G. Urbasch, and K.-M. Weitzel, "Circular dichroism in ion yields in multiphoton ionization of (R)-propylene oxide employing femtosecond laser pulses," *Zeitschrift für Phys. Chemie*, vol. 225, no. 5, pp. 587–594, May 2011, doi: 10.1524/zpch.2011.0103.

[73] C. Lux, M. Wollenhaupt, T. Bolze, Q. Liang, J. Kçhler, C. Sarpe, and T. Baumert, "Circular dichroism in the photoelectron angular distributions of camphor and fenchone from multiphoton ionization with femtosecond laser pulses," *Angew. Chemie Int. Ed.*, vol. 51, no. 20, pp. 5001–5005, May 2012, doi: 10.1002/anie.201109035.

[74] C. S. Lehmann, N. B. Ram, I. Powis, and M. H. M. Janssen, "Imaging photoelectron circular dichroism of chiral molecules by femtosecond multiphoton coincidence detection," *J. Chem. Phys.*, vol. 139, no. 23, p. 234307, Dec. 2013, doi: 10.1063/1.4844295.

[75] M. M. R. Fanood, I. Powis, and M. H. M. Janssen, "Chiral asymmetry in the multiphoton ionization of methyloxirane using femtosecond electron–ion coincidence imaging," *J. Phys. Chem. A*, vol. 118, no. 49, pp. 11541–11546, Dec. 2014, doi: 10.1021/jp5113125.

[76] M. M. R. Fanood, M. H. M. M. Janssen, and I. Powis, "Enantioselective femtosecond laser photoionization spectrometry of limonene using photoelectron circular dichroism," *Phys. Chem. Chem. Phys.*, vol. 17, no. 14, pp. 8614–8617, 2015, doi: 10.1039/C5CP00583C.

[77] C. Lux, M. Wollenhaupt, C. Sarpe, and T. Baumert, "Photoelectron circular dichroism of bicyclic ketones from multiphoton ionization with femtosecond

laser pulses," *ChemPhysChem*, vol. 16, no. 1, pp. 115–137, Jan. 2015, doi: 10.1002/cphc.201402643.

[78] S. Beaulieu, A. Ferré, R. Géneaux, R. Canonge, D. Descamps, B. Fabre, N. Fedorov, F. Légaré, S. Petit, T. Ruchon, V. Blanchet, Y. Mairesse, and B. Pons, "Universality of photoelectron circular dichroism in the photoionization of chiral molecules," *New J. Phys.*, vol. 18, no. 10, p. 102002, Oct. 2016, doi: 10.1088/1367-2630/18/10/102002.

[79] M. M. R. Fanood, M. H. M. Janssen, and I. Powis, "Wavelength dependent photoelectron circular dichroism of limonene studied by femtosecond multiphoton laser ionization and electron-ion coincidence imaging," *J. Chem. Phys.*, vol. 145, no. 12, p. 124320, Sep. 2016, doi: 10.1063/1.4963229.

[80] A. Kastner, T. Ring, B. C. Krüger, G. B. Park, T. Schäfer, A. Senftleben, and T. Baumert, "Intermediate state dependence of the photoelectron circular dichroism of fenchone observed via femtosecond resonance-enhanced multi-photon ionization," *J. Chem. Phys.*, vol. 147, no. 1, p. 013926, Jul. 2017, doi: 10.1063/1.4982614.

[81] A. Comby, S. Beaulieu, M. Boggio-Pasqua, D. Descamps, F. Légare, L. Nahon, S. Petit, B. Pons, B. Fabre, Y. Mairesse, and Valérie Blanchet "Relaxation dynamics in photoexcited chiral molecules studied by time-resolved photoelectron circular dichroism: Toward chiral femtochemistry," *J. Phys. Chem. Lett.*, vol. 7, no. 22, pp. 4514–4519, Nov. 2016, doi: 10.1021/acs.jpclett.6b02065.

[82] S. Beaulieu, A. Comby, D. Descamps, S. Petit, F. Légaré, B. Fabre, V. Blanchet, and Y. Mairesse, "Multiphoton photoelectron circular dichroism of limonene with independent polarization state control of the bound-bound and bound-continuum transitions," *J. Chem. Phys.*, vol. 149, no. 13, p. 134301, Oct. 2018, doi: 10.1063/1.5042533.

[83] R. E. Goetz, T. A. Isaev, B. Nikoobakht, R. Berger, and C. P. Koch, "Theoretical description of circular dichroism in photoelectron angular distributions of randomly oriented chiral molecules after multi-photon photoionization," *J. Chem. Phys.*, vol. 146, no. 2, p. 024306, Jan. 2017, doi: 10.1063/1.4973456.

[84] J. J. Larsen, K. Hald, N. Bjerre, H. Stapelfeldt, and T. Seideman, "Three dimensional alignment of molecules using elliptically polarized laser fields," *Phys. Rev. Lett.*, vol. 85, no. 12, pp. 2470–2473, Sep. 2000, doi: 10.1103/PhysRevLett.85.2470.

[85] A. S. Chatterley, E. T. Karamatskos, C. Schouder, L. Christiansen, A. V. Jørgensen, T. Mullins, J. Kupper, and H. Stapelfeldt, "Communication: Switched wave packets with spectrally truncated chirped pulses," *J. Chem. Phys.*, vol. 148, no. 22, p. 221105, Jun. 2018, doi: 10.1063/1.5028359.

[86] D. Irimia, R. Kortekaas, and M. H. M. Janssen, "In situ characterization of a cold and short pulsed molecular beam by femtosecond ion imaging," *Phys. Chem. Chem. Phys.*, vol. 11, no. 20, p. 3958, 2009, doi: 10.1039/b822960k.

[87] N. de Oliveira, D. Joyeux, M. Roudjane, J. F. Gil, B. Pilette, L. Archer, K. Ito,

and L. Nahon, “The high-resolution absorption spectroscopy branch on the VUV beamline DESIRS at SOLEIL,” *J. Synchrotron Radiat.*, vol. 23, no. 4, pp. 887–900, Jul. 2016, doi: 10.1107/S1600577516006135.

[88] N. de Oliveira, M. Roudjane, D. Joyeux, D. Phalippou, J.-C. Rodier, and L. Nahon, “High-resolution broad-bandwidth Fourier-transform absorption spectroscopy in the VUV range down to 40 nm,” *Nat. Photonics*, vol. 5, no. 3, pp. 149–153, Mar. 2011, doi: 10.1038/nphoton.2010.314.

[89] L. Nahon, N. de Oliveira, G. A. Garcia, J. F. Gil, B. Pilette, O. Marcouille, B. Lagarde, and F. Polack, “DESIRS: a state-of-the-art VUV beamline featuring high resolution and variable polarization for spectroscopy and dichroism at SOLEIL,” *J. Synchrotron Radiat.*, vol. 19, no. 4, pp. 508–520, Jul. 2012, doi: 10.1107/S0909049512010588.

[90] M. A. Śmiałek, M.-J. Hubin-Franskin, J. Delwiche, D. Duflot, N. J. Mason, S. Vrønning-Hoffmann, G. G. B. de Souza, A. M. F. Rodrigues, F. N. Rodrigues, and P. Lima˜o-Vieira, “Limonene: Electronic state spectroscopy by high-resolution vacuum ultraviolet photoabsorption, electron scattering, He(i) photoelectron spectroscopy and ab initio calculations,” *Phys. Chem. Chem. Phys.*, vol. 14, no. 6, pp. 2056–2064, Feb. 2012, doi: 10.1039/c2cp22847e.

[91] A. Vredenborg, W. G. Roeterdink, and M. H. M. Janssen, “A photoelectron-photoion coincidence imaging apparatus for femtosecond time-resolved molecular dynamics with electron time-of-flight resolution of σ = 18 ps and energy resolution ΔE⁄E = 3.5%,” *Rev. Sci. Instrum.*, vol. 79, no. 6, p. 063108, Jun. 2008, doi: 10.1063/1.2949142.

[92] J. Arlt, D. P. Singh , J. O. F. Thompson , A. S. Chatterley , P. Hockett , H. Stapelfeldt, and K. L. Reid, “Photoelectron angular distributions from resonant two-photon ionisation of adiabatically aligned naphthalene and aniline molecules,” *Mol. Phys.*, p. e1836411, Oct. 2020, doi: 10.1080/00268976.2020.1836411.

[93] A. S. Chatterley, C. Schouder, L. Christiansen, B. Shepperson, M. H. Rasmussen, and H. Stapelfeldt, “Long-lasting field-free alignment of large molecules inside helium nanodroplets,” *Nat. Commun.*, vol. 10, no. 1, p. 133, Dec. 2019, doi: 10.1038/s41467-018-07995-0.

[94] C. Bordas, F. Paulig, H. Helm, and D. L. Huestis, “Photoelectron imaging spectrometry: Principle and inversion method,” *Rev. Sci. Instrum.*, vol. 67, no. 6, pp. 2257–2268, Jun. 1996, doi: 10.1063/1.1147044.

[95] V. Dribinski, A. Ossadtchi, V. A. Mandelshtam, and H. Reisler, “Reconstruction of Abel-transformable images: The Gaussian basis-set expansion Abel transform method,” *Rev. Sci. Instrum.*, vol. 73, no. 7, pp. 2634–2642, Jul. 2002, doi: 10.1063/1.1482156.

[96] G. A. Garcia, L. Nahon, and I. Powis, “Two-dimensional charged particle image inversion using a polar basis function expansion,” *Rev. Sci. Instrum.*, vol. 75, no. 11, pp. 4989–4996, Nov. 2004, doi: 10.1063/1.1807578.

[97] G. A. Garcia, B. K. Cunha de Miranda, M. Tia, S. Daly, and L. Nahon, “DELICIOUS III: A multipurpose double imaging particle coincidence

spectrometer for gas phase vacuum ultraviolet photodynamics studies," *Rev. Sci. Instrum.*, vol. 84, no. 5, p. 053112, May 2013, doi: 10.1063/1.4807751.

[98] Z. Qu, Z. Qin, X. Zheng, H. Wang, G, Yao, X. Zhang, and Z. Cui, "Slow-electron velocity-map imaging study of aniline via resonance-enhanced two-photon ionization method," *Spectrochim. Acta Part A Mol. Biomol. Spectrosc.*, vol. 173, pp. 432–438, Feb. 2017, doi: 10.1016/j.saa.2016.09.046.

[99] B. Schaefer, E. Collett, R. Smyth, D. Barrett, and B. Fraher, "Measuring the Stokes polarization parameters," *Am. J. Phys.*, vol. 75, no. 2, pp. 163–168, Feb. 2007, doi: 10.1119/1.2386162.

[100] G. G. Stokes, "On the composition and resolution of steams of polarized light from different souces," *Trans. Cambridge Philos.*, vol. 9, p. 399, 1852.

[101] E. Wolf, "Optics in terms of observable quantities," *Nuovo Cim.*, vol. 12, no. 6, pp. 884–888, 1954, doi: 10.1007/BF02781855.

[102] K.-N. Huang, "Theory of angular distribution and spin polarization of photoelectrons," *Phys. Rev. A*, vol. 22, no. 1, pp. 223–239, Jul. 1980, doi: 10.1103/PhysRevA.22.223.

[103] I. Powis, C. J. Harding, S. Barth, S. Joshi, V. Ulrich, and U. Hergenhahn, "Chiral asymmetry in the angle-resolved O and C $1s^{-1}$ core photoemissions of the R enantiomer of glycidol," *Phys. Rev. A*, vol. 78, no. 5, p. 052501, Nov. 2008, doi: 10.1103/PhysRevA.78.052501.

[104] J. Fidler, P. M. Rodger, and A. Rodger, "Circular dichroism as a probe of chiral solvent structure around chiral molecules," *J. Chem. Soc. Perkin Trans. 2*, no. 2, p. 235, Jan. 1993, doi: 10.1039/p29930000235.

[105] F. Pulm, J. Schramm, J. Hormes, S. Grimme, and S. D. Peyerimhoff, "Theoretical and experimental investigations of the electronic circular dichroism and absorption spectra of bicyclic ketones," *Chem. Phys.*, vol. 224, no. 2–3, pp. 143–155, Dec. 1997, doi: 10.1016/S0301-0104(97)00258-9.

[106] K. B. Wiberg, Y. Wang, M. J. Murphy, and P. H. Vaccaro, "Temperature Dependence of Optical Rotation: α-Pinene, β-Pinene Pinane, Camphene, Camphor and Fenchone," *J. Phys. Chem. A*, vol. 108, no. 26, pp. 5559–5563, Jul. 2004, doi: 10.1021/jp040085g.

[107] T. Müller, K. B. Wiberg, and P. H. Vaccaro, "Cavity Ring-Down Polarimetry (CRDP): A new scheme for probing circular birefringence and circular dichroism in the gas phase," *J. Phys. Chem. A*, vol. 104, no. 25, pp. 5959–5968, Jun. 2000, doi: 10.1021/jp000705n.

[108] T. Lischke, N. Böwering, B. Schmidtke, N. Müller, T. Khalil, and U. Heinzmann, "Circular dichroism in valence photoelectron spectroscopy of free unoriented chiral molecules: Camphor and bromocamphor," *Phys. Rev. A*, vol. 70, no. 2, p. 022507, Aug. 2004, doi: 10.1103/PhysRevA.70.022507.

[109] S. Beaulieu, A. Comby, B. Fabre, D. Descamps, A. Ferre, G. Garcia, R. Geneaux, F. Legare, L. Nahon, S. Petit, T. Ruchon, B. Pons, V. Blancheta, and Y. Mairesse, "Probing ultrafast dynamics of chiral molecules using time-resolved photoelectron circular dichroism," *Faraday Discuss.*, vol. 194, pp.

325–348, 2016, doi: 10.1039/C6FD00113K.

[110] A. Kastner, C. Lux, T. Ring, S. Zìllighoven, C. Sarpe, A. Senftleben, and T. Baumert, “Enantiomeric excess sensitivity to below one percent by using femtosecond photoelectron circular dichroism,” *ChemPhysChem*, vol. 17, no. 8, pp. 1119–1122, Apr. 2016, doi: 10.1002/cphc.201501067.

[111] C. J. Harding and I. Powis, “Sensitivity of photoelectron circular dichroism to structure and electron dynamics in the photoionization of carvone and related chiral monocyclic terpenone enantiomers,” *J. Chem. Phys.*, vol. 125, no. 23, p. 234306, Dec. 2006, doi: 10.1063/1.2402175.

[112] M. Getzlaff and G. Schönhense, “Electronic structure of terpene derivatives,” *J. Electron Spectros. Relat. Phenomena*, vol. 95, no. 2–3, pp. 225–230, Oct. 1998, doi: 10.1016/S0368-2048(98)00212-6.

[113] T. J. Cornish and T. Baer, “An experimental link between the carbon-13 NMR chemical shift of carbonyl carbons and the energy shifts observed in the n→3s optical transition of cyclic ketones,” *J. Am. Chem. Soc.*, vol. 110, no. 19, pp. 6287–6291, Sep. 1988, doi: 10.1021/ja00227a001.

[114] J. W. Driscoll, T. Baer, and T. J. Cornish, “The analysis of conformations and configurations of substituted cyclic ketones by multiphoton ionization,” *J. Mol. Struct.*, vol. 249, no. 1, pp. 95–107, Aug. 1991, doi: 10.1016/0022-2860(91)85057-A.

[115] A. Kastner, G. Koumarianou, P. Glodic, P. C. Samartzis, N. Ladda, S. T. Ranecky, T. Ring, S. Vasudevan, C. Witte, H. Braun, H. G. Lee, A. Senftleben, R. Berger, G. B. Park, T. Schafer and T. Baumert, “High-resolution resonance-enhanced multiphoton photoelectron circular dichroism,” *Phys. Chem. Chem. Phys.*, vol. 22, no. 14, pp. 7404–7411, 2020, doi: 10.1039/D0CP00470G.

[116] D. P. Singh, N. De Oliveira, G. A. Garcia, A. Vredenborg, and I. Powis, “Experimental and Theoretical Investigation of the 3sp(d) Rydberg States of Fenchone by Polarized Laser Resonance-Enhanced-Multiphoton-Ionization and Fourier Transform VUV Absorption Spectroscopy,” *ChemPhysChem*, p. cphc.202000365, Oct. 2020, doi: 10.1002/cphc.202000365.

[117] W. J. Meath and E. A. Power, “On the importance of permanent moments in multiphoton absorption using perturbation theory,” *J. Phys. B At. Mol. Phys.*, vol. 17, no. 5, pp. 763–781, Mar. 1984, doi: 10.1088/0022-3700/17/5/017.

[118] M. A. C. Nascimento, “The polarization dependence of two-photon absorption rates for randomly oriented molecules,” *Chem. Phys.*, vol. 74, no. 1, pp. 51–66, Jan. 1983, doi: 10.1016/0301-0104(83)80007-X.

[119] P. R. Monson and W. M. McClain, “Complete polarization study of the two-photon absorption of liquid 1-chloronaphthalene,” *J. Chem. Phys.*, vol. 56, no. 10, pp. 4817–4825, 1972, doi: 10.1063/1.1676956.

[120] J. A. Tiburcio-Moreno, J. J. Alvarado-Gil, C. Diaz, L. Echevarria, and F. E. Hernández, “Polarization dependent two-photon absorption spectroscopy on a naturally occurring biomarker (curcumin) in solution: A theoretical-experimental study,” *Chem. Phys. Lett.*, vol. 583, pp. 160–164, 2013, doi: 10.1016/j.cplett.2013.07.080.

[121] M. G. Vivas, D. L. Silva, L. De Boni, Y. Bretonniere, C. Andraud, F. Laibe-Darbour, J-C Mulatier, R. Zaleśny, W. Bartkowiak, S. Canuto, and C. R. Mendonca1, "Revealing the electronic and molecular structure of randomly oriented molecules by polarized two-photon spectroscopy," *J. Phys. Chem. Lett.*, vol. 4, no. 10, pp. 1753–1759, 2013, doi: 10.1021/jz4007004.

[122] L. De Boni, C. Toro, and F. E. Hernández, "Synchronized double L-scan technique for the simultaneous measurement of polarization-dependent two-photon absorption in chiral molecules," *Opt. Lett.*, vol. 33, no. 24, p. 2958, Dec. 2008, doi: 10.1364/OL.33.002958.

[123] M. G. Vivas, L. De Boni, Y. Bretonniere, C. Andraud, and C. R. Mendonca, "Polarization effect on the two-photon absorption of a chiral compound," *Opt. Express*, vol. 20, no. 17, p. 18600, Aug. 2012, doi: 10.1364/OE.20.018600.

[124] D. H. Parker, J. O. Berg, and M. A. El-Sayed, "The symmetry of the 6.2 eV two-photon Rydberg state in hexatriene from the polarization properties of the multiphoton ionization spectrum," *Chem. Phys. Lett.*, vol. 56, no. 2, pp. 197–199, Jun. 1978, doi: 10.1016/0009-2614(78)80220-6.

[125] J. O. Berg, D. H. Parker, and M. A. El-Sayed, "Symmetry assignment of two-photon states from polarization characteristics of multiphoton ionization spectra," *J. Chem. Phys.*, vol. 68, no. 12, pp. 5661–5663, 1978, doi: 10.1063/1.435666.

[126] B. A. Heath, G. J. Fisanick, M. B. Robin, and T. S. Eichelberger, "Extracting the two-photon polarization ratio of the n →3 s transition in acetaldehyde from MPI measurements," *J. Chem. Phys.*, vol. 72, no. 11, pp. 5991–5997, 1980, doi: 10.1063/1.439097.

[127] L. Nahon, L. Nag, G. A. Garcia, I. Myrgorodska, U. Meierhenrich, S. Beaulieu, V. Wanie, V. Blanchet, R. Geneauxd, and I. Powis, "Determination of accurate electron chiral asymmetries in fenchone and camphor in the VUV range: sensitivity to isomerism and enantiomeric purity," *Phys. Chem. Chem. Phys.*, vol. 18, no. 18, pp. 12696–12706, 2016, doi: 10.1039/C6CP01293K.

[128] H. Ganjitabar, R. Hadidi, G. A. Garcia, L. Nahon, and I. Powis, "Vibrationally-resolved photoelectron spectroscopy and photoelectron circular dichroism of bicyclic monoterpene enantiomers," *J. Mol. Spectrosc.*, vol. 353, pp. 11–19, Nov. 2018, doi: 10.1016/j.jms.2018.08.007.

[129] B. Salehi, S. Upadhyay, I. Erdogan Orhan, A. K. Jugran , S. L.D. Jayaweera, D. A. Dias, F. Sharopov,, Y. Taheri, N. Martins, N. Baghalpour, W. C. Cho, and J. Sharifi-Rad, "Therapeutic Potential of α- and β-Pinene: A Miracle Gift of Nature," *Biomolecules*, vol. 9, no. 11, p. 738, Nov. 2019, doi: 10.3390/biom9110738.

[130] I. Novak and B. Kovač, "Photoelectron spectroscopy of natural products: terpenes," *Spectrochim. Acta Part A Mol. Biomol. Spectrosc.*, vol. 61, no. 1–2, pp. 277–280, Jan. 2005, doi: 10.1016/j.saa.2004.04.015.

[131] D. Kubala, E. A. Drage, A. M. E. Al-Faydhi, J. Kocísek, P. Papp, V. Matejcík, P. Mach, J. Urban, P. Limão-Vieira, S.V. Hoffmann, S. Matejcík, and N. J. Mason, "Electron impact ionisation and UV absorption study of α- and β-

pinene," *Int. J. Mass Spectrom.*, vol. 280, no. 1–3, pp. 169–173, Feb. 2009, doi: 10.1016/j.ijms.2008.07.035.

[132] A. D. Müller, A. N. Artemyev, and P. V. Demekhin, "Photoelectron circular dichroism in the multiphoton ionization by short laser pulses. II. Three- and four-photon ionization of fenchone and camphor," *J. Chem. Phys.*, vol. 148, no. 21, p. 214307, Jun. 2018, doi: 10.1063/1.5032295.

[133] C. Qiu, J. Smuts, and K. A. Schug, "Analysis of terpenes and turpentines using gas chromatography with vacuum ultraviolet detection," *J. Sep. Sci.*, vol. 40, no. 4, pp. 869–877, Feb. 2017, doi: 10.1002/jssc.201601019.

[134] E. M. Neeman, J. R. Avilés Moreno, and T. R. Huet, "The gas phase structure of α-pinene, a main biogenic volatile organic compound," *J. Chem. Phys.*, vol. 147, no. 21, p. 214305, Dec. 2017, doi: 10.1063/1.5003726.

[135] P. Lahiri, K. B. Wiberg, and P. H. Vaccaro, "A Tale of Two Carenes: Intrinsic Optical Activity and Large-Amplitude Nuclear Displacement," *J. Phys. Chem. A*, vol. 116, no. 38, pp. 9516–9533, Sep. 2012, doi: 10.1021/jp303270d.

[136] V. A. Chuiko, E. N. Manukov, Y. V. Chukhov, and M. M. Timoshenko, "An investigation of terpene hydrocarbons of the carane series by photoelectron spectroscopy," *Chem. Nat. Compd.*, vol. 21, no. 5, pp. 600–605, Sep. 1985, doi: 10.1007/BF00579062.

[137] H. Ganjitabar, "Photoelectron circular dichroism (PECD) of monoterpenes using laser and synchrotron radiation," Universty of Nottingham, 2020.

[138] G. A. Garcia, H. Dossmann, L. Nahon, S. Daly, and I. Powis, "Identifying and Understanding Strong Vibronic Interaction Effects Observed in the Asymmetry of Chiral Molecule Photoelectron Angular Distributions," *ChemPhysChem*, vol. 18, no. 5, pp. 500–512, Mar. 2017, doi: 10.1002/cphc.201601250.

[139] M. M. R. Fanood, H. Ganjitabar, G. A. Garcia, L. Nahon, S. Turchini, and I. Powis, "Intense Vibronic Modulation of the Chiral Photoelectron Angular Distribution Generated by Photoionization of Limonene Enantiomers with Circularly Polarized Synchrotron Radiation," *ChemPhysChem*, vol. 19, no. 8, pp. 921–933, Apr. 2018, doi: 10.1002/cphc.201701248.

[140] C. Lux, A. Senftleben, C. Sarpe, M. Wollenhaupt, and T. Baumert, "Photoelectron circular dichroism observed in the above-threshold ionization signal from chiral molecules with femtosecond laser pulses," *J. Phys. B At. Mol. Opt. Phys.*, vol. 49, no. 2, p. 02LT01, Jan. 2016, doi: 10.1088/0953-4075/49/2/02LT01.

[141] M. Stener, P. Decleva, T. Mizuno, H. Yoshida, and A. Yagishita, "Off-resonance photoemission dynamics studied by recoil frame F1s and C1s photoelectron angular distributions of CH_3F," *J. Chem. Phys.*, vol. 140, no. 4, p. 044305, Jan. 2014, doi: 10.1063/1.4862267.

[142] H. Stapelfeldt, "Alignment of molecules by strong laser pulses," *Eur. Phys. J. D - At. Mol. Opt. Phys.*, vol. 26, no. 1, pp. 15–19, Sep. 2003, doi: 10.1140/epjd/e2003-00064-2.

[143] S. R. Long, J. T. Meek, and J. P. Reilly, "The laser photoelectron spectrum of

gas phase benzene," *J. Chem. Phys.*, vol. 79, no. 7, pp. 3206–3219, Oct. 1983, doi: 10.1063/1.446229.

[144] X. Zhang, J. M. Smith, and J. L. Knee, "High resolution threshold photoelectron spectroscopy of aniline and aniline van der Waals complexes," *J. Chem. Phys.*, vol. 97, no. 5, pp. 2843–2860, Sep. 1992, doi: 10.1063/1.463027.

[145] E. Drougas, J. G. Philis, and A. M. Kosmas, "Ab initio study of the structure of aniline in the S_1 and S_2 $\pi\pi^*$ states," *J. Mol. Struct. THEOCHEM*, vol. 758, no. 1, pp. 17–20, Jan. 2006, doi: 10.1016/j.theochem.2005.06.006.

[146] P. M. Mayer, V. Blanchet, and C. Joblin, "Threshold photoelectron study of naphthalene, anthracene, pyrene, 1,2-dihydronaphthalene, and 9,10-dihydroanthracene," *J. Chem. Phys.*, vol. 134, no. 24, p. 244312, Jun. 2011, doi: 10.1063/1.3604933.

[147] M. C. R. Cockett, H. Ozeki, K. Okuyama, and K. Kimura, "Vibronic coupling in the ground cationic state of naphthalene: A laser threshold photoelectron zero kinetic energy (ZEKE)-photoelectron spectroscopic study," *J. Chem. Phys.*, vol. 98, no. 10, pp. 7763–7772, May 1993, doi: 10.1063/1.464584.

[148] A. Hiraya, Y. Achiba, N. Mikami, and K. Kimura, "Vibrationally resolved photoelectron spectra of jet-cooled naphthalene: Intramolecular relaxation processes in S_1 and S_2 states," *J. Chem. Phys.*, vol. 82, no. 4, pp. 1810–1817, Feb. 1985, doi: 10.1063/1.448415.

[149] M. A. Duncan, T. G. Dietz, and R. E. Smalley, "Two-color photoionization of naphthalene and benzene at threshold," *J. Chem. Phys.*, vol. 75, no. 5, pp. 2118–2125, Sep. 1981, doi: 10.1063/1.442315.

[150] S. M. Beck, D. E. Powers, J. B. Hopkins, and R. E. Smalley, "Jet-cooled naphthalene. I. Absorption spectra and line profiles," *J. Chem. Phys.*, vol. 73, no. 5, pp. 2019–2028, Sep. 1980, doi: 10.1063/1.440421.

[151] F. A. Gianturco, R. R. Lucchese, and N. Sanna, "Calculation of low-energy elastic cross sections for electron-CF_4 scattering," *J. Chem. Phys.*, vol. 100, no. 9, pp. 6464–6471, May 1994, doi: 10.1063/1.467237.

[152] A. P. P. Natalense and R. R. Lucchese, "Cross section and asymmetry parameter calculation for sulfur 1s photoionization of SF_6," *J. Chem. Phys.*, vol. 111, no. 12, pp. 5344–5348, Sep. 1999, doi: 10.1063/1.479794.

[153] X. Song, M. Yang, E. R. Davidson, and J. P. Reilly, "Zero kinetic energy photoelectron spectra of jet-cooled aniline," *J. Chem. Phys.*, vol. 99, no. 5, pp. 3224–3233, Sep. 1993, doi: 10.1063/1.465131.

[154] J. O. F. Thompson *et al.*, "Finite slice analysis (FINA) of sliced and velocity mapped images on a Cartesian grid," *J. Chem. Phys.*, vol. 147, no. 7, p. 074201, Aug. 2017, doi: 10.1063/1.4986966.

[155] J. O. F. Thompson, C. Amarasinghe, C. D. Foley, and A. G. Suits, "Finite slice analysis (FINA)—A general reconstruction method for velocity mapped and time-sliced ion imaging," *J. Chem. Phys.*, vol. 147, no. 1, p. 013913, Jul. 2017, doi: 10.1063/1.4979305.

[156] C. Toro, L. De Boni, N. Lin, F. Santoro, A. Rizzo, and F. E. Hernandez, "Two-

photon absorption circular dichroism: A new twist in nonlinear spectroscopy," *Chem. A. Eur. J.*, vol. 16, no. 11, pp. 3504–3509, 2010, doi: 10.1002/chem.200902286.

[157] "National Center for Biotechnology Information. 'PubChem Compound Summary for CID 6654, alpha-Pinene' PubChem,." https://pubchem.ncbi.nlm.nih.gov/compound/alpha-Pinene (accessed Oct. 22, 2020).